TECHNICAL UNIVERSITY OF CLUJ-NAPOCA
Faculty of Electrical Engineering
Department of Electric Machines and Drives

UNIVERSITÉ LIBRE DE BRUXELLES
Brussels School of Engineering
Department of Bio-, Electro- And Mechanical Systems

Eng. Vlad Petruș

DOCTORAL THESIS

SWITCHED RELUCTANCE MOTORS FOR ELECTRIC VEHICLE PROPULSION – COMPARATIVE NUMERICAL AND EXPERIMENTAL STUDY OF CONTROL SCHEMES

Supervisors:

Prof. Vasile Iancu, Ph.D.

Prof. Johan Gyselinck, Ph.D.

Members of the Committee:

PRESIDENT: Prof. ***Ioan Târnovan,*** *Ph.D.* – dean Faculty of Electrical Engineering, Technical University of Cluj-Napoca

MEMBERS:
Prof. ***Vasile Iancu,*** *Ph.D.* – thesis director, Technical University of Cluj-Napoca
Prof. ***Johan Gyselinck,*** *Ph.D.* – thesis director, Université Libre de Bruxelles
Prof. ***Ion Boldea,*** *Ph.D.* – reviewer, „Politehnica" University of Timișoara"
Prof. ***Jean-Claude Maun,*** *Ph.D.* – reviewer, Université Libre de Bruxelles
Prof. ***Joeri Van Mierlo,*** *Ph.D.* – reviewer, Vrije Universiteit Brussel
Prof. ***Claudia Steluța Marțiș,*** *Ph.D.* - reviewer, Technical University of Cluj-Napoca
Prof. ***Pierre Mathys,*** *Ph.D.* – reviewer, Université Libre de Bruxelles

UNIVERSITÉ LIBRE de BRUXELLES

TECHNICAL UNIVERSITY of CLUJ-NAPOCA

Abstract

Brussels School of Engineering, BEAMS Department

Faculty of Electrical Engineering, Dept. of Electric Machines and Drives

Doctor of Philosophy

Switched Reluctance Motors for Electric Vehicle Propulsion - Comparative Numerical and Experimental Study of Control Schemes

by Vlad Petruş

Policies to reduce emissions from transportation are implemented by different World and European associations. Personal and freight transportation is one of the key contributors in GHG emissions, being the second biggest GHG emitter after energy sector in the European Union. The policies to reduce emissions from transportation are focusing on the optimization of the efficiency of the existing vehicles, the development of new sustainable fuels and propulsion systems and the electrification of the vehicles

The continuously increasing price of the permanent magnets and the shortage of rare earths demand the finding of alternatives for the permanent magnet synchronous machines which is currently the leading technology in several domains as hybrid and full electric propulsion and wind turbines due to their best overall performances.

The good efficiency and the large constant power-speed ratio in addition to low the cost, high reliability and fault-tolerance make the SRM a candidate with real chances on the market of vehicle propulsion. The main drawbacks of the SRM related to the torque ripple, noise and vibration make the research object in R&Ds all over the world.

This thesis is focused on the development of an efficient and robust switched reluctance drive which can be integrated in a hybrid dive train or can be solely used for electric vehicle traction. To achieve this goal, various instantaneous and average torque control techniques are implemented and compared. A converter is designed, built and integrated on a test bench which allows testing SRMs for vehicle propulsion. An investigation on noise production in SRDs ends the thesis.

Acknowledgements

This research was financially supported in the frame of the project Doctoral studies in engineering sciences with purpose to develop knowledge-based society SIDOC (abbreviation from Romanian), Contract POSDRU/88/1.5/S/60078.

I would like to thank my supervisor from Technical University of Cluj-Napoca, Prof. Vasile Iancu, for the freedom granted during the research and my supervisor from Université Libre de Bruxelles, Prof. Johan Gyselinck, for the financial support. Also, I would like to thank Prof. Claudia Steluta Martis from Technical University of Cluj-Napoca for facilitating the communication between the two partner institutions.

I wish to thank our industrial partners, Punch Powertrain from Sint-Truiden, Belgium and LMS from Leuven, Belgium for the interesting discussions we had during this research. I would like to express my gratitude to Punch Powertrain for the SRM they have donated to the university and LMS for providing the noise measurement equipment.

I would like to thank my colleagues from Technical University of Cluj-Napoca anf from Université Libre de Bruxelles for the interesting discussions and pleasant times we have spent together.

I wish to thank my colleague Adrian-Cornel Pop with whom I have spent a lot of time working together during this research for his support, interesting discussions and pleasant times we have spent together during these last three years.

I wish to show my gratitude to my family for their relentless support and for cheering me up when I was away and down.

I am infinitely grateful to my wife for her support and patience during the last couple of years when we were apart for the sake of science.

Contents

Abstract ii

Acknowledgements iii

List of Figures ix

List of Tables xv

Abbreviations xvii

Symbols xix

1 Introduction 1
- 1.1 Background and Motivation . . . 1
- 1.2 Objectives of the Thesis . . . 7
- 1.3 Outline of the Thesis . . . 7

2 Magnetic Characterisation of SRMs 9
- 2.1 FEM-based Electromagnetic Analysis of the SRM . . . 10
- 2.2 Experimental Methods to Determine the Magnetization Curves . . . 16
  - 2.2.1 The AC Method . . . 16
  - 2.2.2 The Flux Linkage Method . . . 17
  - 2.2.3 The Torque Measurement Method . . . 18
- 2.3 Measurement of the Magnetization Curves . . . 18
- 2.4 Conclusions . . . 20

3 Average Torque Control of SRMs 23
- 3.1 Torque Production in SRM . . . 23
- 3.2 Drive Parameter Computation . . . 28
  - 3.2.1 Analytical Drive Parameter Computation . . . 29
  - 3.2.2 Numerical Drive Parameter Computation . . . 31
- 3.3 On-line Average Torque Estimation . . . 39
- 3.4 Direct Average Torque Control . . . 41
- 3.5 Generator Operation of the Switched Reluctance Machine . . . 44
- 3.6 Speed Control of the Switched Reluctance Machine . . . 51
- 3.7 Conclusions . . . 54

4 Instantaneous Torque Control of SRMs **57**
4.1 On-line Instantaneous Torque Estimation . . . 58
4.1.1 Estimation from Phase Currents and Rotor Position . . . 58
4.1.2 Estimation from Phase Fluxes and Rotor Position . . . 58
4.1.3 Estimation from Phase Currents and Voltages . . . 61
4.1.4 Position Estimation . . . 63
4.1.5 Phase Voltage Estimation . . . 64
4.2 Voltage States Definition . . . 64
4.3 Direct Instantaneous Torque Control . . . 65
4.3.1 Operating Principles of DITC . . . 65
4.3.2 Simulation Results of DITC . . . 70
4.3.3 Experimental Results of DITC . . . 70
4.4 Direct Torque Control . . . 73
4.4.1 Operating Principles of DTC . . . 73
4.4.2 Definition of the Switching Vectors and the Switching Table . . . 76
4.4.3 Simulation and Experimental Results of DTC . . . 78
4.5 Comparison of Different Instantaneous Torque Control Techniques . . . 80
4.6 Conclusions . . . 88

5 Converters for SRMs **89**
5.1 Requirements and Topology Selection . . . 91
5.2 Device Ratings . . . 93
5.3 Frequency Stress Calculation . . . 95
5.4 Power Losses in the Converter . . . 97
5.5 Thermal Model of the Converter . . . 99
5.6 Construction of the Converter . . . 101
5.7 Test Bench Description . . . 105
5.8 Switching Strategies in Switched Reluctance Drives . . . 107
5.9 Conclusions . . . 112

6 Noise in SRDs **113**
6.1 Noise Sources in SRMs . . . 113
6.1.1 Magnetic Sources . . . 113
6.1.2 Mechanical Sources . . . 114
6.1.3 Aerodynamic Sources . . . 115
6.1.4 Electronic Sources . . . 115
6.2 Calculation of Structural Eigen Frequencies . . . 116
6.2.1 Roark and Young Method . . . 116
6.2.2 Jordan, Frohne and Uner Method . . . 118
6.2.3 Rayleigh Method . . . 118
6.3 FEA Frequency Determination . . . 119
6.4 Measurements on the Test Bench . . . 119
6.5 Comparison of Frequency Determination Methods . . . 123
6.6 Conclusions . . . 124

7 Conclusions **127**
7.1 Contributions . . . 127

7.2 Future Work 130

A Average Torque Control Drive Parameters **131**

B Converter Types for SRMs **133**
B.1 Dissipative Converters 133
B.2 Magnetic Converters 134
B.3 Resonant Converters 134
B.4 Capacitive Converters 136

C Control Desk Interfaces **145**

D Superior Vibration Modes of the Stator Structure **151**

Bibliography **155**

List of Figures

1.1 Greenhouse gas emissions by sector and mode of transport [1] 2
1.2 Series hybrid power train of PHEVs [2] 3
1.3 Parallel hybrid power train of PHEVs [2] 4
1.4 Series-parallel hybrid power train of PHEVs [2] 5
1.5 Electric power train with SRM 6

2.1 The geometry of the SRM 11
2.2 The electric circuit 11
2.3 The mesh 12
2.4 Mesh in the airgap 12
2.5 Flux lines - unaligned position 13
2.6 Flux lines - intermediate position 13
2.7 Flux lines - aligned position 13
2.8 Magnetic flux density distribution - unaligned position 14
2.9 Magnetic flux density distribution - intermediate position 14
2.10 Magnetic flux density distribution - aligned position 14
2.11 Flux vs. rotor position at constant current 15
2.12 Flux vs. current at constant rotor position 15
2.13 Current vs. rotor position at constant flux 15
2.14 Current vs. flux at constant rotor position 15
2.15 Torque vs. rotor position at constant current 15
2.16 Torque vs. current at constant rotor position 15
2.17 Measurement circuit 18
2.18 Rotor blocking system 18
2.19 Rising current method: voltage and current waveforms 19
2.20 Falling current method: voltage and current waveforms 19
2.21 Magnetization curves: raw data 20
2.22 Magnetization curves: filtered data 20
2.23 Coenergy vs. rotor position at constant current 20
2.24 Torque vs. rotor position at constant current 20

3.1 Primitive single phase SRM [3] 23
3.2 Ideal waveforms of primitive single phase SRM 24
3.3 Typical energy conversion loop 25
3.4 Typical waveforms for low speed motoring 27
3.5 Typical measured voltage and current for low speed motoring 27
3.6 Typical waveforms for low speed motoring 27
3.7 Typical measured voltage and current for high speed motoring 27

3.8 Typical waveforms for very high speed motoring . . . 28
3.9 Feed-forward average torque control of SRM . . . 29
3.10 Inductance, current and voltage waveforms together with the definition of usual quantities . . . 30
3.11 Reference current versus torque and speed (scenario 2) . . . 33
3.12 Turn-on angle versus torque and speed (scenario 2) . . . 34
3.13 Turn-off angle versus torque and speed (scenario 2) . . . 34
3.14 Simulated waveforms of phase current, phase flux and instantaneous torque for a reference torque of 90Nm at 1500rpm (scenario 1) . . . 35
3.15 Simulated waveforms of phase current, phase flux and instantaneous torque for a reference torque of 90Nm at 1500rpm (scenario 2) . . . 35
3.16 Copper losses versus torque and speed (scenario 1) . . . 36
3.17 Torque ripple versus torque and speed (scenario 1) . . . 36
3.18 Copper losses versus torque and speed(scenario 2) . . . 37
3.19 Torque ripple versus torque and speed (scenario 2) . . . 37
3.20 Measured waveforms at 1500rpm and 30Nm using feed-forward average torque control technique . . . 38
3.21 Closed-loop structure of average torque control . . . 38
3.22 Structure of the average torque estimator [4] . . . 39
3.23 Typical quantities for the on-line average torque estimator [4] . . . 40
3.24 Reaction of the average torque estimator at a step change in the average torque 40
3.25 Reaction of the average torque estimator at a ramp change in the average torque 40
3.26 Direct average torque control of SRM . . . 41
3.27 Measured waveforms at 1500rpm and 30Nm using DATC . . . 42
3.28 The measured reaction of the DATC controller at step changes in the reference torque at 1500rpm . . . 42
3.29 The measured reaction of the DATC controller at ramp changes in the reference torque at 1500rpm . . . 43
3.30 The measured reaction of the DATC controller at sinusoidal changes in the reference torque at 1500rpm . . . 43
3.31 Typical current waveforms in generator operation . . . 45
3.32 Typical energy loops in generator operation . . . 45
3.33 Reference current versus torque and speed in generator operation . . . 47
3.34 Turn-on angle versus torque and speed in generator operation . . . 48
3.35 Turn-off angle versus torque and speed in generator operation . . . 48
3.36 Copper losses variation versus torque and speed in generator operation . . . 49
3.37 Torque ripple versus torque and speed in generator operation . . . 49
3.38 Simulated waveforms of phase currents, phase voltages, phase fluxes and instantaneous torque for a load torque of 40Nm at 1000rpm in generating mode . . . 50
3.39 Simulated waveforms of phase currents, phase voltages, phase fluxes and instantaneous torque for a load torque of 40Nm at 2500rpm in generating mode . . . 50
3.40 Simulated waveforms of phase currents, phase voltages, phase fluxes and instantaneous torque for a load torque of 40Nm at 6000rpm in generating mode . . . 50
3.41 Simulated waveforms of phase currents, phase voltages, phase fluxes and instantaneous torque for a load torque of 30Nm at 9000rpm in generating mode . . . 50
3.42 Measured waveforms of phase current and instantaneous torque for a load torque of 10Nm at 2000rpm in generating mode . . . 51

3.43 Measured waveforms of phase current and instantaneous torque for a load torque of 10Nm at 3000rpm in generating mode . . . 52
3.44 Measured waveforms of phase current and voltage in generating mode at 10Nm and 2000rpm . . . 52
3.45 Measured waveforms of phase current and voltage in generating mode at 10Nm and 3000rpm . . . 52
3.46 Speed control of switched reluctance machine . . . 53
3.47 Reaction of the speed controller to a step change in the reference . . . 53
3.48 Reaction of the speed controller to a ramp change in the reference . . . 54

4.1 The electromagnetic torque dependence on phase current and rotor angular position . . . 59
4.2 Electromagnetic torque estimation using phase current and rotor position . . . 59
4.3 The electromagnetic torque dependence on flux linkage and rotor angular position 60
4.4 Electromagnetic torque estimation using phase current and rotor position . . . 60
4.5 The flux linkage dependence on phase current and rotor angular position . . . 61
4.6 The electromagnetic torque dependence on phase current and flux linkage . . . 62
4.7 Electromagnetic torque estimation using phase current and rotor position . . . 62
4.8 Rotor position dependence on phase current and flux linkage . . . 63
4.9 Rotor position estimation using terminal quantities . . . 63
4.10 Phase voltage estimation from transistor gate signals . . . 64
4.11 The three possible voltage states of a phase of an SRM fed by an asymmetric H-Bridge . . . 65
4.12 Closed-loop structure of DITC . . . 66
4.13 Principle exemplification of DITC switching strategy . . . 67
4.14 Simulated torque waveforms at different speed values obtained by using DITC . 68
4.15 The simulated reaction of DITC controller at changes in the reference torque at 1000rpm . . . 68
4.16 The variation of copper losses with the electromagnetic torque at constant speed 69
4.17 The variation of copper losses with the speed at constant electromagnetic torque 69
4.18 Measured torque and phase currents at 500rpm, 15Nm, turn-on angle 37° and turn-off angle 58° . . . 71
4.19 Measured torque and phase currents at 500rpm, 15Nm, turn-on angle 33° and turn-off angle 54° . . . 71
4.20 The measured reaction of DITC controller at changes in the reference torque at 500rpm . . . 72
4.21 Definition of two frame reference axes for phase fluxes of the 3-phase SRM . . . 74
4.22 Definition of two frame reference axes for phase fluxes of the 4-phase SRM . . . 74
4.23 Definition of the space vectors for the 3-phase SRM . . . 77
4.24 Definition of the space vectors for the 4-phase SRM . . . 77
4.25 DTC simulated total torque, flux amplitude and phase currents . . . 79
4.26 DTC measured total torque, flux amplitude and phase currents . . . 79
4.27 DTC simulated flux vector trajectory . . . 80
4.28 DTC measured flux vector trajectory . . . 80
4.29 DTC simulated total torque, flux amplitude and phase currents at a step change of torque reference . . . 81
4.30 DTC measured total torque, flux amplitude and phase currents at a step change of torque reference . . . 81

4.31 DTC simulated total torque, flux amplitude and phase currents at a ramp change of torque reference . . . 82
4.32 DTC measured total torque, flux amplitude and phase currents at a ramp change of torque reference . . . 82
4.33 DTC simulated total torque, flux amplitude and phase currents at a step change of flux reference . . . 83
4.34 DTC measured total torque, flux amplitude and phase currents at a step change of flux reference . . . 83
4.35 DTC simulated flux vector trajectory at a step change of flux reference . . . 84
4.36 DTC measured flux vector trajectory at a step change of flux reference . . . 84
4.37 DTC simulated total torque, flux amplitude and phase currents at a ramp change of flux reference . . . 84
4.38 DTC measured total torque, flux amplitude and phase currents at a ramp change of flux reference . . . 85
4.39 DTC simulated flux vector trajectory at a ramp change of flux reference . . . 85
4.40 DTC measured flux vector trajectory at a ramp change of flux reference . . . 85
4.41 The measured waveforms of torque at 650rpm and a reference torque of 30Nm . 86
4.42 The measured waveforms of phase currents at 650rpm and a reference torque of 30Nm . . . 87

5.1 SRM converter classification by the number of switched per phase [5] . . . 90
5.2 SRM converter classification by commutation type [6] . . . 91
5.3 The asymmetric H bridge . . . 93
5.4 θ_r vs. speed and phase current . . . 95
5.5 Switching frequency vs. speed . . . 98
5.6 Thermal RC network for semiconductor devices from junction to case . . . 100
5.7 Junction case temperature rise of the IGBT and diode in the worst case scenario 100
5.8 Equivalent thermal network of the converter . . . 101
5.9 The power circuit of the converter . . . 101
5.10 SKM400GB12V IGBT module . . . 102
5.11 SKHI23/12R IGBT driver . . . 102
5.12 SKHI10/12R IGBT driver . . . 102
5.13 160MT120KPBF diode bridge rectifier . . . 103
5.14 B43580A5228M electrolytic capacitor . . . 103
5.15 MKP B32656S snubber capacitor . . . 103
5.16 dSPACE 1103 controller board and connector panel . . . 104
5.17 Signal conversion interface . . . 104
5.18 Electronic scheme of one channel of the signal conversion interface . . . 105
5.19 LEM LA205-S current transducer . . . 105
5.20 LEM CV3-1200 voltage transducer . . . 105
5.21 Final converter - front view . . . 106
5.22 Final converter - back view . . . 107
5.23 The experimental set-up . . . 108
5.24 Incremental encoder mounted on DC machine . . . 108
5.25 Variable reluctance resolver mounted on SRM . . . 109
5.26 Electronic board used for resolver signal treatment . . . 109
5.27 Hysteresis current control using hard switching . . . 110

5.28 Hysteresis current control using soft switching . . . 110
5.29 Hysteresis current control using hybrid switching . . . 111
5.30 Switching strategy in generator mode . . . 111

6.1 Noise sources in electric machines [5] . . . 114
6.2 Nodal magnetic force on a stator pole . . . 120
6.3 Radial force on a stator vs. current and rotor position . . . 120
6.4 Vibration mode 0 of the 8/6 SRM . . . 121
6.5 Vibration mode 2 of the 8/6 SRM . . . 121
6.6 Vibration mode 3 of the 8/6 SRM . . . 122
6.7 Vibration mode 4 of the 8/6 SRM . . . 122
6.8 Spectrogram of surface acceleration during run-up test from 0 to 1000rpm . . . 123
6.9 Spectrogram of surface acceleration during run-up test from 0 to 1000rpm . . . 124

A.1 Reference current versus torque and speed (scenario 1) . . . 131
A.2 Turn-on angle versus torque and speed (scenario 1) . . . 132
A.3 Turn-off angle versus torque and speed (scenario 1) . . . 132

B.1 Dissipative converter: R-dump [7] . . . 133
B.2 Magnetic converter: single controllable switch [7] . . . 134
B.3 Resonant converter: C-dump [7] . . . 134
B.4 Resonant converter: Boost [7] . . . 135
B.5 Resonant converter: High demagnetization [7] . . . 135
B.6 Single-capacitor converter: Asymmetric H-bridge [7] . . . 136
B.7 Single-capacitor converter: Shared switch [7] . . . 136
B.8 Single-capacitor converter: H-bridge [7] . . . 137
B.9 Single-capacitor converter: Modified C-dump [7] . . . 137
B.10 Passive boost with two capacitors: Parallel type [7] . . . 138
B.11 Passive boost with two capacitors: Series type [7] . . . 138
B.12 Passive boost with two capacitors: Series-parallel type [7] . . . 139
B.13 Series type passive converter: Split DC-link [7] . . . 139
B.14 Series type passive converter: Doubler DC-link [7] . . . 140
B.15 Active boost converter: Parallel type 1 [7] . . . 140
B.16 Active boost converter: Parallel type 2 [7] . . . 141
B.17 Active boost converter: Parallel type 3 [7] . . . 141
B.18 Active boost converter: Parallel type 4 [7] . . . 142
B.19 Active boost converter: Series type [7] . . . 142
B.20 Active boost converter: Series-parallel type [7] . . . 143

C.1 Control Desk Interface: Hysteresis control . . . 146
C.2 Control Desk Interface: DATC . . . 147
C.3 Control Desk Interface: DITC . . . 148
C.4 Control Desk Interface: DTC . . . 149
C.5 Control Desk Interface: Current profiling . . . 150

D.1 Vibration mode corresponding to 9053Hz . . . 151
D.2 Vibration mode corresponding to 11527Hz . . . 152
D.3 Vibration mode corresponding to 12778Hz . . . 152

D.4 Vibration mode corresponding to 19388Hz 153

List of Tables

2.1 Geometrical dimensions of the SRM 11

4.1 Motoring commutation strategy table of three adjacent phases for DITC 67
4.2 DTC motoring switching table of 3-phase SRM 78
4.3 DTC motoring switching table of 4-phase SRM 78
4.4 Comparison of copper losses computed based on measured currents of different instantaneous torque control techniques at 30Nm 87

6.1 Eigen frequencies of the 8/6 SRM in Hz 125

Abbreviations

AC	**A**lternating **C**urrent
CD	**C**harge-**D**epleting
CS	**C**harge-**S**ustaining
DATC	**D**irect **A**verage **T**orque **C**ontrol
DC	**D**irect **C**urrent
DTC	**D**irect **T**orque **C**ontrol
DITC	**D**irect **I**nstantaneous **T**orque **C**ontrol
EU	**E**uropean **U**nion
EV	**E**lectric **V**vehicle
GHG	**G**reen**h**ouse **G**as
HEV	**H**ybrid **E**electric **V**ehicle
ICE	**I**nternal **C**ombustion **E**ngine
IM	**I**nduction **M**achine
MEV	**M**ore **E**electric **V**ehicle
PHEV	**P**lugged-in **H**ybrid **E**electric **V**ehicle
PM	**P**ermanent **M**agnet
PMSM	**P**ermanent **M**agnet **S**ynchronous **M**achine
RMS	**R**oot **M**ean **S**quare
SRD	**S**witched **R**eluctance **D**rive
SRM	**S**witched **R**eluctance **M**achine

Symbols

D_{g}	rotor outer diameter
D_{out}	stator outer diameter
D_{ry}	rotor yoke outer diameter
D_{shaft}	shaft diameter
D_{sy}	stator yoke inner diameter
e	back emf
f	fundamental frequency
g	airgap length
i_{ph}	phase current
i_{pk}	peak current
i_{ref}	reference current
$\vec{i}_{\mathrm{s}}$	stator current vector
I_{ph}	RMS value of phase current
J	inertia
L_{a}	aligned inductance
L_{ph}	phase inductance
L_{pk}	inductance at peak flux
L_{stk}	stack length
L_{u}	unaligned inductance
N	speed in *rpm*
N_{b}	base speed in *rpm*
N_{c}	number of turns per coil
N_{ph}	number of phases
N_{r}	number of rotor poles
N_{s}	number of stator poles

N_{stk}	number of strokes per revolution
P_{Cu}	copper losses
P_{Fe}	iron losses
P_{in}	input power
P_{M}	mechanical power
P_{out}	output power
R_{ph}	phase resistance
t	time
T_{avg}	average torque
T_{inst}	instantaneous torque
T_{em}	total electromagnetic torque
T_{f}	friction torque
T_{L}	load torque
T_{max}	maximum torque
T_{min}	minimum torque
T_{ph}	phase torque
T_{ref}	reference torque
T_{rip}	torque ripple
$T_{\mathrm{rip,rel}}$	relative torque ripple
u_{ph}	phase voltage
$\vec{v}_{\mathrm{s}}$	stator voltage vector
V_{dc}	DC-bus voltage
W_{c}	coenergy
W_{elec}	electric energy
W_{exc}	excitation energy
W_{f}	field energy
W_{mag}	magnetic energy
W_{mech}	mechanic energy
W_{out}	delivered energy
β_{r}	rotor pole arc
β_{s}	stator pole arc
η	efficiency
λ_{ph}	phase flux

λ_0	initial phase flux
λ_{pk}	peak flux
$\vec{\lambda}_{\mathrm{s}}$	stator flux vector
$\vec{\lambda}_0$	initial flux vector
θ	rotor position
θ_{a}	aligned position
θ_{c}	start of poles overlapping
θ_{d}	end of poles overlapping
θ_{dwell}	dwell angle
θ_{e}	extinction angle
θ_{f}	falling interval
θ_{off}	turn-off angle
θ_{on}	turn-on angle
θ_{r}	rising interval
θ_{stk}	stroke angle
θ_{u}	unaligned position
ω	angular speed in rad/s
ω_{b}	angular base speed in rad/s

To my wife

Chapter 1

Introduction

1.1 Background and Motivation

Personal and freight transportation is one of the key contributors in greenhouse gas (GHG) emissions. In the European Union (EU), the transportation sector constitutes the second biggest GHG emitter after the energy sector, Fig. 1.1. Road transportation represents almost three quarters of EU transport-emitted GHG [8]. While a decrease of emissions was noticed from other sectors, the ones from transport have increased 36% from 1990 until 2011. By 2050 the growth in GHG emissions from transportation is expected to be 50 to 100% higher [9]. The exhaust gas emissions from vehicles can cause extreme pollution when added together in big and crowded cities. Around the world, people in big, heavily populated and polluted cities get sick and die of lung diseases and an increasing number of children are being born with malformations. Also, the level of noise generated by road vehicles inside the cities became alarming. The EU policies to reduce emissions from transportation are focusing on the optimization of the efficiency of the existing vehicles, the development of new sustainable fuels and propulsion systems, and the electrification of the vehicles [8].

A more efficient, more reliable, safer and more environmentally friendly vehicle can be achieved by means of electrification. By their degree of electrification, the vehicles can be divided in four big categories [2]. The first category, having electrified only non-propulsion systems, is represented by the so-called more electric vehicles (MEVs). The electrified non-propulsion systems, besides the classical starter/alternator, pumps, fans and lights, can include power steering, air-conditioning, electromechanical valve control, suspension control, anti-lock braking, throttle actuation and controlled vehicle dynamics. The vehicles with electrified propulsion systems comprise the other three categories: hybrid electric vehicles (HEVs), plugged-in hybrid electric vehicles (PHEVs) and electric vehicles (EVs). The EVs, HEVs or PHEVs are capable of reducing the local air pollution or even the global air pollution if the electric energy is obtained from renewable sources: hydro, wind, wave, solar.

The hybrid power trains for both HEVs and PHEVs are classified as series (Fig. 1.2), parallel (Fig. 1.3) and series-parallel hybrid (Fig. 1.4). The main difference between the power trains of HEVs and PHEVs are related to battery dimension and the possibility of charging. In HEVs the battery is smaller and can be charged only by the vehicle's propulsion system. In PHEVs the battery is larger and besides the propulsion system it can be charged by an external power source. Thus, the charger and the plug from the figures exist only in PHEVs and not in HEVs.

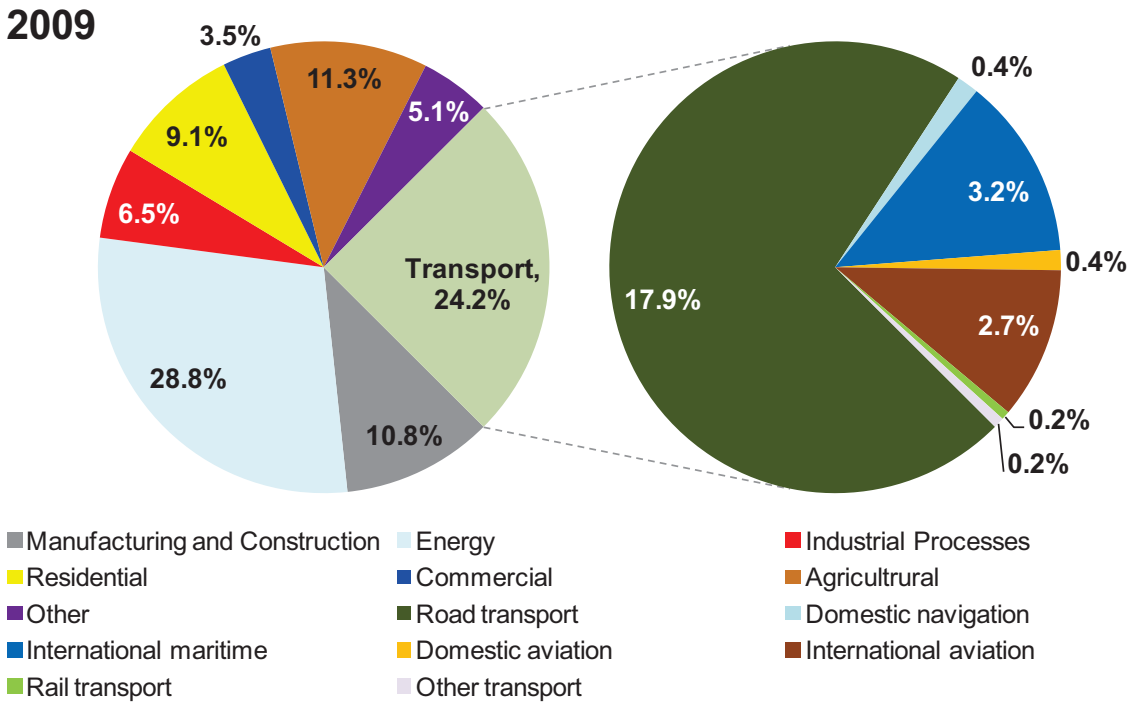

FIGURE 1.1: Greenhouse gas emissions by sector and mode of transport [1]

In a series power train, the internal combustion engine (ICE) is not connected to the wheels [10]. It represents the prime mover of an electric machine working as a generator. The power delivered by the generator is charging the batteries. From the batteries another electric machine is fed, which constitutes the propulsion motor and supplies all the traction power. In a parallel power train both the electric motor and the ICE are connected by mechanical means and together are providing the traction power to the wheels. In a series-parallel hybrid power train, two electric machines, one working as a motor and one as a generator, are providing series and parallel paths for the power.

In HEVs, a hybridization factor can be defined [2], representing the ratio between its peak electrical power and its peak total power (electrical+mechanical). Considering the hybridization factor, four categories of HEVs are defined: micro hybrids with a hybridization factor of 5-10%, mild hybrids with a hybridization factor of 10-25%, power hybrids and energy hybrids with higher hybridization factors. The energy hybrids have a higher capability of storing energy compared to power hybrids, this representing the difference between the two.

Comparing to HEVs, the larger energy storage system of PHEVs can be charged by an external power source. In the same time the PHEV can be integrated in a smart grid and then can represent itself a storage system and a power source. It can be charged during the dips on the load curve of the grid and can provide energy during load peaks. PHEVs are working only with the electrical motor until the energy of the battery is consumed. After the battery is emptied, the ICE is turned on and the vehicle works as a HEV. When the vehicle uses only the electric motor it operates in the so called charge-depleting (CD) mode and when it is using both the electric motor and the ICE, it works in the charge-sustaining (CS) mode.

EVs have a full electric power train and all the propulsion power is supplied by electric motors [2, 10, 11]. They are not equipped with an ICE and their main drawback is related to the limited range due to the limited energy storage capability of the present batteries.

In the near future, until the big step to full electric vehicle is made, the PHEV has fair chances to impose itself on the market. Capable of providing green propulsion for the necessary range of the daily needs due to the possibility of working only with the electric motor, eliminating the pollution from the cities, the PHEV is also capable of offering extended range due to its ICE.

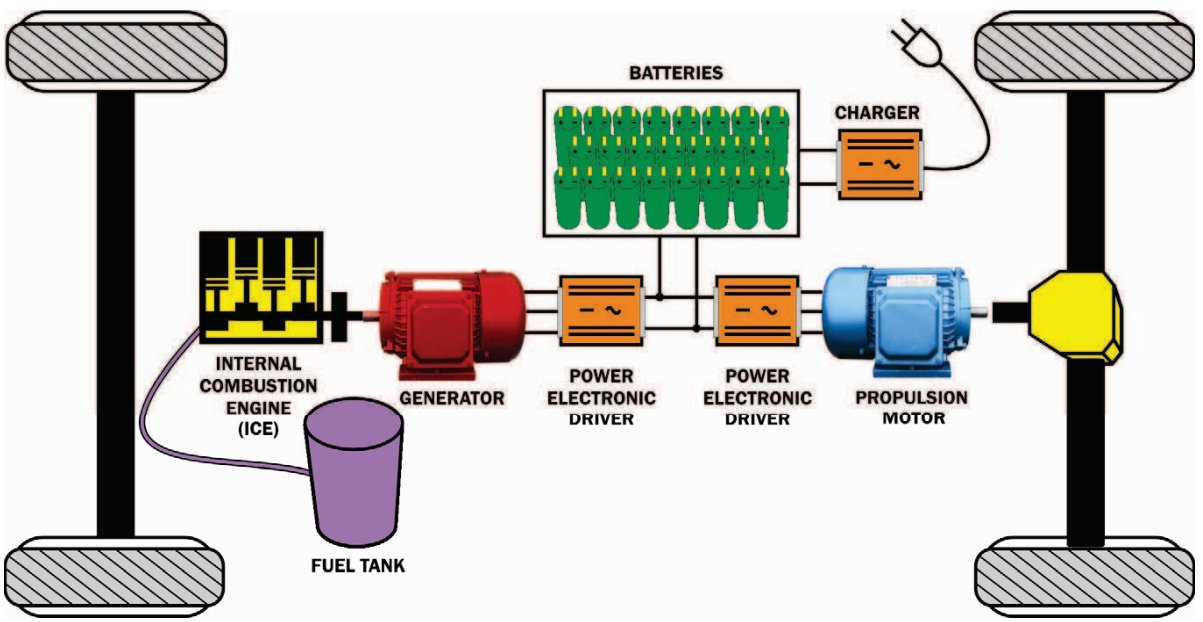

FIGURE 1.2: Series hybrid power train of PHEVs [2]

The choice of electric propulsion systems for HEVs, PHEVs and EVs depends on vehicle constraints (volume and weight of the motor, vehicle type, vehicle weight, payload, etc.), energy source (batteries, fuel cells, ultracapacitors, etc.) and nonetheless driver's demands (acceleration, maximum speed, braking, range, etc.). Taking into account the demands and the possibilities, the electric propulsion train has to come up with performances comparable to the actual road vehicles [2].

The requirements of an electric motor used in vehicle propulsion are the following [10, 11]:

1. High power density
2. High torque density
3. Peak torque capability
4. High torque to inertia ratio
5. Wide speed operation range
6. High efficiency

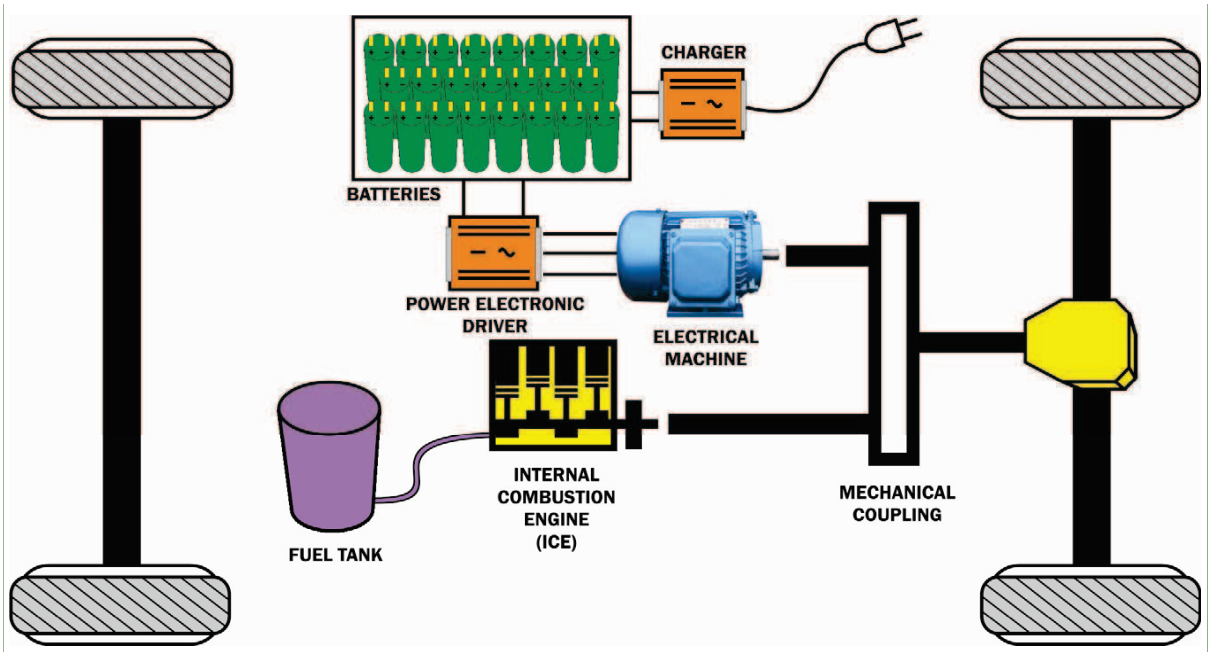

FIGURE 1.3: Parallel hybrid power train of PHEVs [2]

7. Low acoustic noise
8. Low electromagnetic interference
9. Reliability & robustness
10. Fault tolerance & low maintenance
11. Small size & low weight
12. Low cost

High power density and high torque density are leading to a smaller size and a lower weight of the machine. The motor has to be able to produce a peak torque up to two or three times the rated torque. High torque to inertia ratio leads to fast acceleration. In reaching the goal of having more efficient cars, the efficiency of the electric machine is of great importance. Special care must be paid to the 'fuel tank', which in this case are the batteries.

The important characteristics of a motor for an EV or HEV include flexible drive control, fault tolerance, high efficiency, and low acoustic noise. The motor drive must be capable of handling voltage fluctuations from the source and has to produce low electromagnetic interference (EMI). Reliability, robustness and fault tolerance influence directly the maintenance and the related costs. The importance of a low production cost of the machine is all the greater when it comes to mass production.

Electrical machines taken into consideration for vehicle traction are: DC machines, induction machines (IMs), permanent magnet synchronous machines (PMSMs) and switched reluctance machines (SRMs) [2, 10, 11, 12].

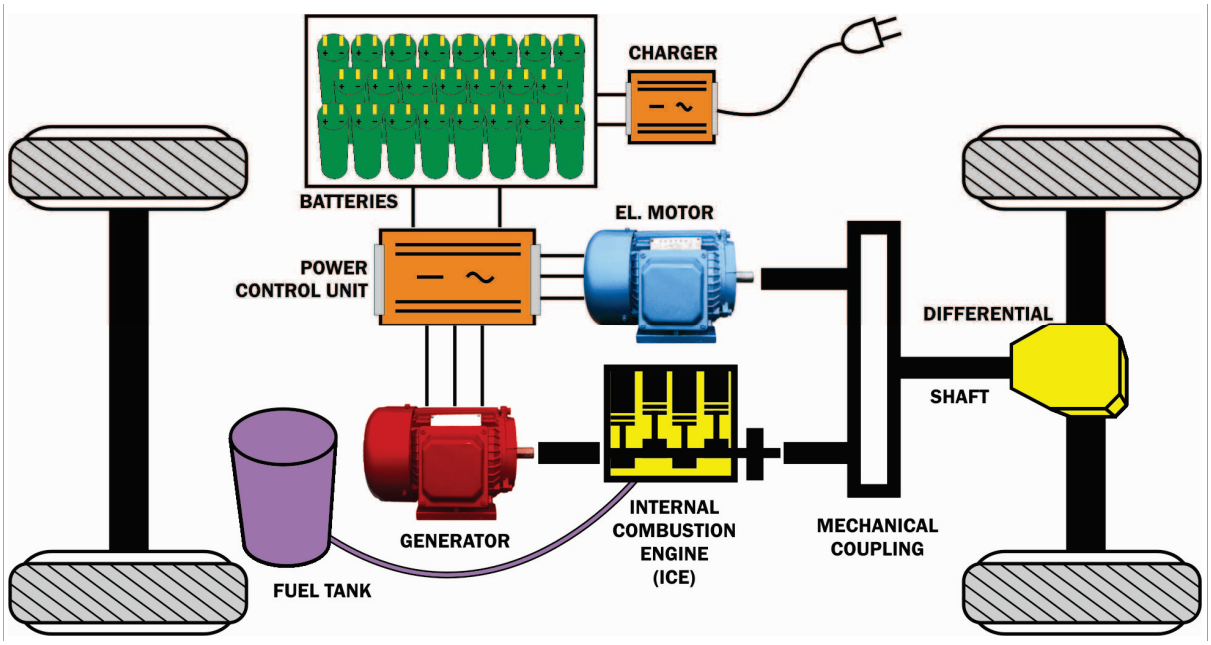

FIGURE 1.4: Series-parallel hybrid power train of PHEVs [2]

DC machines have an established manufacturing technology and their control is uncomplicated. The possibility of control without using power electronics made DC motor drives prominent in the urban and railway transportation in the early days of electric traction. The existence of commutators and brushes decreases the reliability of DC machines, decreases their maximum speed and requires regular maintenance. The commutation process generates electromagnetic interference. The low efficiency, low power density and, thus, increased volume and weight did not qualify the DC motor for electric car propulsion.

Technological advances allowed the use of three phase induction machines in electric power drives. The usage of IMs brought advantages like higher efficiency, higher power density, and, thus, lower volume and weight. The lack of brushes and commutators made them more reliable and maintenance-free. The control of induction machines is more complicated and it demands power electronics to reach desired performance. Even so IMs are confronted with low efficiency at light loads and limited speed operating range. Also temperature related problems have been noticed extreme heating of the rotor.

The permanent magnet synchronous machine has an increased power density and an increased torque density, it is smaller in size and has reduced weight. The lack of rotor winding decreases the machine's losses, making it more efficient and easier to cool. The permanent magnets can be mounted on the surface of the rotor or can be buried in the rotor. Due to similar permeability to that of air, when PMs are mounted on the rotor surface, they behave as non salient synchronous motors. Additional reluctance torque is inflicted by the saliency created by burying the PMs inside the rotor and the robustness is increased. The additional obtained torque increases the speed range at constant power operation. Because of their inherently high power density and high efficiency, PMSM have been credited with the best overall performance.

The shortcomings of the PMSMs are related to manufacturing costs due to their complex structure and the presence of PMs and to the high sensitivity of PMs to high temperatures. The already high and still increasing price of the PMs and the shortage of rare earths are forcing the researchers to come up with alternatives for the PMSM.

The good efficiency and the large constant power-speed ratio in addition to low the cost, high reliability and fault-tolerance make the switched reluctance machine (SRM) a candidate with real chances on the market of vehicle propulsion. The lack of PMs or winding on the rotor not only reduces the cost of the SRM, but also offers increased high-speed operation capability.

Despite their simplicity in construction, their design and control are complex and require well trained specialists in the field. Because their operation under saturation and the fringe effect of pole and slots, their design and control are difficult and subtle [10].

The converter of the SRM drive has a reliable topology. The stator windings are connected in series with the switches of the converter preventing the shoot-through faults at which the AC rotating field machine's converters are exposed to [10]. Compared to PMSMs, SRMs are operating with a lower efficiency and a lower power factor which increases the losses in the machine and demand greater volt-ampere ratings of the power components in the converter

The double saliency and highly nonlinear behaviour produce high torque ripple and high acoustic noise which are the main drawbacks of the SRM. The main drawbacks of the SRM related to the torque ripple, noise and vibration make the research object in R&Ds all over the world.

In vehicle traction, the switched reluctance machine comes as an alternative for the PMSM, whose main drawbacks are related to the price and the availability of the PMs, and for the IMs, which have lower power density and low efficiency at light loads.

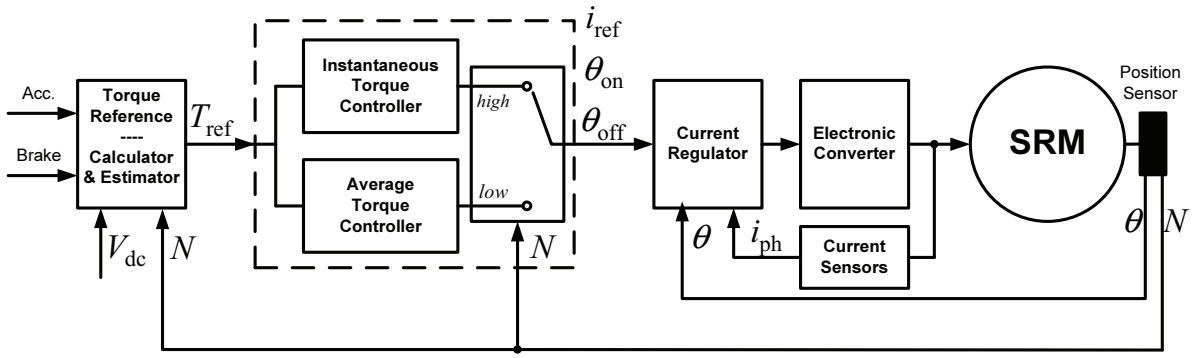

FIGURE 1.5: Electric power train with SRM

A power train for electric propulsion with an SRM is presented in Fig. 1.5. The reference torque is determined by the driver through the acceleration or braking pedal. Taking into account the functioning of the SRM and the demands for the vehicle traction, the torque control technique is selected as a function of speed. At low speeds, the low-frequency torque ripple generates oscillations that may excite resonant frequencies of the drive train, making the vehicle undrivable. The torque has to be very smooth in this operating area, thus an instantaneous torque control technique will be employed. At higher speeds the frequency of the ripple increases, causing high-frequency acoustic noise, disturbing for the human ear. In this operating area the effect of inertia smooths the torque and an average torque control method is sufficient for high

speed operation. The average torque control methods further have the advantage of increased efficiency over the instantaneous torque control methods. The torque controller provides the input values for the current controller which in turn provides the gate signals for the power electronic converter. Position and phase current feed backs are needed for the current controller and for the speed estimation on the basis of which the torque control technique is selected.

1.2 Objectives of the Thesis

The main objective of the thesis is to develop an efficient and robust switched reluctance drive that can be integrated in a hybrid dive train or can be solely used for electric vehicle traction.Looking at the structure of the power train from Fig. 1.5 and trying to fulfil the main objective, smaller secondary objectives, but all serving the same final goal, can be defined.

A model of the SRM, capable of eliminating all unwanted approximations and capable of providing a realistic and accurate behaviour of the machine during transient or steady load conditions, has to be created in order to implement and compare different control techniques.

For the machine to operate in four quadrants, both motor and generator operation have to be studied.

To assure required smooth operating conditions over a wide speed range, average and instantaneous torque control techniques have to be implemented and for each operating point the most suited control technique has to be chosen.

A converter has to be design, built and integrated on a test bench for testing SRMs for vehicle propulsion. The simulation results can be compared to the measured results and this will allow the validation of the described principles.

The acoustic noise problem has to be investigated and the main noise sources have to be identified.

1.3 Outline of the Thesis

Chapter 2. Magnetic Characterization of SRMs is focused on the characterization of the SRM from the electromagnetic point of view by making use of the flux-current-rotor position characteristics also known as magnetization curves.

Chapter 3. Average Torque Control of SRMs is dealing with the control of the average torque of SRMs taking into consideration both motor and generator operation. A closed-loop control technique is implemented in order to overcome the shortcomings of the classical feed forward average torque controller.

Chapter 4. Instantaneous Torque Control of SRMs presents the implementation of two closed-loop instantaneous torque control techniques, namely direct instantaneous torque control (DITC) and direct torque control (DTC), whose results are compared to the results obtained by using the current profiling technique employing three different torque sharing functions.

Chapter 5. Converters for SRMs is focused on the design, the construction of a converter for controlling the SRMs on a wide speed range and its integration on a test bench to test the capabilities of the SRM for vehicle propulsion.

Chapter 6. Noise in SRDs is focused on the identification of the eigen frequencies of the SRM's stator structure by analytical methods, FEM-based sofwares and measurements on the test bench

Chapter 7. Conclusions outlines the contributions of the thesis, draws the conclusions and makes propositions for the future work.

Chapter 2

Magnetic Characterisation of SRMs

The characterisation of the SRM from the magnetic point of view plays an important role in developing and optimizing different control strategies. Accurate prediction of its performance through means of magnetization curves is required for the study of the machine's behaviour under transient (starting, speed reversal, load perturbation) and steady-state conditions.

In the development of the so called torque model of the SRM, for starters, the voltage equation has to be regarded:

$$u_{\mathrm{ph}} = R_{\mathrm{ph}} i_{\mathrm{ph}} + \frac{\mathrm{d}\lambda_{\mathrm{ph}}}{\mathrm{d}t}, \tag{2.1}$$

where u_{ph} is the phase voltage, i_{ph} the phase current, R_{ph} the phase resistance and λ_{ph} the flux linkage.

According to the phase voltage equation of an SRM, the flux linkage can be calculated as the time integral of the phase voltage minus the voltage drop on the phase resistance. Integrating the flux with respect to the current at constant rotor position, the variation of the coenergy is obtained. Further deriving the coenergy with respect to rotor position at constant current, the electromagnetic torque developed by one phase is obtained.

Thus, the torque equation on which the model is based can be written as:

$$T_{\mathrm{ph}}(i,\theta) = \frac{\partial W_{\mathrm{c}}(i,\theta)}{\partial \theta} = \frac{\partial}{\partial \theta}\left(\int_i \lambda_{\mathrm{ph}}(i,\theta)\mathrm{d}i\right) = \frac{\partial}{\partial \theta}\left(\int_i \int_t \left(u_{\mathrm{ph}} - i_{\mathrm{ph}} R_{\mathrm{ph}}\right)\mathrm{d}t\mathrm{d}i\right), \tag{2.2}$$

where θ is the rotor position, W_{c} the coenergy and T_{ph} the phase torque.

Summing the phase torques the total electromagnetic torque T_{em} of the switched reluctance machine is obtained:

$$T_{\mathrm{em}} = \sum_{k=1}^{N_{\mathrm{ph}}} T_{\mathrm{ph},k}(i,\theta), \tag{2.3}$$

with N_{ph} the number of phases.

Adding the mechanical equation (2.4) to the torque equation, the model of the SRM is obtained

$$J\frac{\mathrm{d}\omega}{\mathrm{d}\omega} = T_{\mathrm{em}} - T_{\mathrm{L}} - T_{\mathrm{f}}, \tag{2.4}$$

where J is the inertia, T_{L} the load torque and T_{f} the friction torque.

Extensive work has been carried out in the field of analytical approximation of the characteristics of SRMs, representing a highly demanding task, due to machine's doubly salient structure and elaborated control strategies leading to highly non-linear behaviour. Models of the machine considering sinusoidal variations of flux and torque with respect to rotor position were developed in the early studies. They were introducing great inaccuracies in the model, which led to their elimination. In [13, 14, 15], geometry-based analytical models were developed. Analytical models based on the magnetization curves calculated with finite element method (FEM) [16, 17, 18] or measured on test rigs [19, 20], were developed using different polynomial or Fourier functions for the fitting procedures. The analytical models can be used for procedures like pre-sizing or initial estimations of instantaneous torque or efficiency for particular motor/drive selection, where a trade-off between the accuracy and computation time can be made [20].

These analytical functions introduce errors in the model and even the ones capable of a high grade approximation are usable only on certain machines. The output quantities have values different from the real ones measured on the test bench, making the model unusable for the optimization of the geometry and/or control. Thus the need of building models based directly on the magnetisation curves obtained by FE analysis or by measurements on a test bench, capable of taking into account all non-linearities and eliminating all inaccuracies arose. In the early days, the process of modelling electromagnetic field of SRMs with FEM based software was considered slow and demanding, but nowadays with the evolution of computers the FEM analysis has become imperative in describing the behaviour of SRMs.

2.1 FEM-based Electromagnetic Analysis of the SRM

The FEM-based electromagnetic analysis of an SRM starts by creating the geometry of the real machine. The studied machine is a 4-phase, 30kW peak-power SRM with 8 poles on the stator and 6 poles on the rotor. All phases are composed of two coils connected in parallel, placed on opposite poles, each having 50 turns. The geometrical dimensions of the studied machine are gathered in Table 2.1. The dimensions not specifically named in the table can be calculated on the basis of the given ones.

A 2D model of the machine, created in J-MAG Studio, is illustrated in Fig. 2.1. The corresponding electric circuit can be observed in Fig. 2.2. Due to the considerable axial length of the machine, the end effects of the coils can be neglected and, thus, a 3D analysis is not necessary. The axial symmetry of the machine allows the model of the machine to be reduced to only half of the cross section. In this manner time is saved and the computational power required significantly reduced.

The mesh definition, Fig. 2.3, plays a very important role in the FE analysis. The finer the mesh the more accurate are the achieved results, but the finer the mesh the higher computation time and memory requirements. Thus, a compromise has to be made between the mesh density and the computation effort. The mesh density does not have to be constant in all areas of the studied domain, depending on the analysis purpose. In the present case, due high rate of

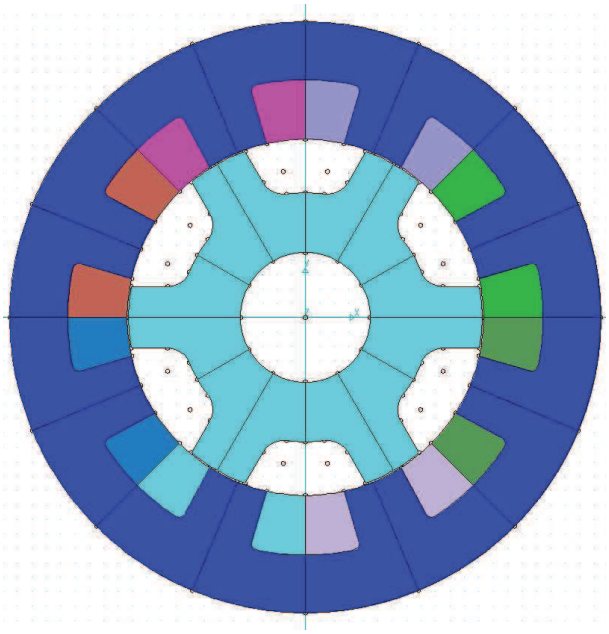

FIGURE 2.1: The geometry of the SRM

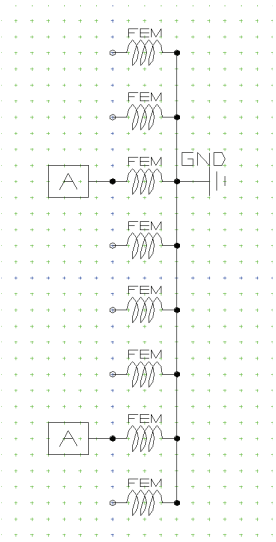

FIGURE 2.2: The electric circuit

TABLE 2.1: Geometrical dimensions of the SRM

Dimension	Notation	Value
Number of phases	N_{ph}	4
Number of stator poles	N_{s}	8
Number of rotor poles	N_{r}	6
Number of turns per coil	N_{c}	50
Stator outer diameter	D_{out}	205mm
Stator yoke inner diameter	D_{sy}	164.8mm
Rotor outer diameter	D_{g}	122.6mm
Rotor yoke outer diameter	D_{ry}	86.4mm
Shaft diameter	D_{shaft}	45mm
Stator pole arc	β_{s}	20°
Rotor pole arc	β_{r}	20°
Airgap width	g	1mm
Stack length	L_{stk}	185mm

change of the magnetic field in the airgap, a finer mesh is demanded in that area. So, 7 layers of elements are present in the airgap as can be seen in Fig. 2.4.

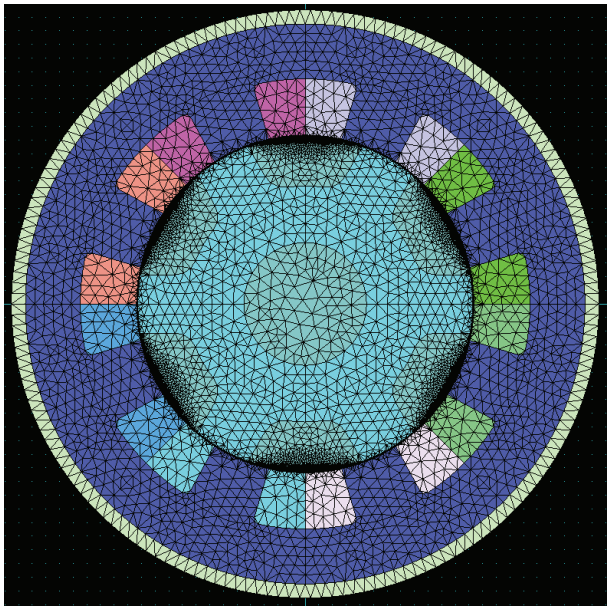

FIGURE 2.3: The mesh

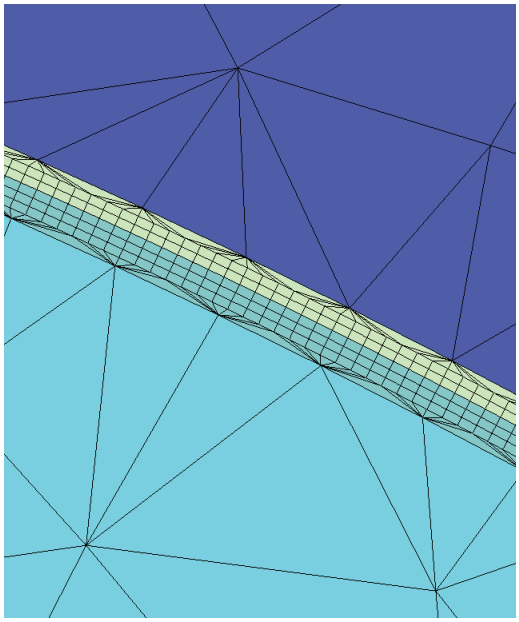

FIGURE 2.4: Mesh in the airgap

The flux lines in the machine at three distinct positions (aligned, intermediate and unaligned) can be observed in Fig. 2.5, Fig. 2.6 and Fig. 2.7. The fringing flux, more accentuated in the unaligned and intermediate positions, causes the non-linear variation of the inductance. To the non-linearity of the phase inductance contributes the saturation of the magnetic circuit, too. The magnetic flux density distribution in the SRM at the unaligned, intermediary and aligned position is illustrated in Fig. 2.8, Fig. 2.9 and Fig. 2.10. The high values of the magnetic flux density noticed in the corners of the stator and rotor poles are leading to higher stress and iron losses in the respective regions.

The variation of flux linkage with current and rotor position can be obtained by FE analysis. Fig. 2.11 illustrates the variation of the flux linkage with the rotor position at constant value of torque and Fig. 2.11, the variation with current at constant rotor position. From these characteristics, the variation of the current versus rotor position and flux can be extracted. The variation of current with rotor position at constant flux is presented in Fig. 2.11 and the variation with current at constant rotor position in Fig. 2.12. Starting from the variation of flux linkage with current and rotor position and calculating the coenergy as an intermediate step, the variation of the electromagnetic torque is found. Fig. 2.15 and Fig. 2.16 illustrate the variation of torque with rotor position at constant current and the variation with current at constant rotor position, respectively.

Storing the variation of current with the linkage flux and rotor position and the variation of torque with the current and rotor position in two look-up tables and using (2.2) and (2.4) a realistic model of the SRM can be created and all the non-linearities are taken into account. Using FEM, the unwanted approximations introduced by the analytic models are eliminated, the precision of the results is increased and the perspective on the machine is more accurate.

To avoid the inaccuracies inherent to the analytical model, the characteristics of current versus rotor position and flux and of torque versus rotor position and current are stored in look-up tables and are introduced in the model of the SRM. In this manner an accurate model of the

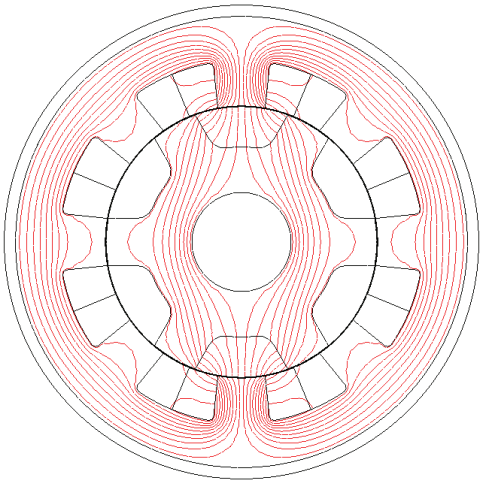

FIGURE 2.5: Flux lines - unaligned position

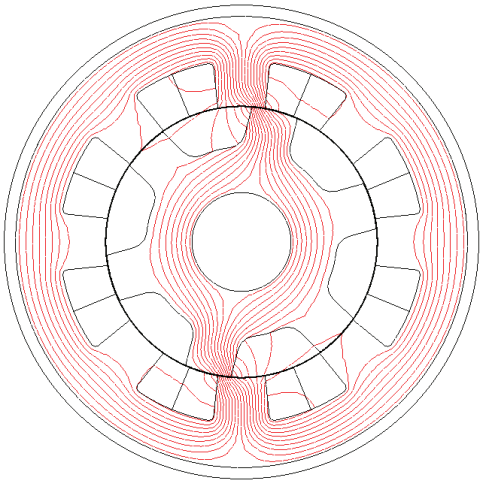

FIGURE 2.6: Flux lines - intermediate position

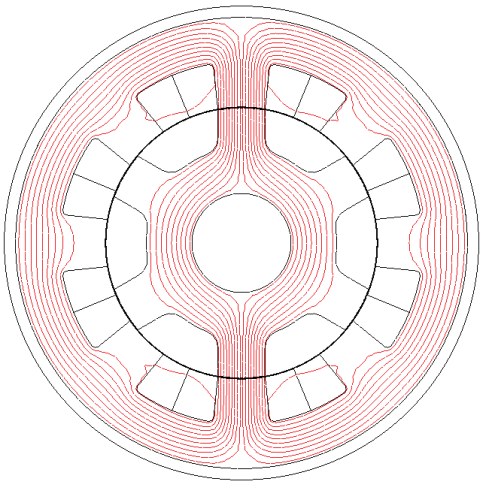

FIGURE 2.7: Flux lines - aligned position

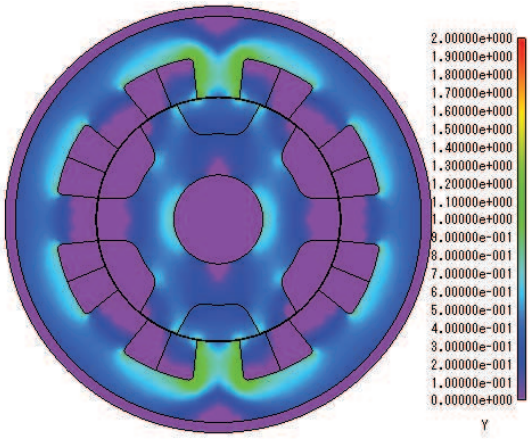

FIGURE 2.8: Magnetic flux density distribution - unaligned position

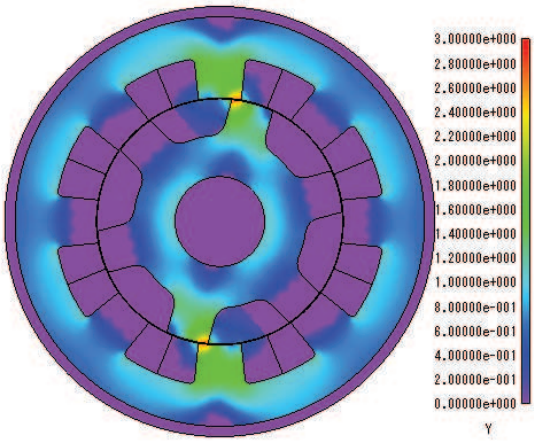

FIGURE 2.9: Magnetic flux density distribution - intermediate position

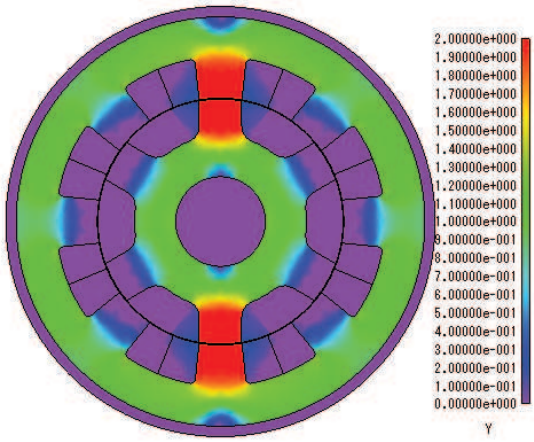

FIGURE 2.10: Magnetic flux density distribution - aligned position

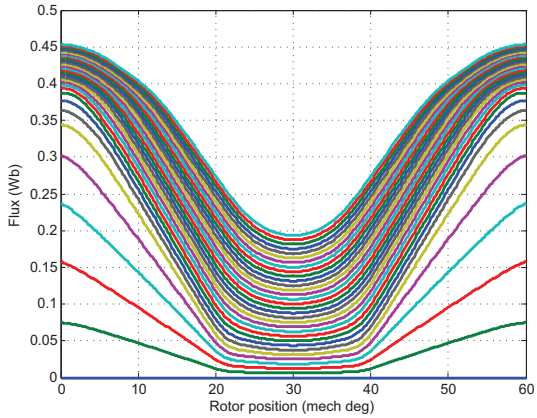

FIGURE 2.11: Flux vs. rotor position at constant current

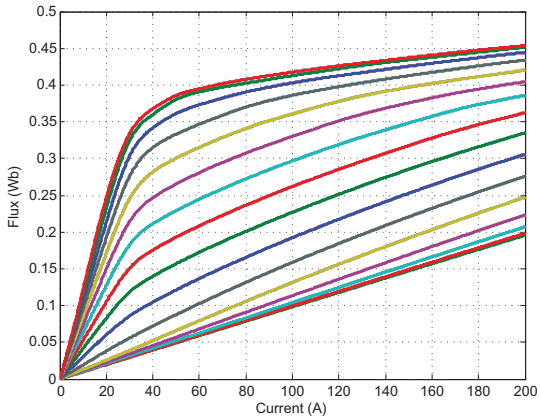

FIGURE 2.12: Flux vs. current at constant rotor position

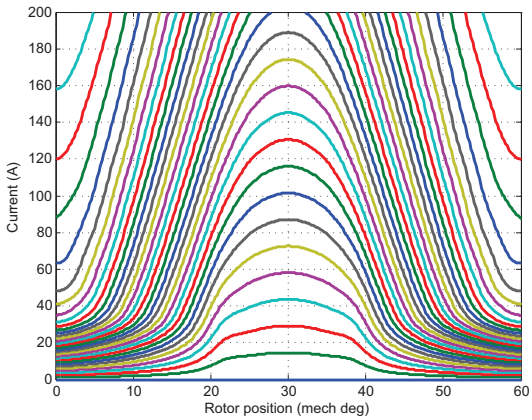

FIGURE 2.13: Current vs. rotor position at constant flux

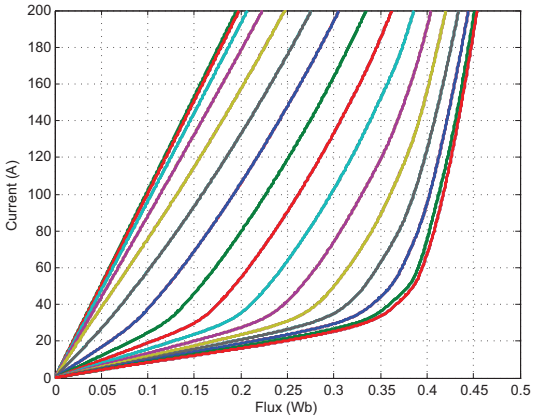

FIGURE 2.14: Current vs. flux at constant rotor position

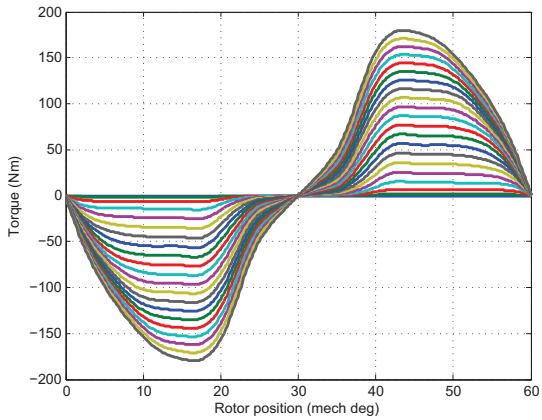

FIGURE 2.15: Torque vs. rotor position at constant current

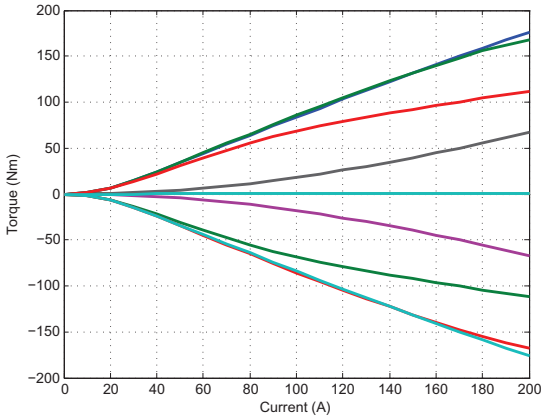

FIGURE 2.16: Torque vs. current at constant rotor position

machine is obtained, capable of providing an objective perspective on the behaviour of the SRM under different operating conditions. The model can be further used in the optimisation of control and/or design. Although these FEM-based models are very close to the real behaviour of the machine, the mutual coupling between phases, reported by previous work as having a small influence on the machine's operation, is not taken into account. If the FEM model is a 2D model, the end-coil effects are neglected, even though for the short stack length machines, their influence can be important and a correction factor should be used [21].

2.2 Experimental Methods to Determine the Magnetization Curves

The magnetization curves describing the behaviour of the SRM can be determined also experimentally, by measurements conducted on the test bench. Further the static torque characteristics can be obtained using the determination of the coenergy as an intermediate step.

2.2.1 The AC Method

The AC method [22, 23, 24] uses a controlled AC voltage source (autotransformer), to obtain the desired value of the AC current in the energized phase. First the rotor has to be fixed in the desired position. For each desired current level and rotor position, the voltage and the current are recorded and the phase impedance Z_{ph} is calculated:

$$Z_{\mathrm{ph}} = \frac{U_{\mathrm{m}}}{I_{\mathrm{m}}}, \tag{2.5}$$

where U_{m} and I_{m} are the RMS values of the measured voltage and current, respectively. The phase reactance X_{ph} is obtained:

$$X_{\mathrm{ph}} = \sqrt{Z_{\mathrm{ph}}^2 - R_{\mathrm{ph}}^2}, \tag{2.6}$$

where R_{ph} is the phase resistance. The phase inductance L_{ph} is:

$$L_{\mathrm{ph}} = \frac{X_{\mathrm{ph}}}{\omega} = \frac{X_{\mathrm{ph}}}{2\pi f}, \tag{2.7}$$

with ω and f the pulsation and the frequency of the AC applied voltage, respectively. Thus the inductance for a given rotor position θ and a given RMS value of the current I can be obtained directly as:

$$L_{\mathrm{ph}}(\theta, I) = \frac{1}{2\pi f}\sqrt{\left(\frac{U_{\mathrm{m}}}{I_{\mathrm{m}}}\right)^2 - R_{\mathrm{ph}}^2}. \tag{2.8}$$

The main advantage of this method is represented by its simplicity, but for each rotor position and current level a separate measurement is required. The multitude of measurements lead to heating and thus the value of the phase resistance changes, leading to inaccuracies. This can be avoided by taking the measurements with long intervals in between.

The non-linear nature of the magnetic circuit produces distortions in the waveform of the current, leading to inaccuracies in the measurements. High accuracy instruments capable of

measuring true RMS are able to eliminate the errors [22]. The AC identification method remains suited for linear magnetic circuits.

Another method employing AC has been presented in [25]. This technique needs a test coil to be mounted on a stator pole. The flux is obtained by digital integration of the back-emf detected by the test coil. The main disadvantage of this method, besides the already presented ones, is represented by the cost and mounting of the test coil.

2.2.2 The Flux Linkage Method

The flux linkage method [19, 22, 23, 24, 26, 27, 28] is based on the phase voltage equation 2.1. According to the voltage equation, the flux can be obtained:

$$\lambda_{\mathrm{ph}} - \lambda_0 = \int_0^t (u_{\mathrm{ph}} - i_{\mathrm{ph}} R_{\mathrm{ph}})\, \mathrm{d}t, \tag{2.9}$$

with λ_0 the initial flux. Further, the inductance is determined:

$$L_{\mathrm{ph}} = \frac{\lambda_{\mathrm{ph}} - \lambda_0}{i_{\mathrm{ph}}}. \tag{2.10}$$

This method can be practically implemented in two ways [22]:

- Measuring the rising current while applying a constant voltage to the phase winding;
- Measuring the falling current while de-energizing the phase winding, while, a priori, a constant DC current was established in the winding.

For both procedures, the rotor has to be blocked in the desired position beforehand and the circuits of the phases on which measurements are not performed have to be opened.

In the case of measuring the rising current under a constant voltage the initial flux is null, both the voltage and the current being initially zero. Due to voltage variations during the measurements, a large capacitor is needed on the output of the supply to maintain the voltage constant. Another capacitor is required to damp the oscillations due to the newly created LC circuit. Higher the currents higher the demanded values of the capacitors. For low power machines, batteries can be used instead of stabilized DC supplies [28]. The oscillations of the DC voltage during the rising time of the current are leading to inaccuracies in the estimation of the magnetisation curves.

To avoid errors related to oscillations, the measurement can be done on the decaying slope of current while de-energizing the phase. The voltage is shut-off only after the desired value of the current was attained and the transitory effects were damped. The voltage across the phase winding will be equal to the voltage drop on the free-wheeling diode (or diodes, depending on the employed circuit).

The treatment of the data can be done on-line by hardware [22] or off-line using post-processing procedures. With the second approach, the errors are reduced to the precision and the accuracy of the acquisition equipment and the integration routine, making the estimation more precise.

2.2.3 The Torque Measurement Method

In [26, 27] the magnetization characteristics are found by measuring the torque at different rotor positions and different current values. Integrating the torque with respect to the rotor position at constant current, the values of the co-energy are found. Further, deriving the co-energy with respect to the phase current at constant rotor position, the values of flux are obtained.

The disadvantages of this method are related to the need of expensive, high precision torque meters [27], or of complex mechanical construction and precise weighting equipment [26].

2.3 Measurement of the Magnetization Curves

Due to economical reasons, the same electronic circuit used for the control of the SRM can be used for the measurement of the magnetization curves. The asymmetric H-bridge based circuit, illustrated in Fig. 2.17, was used for both procedures described by the flux linkage method, namely, measuring the rising current under a constant voltage level and measuring the falling current while de-energizing the phase winding. The DC voltage source is composed of a 3-phase diode bridge rectifier and a capacity connected in parallel with its output. The value of the DC voltage is controlled by controlling the AC voltage level with a plot transformer. The rotor blocking system from Fig. 2.18 is composed of a metallic lever and a subsystem with a screw which allows a very precise positioning of the rotor. While both switches are open and no current is passing through the winding, the voltage on the winding is zero. The rotor is blocked in the wanted position and the value of the DC voltage is set at the wanted level. When both switches are closed, the current in the phase starts rises until it reaches the steady state value under the influence of the DC voltage. When the upper switch is opened the phase is short-circuited, a zero voltage loop is formed through the lower transistor and the corresponding free-wheeling diode and the current starts decreasing. In the two cases the waveforms of the voltage and current are recorded for an off-line processing.

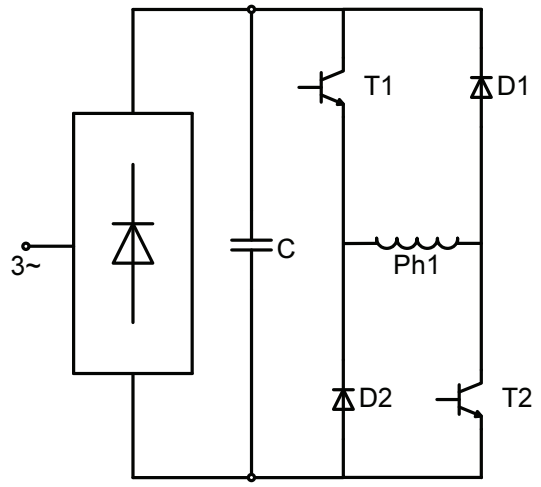

FIGURE 2.17: Measurement circuit

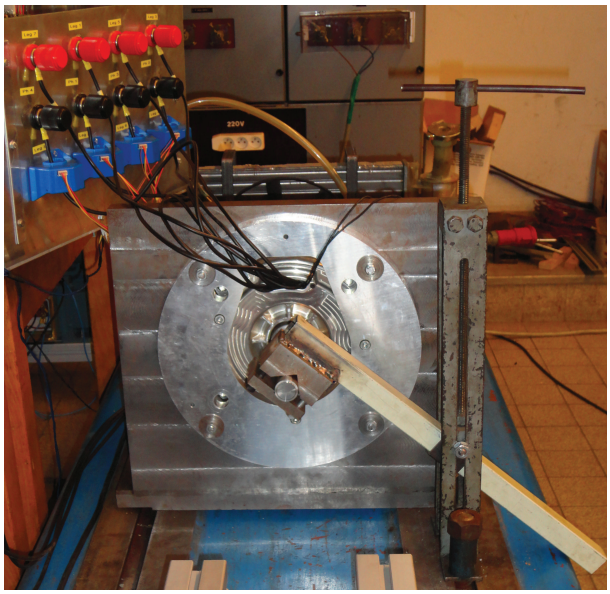

FIGURE 2.18: Rotor blocking system

Considering the rotor position being 0 degrees in the aligned position and 30 degrees in the unaligned positions, the waveforms recorded for the intermediate rotor position of 15 degrees are presented in Fig. 2.19 for the measurement ascending current and in Fig. 2.20. When the ascending current was measured, due to the high current drawn, great oscillations were spotted in the DC voltage. These oscillations are the source of inaccuracies in the estimation of magnetisation curves, thus the registered waveforms were not further used. At the measurement of the falling current was taken only after the steady state was reached. The voltage is not zero during the decaying of the current, in reality, being equal to the voltage drop on the transistor and the free-wheeling diode

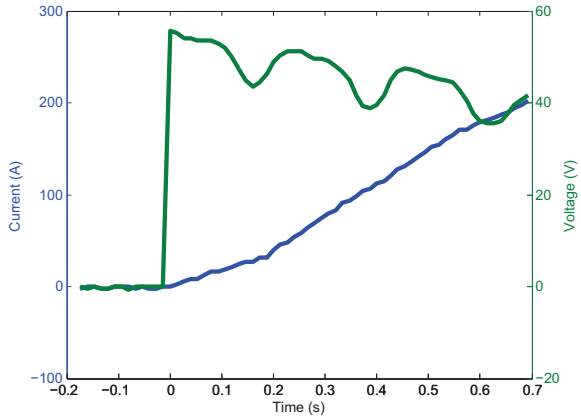

FIGURE 2.19: Rising current method: voltage and current waveforms

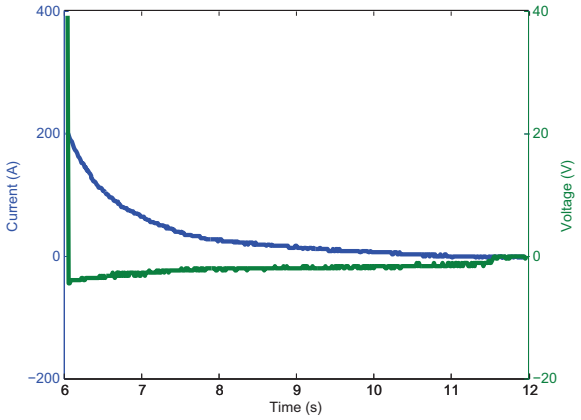

FIGURE 2.20: Falling current method: voltage and current waveforms

Integrating the difference between the measured voltage and the voltage drop on the phase resistance, the characteristics of flux linkage versus phase current at constant rotor position are obtained. Fig. 2.21 illustrates the magnetisation curves from 0 degrees to 30 degrees with a step of 6 degrees, namely at 0, 6, 12, 18, 24 and 30 degrees, respectively.

The raw initial data has to be filtered, Fig. 2.22, in order to be used for the calculation of tables describing the machine's operation. The filtering of the magnetisation curves has to be done mainly due to the demand of the numerical methods capable of working, only, with piecewise monotonous variation of the data.

To obtain the variation of the coenergy, Fig. 2.23, the flux is integrated with respect to the current. The variation of torque, Fig. 2.24, is obtained by deriving the coenergy with respect to the rotor position.

The errors in the measurement of the magnetization curves have multiple causes [27]: movement of the rotor during the measurement, variation of the resistance with the temperature, effect of eddy currents, the effect of numerical methods and the imperfections in the measurement equipment. The movement of the rotor leads to the measurement of an inexact characteristic corresponding to a certain angle and if the position deviation is large it can lead to the intersection of two characteristics. The errors introduced by the variation of the phase resistance with temperature can be avoided by increasing the interval between measurements. The effect of the eddy currents can be eliminated by conducting multiple measurements at a constant current instead of transient measurement [27].

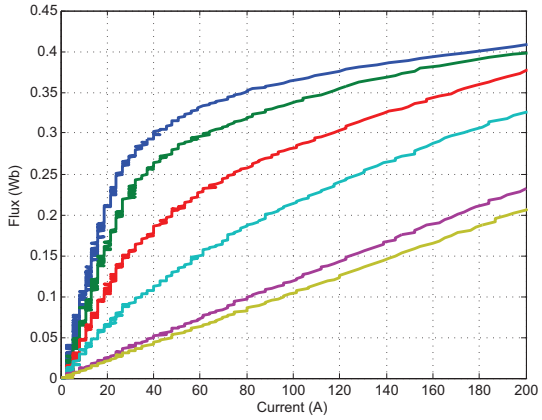

FIGURE 2.21: Magnetization curves: raw data

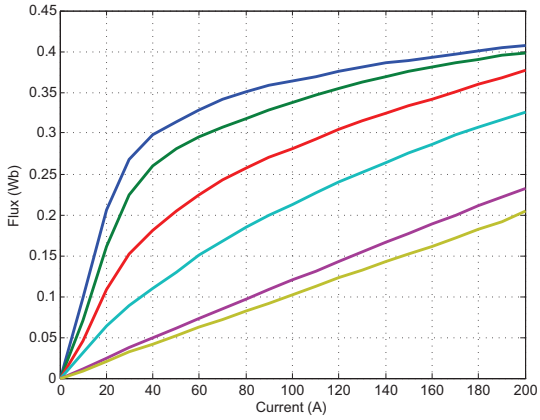

FIGURE 2.22: Magnetization curves: filtered data

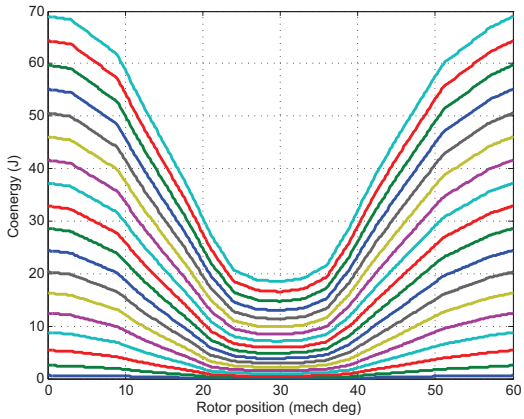

FIGURE 2.23: Coenergy vs. rotor position at constant current

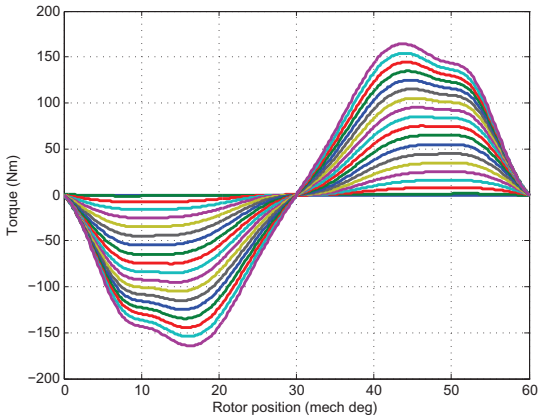

FIGURE 2.24: Torque vs. rotor position at constant current

2.4 Conclusions

The second chapter has been focused on the electromagnetic characterization of SRMS by investigating the flux/current/rotor position characteristics. An accurate torque model of the machine capable of eliminating the unwanted approximations and capable of providing a close to reality behaviour of the machine has been built based on the magnetization curves.

Firstly, a standard approach using 2D FEM has been used to determine the family of curves. Then, several experimental methods for finding the magnetization curves have been described, together with their advantages and shortcomings: AC method, flux linkage method and torque measurement method. The available measurement devices, incapable of measuring the true RMS values, are not taking into account the saturation of the magnetic circuit and thus, the AC method has not been performed. The flux linkage method measuring the falling current was preferred over the method measuring the rising current due to the inaccuracies introduced in the measurement by the voltage oscillations. A rotor blocking system for maintaining fixed the rotor position during measurements has been built.

The experiments seem to reasonably agree with FEM 2D results. Analysing the two families of magnetisation curves, the biggest difference is less than 10%. The differences originate from the effect of the end-coil not taken into account by FEM 2D the movement of the rotor during the measurement, the variation of the resistance with the temperature ,the effect of eddy currents, the effect of numerical methods and the imperfections in the measurement equipment. Some corrections have to be made to the FEM 2D characteristics before they can be used in the torque model of the machine.

Chapter 3

Average Torque Control of SRMs

3.1 Torque Production in SRM

In a switched reluctance machine the electromagnetic torque is produced by the tendency of its moveable part (the rotor in this case) to move to a position where the inductance of the excited winding is maximized and the reluctance of the magnetic circuit is minimized [29]. A primitive single phase machine Fig. 3.1 is used to illustrates the principle of torque production in an SRM Fig. 3.2. To simplify the analysis, the magnetic saturation is not taken into account, resulting in a constant slope of the inductance from the position where the rotor pole starts to overlap with the stator pole to the aligned position. The fringing flux is ignored, thus, a constant value of the inductance from the unaligned position to the position where the rotor pole start to overlap with the stator pole can be considered.

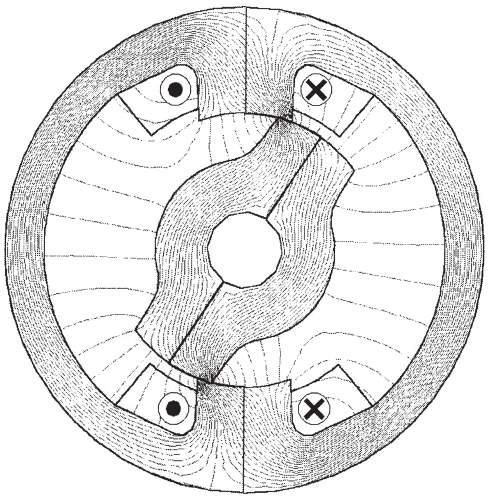

FIGURE 3.1: Primitive single phase SRM [3]

The electromagnetic energy conversion can be studied considering the magnetization curves. The magnetization curve is the variation of the flux-linkage λ_{ph} as a function of phase current i_{ph} at a constant rotor position θ. In Fig. 3.3, three magnetization curves are depicted: one in the unaligned position θ_{u} and two in the aligned position θ_{a}, one with the saturation taken into account and one without saturation. The stored magnetic energy W_{f} and the co-energy W_{c} are defined as [3]:

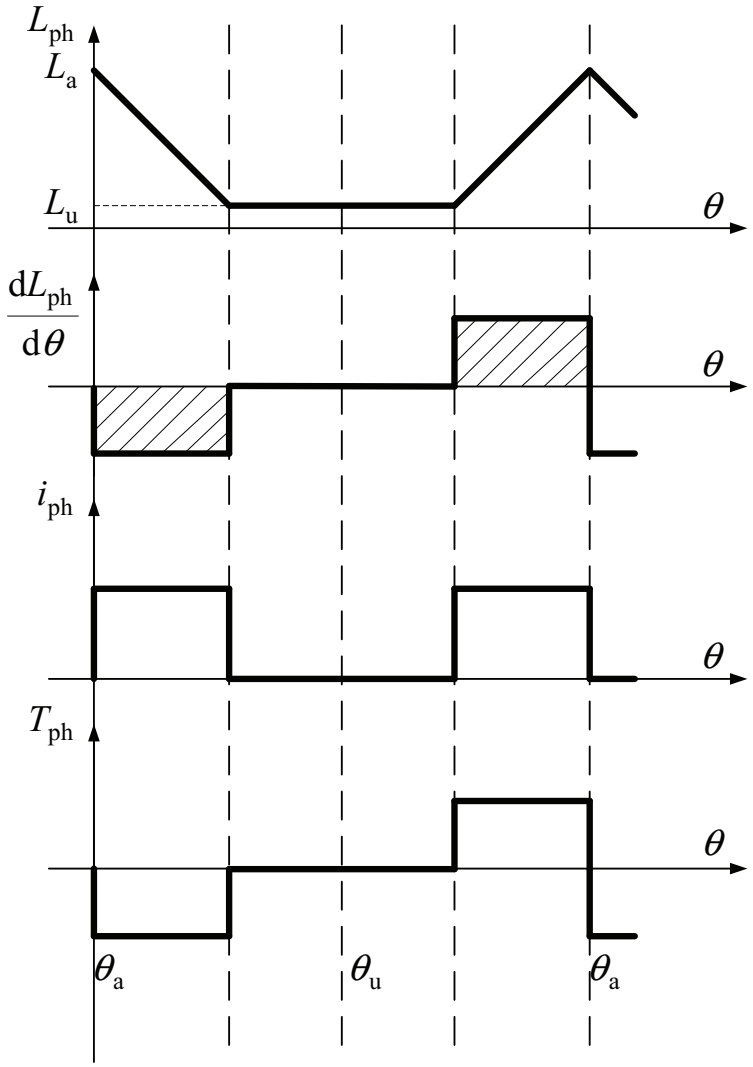

FIGURE 3.2: Ideal waveforms of primitive single phase SRM

$$W_c = \int_0^i \lambda_{ph} di, \tag{3.1}$$

$$W_f = \int_0^\lambda i_{ph} d\lambda. \tag{3.2}$$

The co-energy W_c varies with rotor position θ to produce torque T_e [30]:

$$T_e = \left(\frac{dW_c}{d\theta}\right)_{i=ct.}. \tag{3.3}$$

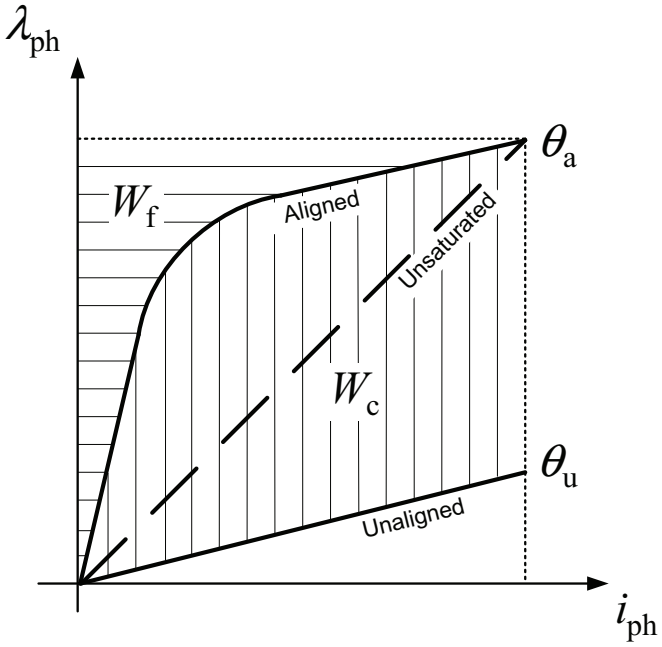

FIGURE 3.3: Typical energy conversion loop

In the absence of magnetic saturation the flux becomes:

$$\lambda_{\mathrm{ph}} = L_{\mathrm{ph}} i_{\mathrm{ph}} \tag{3.4}$$

with L_{ph} the phase inductance, and, thus:

$$W_{\mathrm{f}} = W_{\mathrm{c}} = \frac{1}{2} i_{\mathrm{ph}}^2 L_{\mathrm{ph}}. \tag{3.5}$$

In the switched reluctance machines operating unsaturated, the energy conversion is very poor. The saturated SRMs are far more effective but their behaviour becomes non-linear [21]. The effect of saturation is to increase the co-energy and to decrease the magnetic energy.

Further, considering a linear variation of the phase inductance with the rotor position, for a constant current pulse, the torque is constant over the active range:

$$T_{\mathrm{e}} = \frac{1}{2} i_{\mathrm{ph}}^2 \frac{L_{\mathrm{ph}}}{\mathrm{d}\theta}. \tag{3.6}$$

The square of the current from (3.6) shows that the electromagnetic torque does not depend on the sense of the current through the coil. The sign of the torque is the same as the sign of the slope of the inductance $L_{\mathrm{ph}}/\mathrm{d}\theta$. To produce a positive torque the phase has to be energized on the increasing slope of the inductance, whereas to produce a negative torque the phase has to be energized on the decreasing slope of the inductance.

The primitive single phase SRM from Fig. 3.1 is useful only for the analysis of torque production. Despite its capability of producing a positive average torque, this torque is discontinuous and moreover the machine cannot self start from every position, the torque being zero in the aligned and in the unaligned position. To supply continuous unidirectional torque and self-starting

capability from any rotor position, the SRM is provided with more phases and, thus, more poles on both the stator and the rotor [3].

Torque in SRMs is, thus, produced by pulses of phase current synchronized with rotor position [3]. The number of strokes per revolution N_{stk} is given by the number of phases N_{ph} and the number of rotor poles N_{r} and for a machine with classical structure:

$$N_{\text{stk}} = N_{\text{ph}} N_{\text{r}}. \tag{3.7}$$

The stroke angle θ_{stk} is 360° divided by the number of strokes per revolution:

$$\theta_{\text{stk}} = \frac{360^\circ}{N_{\text{stk}}} = \frac{360^\circ}{N_{\text{ph}} N_{\text{r}}}. \tag{3.8}$$

The fundamental frequency f in Hz of the current in each phase is:

$$f = \frac{N}{60} N_{\text{r}}, \tag{3.9}$$

where N is speed in rpm.

The number of strokes per second f_{stk} is calculated by multiplying the fundamental frequency by the number of phases:

$$f_{\text{stk}} = N_{\text{ph}} f. \tag{3.10}$$

This frequency, together with its harmonics, is found in the flux waveform in various parts of the magnetic circuit, and thus, plays an important role in the calculation of iron losses.

Besides the DC-machine and the AC rotating-field machines, the relationship between torque and phase current is highly non-linear and speed dependent due to magnetic saturation and non-sinusoidal variation of phase inductance with rotor position. To fully control torque, besides phase current i_{ph}, the commutation angles, turn-on angle θ_{on} and turn-off angle θ_{off}, have to be changed in accordance with reference torque and speed.

The 8/6 SRM presented in the previous chapter has the rotor pole pitch of 60°. The aligned position is considered to be at 0° and the unaligned position at 30°. At low speeds, where the back-emf e is low compared to the DC-bus voltage, the current can be regulated by chopping. Fig. 3.4 presents the typical waveforms of current, flux and torque in the studied machine at 500rpm. The reference value of the current is imposed 50A, while the turn-on angle θ_{on} and the turn-off angle θ_{off} are chosen to be 35° and 55°, respectively. At the beginning of the conduction period, very little torque is produced because the inductance is almost constant and thus its slope is almost zero. Approaching the angle where the stator and the rotor poles start to overlap θ_{c}, the slope of the inductance starts to increase and thus the torque production augments. After the turn-off angle, negative voltage is applied to the phase and the current rapidly falls to zero before the aligned position to avoid negative torque production. The flux increases with a constant slope due to the almost constant variation of the inductance. The inductance starts to increase at the approach to the angle where the poles start to overlap θ_{c} and increases with an almost constant slope until the turn-off angle θ_{off}. At the end of the commutation the flux falls back to 0 under the influence of the negative DC-bus voltage applied

to the phase. Typical waveforms of phase voltage and current at low speeds measured with the oscilloscope are shown in Fig. 3.5

At high speed the emf is increased and the available voltage is insufficient for chopping, thus the torque is controlled only by varying the firing angles. Fig. 3.6 presents the typical waveforms of current, flux and torque in the studied machine at 3000rpm. The turn-on θ_{on} and turn off θ_{off} angles are set at 35° and 55°. The current, under the influence of the DC-bus voltage, grows almost linearly in the area where the rotor and stator pole are not overlapped. At θ_c where the poles start to overlap the back-emf e increases suddenly to a value greater than the DC-bus voltage and forces the current to decrease. Due to high speed the current cannot be always cancelled before aligned position and negative torque production can occur. Typical waveforms of phase voltage and current at high speeds measured with the oscilloscope are shown in Fig. 3.7.

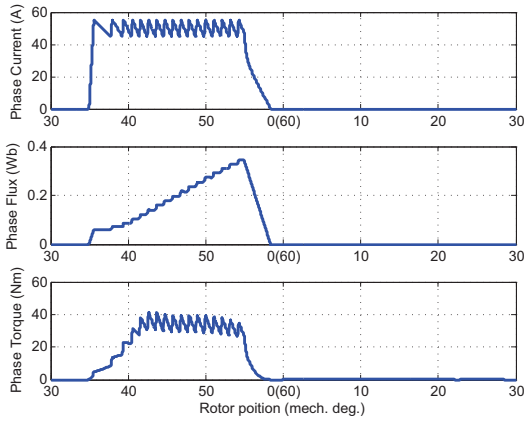

FIGURE 3.4: Typical waveforms for low speed motoring

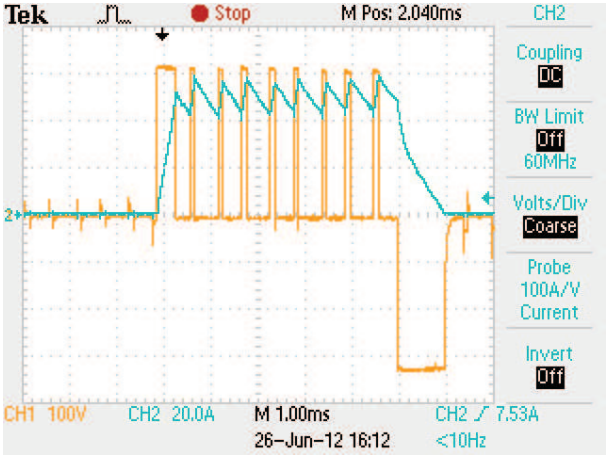

FIGURE 3.5: Typical measured voltage and current for low speed motoring

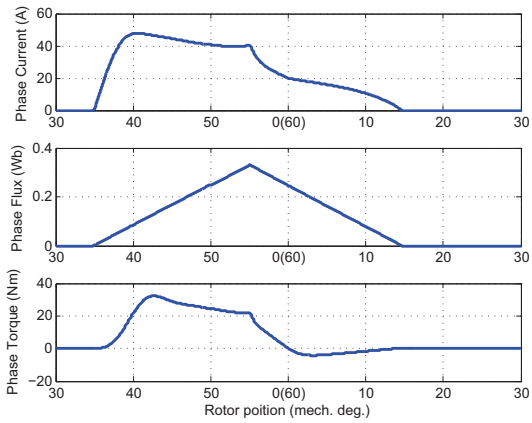

FIGURE 3.6: Typical waveforms for low speed motoring

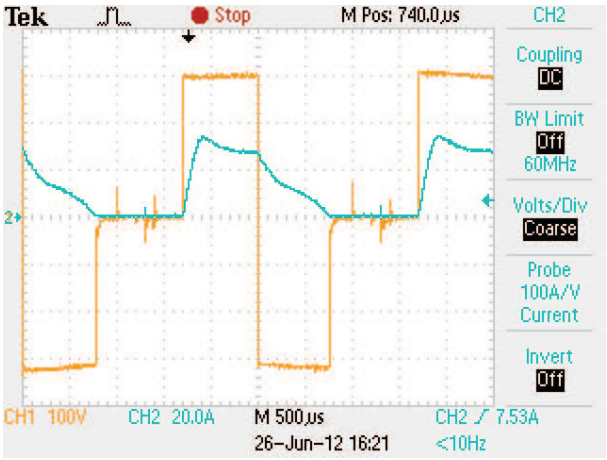

FIGURE 3.7: Typical measured voltage and current for high speed motoring

The value of the back-emf is proportional to the speed and, thus, at very high speeds the turn-on angle has to be advanced to an angle before the aligned position where the sum of fluxing and de-fluxing interval become equal to the rotor pole pitch. At this point the current does not reach anymore zero value and the machine enters in what is called continuous conduction, Fig. 3.8.

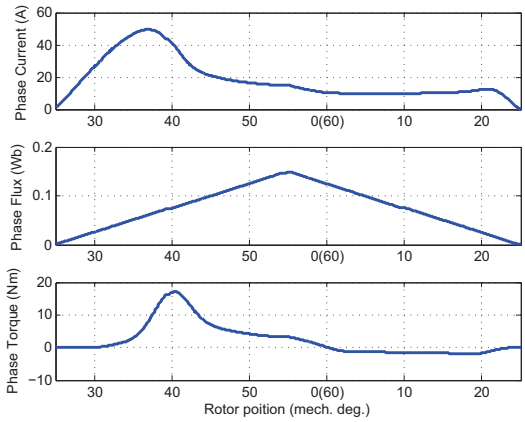

FIGURE 3.8: Typical waveforms for very high speed motoring

The task of the torque controller is to properly adjust the control variables for each operating point from the torque speed characteristic. Two different approaches are to be found in the literature [31]:

- The switching angles are kept constant while the torque is controlled only through the reference current. In this manner a very simple and low-cost controller can be realized, but with limited operating area in the torque-speed plane and not optimized from the efficiency point of view. This approach is used for low-cost applications such as fans, pumps and household appliances which usually have a constant operation point.
- All control variables are changed in order to reach the wanted operation point. The structure of the controller is more complex, but it does not limit the operating area in the torque-speed plane. Moreover, an optimization regarding the torque ripple and/or efficiency can be done.

In a vehicle, the controller represents the interface between the driver and the traction drive. The controller requires high robustness and dynamics to provide the needed comfort to the driver and the passengers. In Fig. 3.9 is illustrated a basic feed-forward torque control based on the tables of the phase current i_{ph}, turn-on θ_{on} and turn-off θ_{off} angles as functions of electromagnetic torque T_{e} and speed N. In traction drives, where the variation of the DC-bus voltage V_{dc} plays an important role in the stability of the controller, the aforementioned tables have an extra dimension corresponding to this DC-bus voltage. The extra dimension increases the computational effort and requires more expensive hardware.

3.2 Drive Parameter Computation

The influence of the firing angles on the performance of the average torque controller is studied in several papers [32, 33, 34, 35, 36]. Before starting a discussion on setting the proper control parameters for the driver, explications regarding the control parameters and the quantities used to calculate them are illustrated in Fig. 3.10. The angles θ_{a} and θ_{u} represent the aligned and the unaligned position, θ_{on} and θ_{off} are the turn-on and turn-off angles, and θ_{e} is the extinction angle, where the current becomes zero. θ_{c} and θ_{d} are the rotor positions where the rotor and the

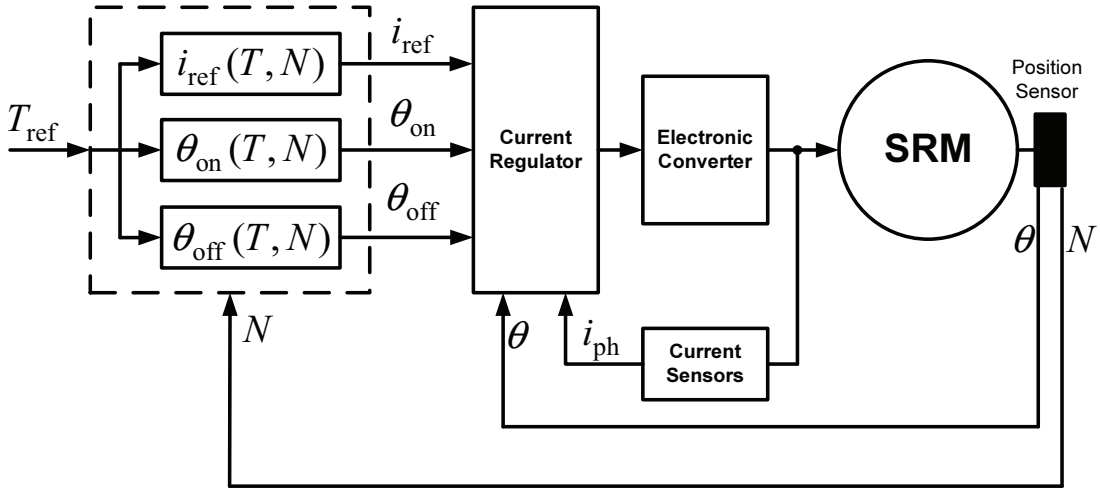

FIGURE 3.9: Feed-forward average torque control of SRM

stator poles start to overlap and the inductance starts increasing and the rotor position where the pole overlapping finishes and the inductance reaches its unaligned value, respectively. θ_r and θ_f are the rising and the falling interval of the current and θ_{dwell} is the dwell angle defined as the difference between the turn-off angle and the turn-on angle:

$$\theta_{dwell} = \theta_{off} - \theta_{on}. \tag{3.11}$$

L_a and L_u are the values of the inductance in the aligned and the unaligned position, respectively. i_{ref} is the reference value of the current, while Δi is the width of the hysteresis band.

3.2.1 Analytical Drive Parameter Computation

An expression for the turn-on angle θ_{on} was proposed by Bose [37]. He considered that the current has to reach its reference value in the point where the rotor and stator poles start to overlap and the torque producing region begins. Considering a linear increasing of the current, the rising interval θ_r is:

$$\theta_r = \frac{L_u \omega}{V_{dc}} i_{ref}, \tag{3.12}$$

where L_u is the inductance in the unaligned position, ω the speed in rad/s, V_{dc} the DC-bus voltage and i_{ref} the reference current.

Thus, the turn-on angle θ_{on} is in front of the position where the overlapping begins θ_c with the current rising interval θ_r:

$$\theta_{on} = \theta_c - \theta_r = \theta_c - \frac{L_u \omega}{V_{dc}} i_{ref}. \tag{3.13}$$

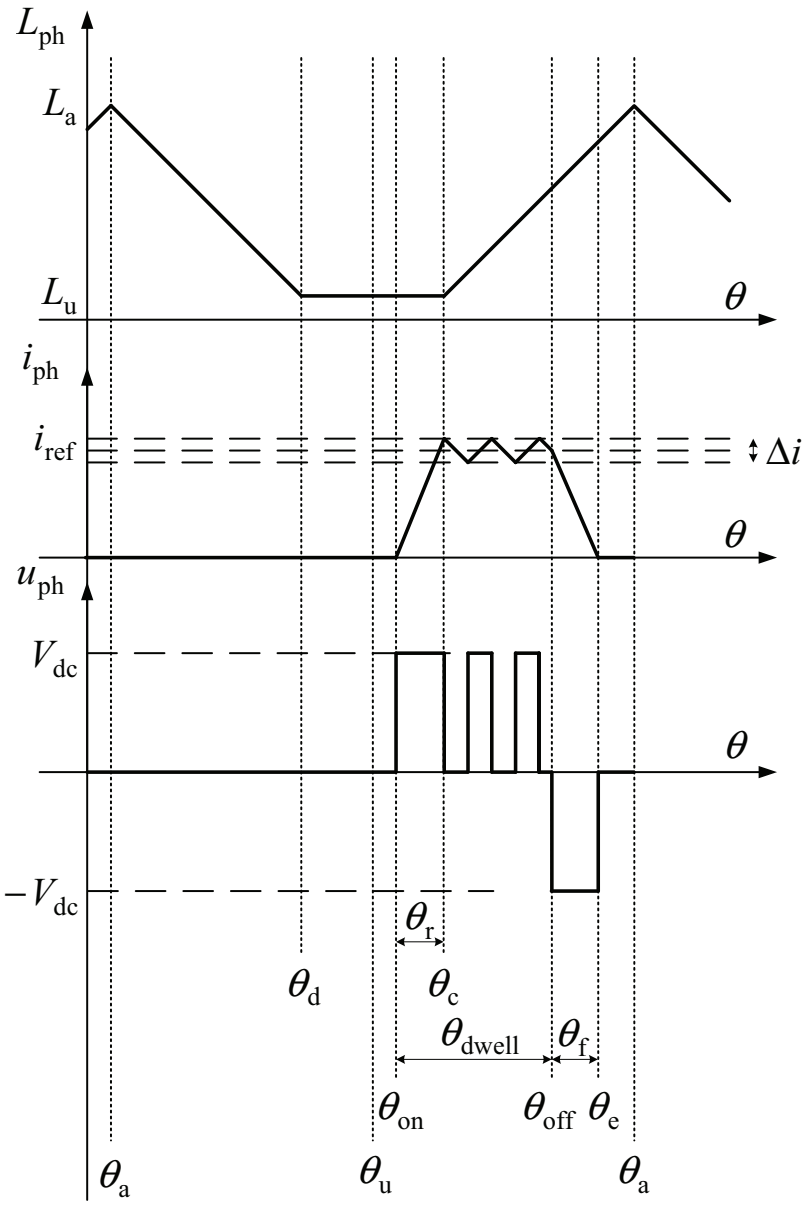

FIGURE 3.10: Inductance, current and voltage waveforms together with the definition of usual quantities

If the turn on-angle θ_{on} is advanced beyond the value calculated with (3.13) the conduction period is expanded in a region where the inductance profile is flat and does not contribute to the torque production, whereas the copper losses are increased and hence the efficiency decreased.

The turn-off angle θ_{off} can be calculated with the expression proposed by Gribble [38]:

$$\theta_{off} = \theta_a - \frac{\theta_c}{2}\left(-\alpha + \sqrt{\alpha^2 + \frac{24 i_{ref}(1-x)N}{R_{ua} V_{dc} \theta_c}}\right), \tag{3.14}$$

where θ_a is the angle in the aligned position and x is a constant between $1/\sqrt{2}$ and $2/3$. $R_{ua} = R_u - R_a$ and $\alpha = R_a/R_{ua}$, where R_a and R_u are the reciprocals of the aligned inductance L_a and unaligned inductance L_u, respectively.

In [39] and [40] an on-line efficiency optimization scheme is presented. Firing angles are computed on-line using (3.13) and (3.14). In steady state operation the initial selection of the angles is fine-tuned by means of an algorithm that minimizes the input power of the drive. Due to continuously changing operating point, this method is not suited for traction drives.

In [32, 33, 41, 42], a method to improve both the torque ripple and the efficiency is proposed with an on-line calculation of the firing angles. The turn-on angle θ_{on} can be calculated with the expression proposed by Bose 3.13. Empirically was determined that the optimal turn-off angle for the highest efficiency has to be chosen so that the fluxes of two neighbouring phases are equal to half of the peak flux-linkage on their intersection angle. Thus θ_{off} is defined as:

$$\theta_{off} = \theta_c + (2\theta_{stk} - \theta_f)\left[1 - \frac{\theta_r}{\theta_f}\right], \tag{3.15}$$

where θ_{stk} is the stroke angle and θ_f is the interval needed for the current to vanish. The current rising interval θ_r and the current decaying interval θ_f have to be obtained by means of simulation or by measurements conducted on a test-bench. This is a time-consuming task which introduces uncertainties in the controller leading to errors. The optimal operating point is reached by treating the error of speed through a PI-controller which gives the reference current. Taking into account the simplifying hypothesis made for the calculation of the firing angles further improvement can be made to obtain a controller with a better efficiency.

3.2.2 Numerical Drive Parameter Computation

The multitude of simplifying hypothesis makes these methods inaccurate. So, the need of optimizations techniques capable of considering all non-linearities of the SRM arose. In the beginning the maximization of the average torque per ampere was aimed at [37, 43], but soon the need of a secondary objective such as efficiency minimization or torque-ripple minimization has been acknowledged [38, 44]. Optimization of firing angles with multiple secondary objectives using weight factors are presented in [45, 46, 47]

In a multiphase SRM, the total instantaneous torque T_{inst} is given by the sum of the individual phase torques $T_{ph,k}$:

$$T_{inst} = \sum_{k=1}^{N_{ph}} T_{ph,k}. \tag{3.16}$$

The average torque T_{avg} can be obtain by integration:

$$T_{avg} = \frac{1}{\tau}\int_0^{\tau} T_{inst}\mathrm{d}t, \tag{3.17}$$

where the fundamental period τ is obtained from the fundamental frequency f:

$$\tau = \frac{1}{f} = \frac{60}{N}\frac{1}{N_\mathrm{r}}, \tag{3.18}$$

where N is speed in rpm and N_r is the number of rotor poles.

The peak-to-peak torque ripple is given by:

$$T_\mathrm{rip} = T_\mathrm{max} - T_\mathrm{min}, \tag{3.19}$$

where T_max and T_min are the maximum and the minimum value of torque, respectively. Further the relative torque ripple can be defined:

$$T_\mathrm{rip,rel} = \frac{T_\mathrm{rip}}{T_\mathrm{avg}}. \tag{3.20}$$

The average copper losses P_Cu on a fundamental period τ can be calculated with:

$$P_\mathrm{Cu} = \sum_{k=1}^{N_\mathrm{ph}} \left(\frac{1}{\tau} \int_0^\tau I_{\mathrm{ph},k} R_\mathrm{ph} \right), \tag{3.21}$$

where I_ph is the RMS value of the phase current.

The iron losses P_Fe can be computed on the basis of the Steinmetz equation

$$P_\mathrm{Fe} = k_\mathrm{h} f \hat{B}^{\alpha+\beta\hat{B}} k_\mathrm{e} f \hat{B}^2, \tag{3.22}$$

where f is the fundamental frequency, $\hat{B}$ is the peak-value of the magnetic flux density, k_h and k_e the hysteresis and eddy-current losses coefficients and α and β two material coefficients fitted on the basis of the material magnetisation curves.

Considering the mechanical power P_M equal to the product of the average torque T_avg and the angular speed ω:

$$P_\mathrm{M} = T_\mathrm{avg}\omega, \tag{3.23}$$

the efficiency can be further calculated:

$$\eta = \frac{P_\mathrm{M}}{P_\mathrm{M} + P_\mathrm{Cu} + P_\mathrm{Fe}}. \tag{3.24}$$

The above mentioned quantities are a posteriori calculated on the basis of a MATLAB/Simulink model. Using the Simulink model, an optimization routine based on exhaustive search is created with 3 degrees of freedom (DoFs), which also represent the output of the routine, turn-on angle θ_on, turn-off angle θ_off and reference current i_ref. The performance parameters used by the function are the torque per ampere coefficient TPA, the relative torque ripple $T_\mathrm{rip,rel}$ and the efficiency η considering the copper losses P_Cu. The torque per ampere coefficient is defined as:

$$TPA = \frac{T_\mathrm{avg}}{I_\mathrm{ph}}, \tag{3.25}$$

with I_{ph} the RMS value of the phase current.

A multi-objective minimization function is defined and, modifying the weight factors, two scenarios are further developed. In the first scenario the copper losses play the most important role with a ratio of 3:1 between the weight factor of copper losses and the weight factor of torque ripple and in the second the ratio of the weight factors is inverted, the most important role being played by the torque ripple.

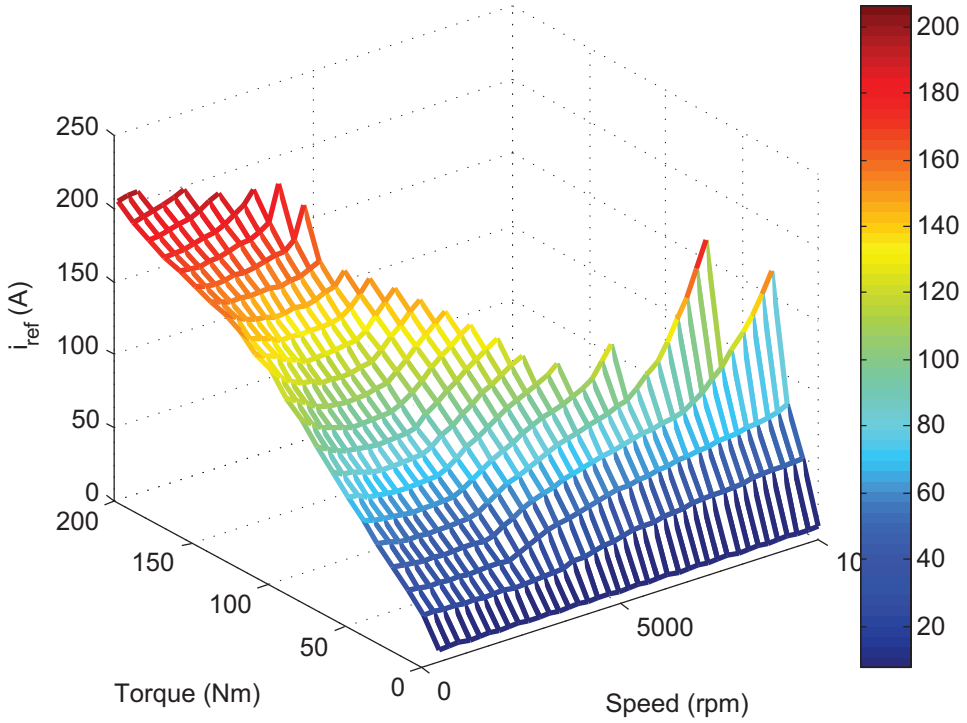

FIGURE 3.11: Reference current versus torque and speed (scenario 2)

The tables with the values of the three output variables i_{ref}, θ_{on} and θ_{off} for the second scenario are presented in Fig. 3.11, Fig. 3.12 and Fig. 3.13, respectively. For the firs scenario, the output data is shown in Appendix A. The variation with torque and speed of the raw output data coming from the optimisation procedure is not smooth. If the variation of the control parameters is not monotonic, malfunctions of the controller and/or unwanted acoustic noise in the drive can be felt and thus the quantities have to be passed through a smoothing procedure. Fig. 3.11, Fig. 3.12 and Fig. 3.13 illustrate the smooth variation of the control parameters. The reference current i_{ref} increases with torque and slightly with speed. The turn-on θ_{on} and turn-off angles θ_{off} have to be advanced with the increase of speed and torque, what is confirmed by Fig. 3.12 and Fig. 3.13. As mentioned before, the turn-on angle has to be chosen in such a manner that the current reaches its reference value in the point where the slope of the inductance starts to increase and torque production is optimum and the turn-off angle has to be chosen such that the current becomes zero before the aligned position to avoid negative torque production.

The waveforms of the current, flux and torque at a reference value of torque of 90Nm and a rated speed of 1500rpm for both scenarios are presented in Fig. 3.14 and in Fig. 3.15. In the first scenario the reference torque is attained with a lower current and thus lower losses than in the second scenario but with higher torque ripple. The turn-on angle θ_{on} is 35.31°, the turn-off

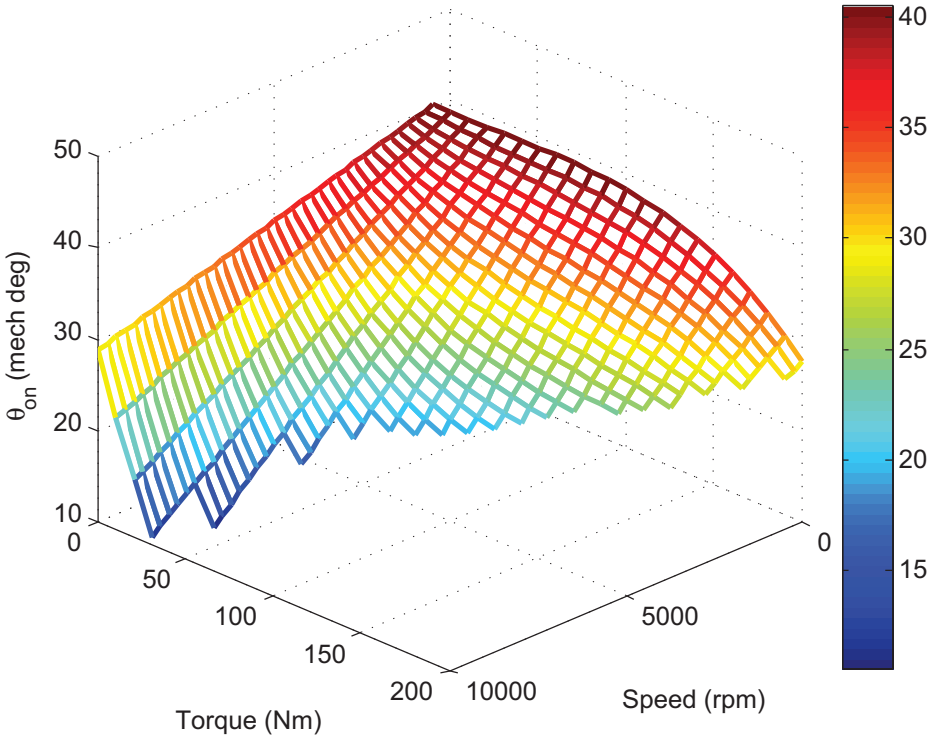

FIGURE 3.12: Turn-on angle versus torque and speed (scenario 2)

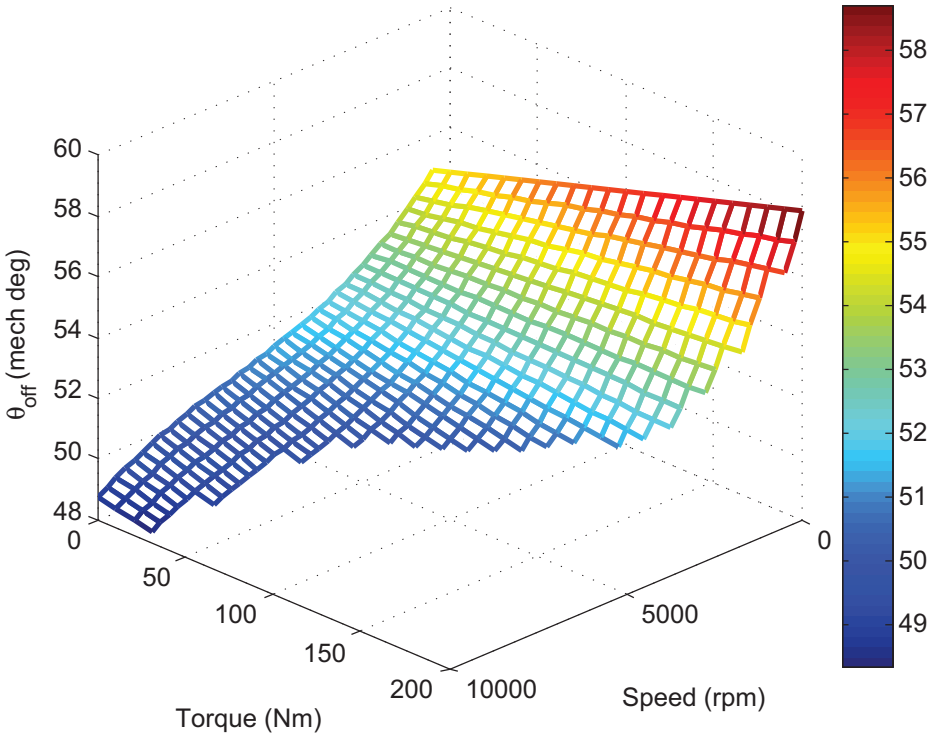

FIGURE 3.13: Turn-off angle versus torque and speed (scenario 2)

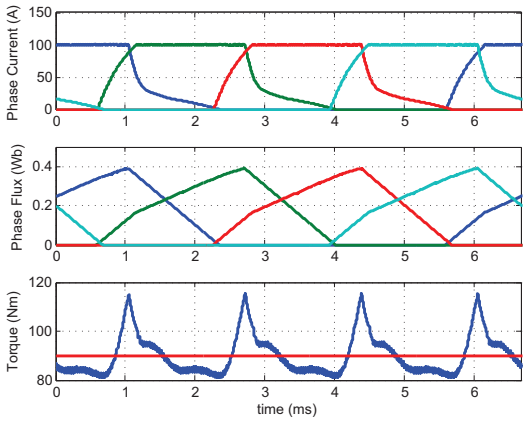

FIGURE 3.14: Simulated waveforms of phase current, phase flux and instantaneous torque for a reference torque of 90Nm at 1500rpm (scenario 1)

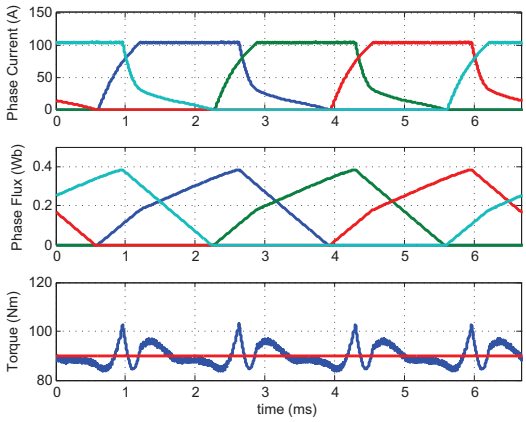

FIGURE 3.15: Simulated waveforms of phase current, phase flux and instantaneous torque for a reference torque of 90Nm at 1500rpm (scenario 2)

angle θ_{off} is 54.47° and the reference current i_{ref} is 100.85A. The absolute torque ripple T_{rip} and the relative torque ripple $T_{\text{rip,rel}}$ are 34.5Nm and 0.38, respectively, obtained for a maximum value of torque T_{max} of 115.5Nm and a minimum value of T_{min} of 81Nm. In the second scenario the reference current i_{ref} is 104.37, and the turn-on angle θ_{on} and the turn-off angle θ_{off} are 35.39° and 53.57°. The maximum T_{max} and the minimum T_{min} registered torque ripple are 83.7Nm and 103Nm. The absolute torque ripple T_{rip} is 19.3Nm, while the relative ripple $T_{\text{rip,rel}}$ is 0.21. The torque ripple is decreased by 17% but with an increase in losses.

Further, the maps of copper losses and torque ripple are presented in the speed-torque plane on the entire operating area. Fig. 3.16 and Fig. 3.17 present the maps of the two quantities for the first scenario, while Fig. 3.18 and Fig. 3.19 for the second scenario. In the first scenario, when the focus is on the copper losses, it can be seen that the losses are increasing with torque and slightly with speed. The ripple has two critical areas: at low speed and high currents where the absolute value of the ripple can take values over 80Nm and at high speed where the relative ripple has values over 75%. In the second scenario the torque ripple is improved over the whole operating range. In both critical areas the relative ripple is improved with more than 20% and in other point from the torque speed plane improvements up to 40% where spotted. The losses are increasing over the whole operating range, but mainly in the low speed and high torque region region. Depending on the operating point, the copper losses in the first scenario can be improved up to 10-15%.

Fig. 3.20 illustrates the experimentally obtained waveforms of the current and electromagnetic torque produced by the machine at 1500rpm and a reference torque of 30Nm. A difference of more than 1Nm can be seen between the reference and the produced torque. Several measurements were conducted and differences of 0.5 up to 2Nm were spotted. The main cause of the offset is represented by the calculations done in ideal conditions. Different phenomena like the variation of the machine's parameters under the influence of the environmental factors, asymmetries and other fabrication inaccuracies are not taken into account.

The variation of the DC-bus has a great influence on the controller. This is a current problem in electric vehicles taking into account that the DC-bus can vary with ±50V or even more. In the classical feed-forward average torque control of the SRMs, another dimension represented by the DC-bus voltage is introduced in the tables of the reference current and firing angles. The

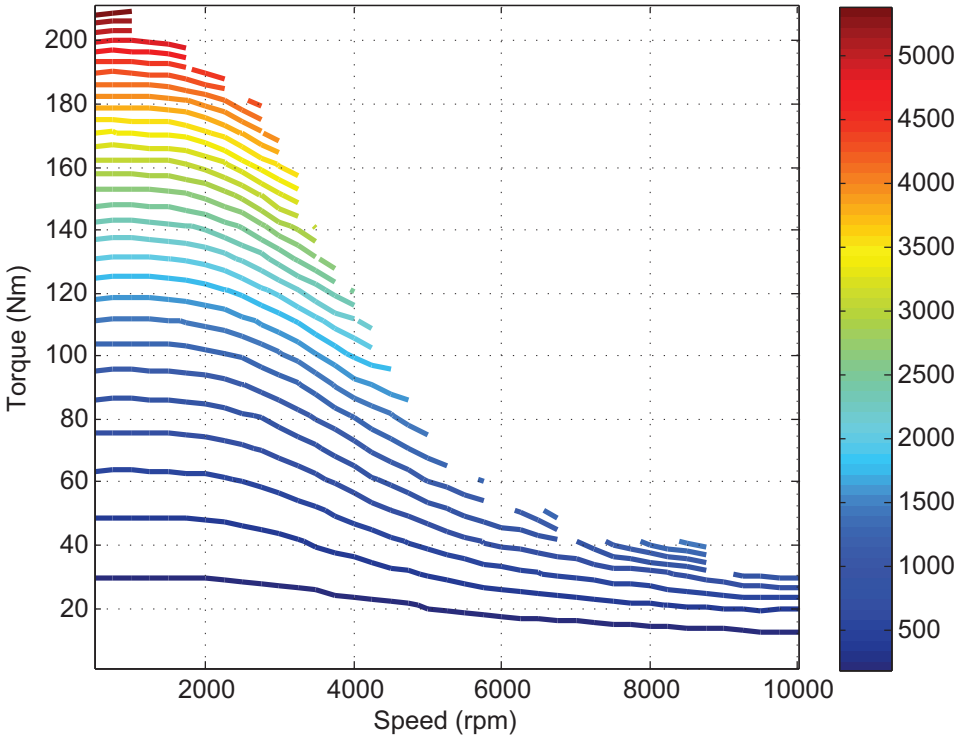

FIGURE 3.16: Copper losses versus torque and speed (scenario 1)

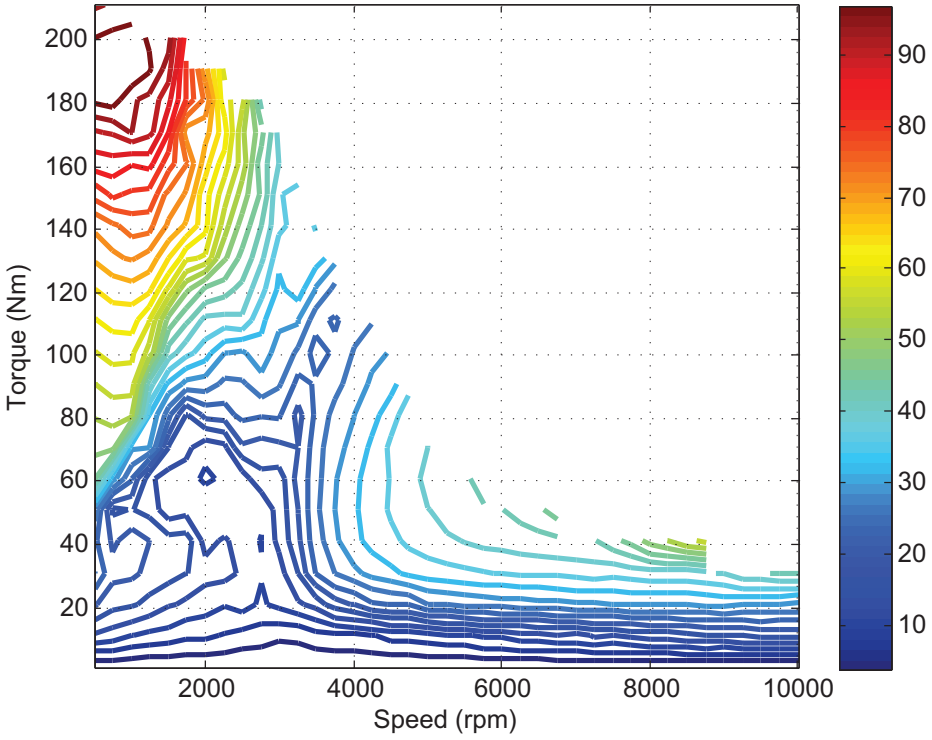

FIGURE 3.17: Torque ripple versus torque and speed (scenario 1)

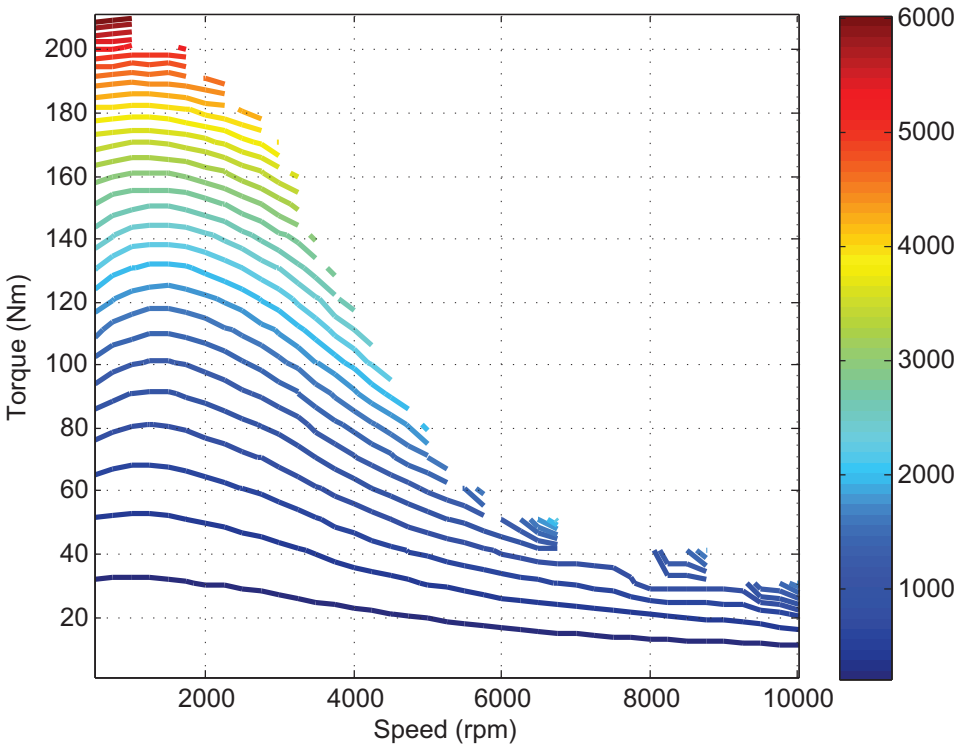

FIGURE 3.18: Copper losses versus torque and speed(scenario 2)

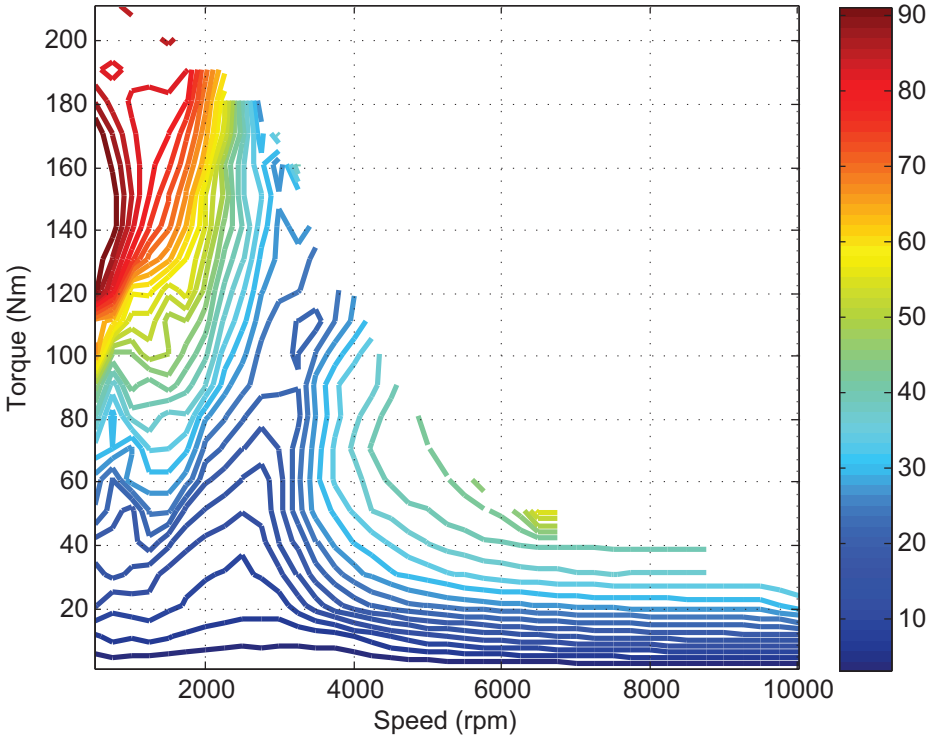

FIGURE 3.19: Torque ripple versus torque and speed (scenario 2)

third dimension increases considerably the already complex process of determining the control parameters. This demands higher computational effort from the controller and more complex and expensive hardware.

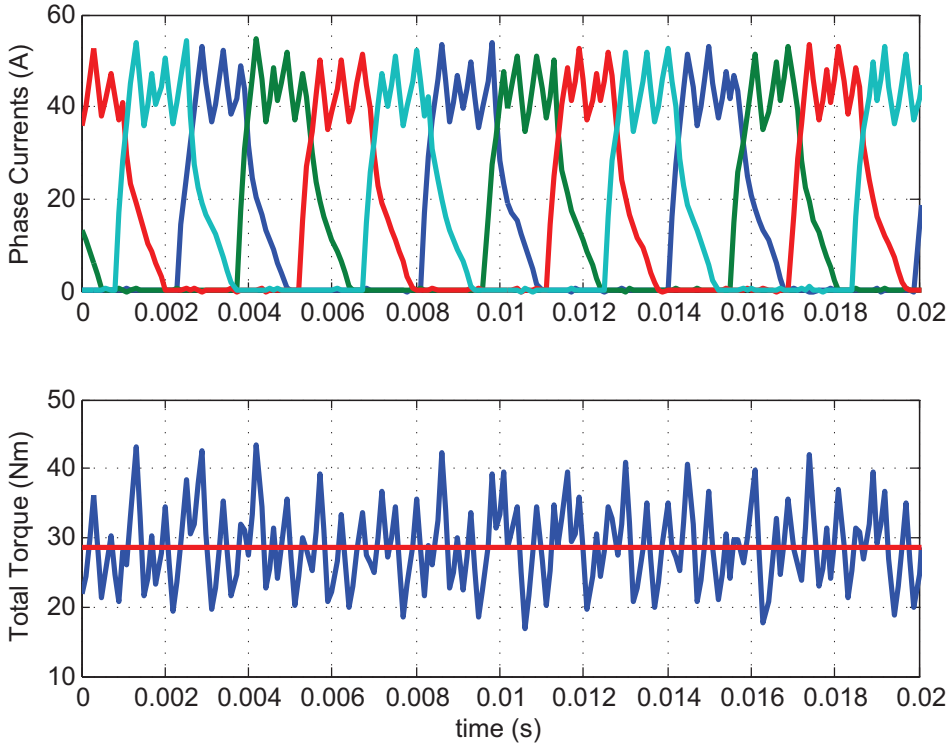

FIGURE 3.20: Measured waveforms at 1500rpm and 30Nm using feed-forward average torque control technique

To avoid increasing the using a 3D look-up table leading to expensive systems a closed-loop average toque control was proposed in the literature [4, 31, 48]. This closed-loop method was called Direct Average Torque Control (DATC) and its block diagram is presented in Fig. 3.21. In order to implement a closed-loop average torque control, the average torque has to be estimated on-line.

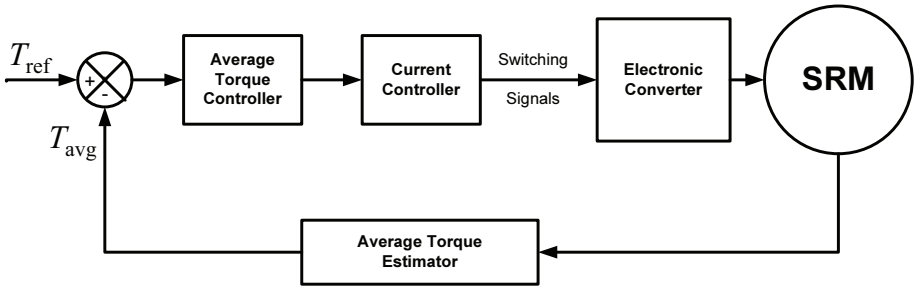

FIGURE 3.21: Closed-loop structure of average torque control

3.3 On-line Average Torque Estimation

The closed-loop average torque control techniques require on-line torque estimation. The on-line average torque estimation in an SRM, as the instantaneous-torque estimation, is not an easy task. For SRMs with a higher phase number than three, two or more phases can contribute at once to the electromagnetic torque production.

The average electromagnetic torque estimation in switched reluctance machine requires the estimation of the phase flux. The phase flux λ_{ph} can be estimated from the terminal quantities, phase current i_{ph} and phase voltage u_{ph} and the phase voltage equation:

$$\frac{\mathrm{d}\lambda_{\mathrm{ph}}}{\mathrm{d}t} = u_{\mathrm{ph}} - R_{\mathrm{ph}} i_{\mathrm{ph}}. \tag{3.26}$$

The quantity of energy converted from electrical energy W_{elec} to mechanical energy W_{mech} corresponding to the area of the co-energy loop, can be further calculated:

$$W_{\mathrm{mech}} = \oint i_{\mathrm{ph}} \frac{\mathrm{d}\lambda_{\mathrm{ph}}}{\mathrm{d}t} \mathrm{d}t. \tag{3.27}$$

The average electromagnetic torque can be calculated using the torque equation:

$$T_{\mathrm{avr}} = \frac{N_{\mathrm{ph}} N_{\mathrm{r}}}{2\pi} W_{\mathrm{mech}}. \tag{3.28}$$

If the torque is estimated using the terminal quantities of only one phase, the on-line computational effort and the need of extra and expensive hardware will be reduced. Using the terminal quantities of only one phase will assume a constant torque over an entire electric cycle, meaning four strokes in the given case. This limits the speed and the quality of the response of the controller. Superior results in the torque response are achieved with the estimation of torque of all phases. To avoid the usage of expensive hardware, the phase voltage estimation presented in Fig. 4.10 can be used.

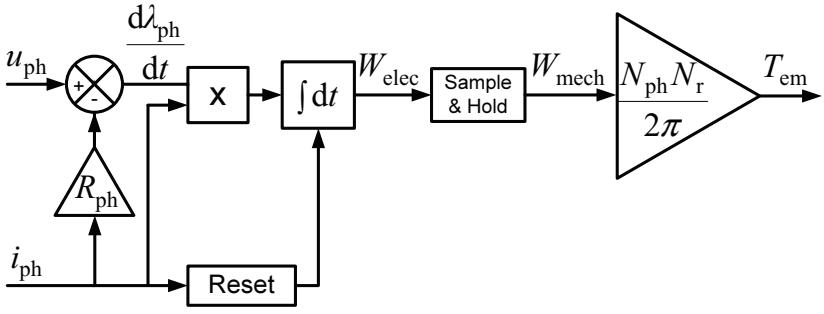

FIGURE 3.22: Structure of the average torque estimator [4]

The structure of the average torque estimator seen in Fig. 3.22 shows that the calculation of torque is based on the energy balance. The integrator has to be reset each time the current becomes zero to avoid drift on the electrical energy. A sample and hold block is used to

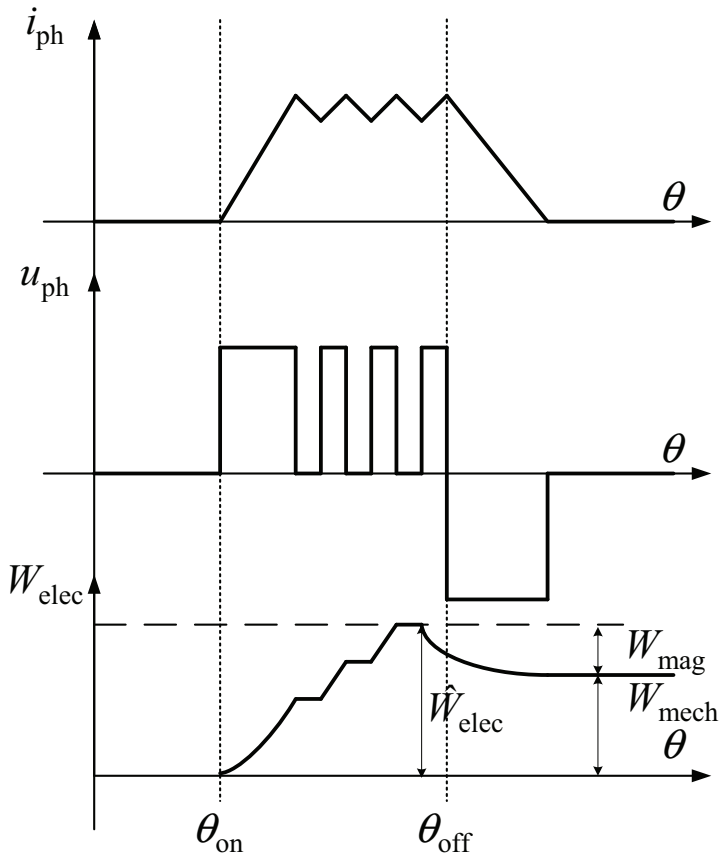

FIGURE 3.23: Typical quantities for the on-line average torque estimator [4]

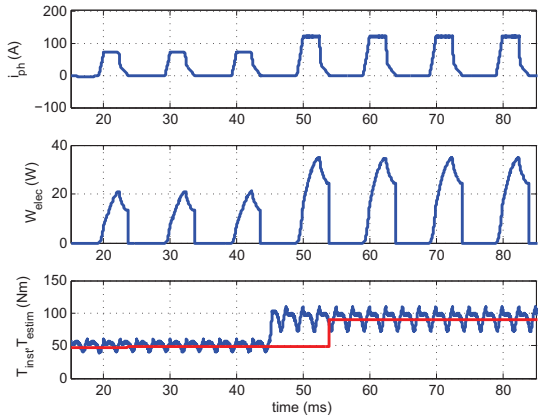

FIGURE 3.24: Reaction of the average torque estimator at a step change in the average torque

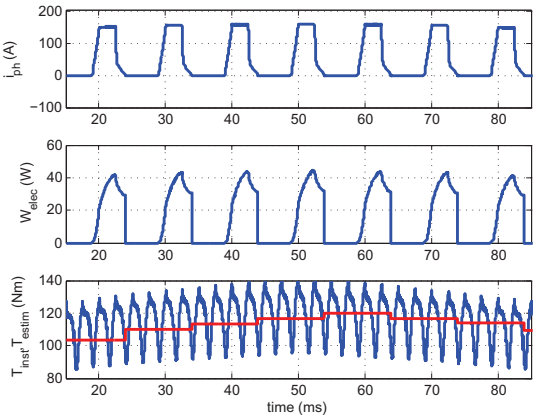

FIGURE 3.25: Reaction of the average torque estimator at a ramp change in the average torque

determine the mechanical energy. The typical quantities for the on-line average torque estimator are illustrated in Fig. 3.23

Another way to estimate the average torque is to use one of the the instantaneous torque estimation techniques described in Section 4.1 and to average the sum of the phase torques on the fundamental period τ using (3.17).

Fig. 3.24 and Fig. 3.25 show the reaction of the estimator to a step change and to a ramp change in the reference torque. In both figures from top to bottom are the phase current the electric energy and the instantaneous torque and the average estimated torque. The estimated average torque shows a delay of one electrical period. If the estimation is made using the terminal quantities of all four phases, the delay can be reduced to one fourth of the electrical period, but this will increase the computational effort.

3.4 Direct Average Torque Control

The open-loop controller is sensitive to variations of machine parameters, which are influenced by environmental conditions. The control variables are estimated off- or on-line in ideal conditions. Thus, the experimental drive output is susceptible to deviate from the reference torque value. To avoid these unwanted deviations between the torque reference and the torque output, it becomes desirable to track the average torque by adjusting the variables in a closed-loop control.

The error of torque is treated by a PI-controller and added to the reference torque, Fig. 3.26. The sum of the reference torque and the output of the PI-controller represents the new reference fed to the look-up tables of the control parameters. Fig. 3.27 shows the measured waveforms of the phase currents and electromagnetic torque at 1500rpm and a reference torque of 30Nm. The offset between the reference and the average value of torque, noticed when the feed-forward open-loop controller was used, has been eliminated .

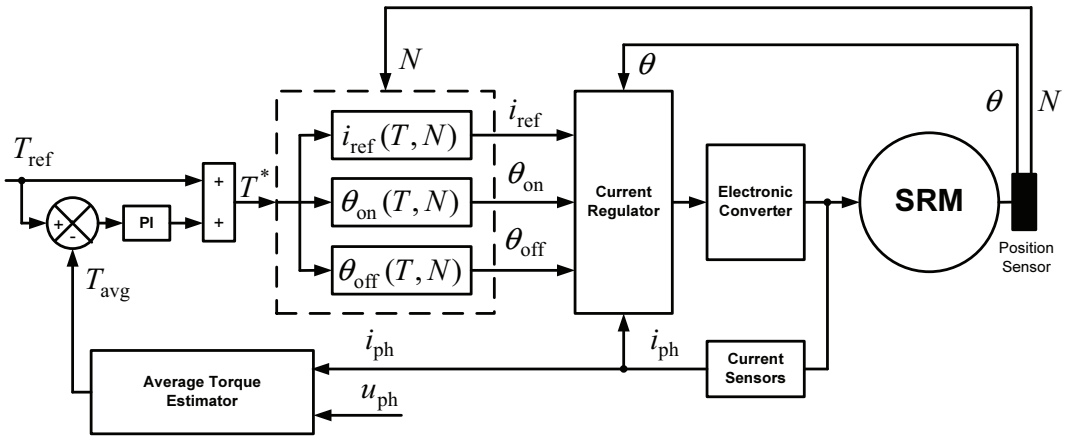

FIGURE 3.26: Direct average torque control of SRM

In Fig. 3.28, Fig. 3.29 and Fig. 3.30 the reaction of the torque controller at different changes in the reference is illustrated, while the speed is maintained constant at 1500rpm. With red is represented the reference and with blue is the instantaneous value of the electromagnetic torque. In Fig. 3.28 the reference torque is step changed from 10Nm to 25Nm and back. Fig. 3.29 the

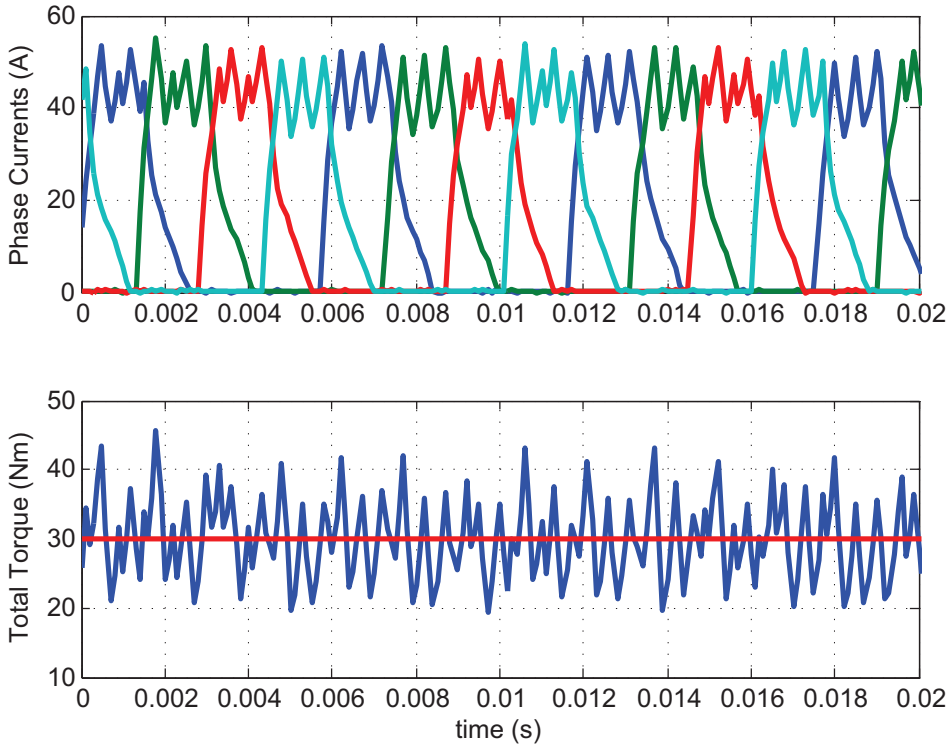

FIGURE 3.27: Measured waveforms at 1500rpm and 30Nm using DATC

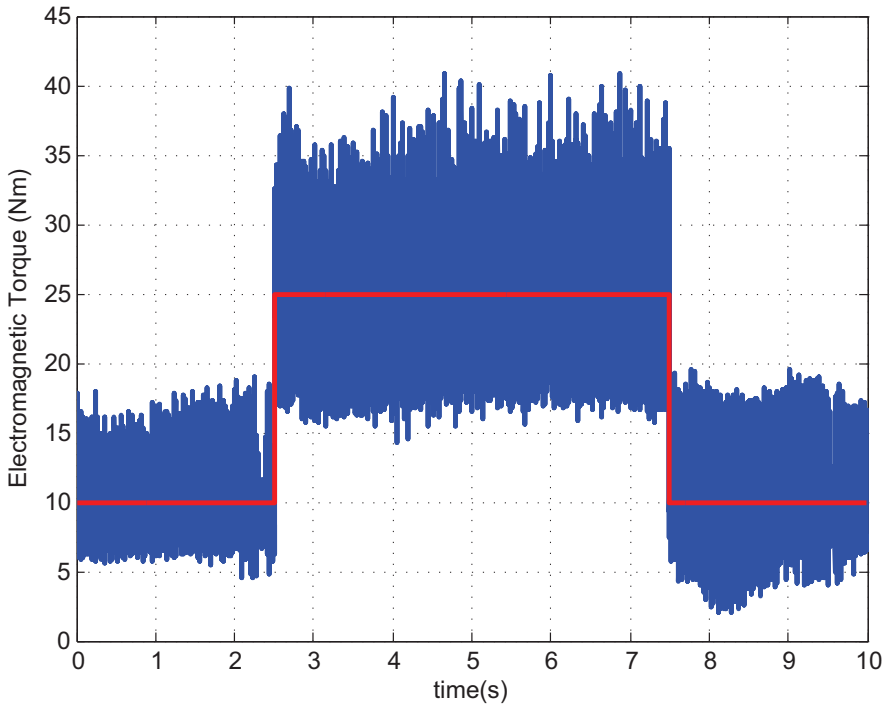

FIGURE 3.28: The measured reaction of the DATC controller at step changes in the reference torque at 1500rpm

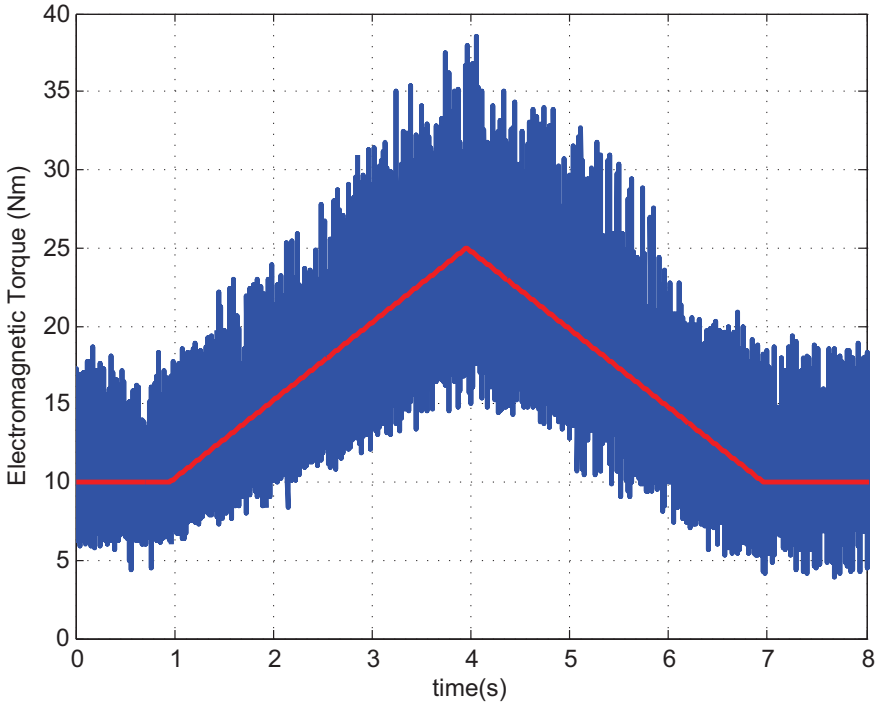

FIGURE 3.29: The measured reaction of the DATC controller at ramp changes in the reference torque at 1500rpm

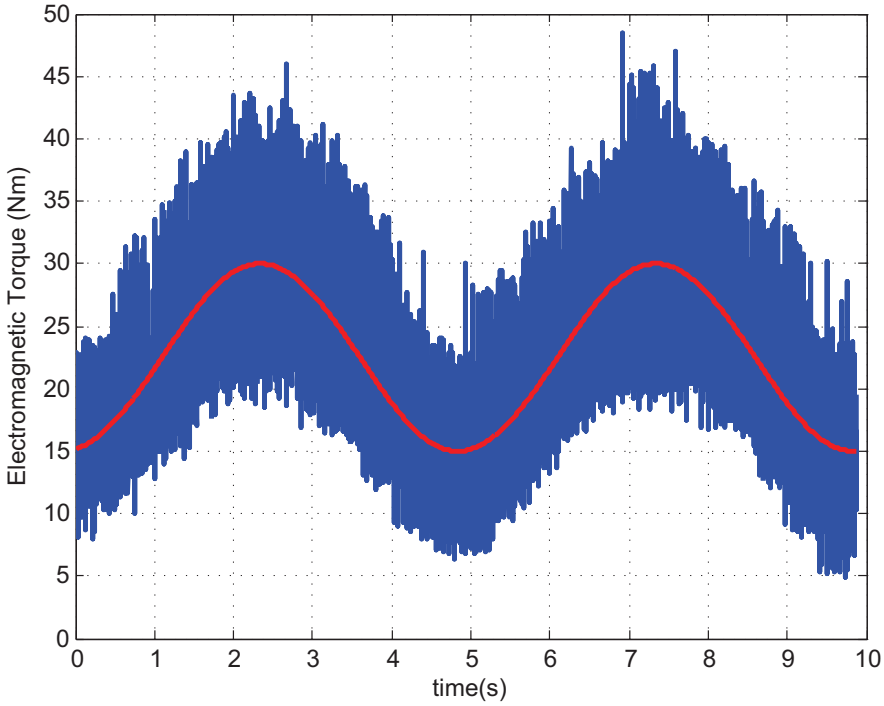

FIGURE 3.30: The measured reaction of the DATC controller at sinusoidal changes in the reference torque at 1500rpm

reference increases from 10Nm to 25Nm during 3 seconds with a constant slope and decreases back to 10 Nm in the same interval of time and with the same slope. A sinusoidal variation of the reference can be seen in Fig. 3.30 with a continuous component of 22.5Nm, an amplitude of 7.5Nm and a period of 5 seconds. The controller is capable of following the variation of the reference and no offset is observed between the mean value of torque and its reference.

3.5 Generator Operation of the Switched Reluctance Machine

The switched reluctance generator (SRG) is developed for wide-speed range applications where its characteristics make it commercially attractive, being compatible with extremely demanding applications. It is used for wind turbines [49, 50, 51, 52], for aerospace applications [53, 54, 55], as starter/generator for hybrid electric vehicles [56, 57, 58] and for electric vehicle traction [59, 60]. For the aerospace and automotive applications the behaviour of the SRG at high-speed operation is exploited, while for the wind energy application high-torque production is needed at low speed.

The SRM operates as a generator if the current flows in the phase when the slope of the inductance is negative, $\mathrm{d}L_{\mathrm{ph}}/\mathrm{d}\theta < 0$ [3]. Between the turn-on angle θ_{on}, situated around the aligned position where the inductance is maximum, and the turn-off angle θ_{off}, situated long before the phase inductance reaches its minimum value [30], the phase is energized, power being supplied from the DC-bus to the machine. From the turn-off angle θ_{off} to the extinction angle θ_{e}, generated power is returned to the DC-bus.

The voltage equation for one phase can be written as [21]:

$$\begin{aligned} u_{\mathrm{ph}} &= R_{\mathrm{ph}} i_{\mathrm{ph}} + \frac{\mathrm{d}\lambda_{\mathrm{ph}}}{\mathrm{d}t} \\ &= R_{\mathrm{ph}} i_{\mathrm{ph}} + L_{\mathrm{ph}} \frac{\mathrm{d}i_{\mathrm{ph}}}{\mathrm{d}t} + i_{\mathrm{ph}} \frac{\mathrm{d}\theta}{\mathrm{d}t} \frac{\mathrm{d}L_{\mathrm{ph}}}{\mathrm{d}\theta} \\ &= R_{\mathrm{ph}} i_{\mathrm{ph}} + L_{\mathrm{ph}} \frac{\mathrm{d}i_{\mathrm{ph}}}{\mathrm{d}t} + \omega i_{\mathrm{ph}} \frac{\mathrm{d}L_{\mathrm{ph}}}{\mathrm{d}\theta}, \end{aligned} \tag{3.29}$$

where u_{ph} is the phase voltage, i_{ph} is the phase current, R_{ph} is the phase resistance, λ_{ph} is the phase flux, L_{ph} is the phase inductance and ω is the angular speed in rad/s. The last term of the equation is called the back emf:

$$e = \omega i_{\mathrm{ph}} \frac{\mathrm{d}L_{\mathrm{ph}}}{\mathrm{d}\theta}. \tag{3.30}$$

In Fig. 3.31 the typical current waveforms of the current in generator operation are illustrated. For the simplification of the analysis, the variation of the inductance is considered linear. The phase voltage is equal to the DC-bus voltage, $u_{\mathrm{ph}} = V_{\mathrm{dc}}$, during phase excitation and equal to the negative value of the DC-bus voltage while generating, $u_{\mathrm{ph}} = -V_{\mathrm{dc}}$. In the fist case, after the phase energization is finished, the current is still increasing. This is typical for speeds higher than the base speed $\omega > \omega_{\mathrm{b}}$, where the back-emf is greater than the supply voltage $|e| > |V_{\mathrm{dc}}|$. In the second case, after the phase energization is finished, the current remains constant until the inductance reaches its minimum value. This happens at a speed equal to the base speed

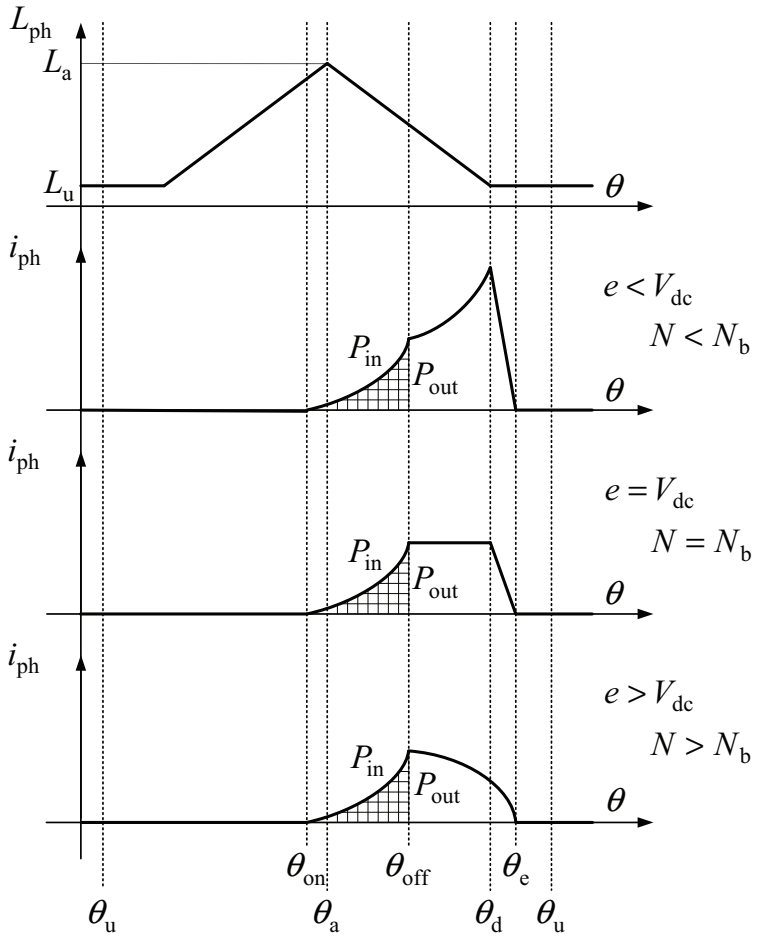

FIGURE 3.31: Typical current waveforms in generator operation

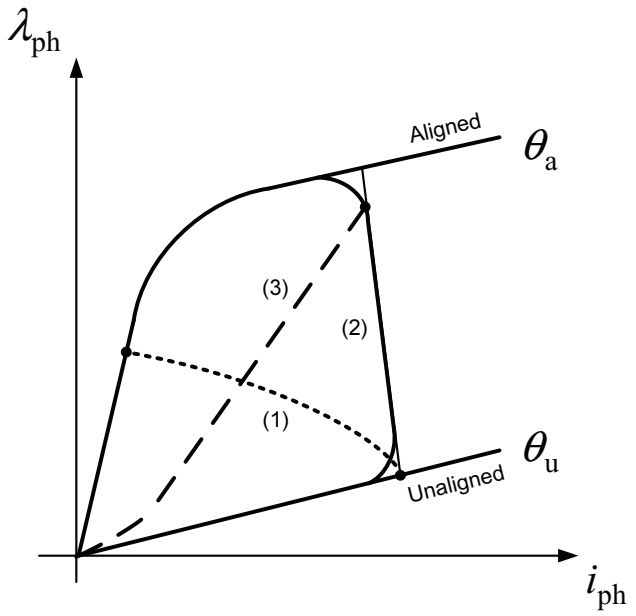

FIGURE 3.32: Typical energy loops in generator operation

$\omega = \omega_b$, where the back-emf is equal to the supply voltage $|e| = |V_{dc}|$. In the third case, after the phase energization is finished, the current is decreasing. This is typical for speeds lower than the base speed $\omega < \omega_b$, where the back-emf is smaller than the supply voltage $|e| < |V_{dc}|$. The typical energy loops in generator operation corresponding to the aforementioned cases are presented in Fig. 3.32.

For a constant DC-bus voltage, the excitation energy can be calculated as:

$$W_{exc} = \frac{V_{dc}}{\omega} \int_{\theta_{on}}^{\theta_{off}} i_{ph} d\theta. \tag{3.31}$$

The delivered energy is:

$$W_{out} = \frac{V_{dc}}{\omega} \int_{\theta_{off}}^{\theta_e} i_{ph} d\theta. \tag{3.32}$$

An excitation penalty can be defined as:

$$\epsilon = \frac{W_{exc}}{W_{out}}. \tag{3.33}$$

For the same generated energy, the penalty is smaller in the first case than for the other two cases. However, the torque area is small and the energy conversion ratio is not optimum [30]. In the second case the energy conversion loop is the largest, thus, the second case is more effective in energy conversion.

The peak value of the current i_{pk} can be calculated as the peak value of flux λ_{pk} divided by the value of the inductance at the point where the peak flux is reached L_{pk}:

$$i_{pk} \approx \frac{\lambda_{pk}}{L_{pk}}. \tag{3.34}$$

For the first considered case from Fig. 3.31, the peak value of the current occurs at the angle where the overlapping of rotor and stator poles ends θ_d and the inductance reaches its unaligned value L_u. Thus 3.34 becomes [30]:

$$i_{pk} = \frac{1}{L_u} \frac{V_{dc}}{\omega} (\theta_e - \theta_d) \approx \frac{1}{L_u} \frac{V_{dc}}{\omega} (\theta_{off} - \theta_{on} + \theta_{off} - \theta_d). \tag{3.35}$$

For the second and the third considered cases from Fig. 3.31, the peak value of the current occurs at the turn-off angle θ_{off}. Due to its linear variation in the ideal case, the peak value of the inductance is considered to be proportional with the difference $\theta_d - \theta_{off}$ and (3.34) becomes [30]:

$$i_{pk} = \frac{1}{L_u} \frac{V_{dc}}{\omega} \frac{\theta_{off} - \theta_{on}}{\theta_d - \theta_{off}}. \tag{3.36}$$

Both (3.35) and (3.36) show that a smaller turn-off angle leads to a smaller peak current. While generating, as in the case of motoring, the control of the torque and output power can be realized by controlling the firing angles θ_{on} and θ_{off}.

Speed or voltage control for maximum wind power extraction is typically used for wind generators. In hybrid or fully electric vehicles where the regenerated energy is used for recharging the battery, a torque control is used in generator mode. The state of charge of the battery dictates the reference torque from the required current. When braking (generating) on EVs, fast, precise and robust torque response is required from high speed down to zero speed, thus a reliable position sensor together with a robust torque controller is mandatory.

In Fig. 3.33, Fig. 3.34 and Fig. 3.35 the variation of the control parameters, calculated with the same procedure as for motor operation, is presented. The torque ripple was considered to be the most important performance parameter, having a weight factor three times greater than the weight factor of copper losses.

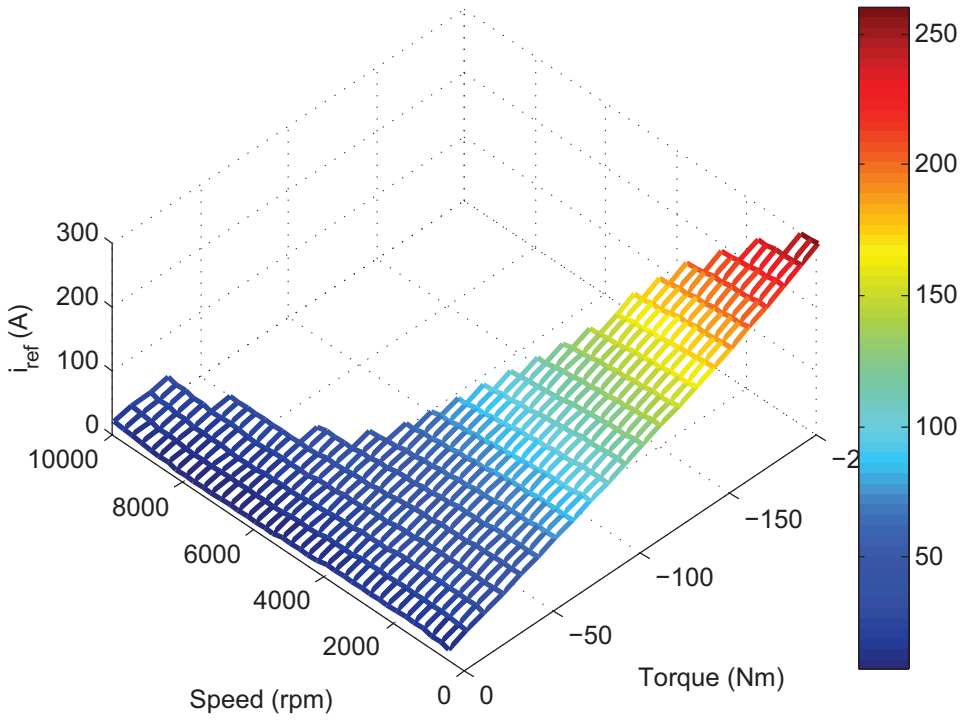

FIGURE 3.33: Reference current versus torque and speed in generator operation

Fig. 3.36 and Fig. 3.36 illustrate the variation of copper losses and torque ripple on the entire operating range from the torque-speed plane. The copper losses are increasing with the torque and slightly with speed. As in the case of motoring, the torque ripple has two critical areas, at low speed and at very high speed where the relative torque ripple can reach values of 50% and 80-90%, respectively.

Fig. 3.38, Fig. 3.39, Fig. 3.40 and Fig. 3.41 present the simulated waveforms of phase currents, phase voltages and phase fluxes and instantaneous electromagnetic torque. In all four cases the current rises under the influence of a positive voltage pulse. after the current reaches the reference value it is controlled within a hysteresis band by applying zero voltage or negative

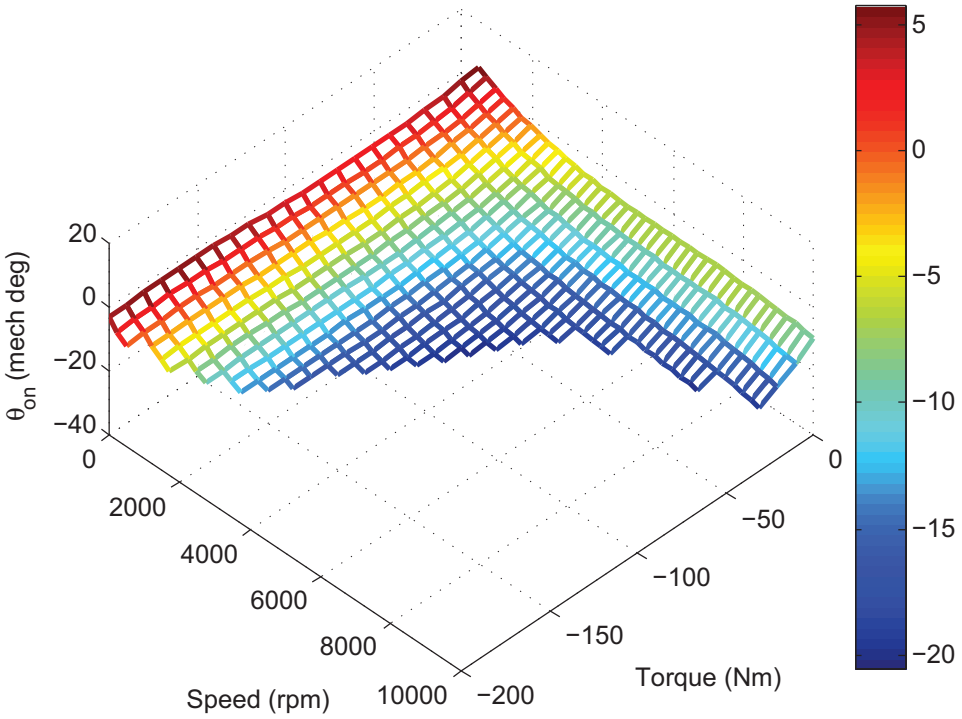

FIGURE 3.34: Turn-on angle versus torque and speed in generator operation

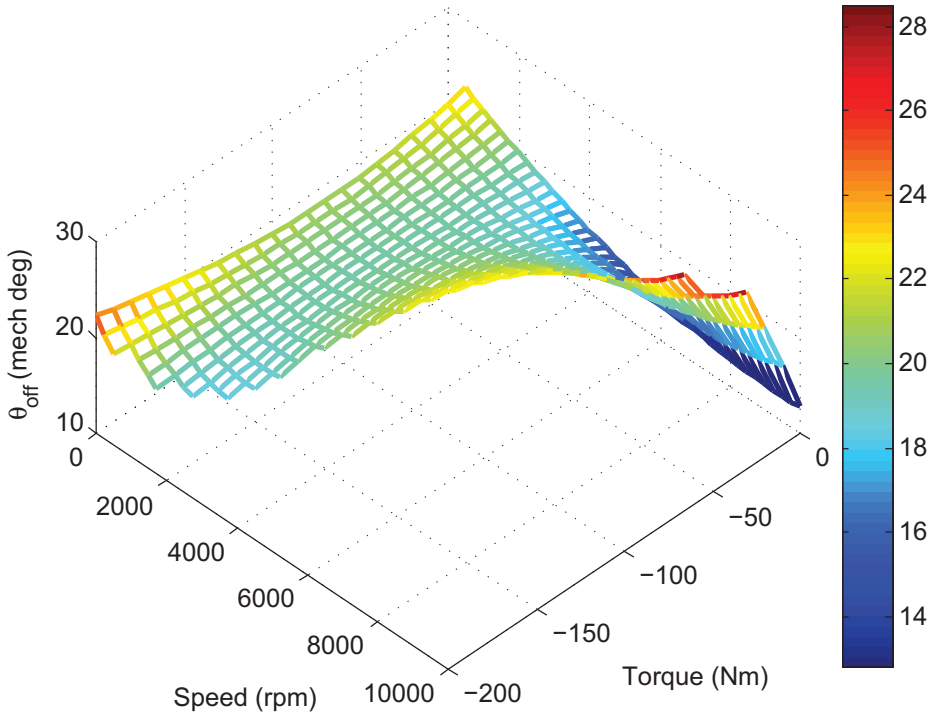

FIGURE 3.35: Turn-off angle versus torque and speed in generator operation

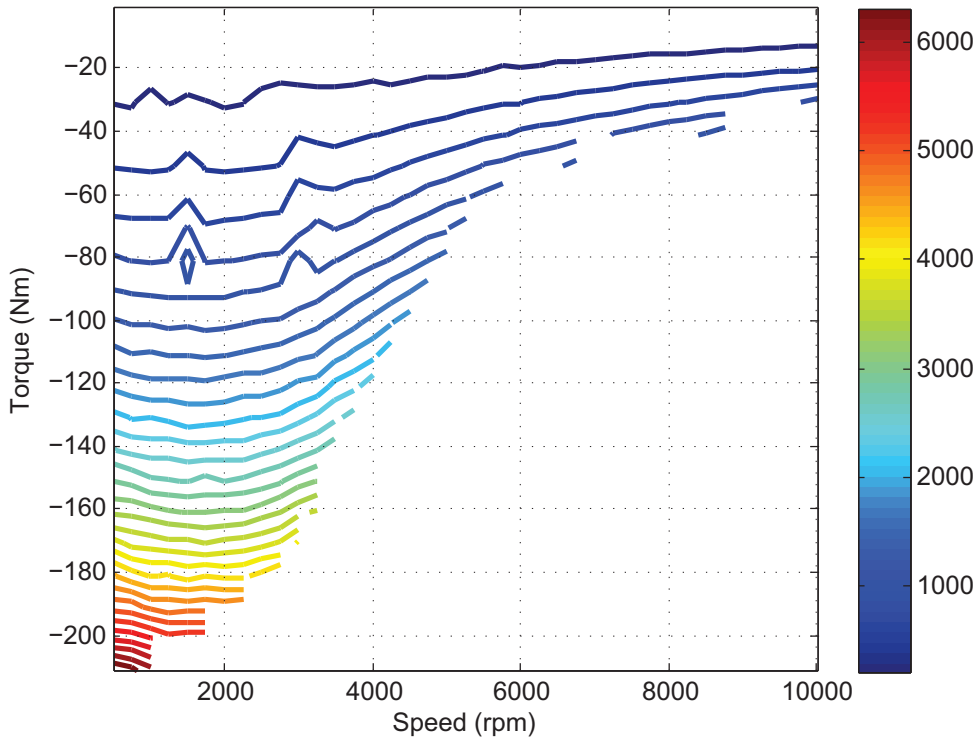

FIGURE 3.36: Copper losses variation versus torque and speed in generator operation

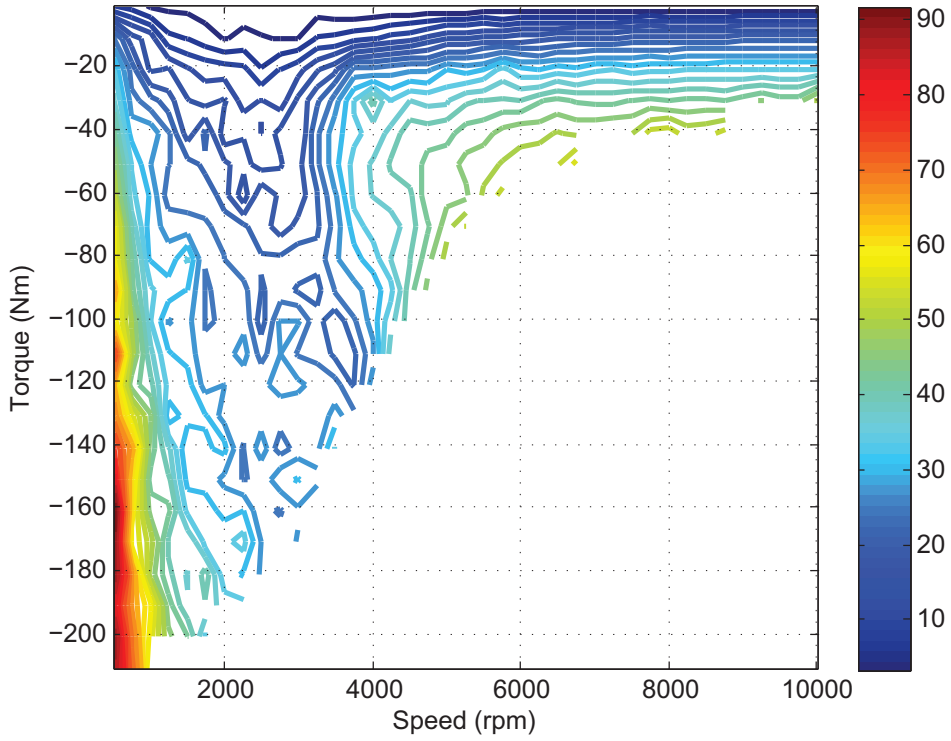

FIGURE 3.37: Torque ripple versus torque and speed in generator operation

voltage to the phase. Controlling the current on the negative slope of the inductance it is not necessary to apply positive voltage for the current to increase. Letting the current to increase under zero voltage and not positive decreases the switching frequency and, thus, the associated losses. Using the classical soft chopping for generator operation is not possible because at high speeds the back-emf has a greater value than the DC-bus voltage and the current cannot be controlled within the hysteresis band. If the instantaneous value of the current is not well controlled, it leads to high torque ripple and speed oscillations. Employing hard chopping makes possible the control of the current but the switching frequency and the associated losses are considerably increased.

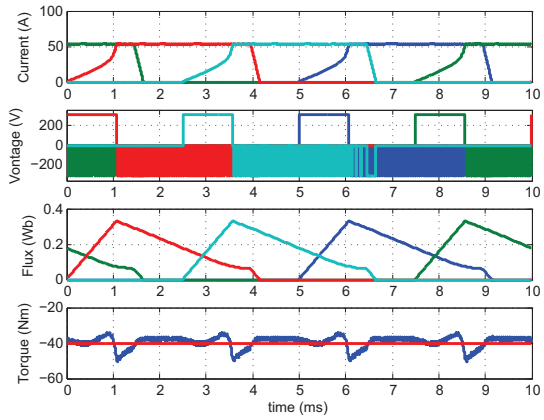

FIGURE 3.38: Simulated waveforms of phase currents, phase voltages, phase fluxes and instantaneous torque for a load torque of 40Nm at 1000rpm in generating mode

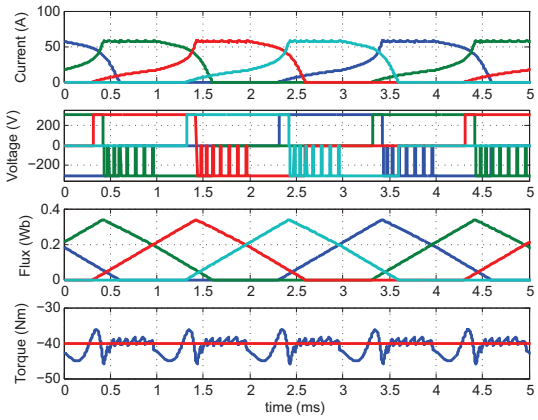

FIGURE 3.39: Simulated waveforms of phase currents, phase voltages, phase fluxes and instantaneous torque for a load torque of 40Nm at 2500rpm in generating mode

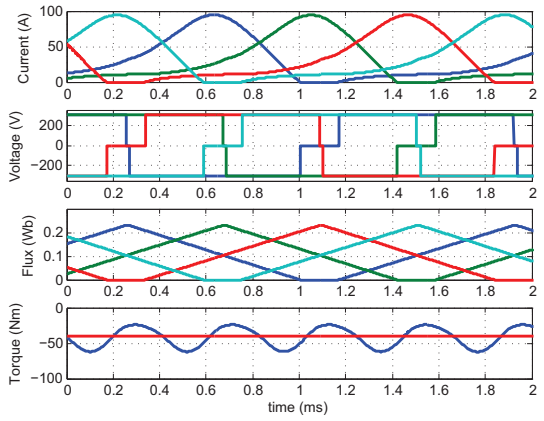

FIGURE 3.40: Simulated waveforms of phase currents, phase voltages, phase fluxes and instantaneous torque for a load torque of 40Nm at 6000rpm in generating mode

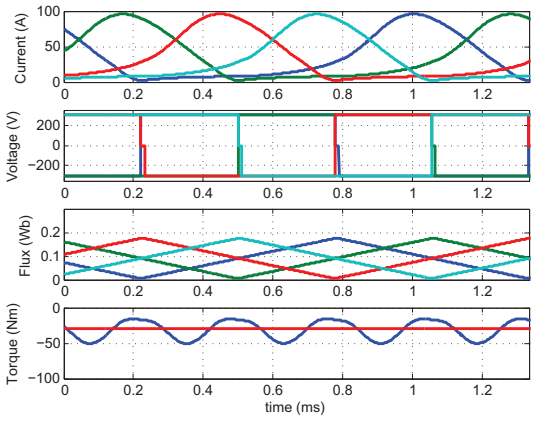

FIGURE 3.41: Simulated waveforms of phase currents, phase voltages, phase fluxes and instantaneous torque for a load torque of 30Nm at 9000rpm in generating mode

In Fig. 3.38 and Fig. 3.39 the value of the back-emf is lower than the DC-bus voltage and the current is kept within the borders of the hysteresis band by chopping. At higher speeds, Fig. 3.40, the value of the back-emf is considerably increased and the controller enters in single pulse conduction mode. The time interval for the current to reach its reference value under the positive voltage pulse is long due to the high value of the phase inductance. The current cannot

be controlled within the hysteresis band and continues to increase after the negative voltage is applied to the phase. The current shuts down only after the slope of the inductance becomes close to zero. At very high speed, Fig. 3.41, the phase current does not have the time to vanish and the machine enters in continuous conduction. The relative torque ripple is great at high speed leading to speed oscillations.

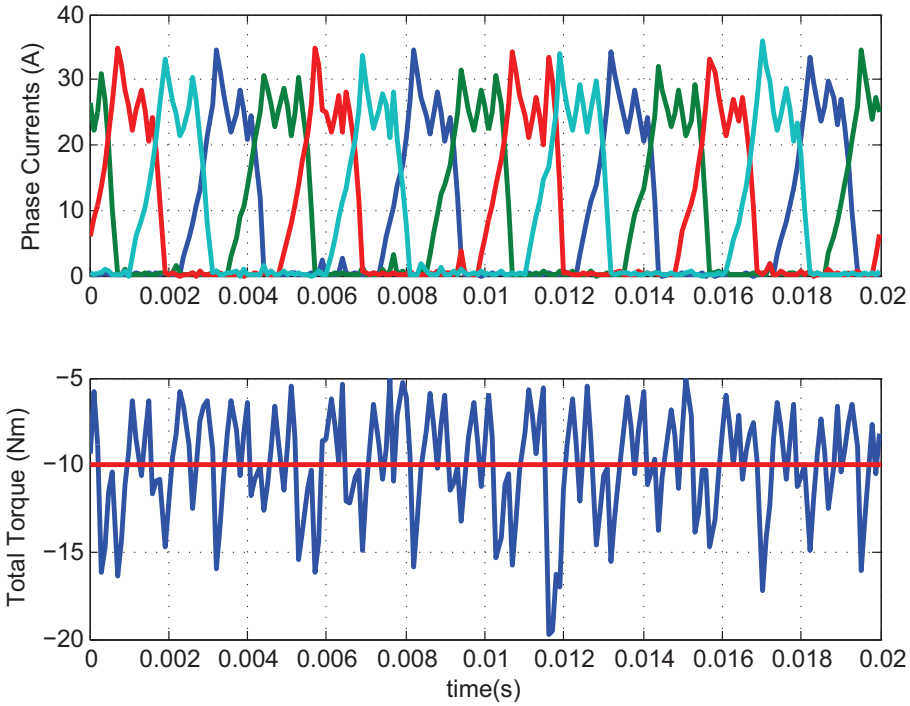

FIGURE 3.42: Measured waveforms of phase current and instantaneous torque for a load torque of 10Nm at 2000rpm in generating mode

In Fig. 3.42 and Fig. 3.43 are presented the measured waveforms of the phase currents and the instantaneous torque for a load torque of 10Nm at 2000rpm and 3000rpm respectively. Fig. 3.44 and Fig. 3.45 present the waveforms of one phase current and the corresponding phase voltage measured on the oscilloscope in the two cases. The current is controlled by chopping at 2000rpm and by single pulse at 3000rpm, respectively. The current at 3000rpm is decreasing under the influence of the negative voltage, meaning that the back-emf is smaller than the DC-bus voltage.

3.6 Speed Control of the Switched Reluctance Machine

Usually, the electric machines used for vehicle propulsion are torque controlled. The new intelligent systems equipping road vehicles come with an option called “cruise control”. The cruise control takes over the controller to maintain a steady speed set by the driver. This demands, besides the torque controller, an external speed loop, Fig. 3.46.

When the speed of an SRM is controlled via a speed loop, the reference torque is generated on the basis of the speed error amplified by a PI-controller. The output of the controller, together with speed, serves as input for the look-up tables in which the control parameters are stored.

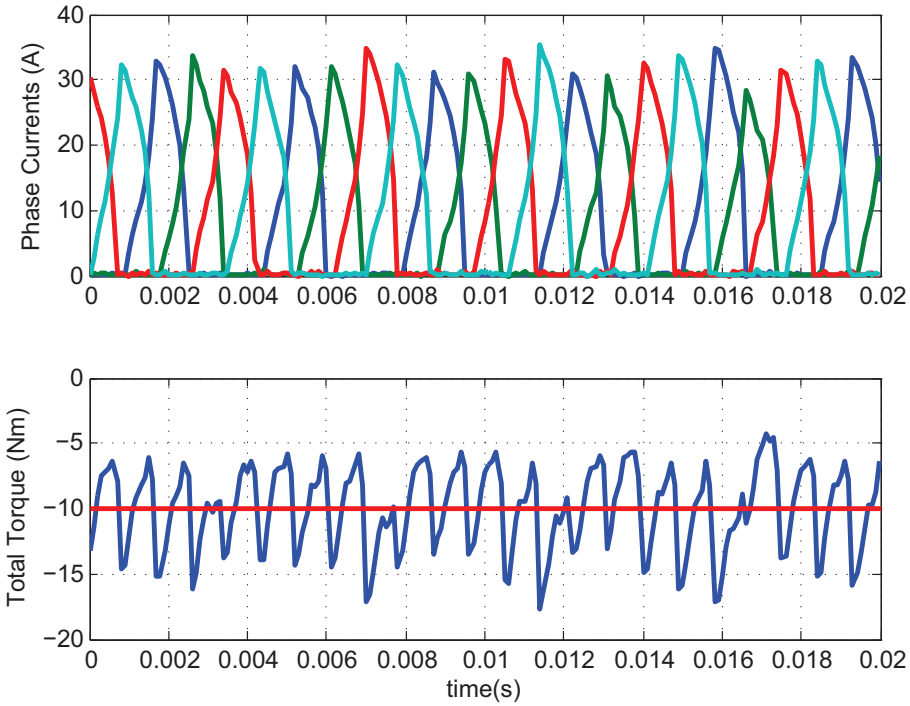

FIGURE 3.43: Measured waveforms of phase current and instantaneous torque for a load torque of 10Nm at 3000rpm in generating mode

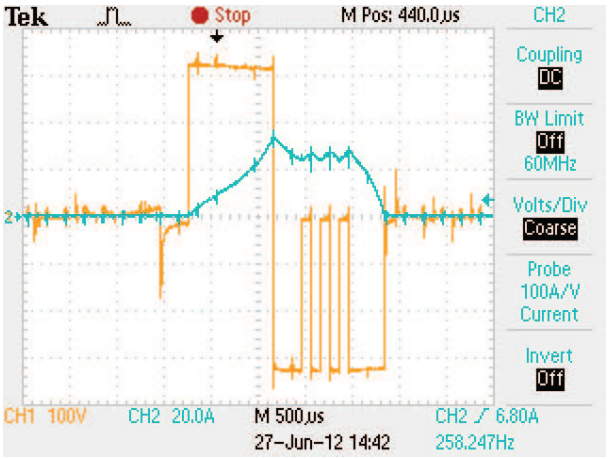

FIGURE 3.44: Measured waveforms of phase current and voltage in generating mode at 10Nm and 2000rpm

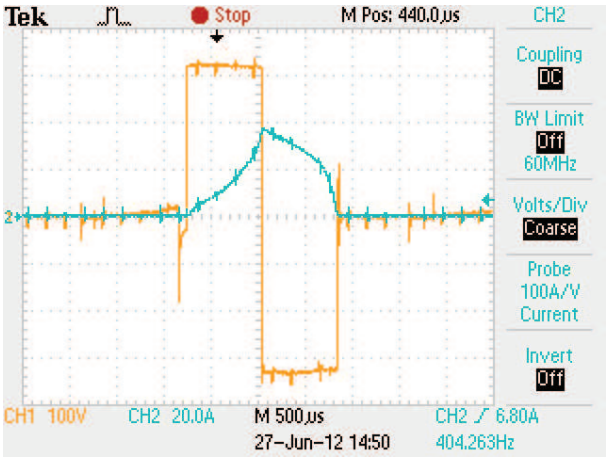

FIGURE 3.45: Measured waveforms of phase current and voltage in generating mode at 10Nm and 3000rpm

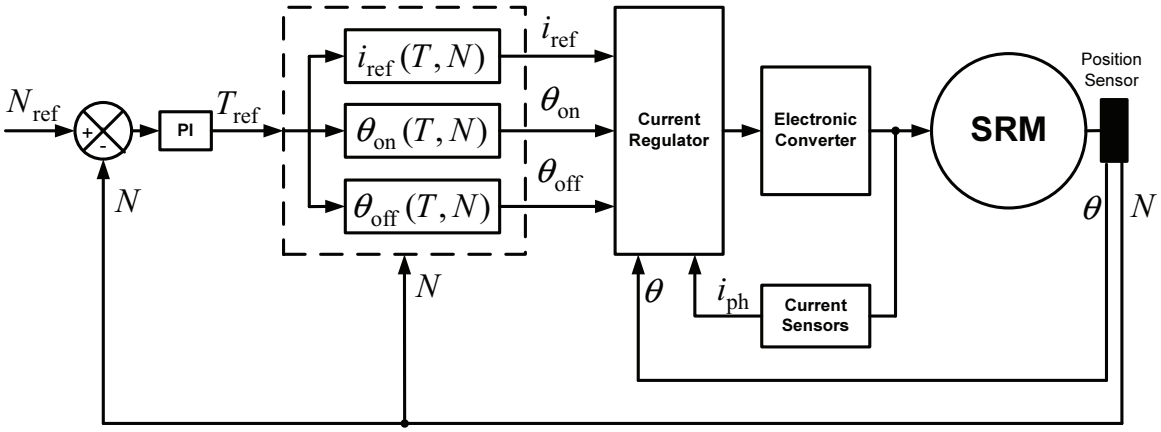

FIGURE 3.46: Speed control of switched reluctance machine

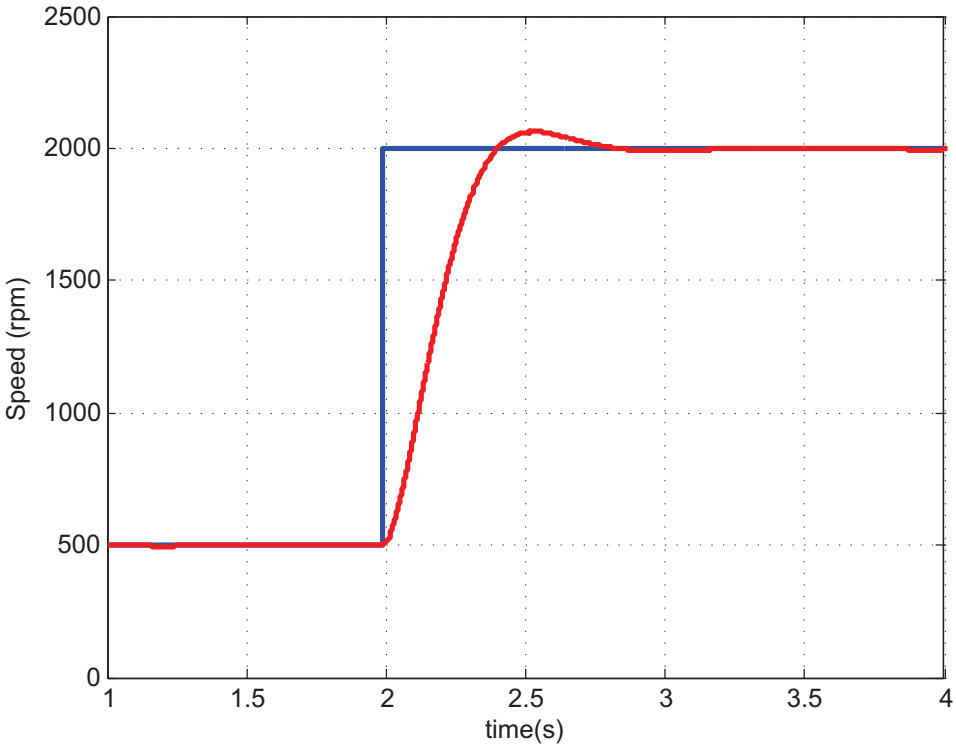

FIGURE 3.47: Reaction of the speed controller to a step change in the reference

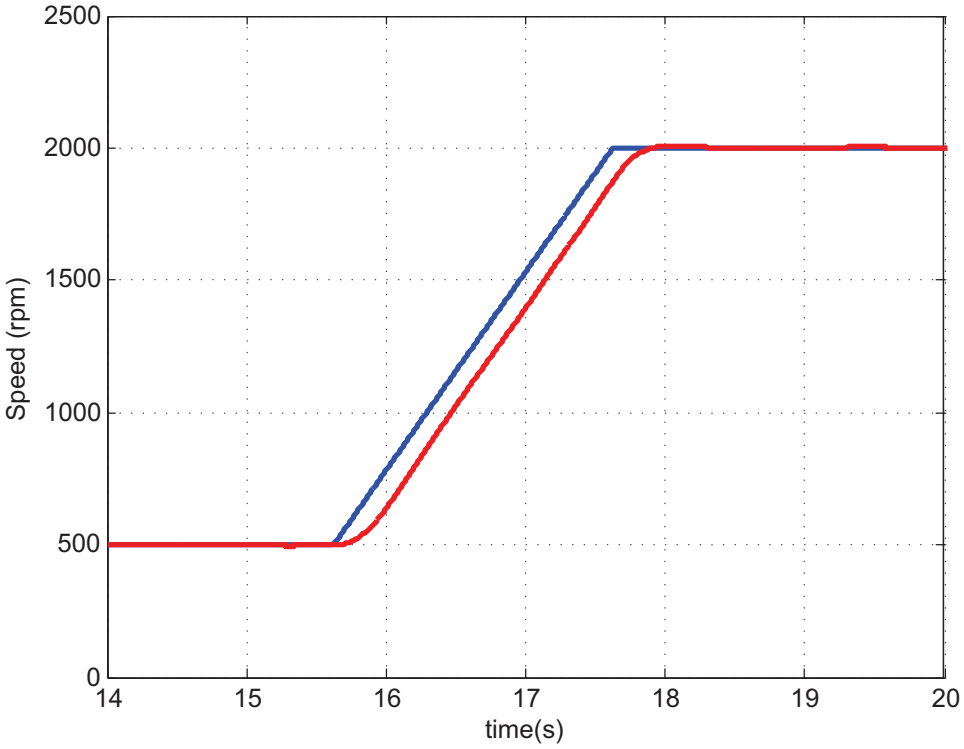

FIGURE 3.48: Reaction of the speed controller to a ramp change in the reference

Fig. 3.47 shows the reaction of the controller measured on the test bench at a step change in the reference speed from 500rpm to 2000rpm under a load torque of 30Nm. The speed reaches the reference value in less than 0.4 seconds and reaches steady state in less than 1.5 seconds. The overshoot in this case is 60rpm which represent 3% of the reference speed. Fig. 3.48 presents the reaction of the speed controller measured on the test bench at a ramp change in the reference from 500rpm to 2000rpm in 2 seconds with a constant slope. The delay between the reference value of speed and the measured reaction is given by the mechanical constant of the system.

3.7 Conclusions

The third chapter has been dealing with the control of the average torque of SRMs taking into consideration both motor and generator operation. The control parameters of the average torque controller (reference current, turn-on angle, turn-off angle) have been calculated using an optimization procedure for two different scenarios. This helps to eliminate the inaccuracies introduced by the analytical formulas describing the dependency of the control parameters on speed and torque. Through means of simulation and experimental results, the shortcomings of the open-loop average torque controller, mainly regarding the offset between the reference and the measured torque, have been shown.

To overcome these shortcomings, a closed loop control technique called direct average torque control has been implemented. For the implementation of the closed-loop average torque controller an on-line estimation of the average torque has been made on the basis of the coenergy per phase energy cycle. From simulation, good results have been shown in steady state, but

slow torque response. The response can be increased 4 times by using the terminal quantities of all phases for the estimation. The observed torque ripple and the slow torque response make this method to be suited only for high speed where torque pulsations in SRMs are inevitable.

The generator operation of the SRM has been studied and the control parameters have been calculated using the same procedure as for motoring. The soft switching is not usable in generator operation and hard switching has been replaced with a hybrid technique reducing the switching frequency and thus the associated losses.

A speed controller has been implemented based on a proportional integral regulator to satisfy the road vehicle demand of cruise control option.

Chapter 4

Instantaneous Torque Control of SRMs

For high dynamic applications, like electric vehicle propulsion, the drive is required to operate on a wide range in the torque speed plane. The continuously changing operating point in the traction drives demands the SRD to deliver high performance over a wide operating range. Moreover, at low speeds, the torque ripple has to be minimized in order to avoid undesired speed oscillations and to avoid the excitation of resonant frequencies in the drive train which can cause vibrations in the whole vehicle.

To overcome ripple related drawbacks, different torque-ripple minimization techniques have been proposed in the literature regarding the design and the control of SRMs.

Rotor skewing and pole shaping are the main mechanical design features used to minimize the ripple. These methods are effective only on a limited operating range and also the maximum torque is decreased due to the enlarged air-gap [61]. This can be translated into lower torque density, which is not an option for the vehicle traction applications confronting the limited space in a vehicle.

To overcome the inconveniences represented by the salient structure and the highly non-linear behaviour of the SRM, different torque control techniques (instantaneous & average) were developed.

A wider operating range, but still limited, can be achieved by profiling the waveforms of the current or flux, off-line or on-line [5, 62, 63]. The cumbersome and time-consuming pre-calculations needed in order to find the optimal profile of the phase current or flux together with the demand for a precise position measurement and the lack of highly trained specialists in the field may cause a delay in the spread of SRDs on the market.

Chapter 5 begins with a discussion on the on-line estimation of the instantaneous torque produced in the SRM. Two instantaneous torque control methods are next presented, namely Direct Torque Control and Direct Instantaneous Torque Control, together with their modelling and practical implementation. The chapter ends with a comparison between the classical current profiling technique and the described methods.

4.1 On-line Instantaneous Torque Estimation

An instantaneous-torque estimation is imperative for an instantaneous torque control implementation. In the absence of an efficient torque meter, the instantaneous torque has to be precisely estimated. In the automotive industry, due to aspects regarding space and price, the estimation is also preferred over the measurement.

The instantaneous-torque estimation in an SRM is not a trivial task. Thus, several estimation techniques were developed over time [64]. The first developed analytical methods are not taking into consideration the non-linearities of the model of the SRM. To compensate the non-linearities, tables for correction were added to the linear models. The accuracy of the estimation did not reach acceptable error tolerances.

Nowadays, the models of the machines are created using experimental measurements and/or finite element analysis. So obtained data can be further used for an accurate estimation of the machine's performances.

The estimation of instantaneous torque can be done using different characteristics of the machine stored in look-up tables: $T_{\text{ph}}(i_{\text{ph}}, \theta)$, $T_{\text{ph}}(\lambda_{\text{ph}}, \theta)$, $T_{\text{ph}}(i_{\text{ph}}, \lambda_{\text{ph}})$, where T_{ph} is the phase torque, i_{ph} is the phase current, λ_{ph} is the phase flux and θ is the rotor position. Using these tables, three estimation methods will further be discussed.

4.1.1 Estimation from Phase Currents and Rotor Position

The first table, torque versus phase current and rotor position (Fig. 4.1), and likely the most used one, employs the phase currents and the rotor position for the estimation of the torque as illustrated in Fig. 4.2. The need of a continuous and accurate rotor position measurement represent a drawback of this method.

4.1.2 Estimation from Phase Fluxes and Rotor Position

The second table, torque as a function of flux linkage and rotor position, Fig. 4.3, does not use the phase currents but the phase flux for the torque estimation, Fig. 4.4.

To calculate the flux linkage, the phase voltage equation of an SRM has to be considered:

$$u_{\text{ph}} = R_{\text{ph}} i_{\text{ph}} + \frac{\mathrm{d}\lambda_{\text{ph}}}{\mathrm{d}t}, \tag{4.1}$$

where u_{ph} is the phase voltage, i_{ph} the phase current, λ_{ph} the phase flux and R_{ph} the phase resistance. The flux linkage can be obtained by integration:

$$\lambda_{\text{ph}} = \int (u_{\text{ph}} - R_{\text{ph}} i_{\text{ph}}) \mathrm{d}t. \tag{4.2}$$

To estimate the flux linkage, both the phase voltages and currents have to be used. So, besides the already existing current sensors, at least one voltage sensor has to be installed on one phase. The existence of only one voltage sensor forces the controller to consider a constant torque over four strokes, situation unacceptable for an instantaneous control technique. Thus the existence

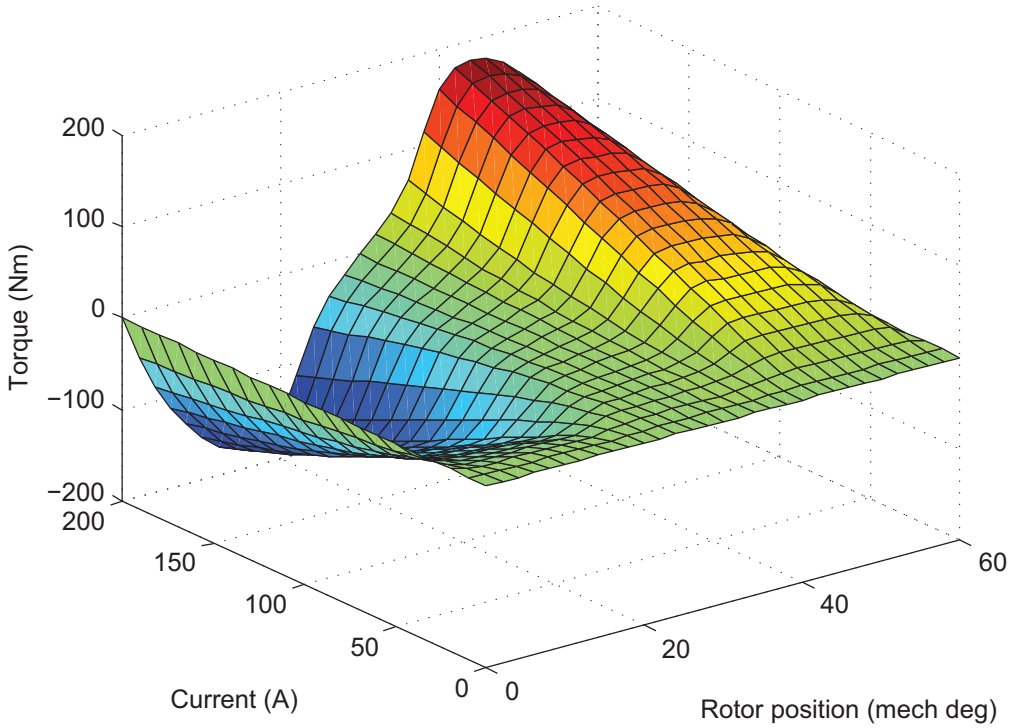

FIGURE 4.1: The electromagnetic torque dependence on phase current and rotor angular position

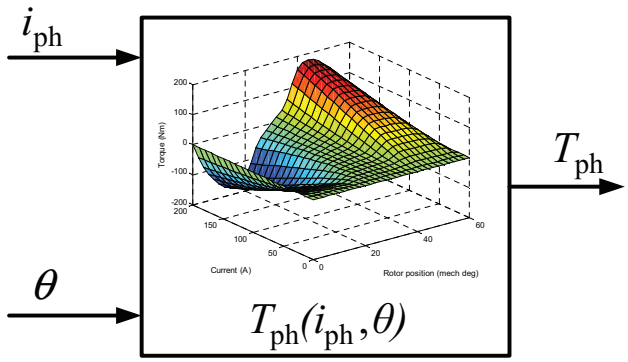

FIGURE 4.2: Electromagnetic torque estimation using phase current and rotor position

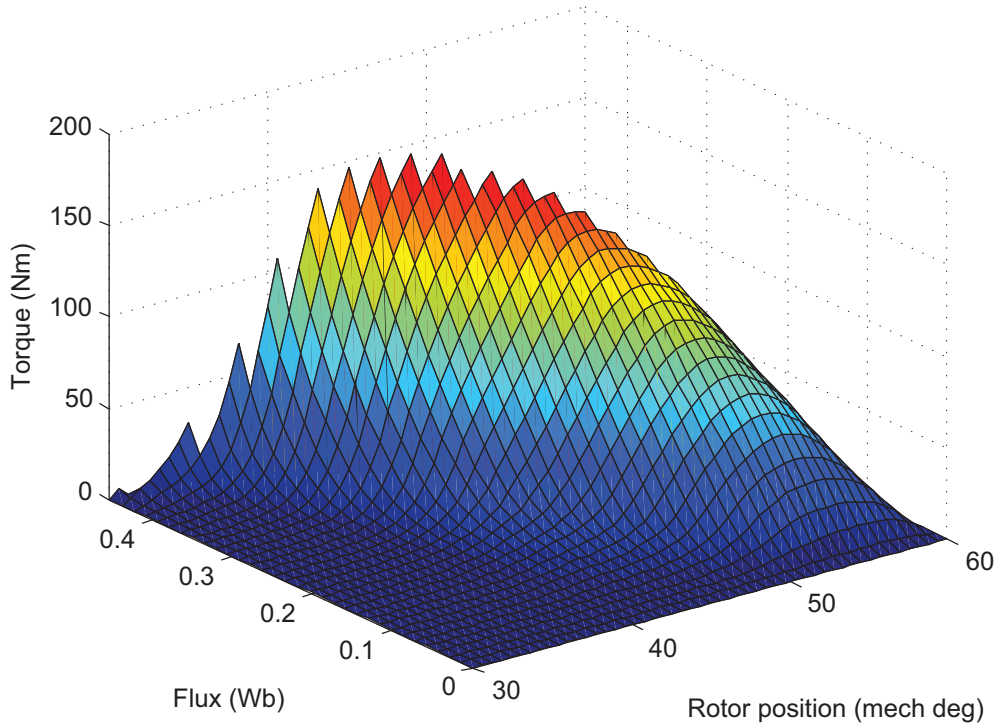

FIGURE 4.3: The electromagnetic torque dependence on flux linkage and rotor angular position

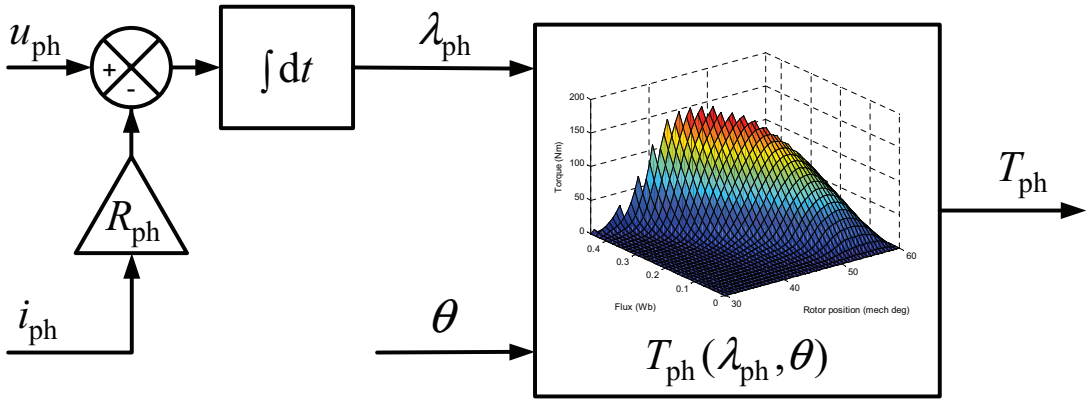

FIGURE 4.4: Electromagnetic torque estimation using phase current and rotor position

of a voltage sensor on each phase is required. This increases the overall price of the drive, also a sensitive problem in the automotive industry. Moreover, the implementation of (4.2) in the controller will introduce delays. Using this table, the need of position measurement is not eliminated. The second table (Fig. 4.3) is therefore not used in practice.

4.1.3 Estimation from Phase Currents and Voltages

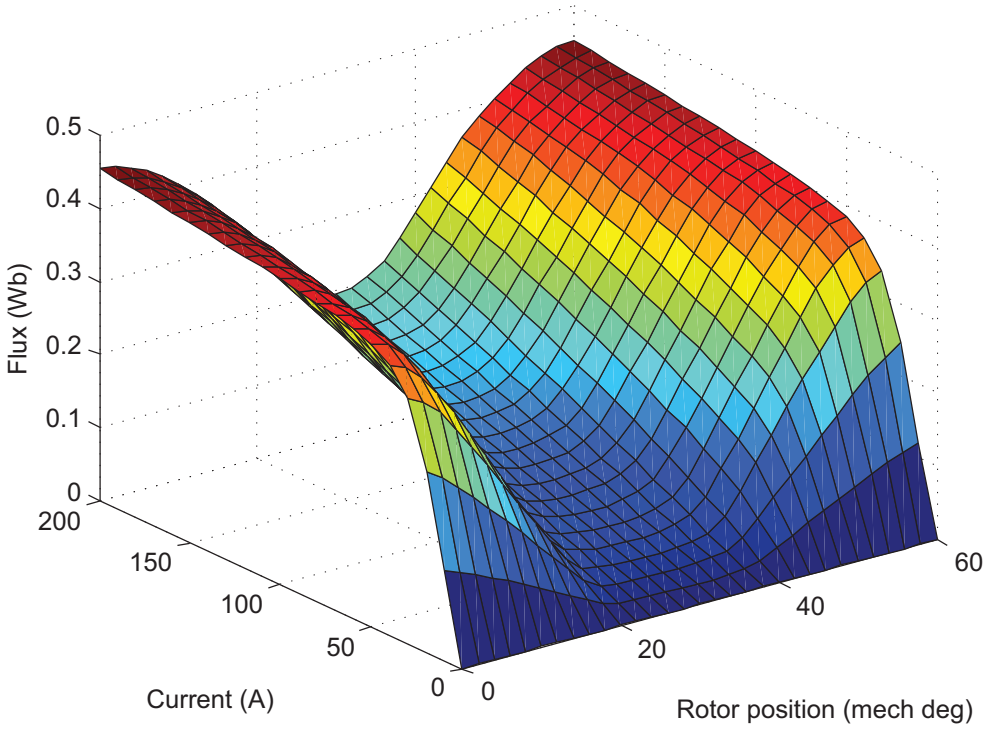

FIGURE 4.5: The flux linkage dependence on phase current and rotor angular position

Another instantaneous torque estimation technique uses the tables of torque (Fig. 4.1) and flux (Fig. 4.5) as a function of phase current and rotor position in order to avoid the need of a precise position measurement. Combining the static torque characteristics with the flux linkage characteristics and eliminating the rotor position, the characteristics of torque as a function of phase current and flux linkage, $T_{\mathrm{ph}}(i_{\mathrm{ph}}, \lambda_{\mathrm{ph}})$, can be obtained (Fig. 4.6). The table has to be mirrored with respect to current-flux plane for negative values of the torque. Using the data in this table the torque can be estimated independently of the rotor position, only by measuring the phase currents and voltages. To be able to estimate the torque from the phase voltages and currents, (4.2) has to be implemented in the controller.

Taking into account the price of wide bandwidth voltage sensors and the frequency limitations imposed by the prototyping tool, the authors decided to estimate the instantaneous torque from the phase currents and rotor position, using the table $T_{\mathrm{ph}}(i_{\mathrm{ph}}, \theta)$.

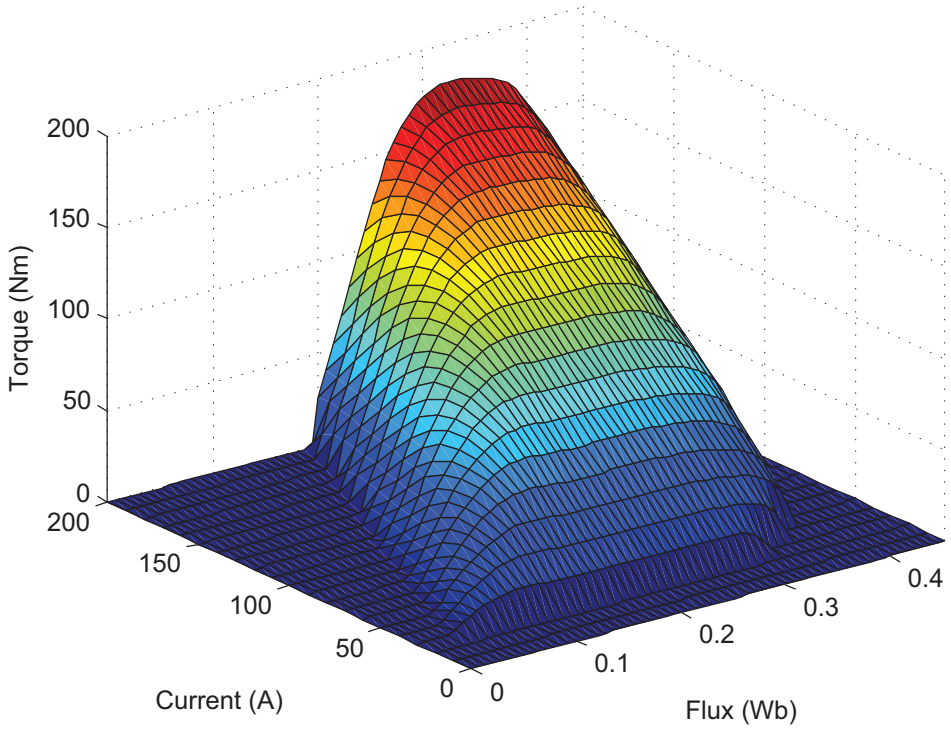

FIGURE 4.6: The electromagnetic torque dependence on phase current and flux linkage

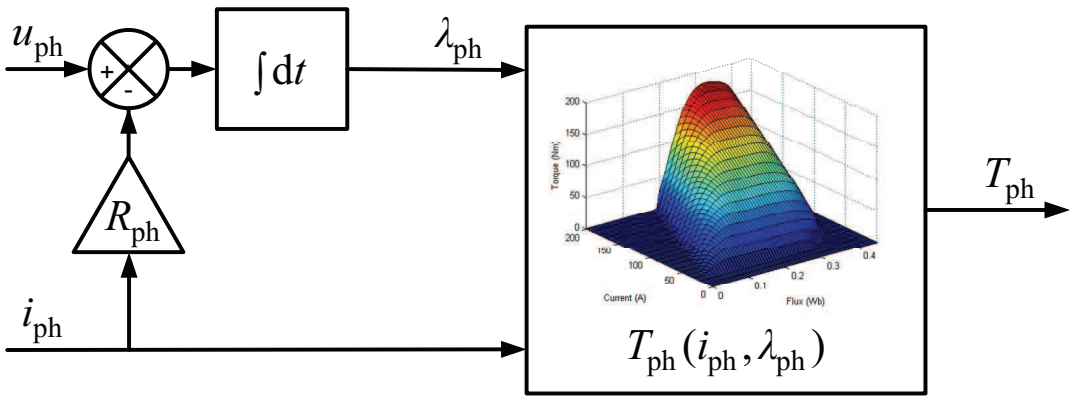

FIGURE 4.7: Electromagnetic torque estimation using phase current and rotor position

4.1.4 Position Estimation

By combining the tables of torque (Fig. 4.1) and flux (Fig. 4.1) as a function of phase current and rotor position and eliminating the torque, a table for the position as a function of phase current and linkage flux can be obtained (Fig. 4.8). Using the mentioned table as in Fig. 4.9, a sensorless control can be achieved [65] on a limited operating range operating range.

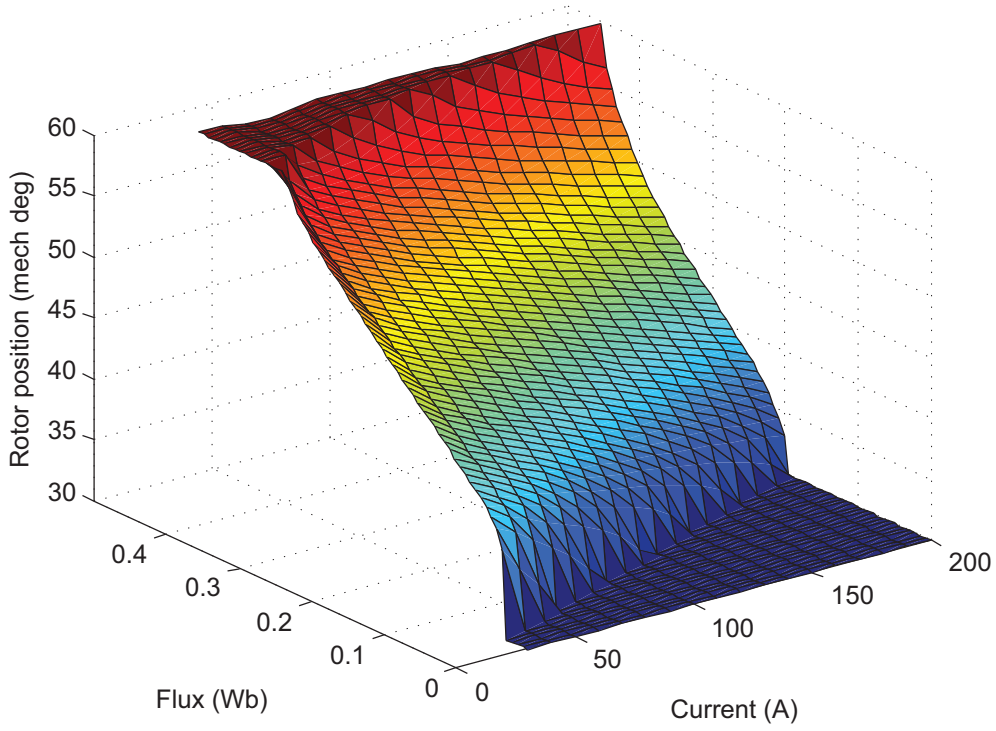

FIGURE 4.8: Rotor position dependence on phase current and flux linkage

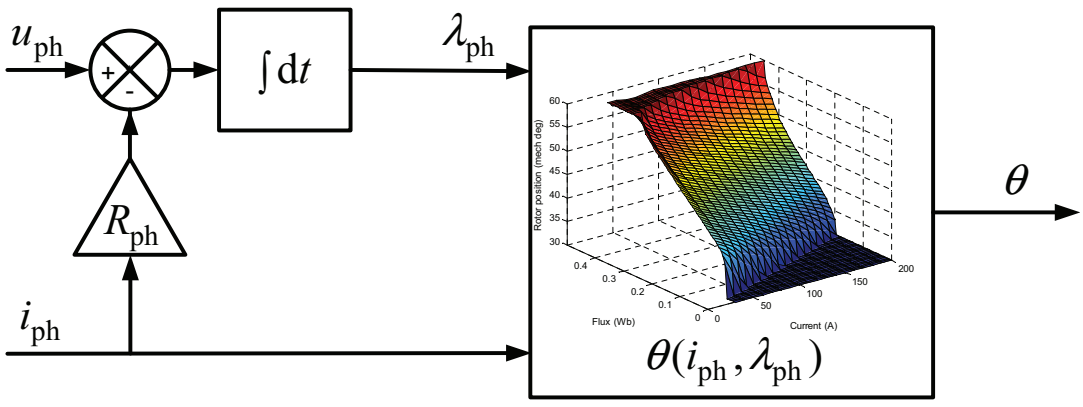

FIGURE 4.9: Rotor position estimation using terminal quantities

4.1.5 Phase Voltage Estimation

To avoid the mounting of expensive voltage sensors on each phase, an estimation of all phase voltages can be done from the transistor gate signals and using only one inexpensive voltage sensor for the measurement of the DC-bus voltage. The logic of the estimation is presented in Fig. 4.10.

When both switches are on, the voltage across the phase is positive and equal to the DC-bus voltage. While both switches are off and a non-zero current is measured, the voltage across the phase winding is negative and equal to minus the DC-bus voltage. For all other combinations the phase voltage is equal to zero. The voltage drop on the semiconductor components has to be taken into account for a better estimation of the phase voltage.

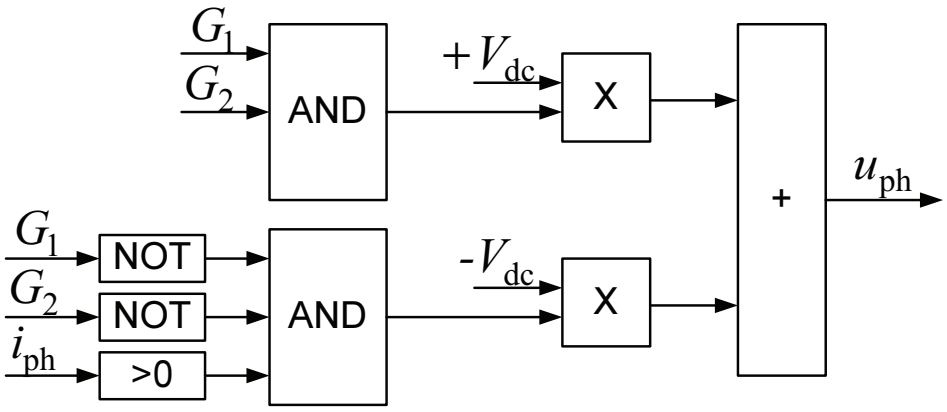

FIGURE 4.10: Phase voltage estimation from transistor gate signals

4.2 Voltage States Definition

For an SRM with each phase fed by an asymmetric H-bridge, for a unidirectional current, three possible voltage states S_j are defined as (Fig. 4.11):

a) $S_j = 1$, both switches are on and positive voltage is applied to the phase;

b) $S_j = 0$, one switch is on and the other is off and a zero voltage loop occurs;

c) $S_j = -1$, both switches are off, the voltage on the phase is negative and the freewheeling current flows through the diodes.

The voltage states are employed in the definition of the switching tables for both Direct Instantaneous Torque Control (DITC) and Direct Torque Control (DTC) and also for the definition of space voltage vectors used to define the switching vectors in the case of DTC.

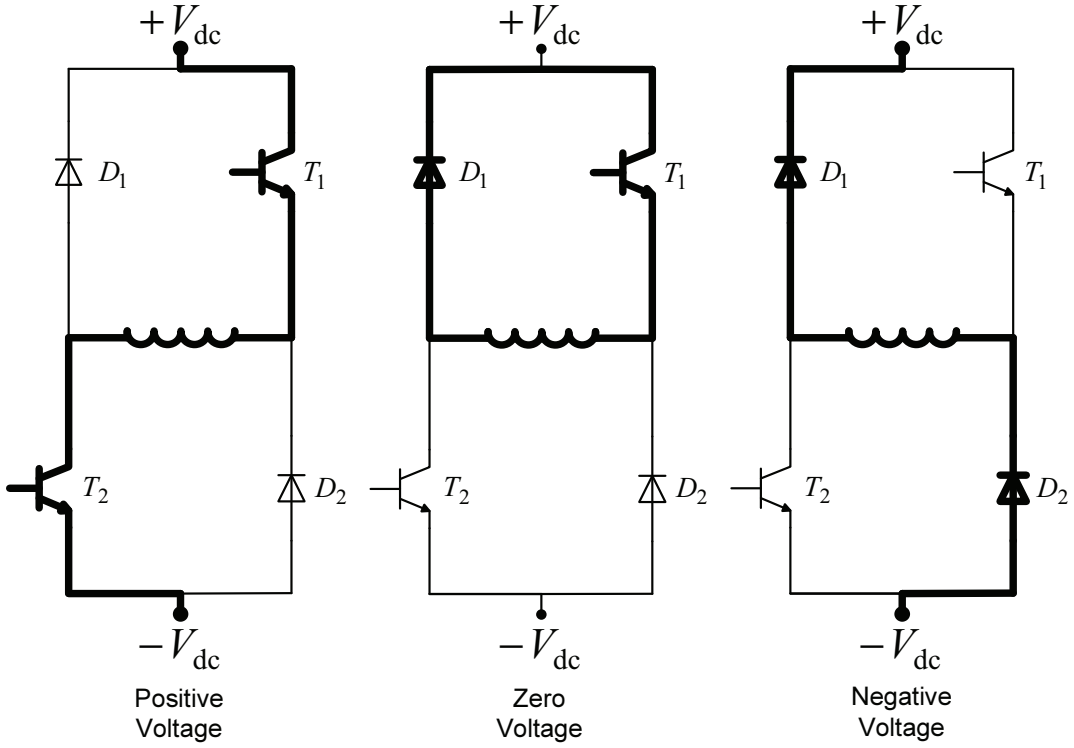

FIGURE 4.11: The three possible voltage states of a phase of an SRM fed by an asymmetric H-Bridge

4.3 Direct Instantaneous Torque Control

The so-called Direct Instantaneous Torque Control technique was proposed by Inderka and De Doncker from RTW Aachen in the early 2000s [66, 67]. The proposed closed-loop architecture uses a simple hysteresis controller to compare the instantaneous value of torque with its reference in order to generate the switching signals for the electronic converter [65, 66, 67, 68, 69, 70, 71]. DITC does not use flux or current profiling techniques and does not require a very precise position measurement.

Section 4.3 presents the implementation of the DITC. The functioning principles of DITC are discussed together with its advantages. Simulation and experimental results are shown and analysed.

4.3.1 Operating Principles of DITC

The DITC is a closed loop instantaneous torque control technique, Fig. 4.12, employing a simple hysteresis controller equipped with two hysteresis bands (an interior band and an exterior band) in order to maintain the torque at its reference value, within the imposed tolerances. The method uses the concept of phase torque sharing without using pre-calculated torque-sharing functions.

During single-phase conduction interval of phase n, between the turn-off angle of the phase $n-1$ and the turn-on angle of the phase $n+1$, the controller changes only the state of the energized phase n in order to regulate the torque. At phase commutation, between the turn-on angle of

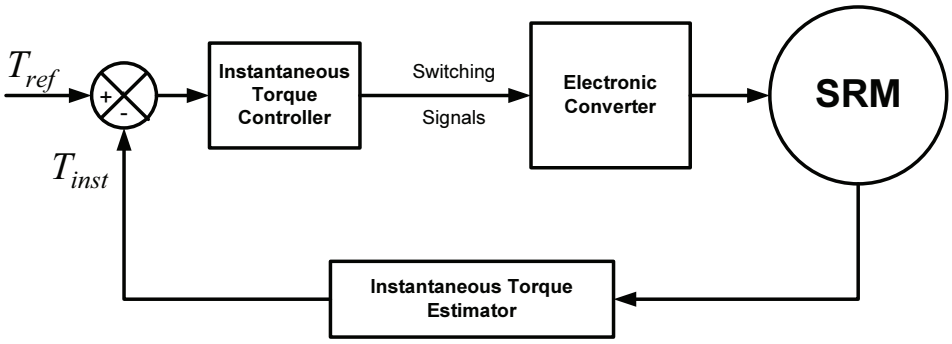

FIGURE 4.12: Closed-loop structure of DITC

the incoming phase, $n+1$, and the turn-off angle of the outgoing phase, n, the states of the two phases are being modified and their individual torque is controlled by controlling the total torque. The commutation strategy further implemented in the controller is presented in Table 4.1. The small "x" means the phase is not taken into account for torque production, while the state, S_j, of one torque productive phase is explained in section 4.4.1.

Each phase is enabled between its turn-on and turn-off angles. Soft chopping is employed by the converter in single-phase conduction: either the positive DC-link voltage is applied to the phase ($S_j = 1$), either a zero-voltage loop is created ($S_j = 0$). The states of two phases are being switched at phase commutation. While the incoming phase is not capable of producing the required torque, the outgoing phase, previously switched to zero-voltage state, contributes to the torque production by changing the state to $S_j = 1$. After it reaches its turn-off angle, the outgoing phase is being demagnetized, $S_j = -1$. Also, the outgoing phase can be demagnetized during phase commutation, if the incoming phase is capable of producing the reference torque by itself.

As can be seen in Fig. 4.13, at the beginning of the conduction period the incoming phase is energized and the outgoing phase is switched into zero-voltage state. When the total torque reaches a value lower than the one permitted by the exterior hysteresis band, the outgoing phase will be excited again with positive voltage, $S_j = 1$. After a certain point, the incoming phase is able to control the torque by itself, so the outgoing phase will be switched into the zero-voltage loop. If the highest value of torque is reached, the outgoing phase is demagnetized, $S_j = -1$, in order not to demagnetize the incoming phase. For preventing negative torque production, at the end of the conduction period, negative voltage is applied to the phase and the current is rapidly shut down.

The strategy used by the DITC automatically commutates the phases and regulates their torque independently of a precise knowledge of rotor position or switching angles.

Due to the usage of the zero-voltage state, the switching frequencies of DITC are considerably reduced compared to the switching frequencies of current profiling techniques employing hard chopping. DITC can be used over a wide operating range with good ripple reduction performances.

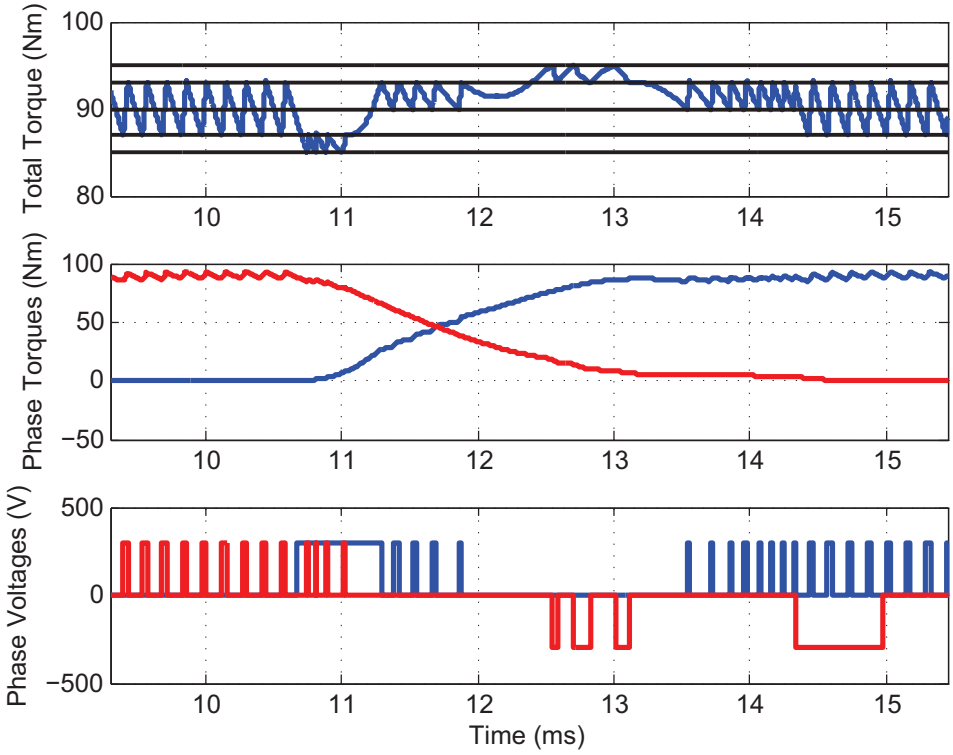

FIGURE 4.13: Principle exemplification of DITC switching strategy

TABLE 4.1: Motoring commutation strategy table of three adjacent phases for DITC

Ph $n-1$ Enable	Ph n Enable	Ph $n+1$ Enable	Ph $n-1$ S_j	Ph n S_j	Ph $n+1$ S_j
0	0	0	x	x	x
1	0	0	1/0	x	x
1	1	0	1/0/-1	1/0	x
0	1	0	-1/x	1/0	x
0	1	1	x	1/0/-1	1/0
0	0	1	x	-1/x	1/0

DITC does not necessitate cumbersome and time-consuming pre-calculations and it can straightforwardly be applied to any of the SRMs, regardless of the number of phases, rotor and stator poles, while the profiling has to be done independently for every machine

The algorithm of DITC can be extended to a multiphase torque-sharing theory for SRMs having the number of phases greater than four [71].

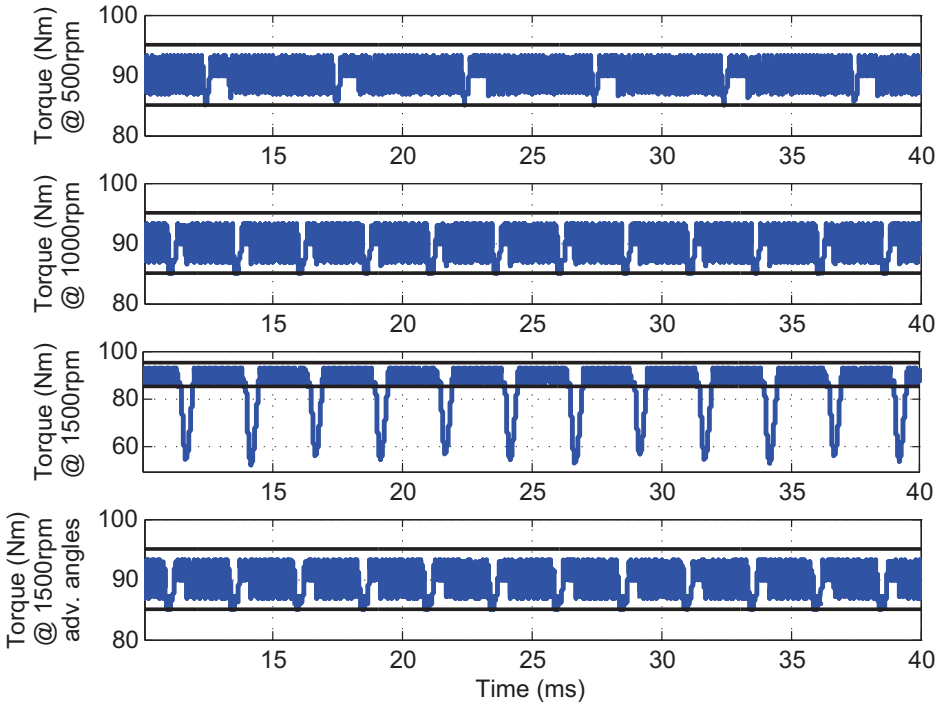

FIGURE 4.14: Simulated torque waveforms at different speed values obtained by using DITC

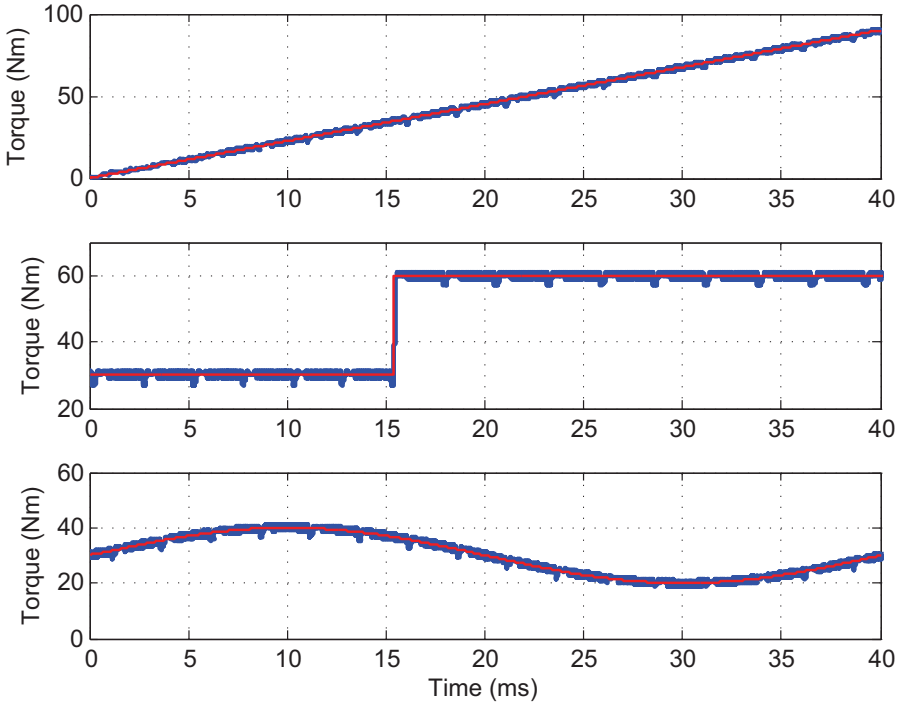

FIGURE 4.15: The simulated reaction of DITC controller at changes in the reference torque at 1000rpm

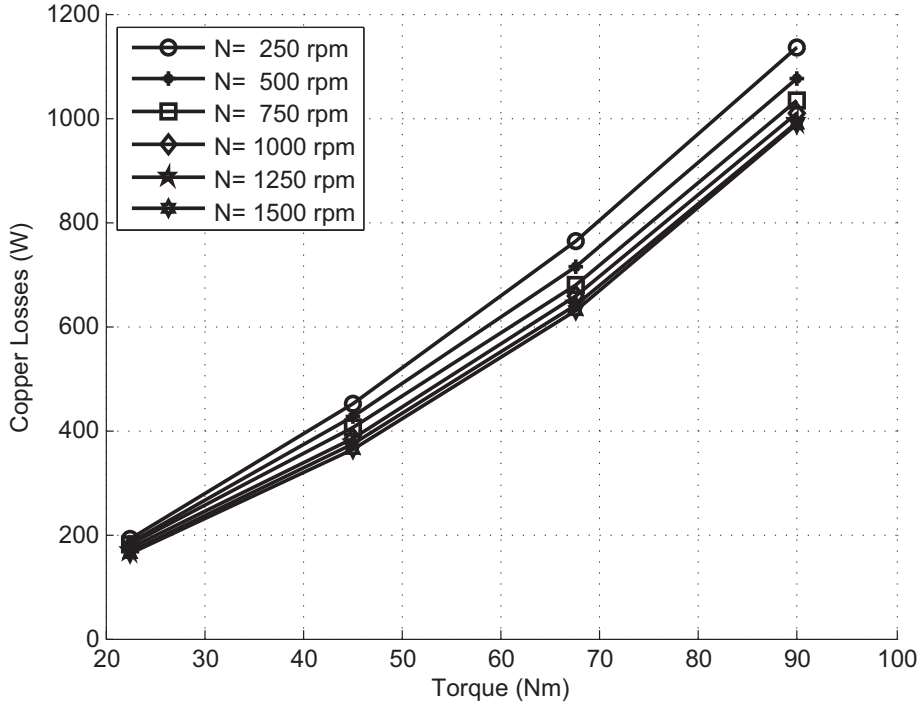

FIGURE 4.16: The variation of copper losses with the electromagnetic torque at constant speed

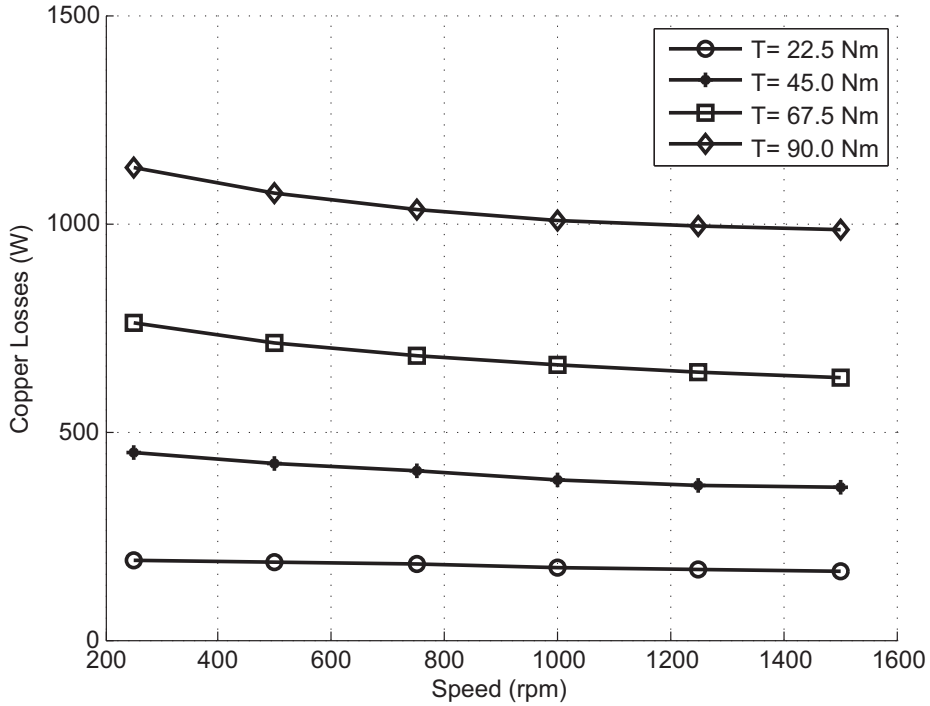

FIGURE 4.17: The variation of copper losses with the speed at constant electromagnetic torque

4.3.2 Simulation Results of DITC

The MATLAB/Simulink model of DITC, developed in order to test the reliability of the above discussed principles, is based on a 4-phase, 8/6, 30kW peak-power SRM with a rated power of 15kW at a base speed of 1500rpm and a rated torque of 90Nm. The hysteresis controller used to generate the switching signals has the inner band set at ±3Nm and the outer band at ±5Nm.

The extensive simulations carried out prove the attainability of a smooth rated torque up to base speed, by advancement of the switching angles in accordance with the operation point. Fig. 4.14 shows the performance of the controller in maintaining the rated torque at different speed up to 1500rpm. A smooth waveform of torque is reached at the base speed after the necessary correction of the angles was made.

The reaction of the controller at changes in the reference is tested and the results are presented in Fig. 4.15. Throughout all simulations the speed is maintained constant at 1000rpm.

Firstly, the reference torque is increased with a constant slope from 0Nm up to the rated torque in 40 ms . The controller proves its capability in maintaining the instantaneous torque value within the hysteresis bands.

Secondly the reference is step varied from 30Nm to 60Nm. The time for the controller to reach the new value is less than 0.2ms and no overshoots are spotted.

Thirdly, the reference of the torque is sinusoidally varying with an amplitude of 10Nm and a continuous component of 30Nm. The controller reacts with the same performances and robustness as in the precedent cases and the instantaneous torque remains within the imposed tolerances.

After proving its capability in maintaining a smooth torque against highly varying reference, the performance of the DITC is further tested regarding its efficiency. The DITC technique is recommended for operation points below the base speed, where the copper losses play the most important role in the equation of the overall efficiency. The copper losses, P_{Cu} are calculated with:

$$P_{\mathrm{Cu}} = \sum_{k=1}^{N\mathrm{ph}} I_{\mathrm{ph},k}^2 \, R_{\mathrm{ph}}. \tag{4.3}$$

where I_{ph} is the RMS value of the phase current, R_{ph} is the phase resistance and N_{ph} is the number of phases.

The increase of the copper losses with the torque at constant speed can be observed in Fig. 4.16. While operating in the constant torque region of the speed-torque characteristic, below the base speed, every value of torque up to the rated value can be attained. For a constant torque reference, the copper losses mildly decrease with speed, Fig. 4.17, due to the changes in the ascending and descending slopes of the phase current.

4.3.3 Experimental Results of DITC

The estimated total torque together with the phase currents for two sets of different firing angles can be observed in Fig. 4.18 and Fig. 4.19. The operating point of the machine in both cases is 500rpm and 15Nm. In the first case the turn-on angle is 37° and the turn-off angle is 58°, while

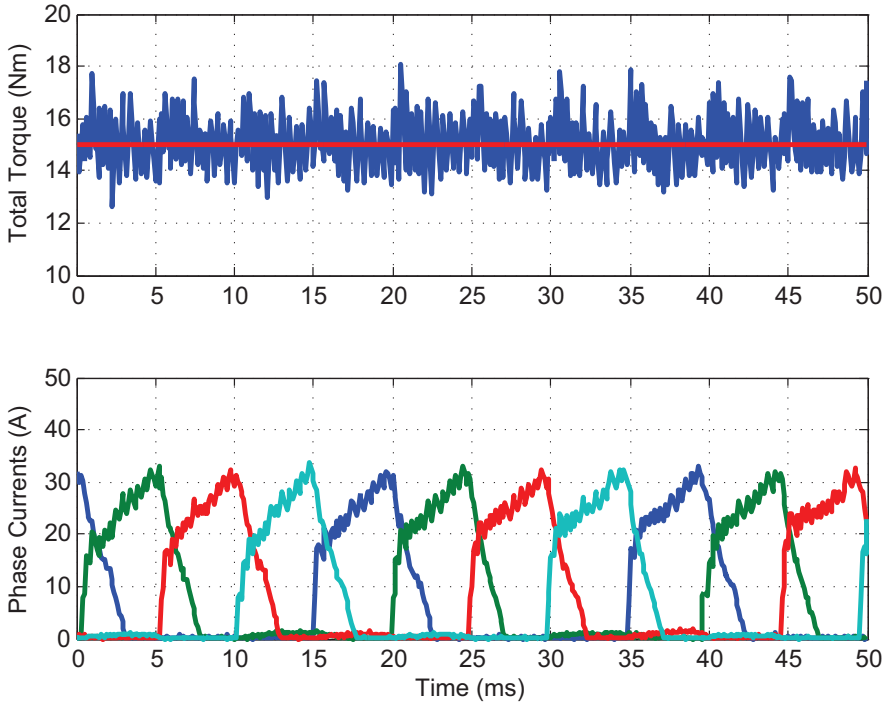

FIGURE 4.18: Measured torque and phase currents at 500rpm, 15Nm, turn-on angle 37° and turn-off angle 58°

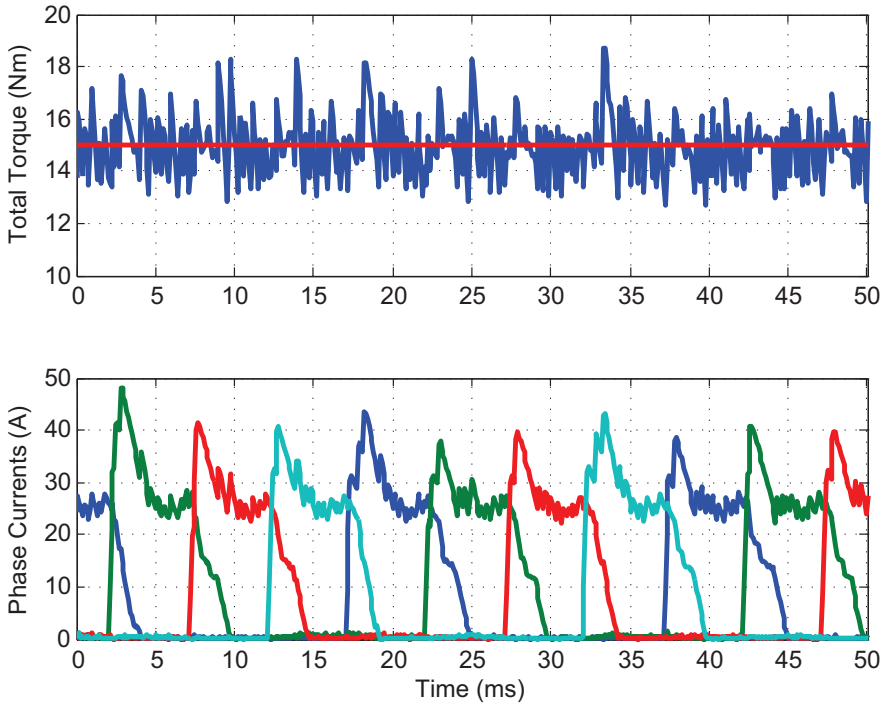

FIGURE 4.19: Measured torque and phase currents at 500rpm, 15Nm, turn-on angle 33° and turn-off angle 54°

in the second case the angles are 33° and respectively 54°. The values of the hysteresis bands are set and preserved during all performed experiments at ±1Nm and respectively ±2Nm.

The total instantaneous torque is successfully maintained within the hysteresis bands at the expense of increased copper losses in the case of improperly set switching angles. Crossings of the exterior band can be observed due to the limited switching frequency admitted by the prototyping tool. The DITC controller is not affected by inaccurate rotor position detection or by inaccurate switching instances. Still, the accuracy of rotor position detection is of an extreme importance for the instantaneous torque estimation in the actual case.

The capability of the controller in following rapid variation of the references, while an external speed loop maintains constant the speed of the drive at 500rpm, is demonstrated in Fig. 4.20. In the first case a ramp reference increasing and decreasing linearly from 10Nm to 20Nm and back to 10Nm in 0.7 seconds is imposed. The controller is able to maintain, with a small deviation, the instantaneous value of the torque within the hysteresis band.

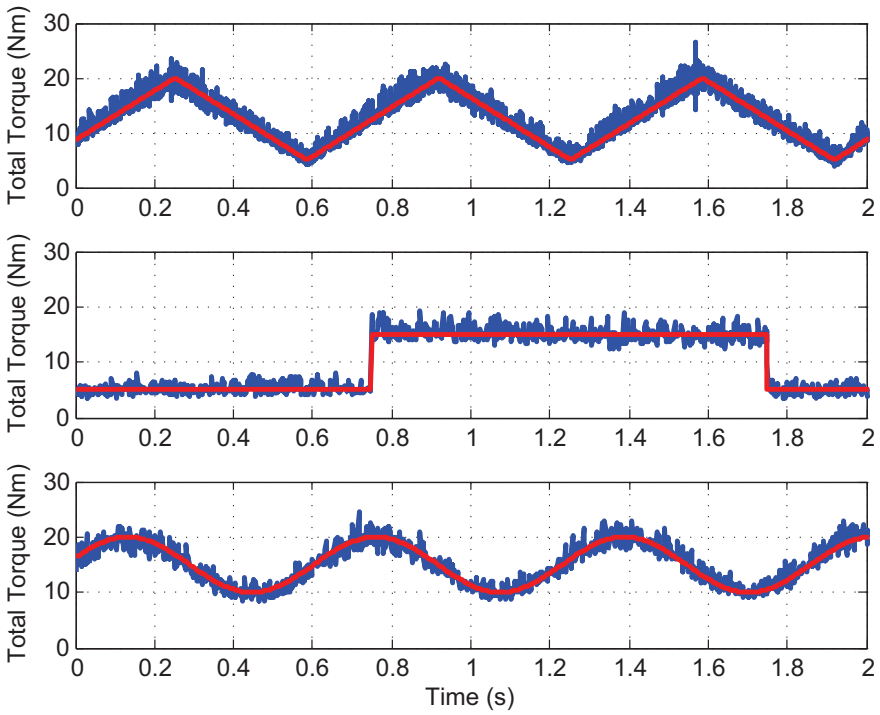

FIGURE 4.20: The measured reaction of DITC controller at changes in the reference torque at 500rpm

In the second case the reference is step changed from 5Nm to 15Nm and back. The produced torque is able to reach the new value in 2ms and without unnecessary and unwanted overshoots.

In the third case a sinusoidal reference with an amplitude of 5Nm, a continuous component of 15Nm and a frequency of 1.5Hz is followed with the same stringency.

The reliability of the method was tested through means of simulation and experimental measurements on the test bench. The DITC proved its performances regarding torque ripple minimization and wide operation range, being able to maintain a smooth rated torque at the base speed.

The immunity against inaccurate rotor position detection and against inaccurate switching instances confers an increased robustness to this technique.

The controller was capable of fast reaction to large and rapid changes in the reference and it is able to reduce the torque anomalies inflicted by non-electrical considerations.

The easy and rapid implementation on any type of SRM, without complex and time-consuming pre-calculations, provides a substantial advantage of DITC over profiling techniques.

4.4 Direct Torque Control

Direct Torque Control for AC drives was developed in the early '80s and it was quickly accepted by industry, industrial drives with DTC being available on the today's market [72]. DTC abandons the current control and controls the torque by directly modifying the stator vector voltage in accordance with the errors of flux and torque. DTC is characterized by fast dynamics, simplicity, and robustness [72, 73, 74, 75, 76, 77, 78, 79, 80, 81].

The first papers on DTC for SRMs appeared in the late '90s and in the early 2000s, being focused on the 3-phase machines [82, 83, 84, 85]. The 5-phase DTC for SRMs is explained in [86], where the phase transposition phenomenon is clarified. Due to the problems regarding the even number of phases, only very few papers on DTC for 4-phase SRMs are found in literature. In [87] a machine with shortened flux paths is presented and the consideration that the electrical angle and the mechanical angle between the phases are both equal to 45 is made. The consideration that the electrical angle between the phases is 90 is made in [88], but only few simulation results are presented at fixed values of speed, flux and torque.

Section 4.4 presents the implementation of DTC technique for SRMs. A discussion on the functioning principles of DTC, its advantages and disadvantages is made. The task of choosing the switching vectors for machines with both odd and even phase number is clarified in subsection 4.4.2. Simulation and experimental results are shown and analysed.

4.4.1 Operating Principles of DTC

In order to be able to apply the principles of DTC on a SRM, the functioning equations have to be studied. The stator flux vector is equal to the time integral of the stator voltage vector minus the voltage drop on the stator resistance:

$$\vec{\lambda}_{\mathrm{s}} = \int_0^t (\vec{v}_{\mathrm{s}} - R_{\mathrm{s}}\vec{i}_{\mathrm{s}})\mathrm{d}t + \vec{\lambda}_0. \tag{4.4}$$

The resistance being usually small, the resistive voltage drop can be neglected at high voltage, thus:

$$\vec{v}_{\mathrm{s}} = \frac{d\vec{\lambda}_{\mathrm{s}}}{\mathrm{d}t}. \tag{4.5}$$

Considering a sufficiently small time interval, (4.5) becomes:

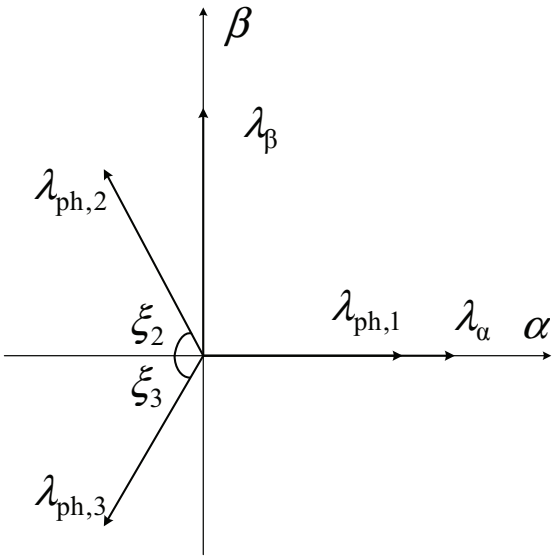

FIGURE 4.21: Definition of two frame reference axes for phase fluxes of the 3-phase SRM

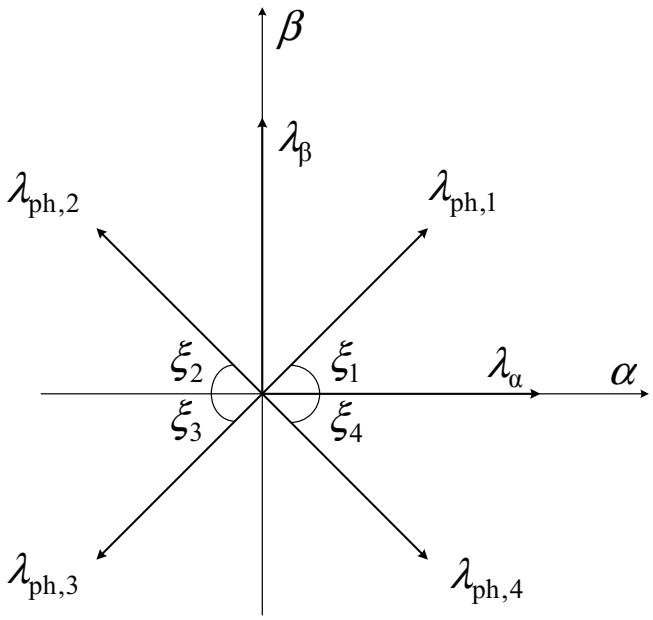

FIGURE 4.22: Definition of two frame reference axes for phase fluxes of the 4-phase SRM

$$\Delta\vec{\lambda}_{\mathrm{s}} = \vec{v}_{\mathrm{s}}\ \Delta t, \tag{4.6}$$

which shows that the space voltage vector applied to one phase produces a variation of the stator flux vector in the same direction as the voltage vector and a variation in magnitude proportional with the vector's magnitude and the time interval during which it is applied. The magnitude of the phase flux is time dependent, but its direction remains along the pole axis. The stator flux vector can be calculated by the transformation of the phase flux vectors onto a stationary orthogonal frame. Exemplifications for SRMs with 3 and 4 phases are made in Fig. 4.21 and Fig. 4.22, respectively.

The components of the stator flux vector on the two axes, α and β, of the orthogonal frame can be calculated as:

$$\lambda_\alpha = \sum_{k=1}^{N_{\mathrm{ph}}} \lambda_k \cos(\xi_k), \tag{4.7}$$

$$\lambda_\beta = \sum_{k=1}^{N_{\mathrm{ph}}} \lambda_k \sin(\xi_k), \tag{4.8}$$

where ξ_k is the angle made by the flux vector of phase k with the α axis of the orthogonal frame.

The stator flux is further defined by its amplitude and orientation:

$$\lambda_{\mathrm{s}} = \sqrt{\lambda_\alpha^2 + \lambda_\beta^2}, \tag{4.9}$$

$$\delta_\lambda = arctan\frac{\lambda_\alpha}{\lambda_\beta}. \tag{4.10}$$

According to [82] and [83] the torque can be approximated by:

$$T \approx i\frac{d\lambda_{\mathrm{s}}(\theta, i)}{\mathrm{d}\theta}. \tag{4.11}$$

Maintaining the magnitude of flux within a hysteresis band, the sign of the variation of the produced torque is the same as the sign of the stator flux variation with respect to rotor position. To produce a positive variation of torque, the flux vector has to be ahead of the rotor in the direction of the movement. While the flux vector is behind the rotor in the direction of movement, it produces a negative variation of the torque. These positive and negative variations of flux with respect to the rotor position are called in the literature flux acceleration and respectively flux deceleration. After this discussion, the two principles of the DTC technique can be expressed [82, 86]:

a) The magnitude of the stator flux vector is kept constant (within a hysteresis band);

b) The torque is controlled by accelerating or decelerating the stator flux vector.

Similar to AC drives, equivalent voltage space vectors can be defined for every phase, the electrical angle between them being equal to $2\pi/N_{\text{ph}}$ rad.

When the positive voltage is applied to the phase the voltage space vector can be defined, the same vector being defined but in the reverse direction when freewheeling occurs. In order to control the stator flux, the voltage space vectors are used to define switching vectors which are selected after a switching logic defined in the so-called switching table.

4.4.2 Definition of the Switching Vectors and the Switching Table

In this section, a discussion on how to define the switching vectors for SRMs with both odd and even number of phases, with exemplification of the 3-phase and on the 4-phase machine, is made.

The phase voltage vectors need to be drawn with the origin in the same point and an angle between them of $2\pi/N_{\text{ph}}$ rad. Usually the first phase is located on the x-axis of a Cartesian plane, but this is not imperative, as will be seen in the example of the 4-phase machine.

For the SRMs with odd number of phases the phase vectors can be prolonged in the negative side in order to form $2N_{\text{ph}}$ zones of equal angles (π/N_{ph} rad). In the centre of each zone will lay a switching vector which will be obtained by energizing the phase which delimits the zone with its positive direction and freewheeling the current from the phase which delimits the zone with its negative direction. The rest of the phases are controlled in such a manner that the zero loop occurs. The definition of the vectors can be seen in Fig. 4.23 and the switching logic is defined in the Table 4.2.

For the SRMs with even number of phases, after drawing the phase voltage vectors, N_{ph} circle sectors are formed. In the middle of each sector another vector will be drawn. These $2N_{\text{ph}}$ directions will be the directions of the switching vectors. So as to define one vector, an imaginary Cartesian coordinate system is considered with its y-axis in the same direction as the considered vector. The phase voltage vectors that have a positive component on the y-axis are energized and the ones that have a negative component are let to freewheel. The voltage vectors with components only on the x-axis are controlled in such a manner that the zero loops occurs. This operation has to be repeated for each space vector .The $2N_{\text{ph}}$ zones of equal angles (π/N_{ph} rad) are to be considered with the centres on the above defined vectors. The definition of the vectors can be seen in Fig. 4.24 and the switching logic is defined in the Table 4.3.

This procedure for defining the voltage vectors can be used for any SRM with odd or even number of phases greater than two.

In Fig. 4.23 and Fig. 4.24 the voltage space vectors for the DTC are defined for both the 3-phase and the 4-phase machine. Each vector is lying in the centre of a sector with π/Nph radians. Analysing the vectors and taking into account the two principles of the DTC, the so called switching tables can be built. Table 4.2 and Table 4.3 are illustrating the switching logic for the 3-phase and respectively the 4-phase machine.

Considering the flux vector laying in an arbitrary k-th zone, for the 3-phase SRM, the vectors $V_{\text{k}+1}$, $V_{\text{k}-1}$ are used to increase the flux, while the vectors $V_{\text{k}+2}$, $V_{\text{k}-2}$ to decrease the flux. The torque is increased using vectors $V_{\text{k}+1}$, $V_{\text{k}+2}$ and decreased using vectors $V_{\text{k}-1}$, $V_{\text{k}-2}$. For the 4-phase SRM the vectors $V_{\text{k}+1}$, $V_{\text{k}-1}$ are used to increase the flux, while the vectors $V_{\text{k}+3}$, $V_{\text{k}-3}$ to decrease the flux. $V_{\text{k}+1}$, $V_{\text{k}+3}$ are used to increase the torque and $V_{\text{k}-1}$, $V_{\text{k}-3}$ to decrease the torque.

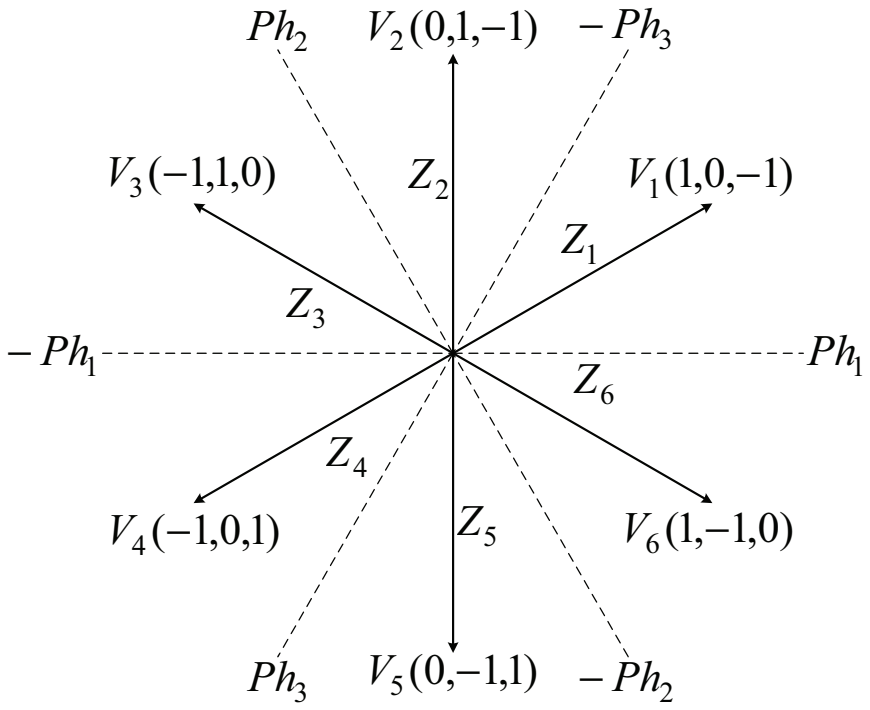

FIGURE 4.23: Definition of the space vectors for the 3-phase SRM

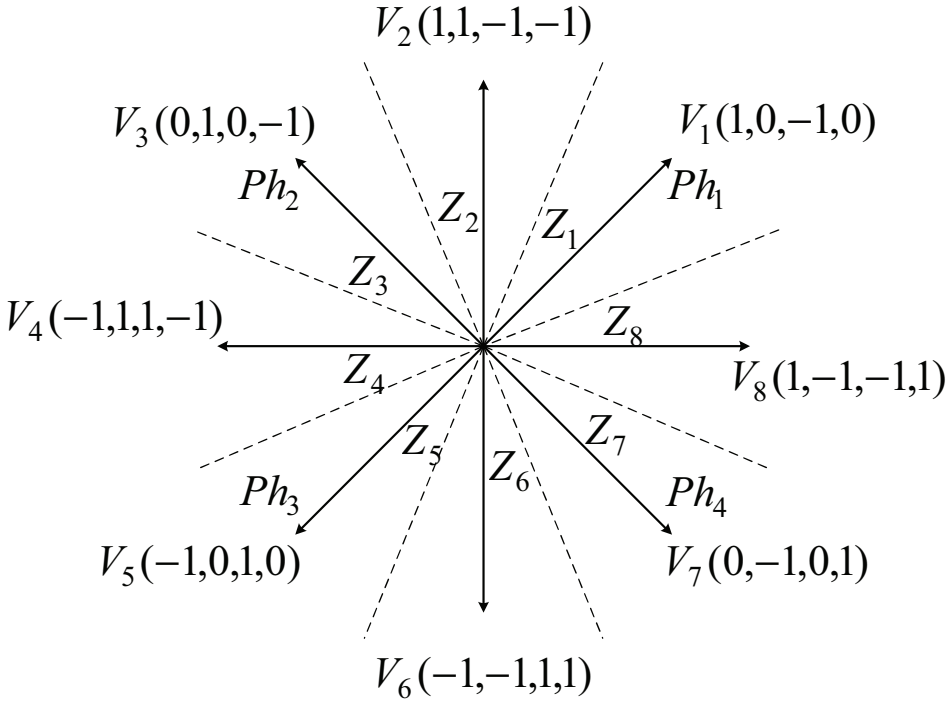

FIGURE 4.24: Definition of the space vectors for the 4-phase SRM

TABLE 4.2: DTC motoring switching table of 3-phase SRM

λ_s	↗	↗	↘	↘
T_{em}	↗	↘	↗	↘
V	V_{k+1}	V_{k-1}	V_{k+2}	V_{k-2}

TABLE 4.3: DTC motoring switching table of 4-phase SRM

λ_s	↗	↗	↘	↘
T_{em}	↗	↘	↗	↘
V	V_{k+1}	V_{k-1}	V_{k+3}	V_{k-3}

4.4.3 Simulation and Experimental Results of DTC

Extensive simulations are carried out on the MATLAB/Simulink model of the DTC developed on the afore discussed principles. Two hysteresis comparators are used to maintain the values of the stator flux and of the total torque within the imposed limits. For every zone k determined by the position sensor, the selection of the switching vectors is made based on the signals from the two hysteresis comparators. Both in the model and on the test bench, the hysteresis band for the torque is set at $\pm$1Nm, while the band for the stator flux is set at $\pm$0.01Wb and they are kept at these values throughout all simulations and measurements. The speed is maintained constant at 250rpm trough all carried out tests.

For the steady state tests, the reference torque is imposed at 30Nm and the stator flux amplitude at 0.3Wb. Fig. 4.25 and Fig. 4.26 show the capability of the controller to maintain the amplitudes of torque and flux within the imposed limits. The exceeding of torque and flux hysteresis bands in the simulated results with less than 1% is attributed to the step size of the simulation, while the exceeding in the measured waveforms can be put on the account of mutual inductances, non-ideal devices, noise, delays and measurement errors. Fig. 4.27 and Fig. 4.28 present the simulated and measured flux vector trajectory, respectively. Due to steady state operation, the phase currents, as well as the phase fluxes, become and periodic even though they are not directly controlled.

It is observed the high value of the current needed to diminish the torque ripple and to maintain a smooth torque. This high current leads to high copper losses, thus to heating, forcing the use of DTC on a limited operating range. The accentuated overlapping of the phase currents, practically the currents never reaching 0A value, leads to a low torque/ampere ratio. The method is suited for starting the machine and for low-speed operation up to a certain speed where the inertia interferes and smooths the torque and an average torque control technique can be employed with higher efficiency.

More simulations were conducted in order to test the capabilities of the DTC technique. The reference of the torque is step changed from 5Nm to 15Nm and back, while the flux is maintained constant at 0.3Wb. The torque response is very fast, reaching the given value in less than 0.2ms in simulation, Fig. 4.29, and 2ms, Fig. 4.30, on the test rig. The variation of the phase currents is also presented in the mentioned figures.

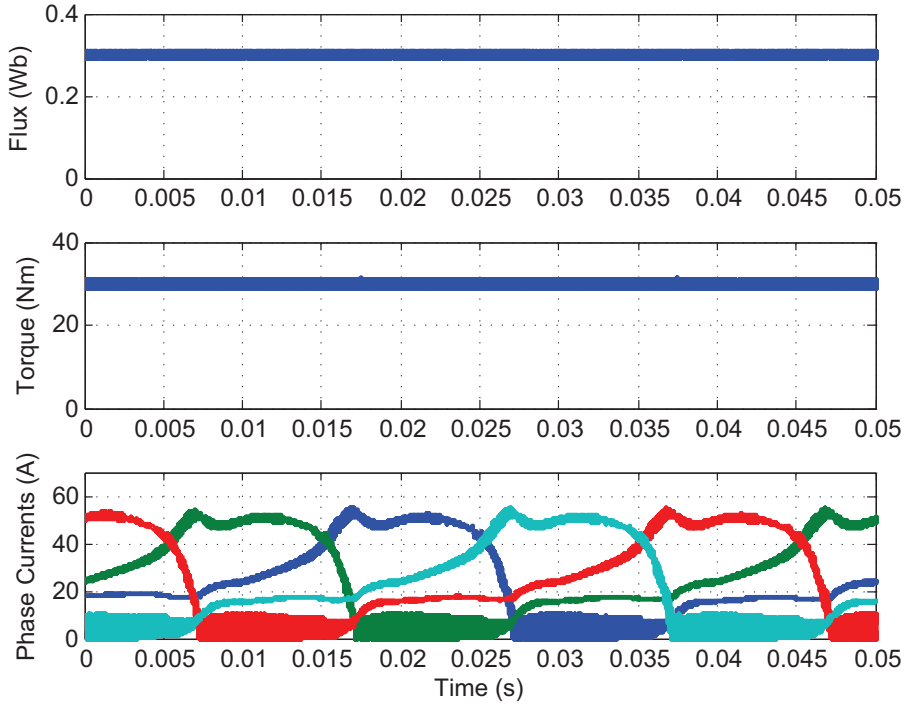

FIGURE 4.25: DTC simulated total torque, flux amplitude and phase currents

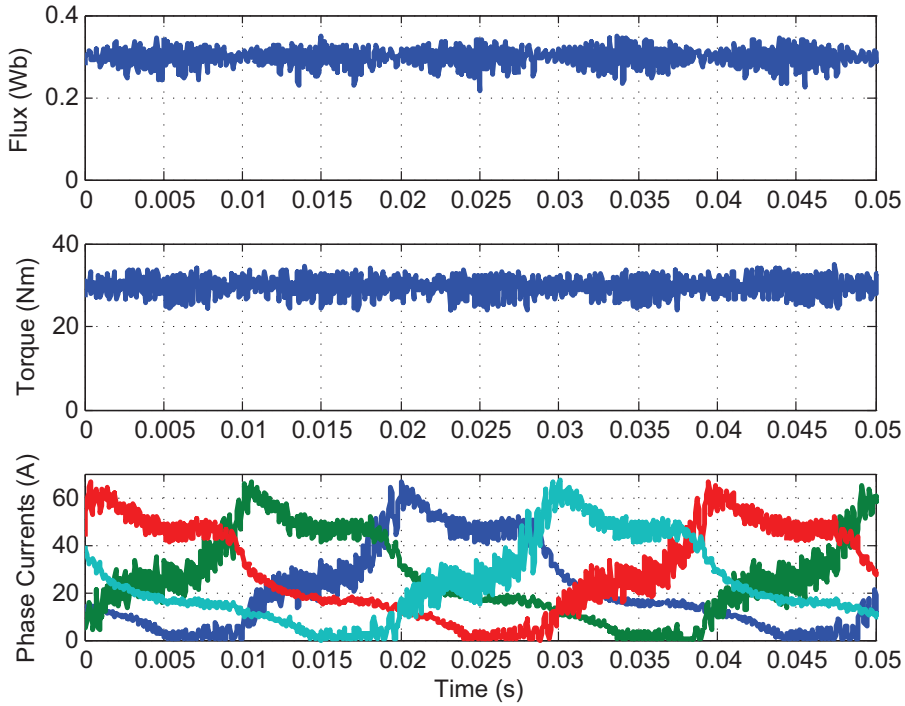

FIGURE 4.26: DTC measured total torque, flux amplitude and phase currents

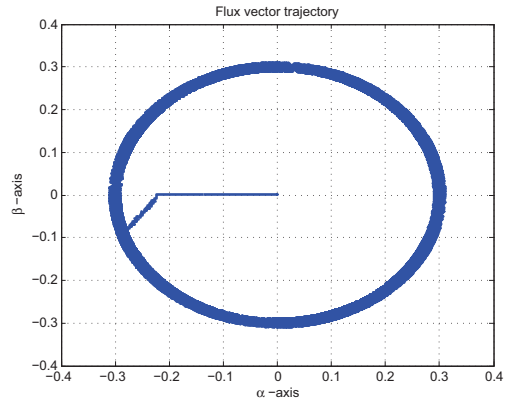

FIGURE 4.27: DTC simulated flux vector trajectory

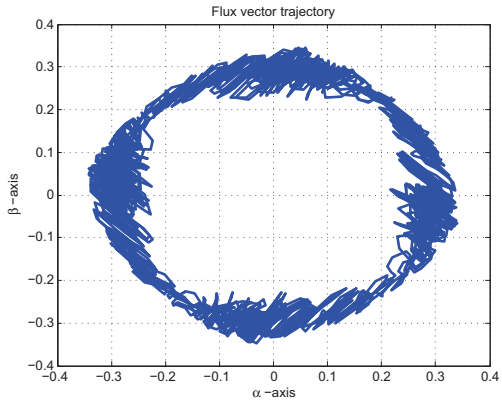

FIGURE 4.28: DTC measured flux vector trajectory

Further, the reference of the torque is linearly changed, from 5Nm to 15Nm in a time interval of 0.05s and then decreased in the same time interval back to 5Nm. The simulated and measured torque response and the current waveforms are presented in Fig. 4.31 and Fig. 4.32, respectively.

Fig. 4.33 and Fig. 4.34 present the response of the system for several step changes in the reference of flux from a value of 0.25Wb to a value of 0.35Wb and back. The reference value of torque is imposed constant at 10Nm. The stator flux follows its reference in less than 0.2ms in simulation and less than 2ms on the test rig.

A linear change of the reference of the stator flux is imposed. During a time interval of 0.05s the flux is increased from 0.25Wb to 0.35Wb and then again decreased to 0.25Wb in the same time interval. The response of the system can be seen in Fig. 4.37 and Fig. 4.38. The phase currents vary proportionally with the flux vector amplitude value. In [89] was shown that even for small values of the reference flux which are not in accordance with the reference torque, the phase currents are increasing, but in such a manner to decrease the flux vector amplitude. This leads to high copper losses and low torque/ampere ratio. Thus the imposed value of the flux has to be chosen in accordance with the value of the reference torque to minimise the losses.

The reliability of DTC and its performances were tested by means of simulation and experimental measurements on the test bench.

The influence of linear and step changes of both flux and torque references on the currents waveforms and on the performance of the control scheme has been studied and discussed. The flux needs to be kept close to the rated value, else unnecessary current losses occur.

The controller was capable of fast reaction to large and rapid changes in the reference and it is and can be straightforwardly applied to any type of SRM without needing time consuming pre-calculations.

4.5 Comparison of Different Instantaneous Torque Control Techniques

In [90] three torque-sharing functions for current-profiling, optimised for low losses while operating in smooth-torque conditions, are discussed and implemented on the same SRM. Starting

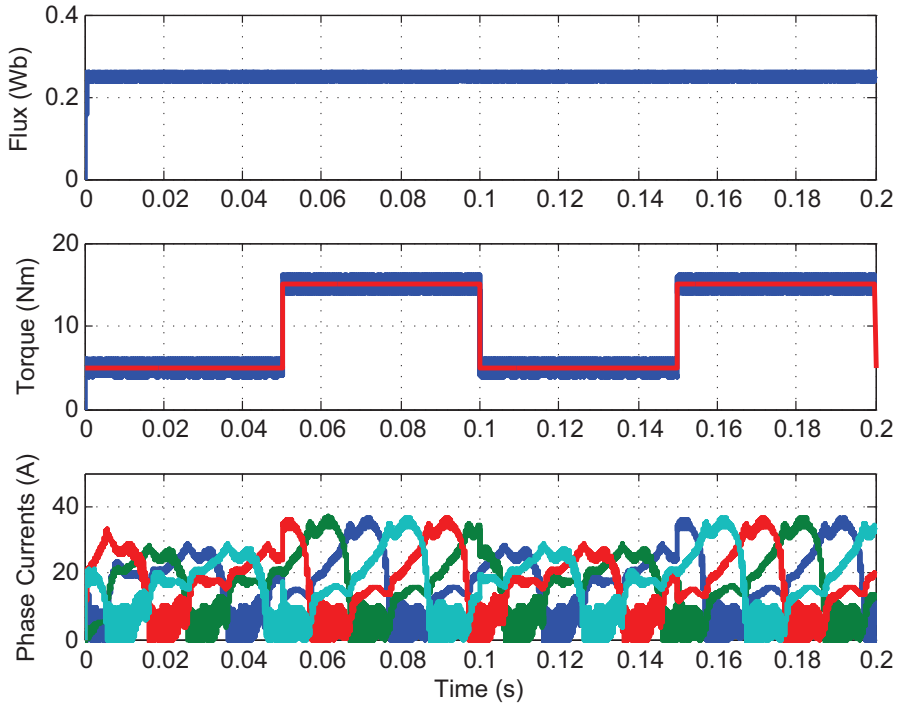

FIGURE 4.29: DTC simulated total torque, flux amplitude and phase currents at a step change of torque reference

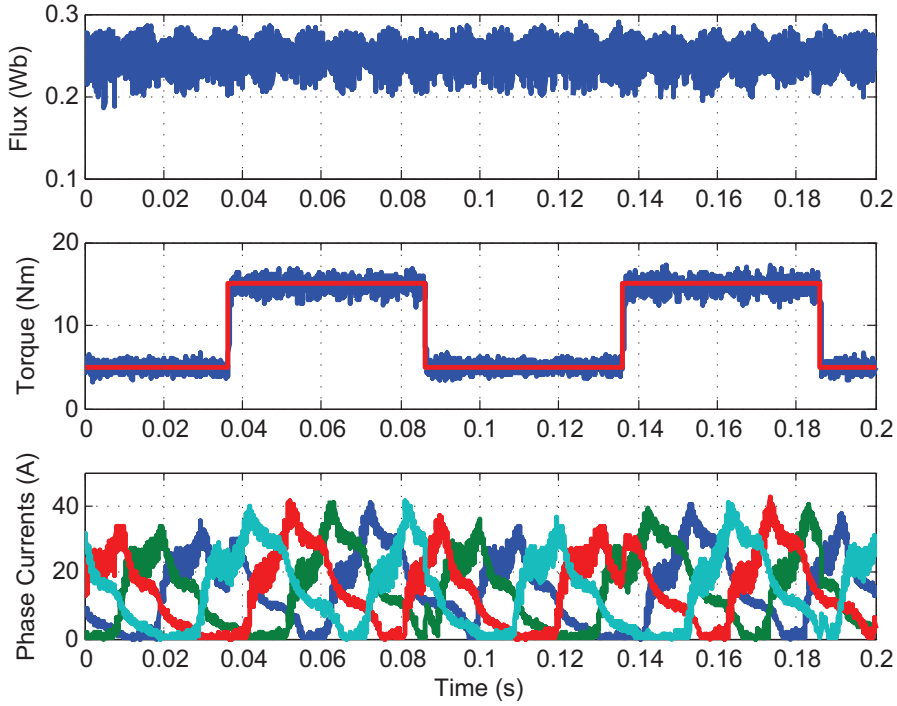

FIGURE 4.30: DTC measured total torque, flux amplitude and phase currents at a step change of torque reference

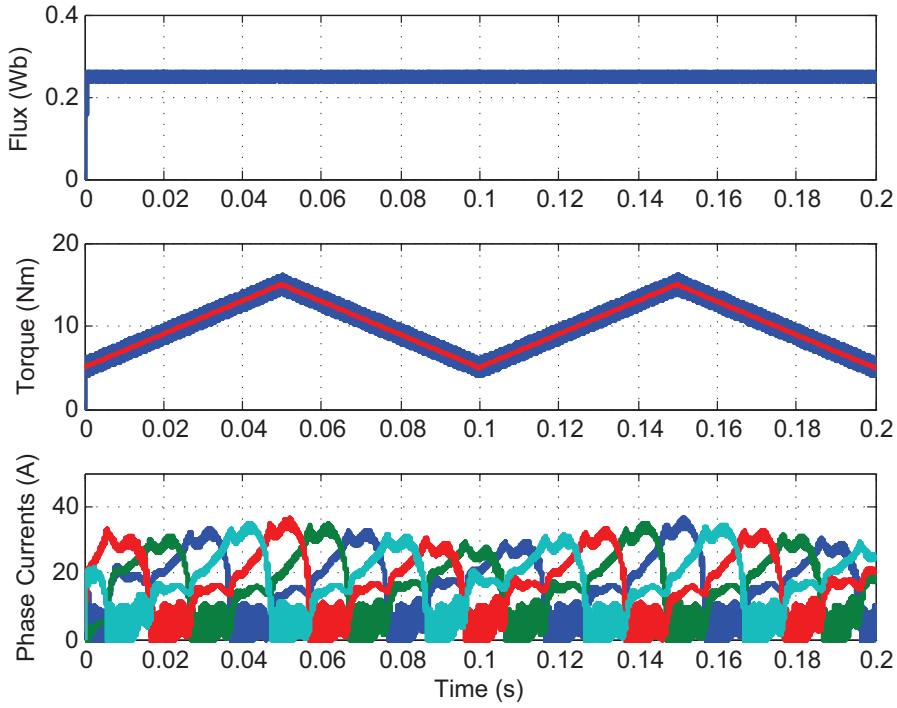

FIGURE 4.31: DTC simulated total torque, flux amplitude and phase currents at a ramp change of torque reference

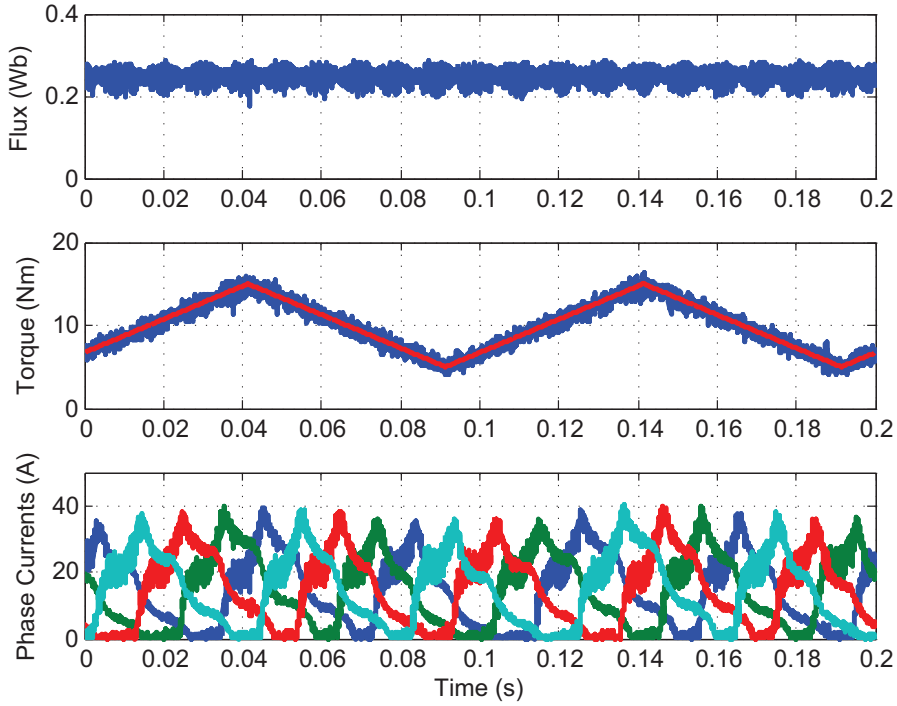

FIGURE 4.32: DTC measured total torque, flux amplitude and phase currents at a ramp change of torque reference

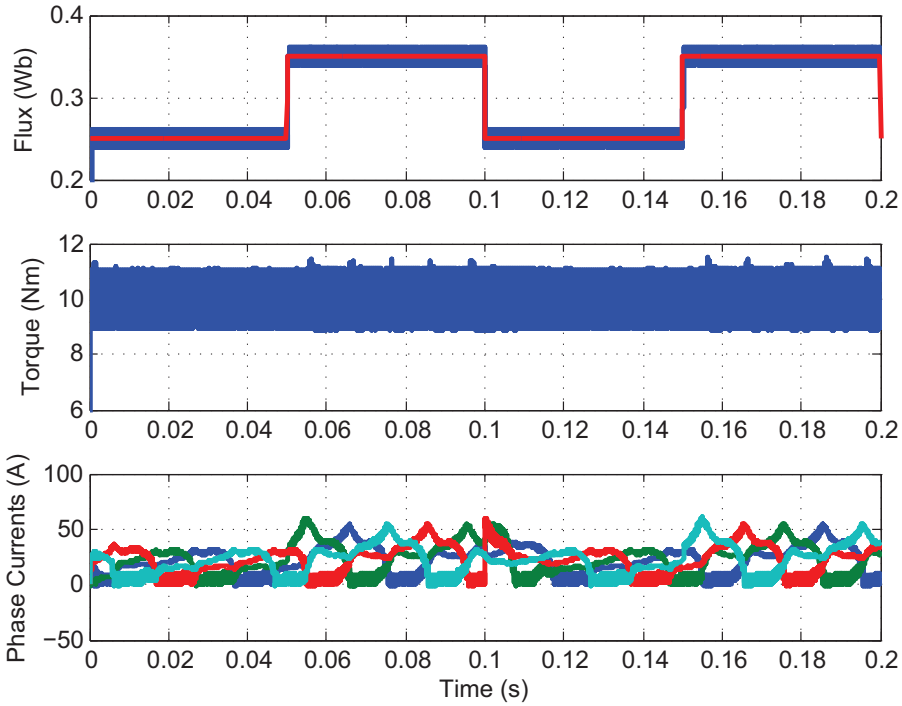

FIGURE 4.33: DTC simulated total torque, flux amplitude and phase currents at a step change of flux reference

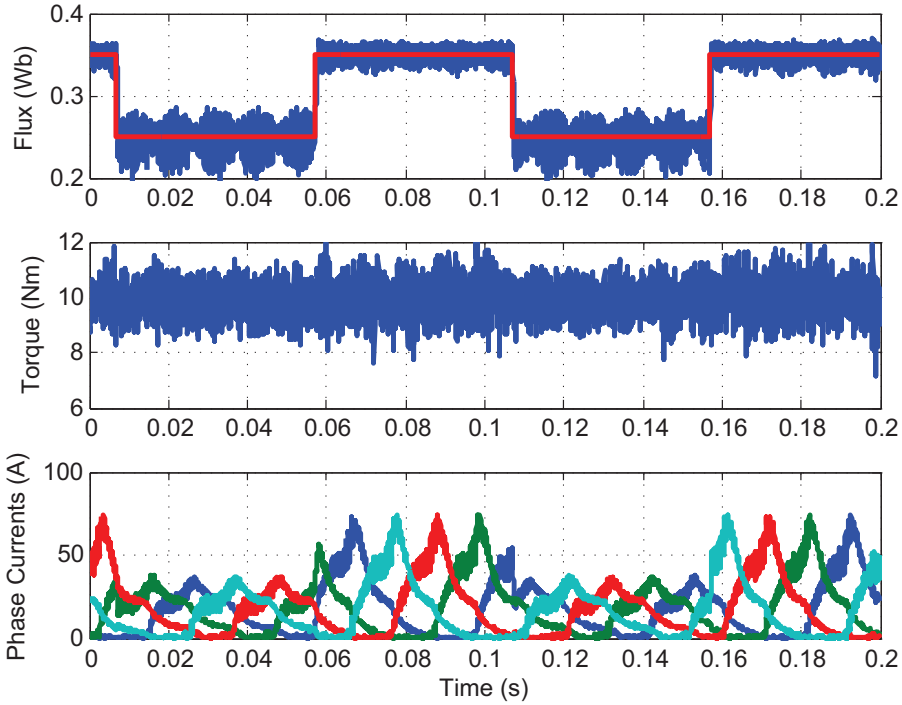

FIGURE 4.34: DTC measured total torque, flux amplitude and phase currents at a step change of flux reference

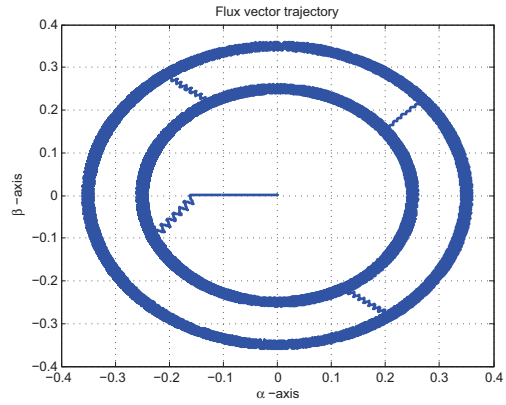

FIGURE 4.35: DTC simulated flux vector trajectory at a step change of flux reference

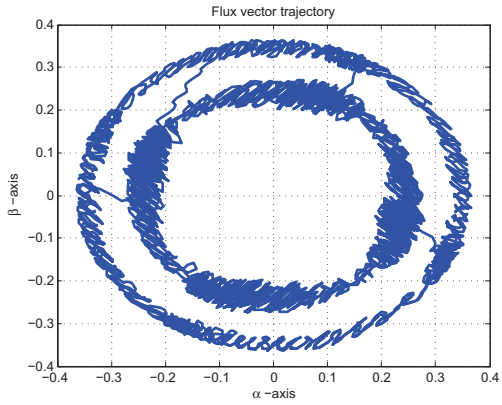

FIGURE 4.36: DTC measured flux vector trajectory at a step change of flux reference

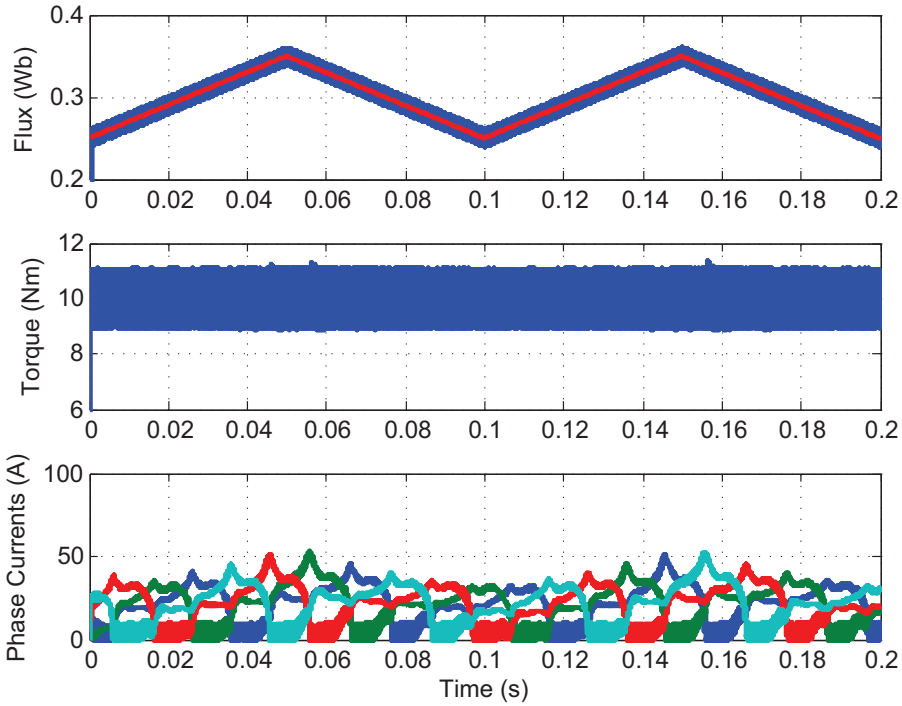

FIGURE 4.37: DTC simulated total torque, flux amplitude and phase currents at a ramp change of flux reference

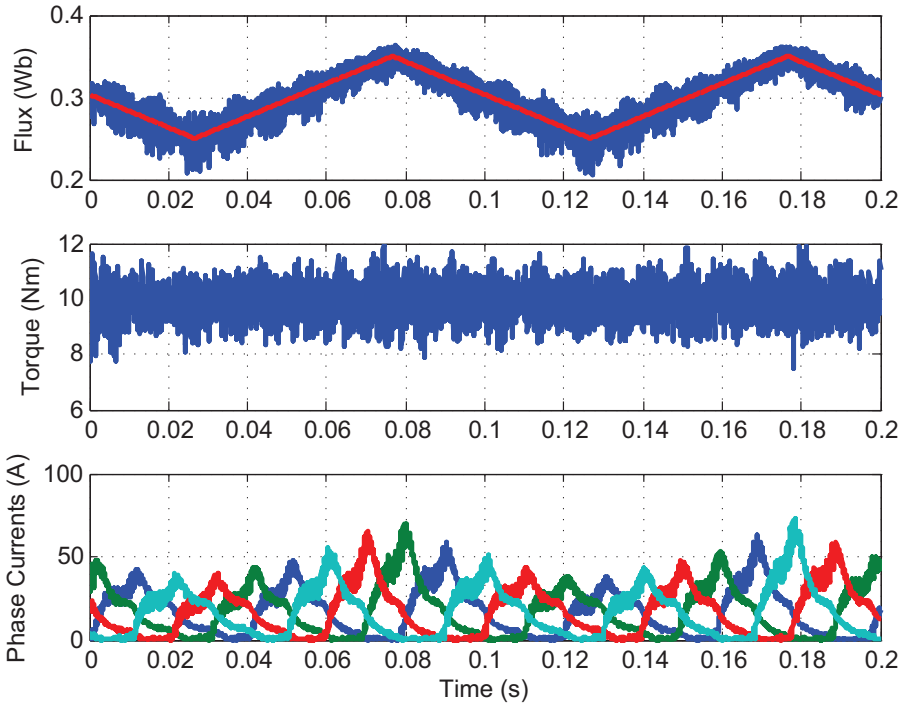

FIGURE 4.38: DTC measured total torque, flux amplitude and phase currents at a ramp change of flux reference

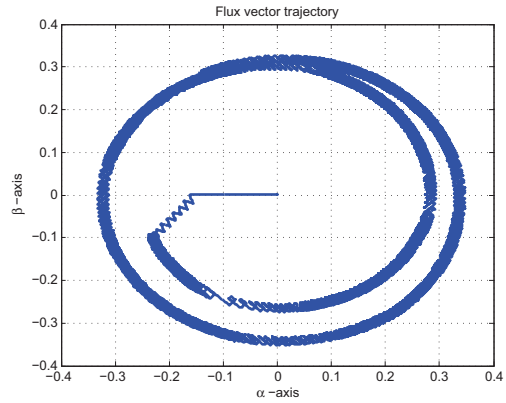

FIGURE 4.39: DTC simulated flux vector trajectory at a ramp change of flux reference

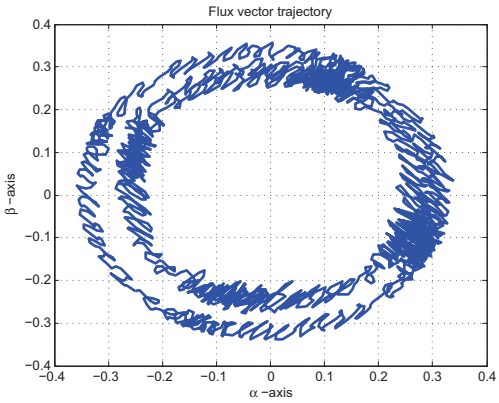

FIGURE 4.40: DTC measured flux vector trajectory at a ramp change of flux reference

from the basic rectangular variation, the ascending and the descending flanks of the function are modelled using a cosine, exponential and a generalisation of the cubic variation (further referred to as piecewise cubic torque-sharing function).

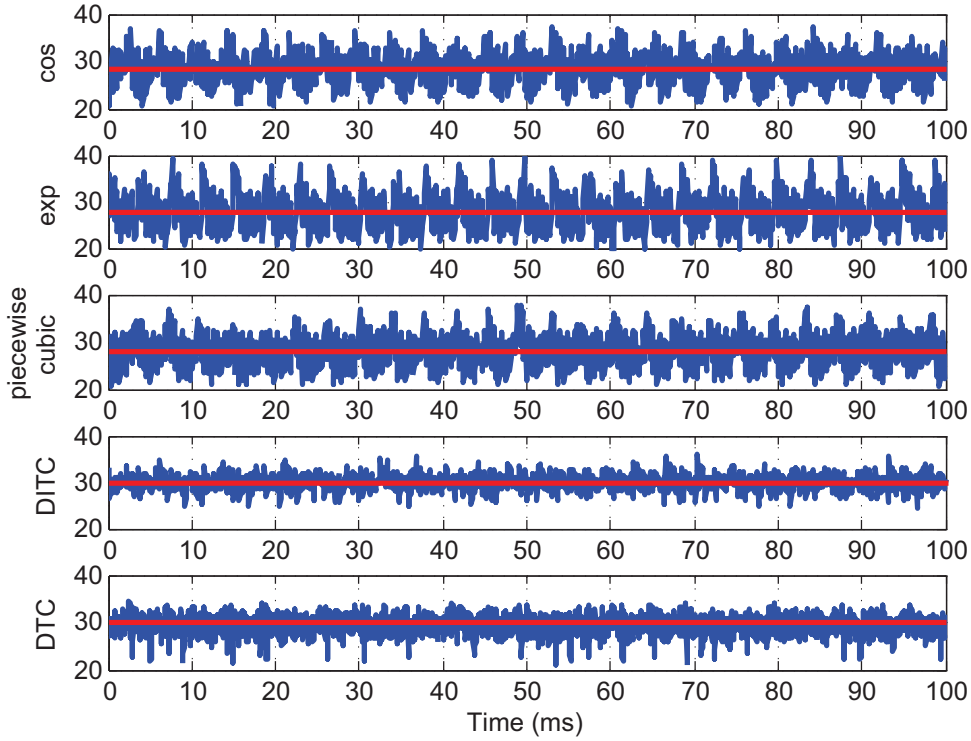

FIGURE 4.41: The measured waveforms of torque at 650rpm and a reference torque of 30Nm

Fig. 4.41 shows the instantaneous torque and the mean value of torque for the three torque-sharing functions and for DITC and DTC at 650rpm and a reference torque of 30Nm. For the open-loop current-profiling control, offsets between the reference and the mean value of the torque are noticed: 1.64Nm for the cosine function, 2.37Nm for the exponential function and 2.22Nm for the piecewise cubic function. The offsets appear due to DC-bus voltage variation, the phase resistance dependency on the temperature, manufacturing imperfections or other environmental influences.

Being closed-loop instantaneous-torque control techniques, DITC ad DTC do not allow any offset between the reference and the actual torque like the open-loop torque-control techniques do. Both closed-loop control methods are capable to compensate the less torque produced by the last phase in SRMs with long flux paths. If the torque is measured with a torque meter directly on the shaft, the two methods are able to damp oscillations or ripples of the torque of mechanical origin.

The currents measured on the phases of the machine in all five cases at 650rpm and 30Nm are presented in Fig. 4.42. The cosine and exponential functions, together with DTC need considerably more peak current to produce the same torque as the piecewise cubic function and DITC. The conduction period of one phase while using DTC is very long, the phase being close to continuous conduction. The copper loses at 250rpm and 650rpm and a reference torque of 30Nm are calculated on the basis of the measured currents and presented in Table 4.4. At

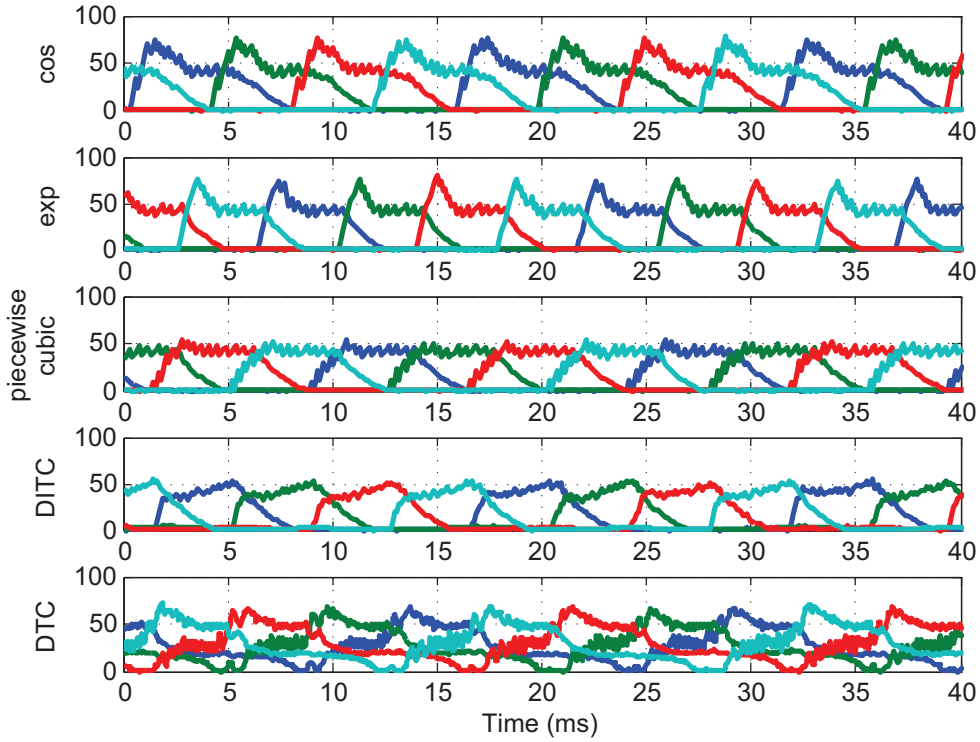

FIGURE 4.42: The measured waveforms of phase currents at 650rpm and a reference torque of 30Nm

very low speed (250rpm) the variation of the copper losses of the current profiling techniques and DITC regarding the copper losses is less than 5%, while DTC has losses higher with 72 to 82%. Increasing the speed higher variations of the efficiency can be noticed. At 650rpm the copper losses of piecewise cubic function are 200W, with 15% less than the exponential function and 50% less than cosine function. DTC still has losses over 80%, while DITC has 7.5% less copper losses than the piecewise cubic function. The losses of DITC can be further improved by calculating optimised switching angles.

TABLE 4.4: Comparison of copper losses computed based on measured currents of different instantaneous torque control techniques at 30Nm

Method	Copper losses (W)	
	@250rpm	@650rpm
cos	180.9	299.3
exp	187.7	228.4
piecewise cubic	183.8	200.4
DITC	190.4	185.4
DTC	329.2	365.1

4.6 Conclusions

The fourth chapter has been presented the implementation of two closed-loop control techniques, namely direct instantaneous torque control and direct torque control, whose results are compared to the results obtained by using current profiling technique employing three different torque sharing functions.

DITC is developed on the basis of the paper of de Doncker. The issue of on-line estimation of the instantaneous torque is first addressed in the chapter, by describing three different estimation methods. The first uses the rotor position and the phase currents to estimate the torque. The second uses flux calculated on the basis of the terminal quantities and the rotor position to estimates torque. In the third, the need of knowing of rotor position is eliminated from the estimation by using the characteristics of torque as a function of phase current and flux linkage. In a similar way, by using the table of rotor position as a function of phase current and flux, a sensorless operation can be achieved on a limited range. A method to estimate the phase voltage using the switching signals and an inexpensive voltage sensor is also presented.

DITC is using the phase torque sharing principle without using precalculated torque sharing functions. The switching of the phase voltages is based on the hysteresis control of the total torque of the machine and the commutation of phases does not necessitate a precise knowledge of rotor position.

DTC makes an analogy between the AC rotating field machines and SRMs. Voltage vectors are defined for all phases and are further used for the definition of the switching vectors. An interesting discussion on how to choose the switching vector for all SRMs, regardless of the number of phases, is made.

The chapter ends with a comparison regarding torque ripple and copper losses between DTC and DITC on one hand and current profiling using three different torque sharing functions on the other hand. In terms of torque ripple both DTC and DITC have shown good results and both methods have been capable of eliminating the offset between the reference and the measured value of torque. In terms of copper losses DITC has shown slightly better results than profiling techniques, but the lack of a travelling field in the machine has led to higher losses when DTC was employed.

The easy and rapid implementation on any type of SRM, without complex and time-consuming precalculations confers a substantial advantage of DITC and DTC over profiling techniques.

Chapter 5

Converters for SRMs

The performances and characteristics of the converter play an important role in the overall performance of the whole SRD. Extensive work has been carried out in the last decades in the field of SRM converters and several varieties of general or particular use architectures were developed. Likewise, topologies with reduced number of power switches [91, 92, 93], with faster excitation time [94, 95], with faster demagnetization time [96, 97, 98], with higher efficiency [99, 100] and higher power factor [101, 102] have emerged.

A classification of the power converters for SRDs considering the number of power switches per phase as a criterion [5, 7] is made in Fig. 5.1. Topologies with q, $q+1$, $1.5q$ and $2q$ switches can be distinguished, where q represents the number of phases. A two-stage converter is included in this classification. Besides the two-stage converter, the assumption that the input voltage of the converters is a DC voltage, coming from a battery or a rectifier, is made. Using this classification it is easy to calculate the cost of the semiconductor components, but important aspects related to the functioning of the converter are not taken into account.

Another classification, Fig. 5.2, is made taking into account the type of commutation: dissipative, magnetic, resonant and capacitive [6, 7]. Several converter topologies are presented in Appendix B.

In the dissipative converters, none of the stored magnetic energy returns to the DC-link capacitor, all of it being dissipated in one or more resistors. This type of converter has the advantage of simplicity, low number of semiconductor components resulting in low cost. The losses are high because none of the magnetic energy is recuperated, leading to heating. At the end of the conduction period, the current in the phase needs a longer time to cancel when the energy is dissipated in the resistor than in the case when the energy is sent back to the source, creating problems in high speed applications. For high power drives the size of the dissipative resistors is increased and the heating severe, making this type of converter usable only for low power. Having high losses on the converter the overall efficiency of the drive is significantly reduced.

The magnetic converter can be used only for SRMs with magnetically coupled bifilar windings or with auxiliary windings. Using a small number of semiconductor components, it has a reduced cost and it is capable of returning the magnetic stored energy to the source. Bifilar construction of the windings is not economical for large motors [5]. The power density of the machine is reduced due to the larger slot required by the bifilar construction.

The resonant converter has one or more inductances which together with extra power switches and diodes, are used to create a buck, a boost or a resonant voltage source with a secondary

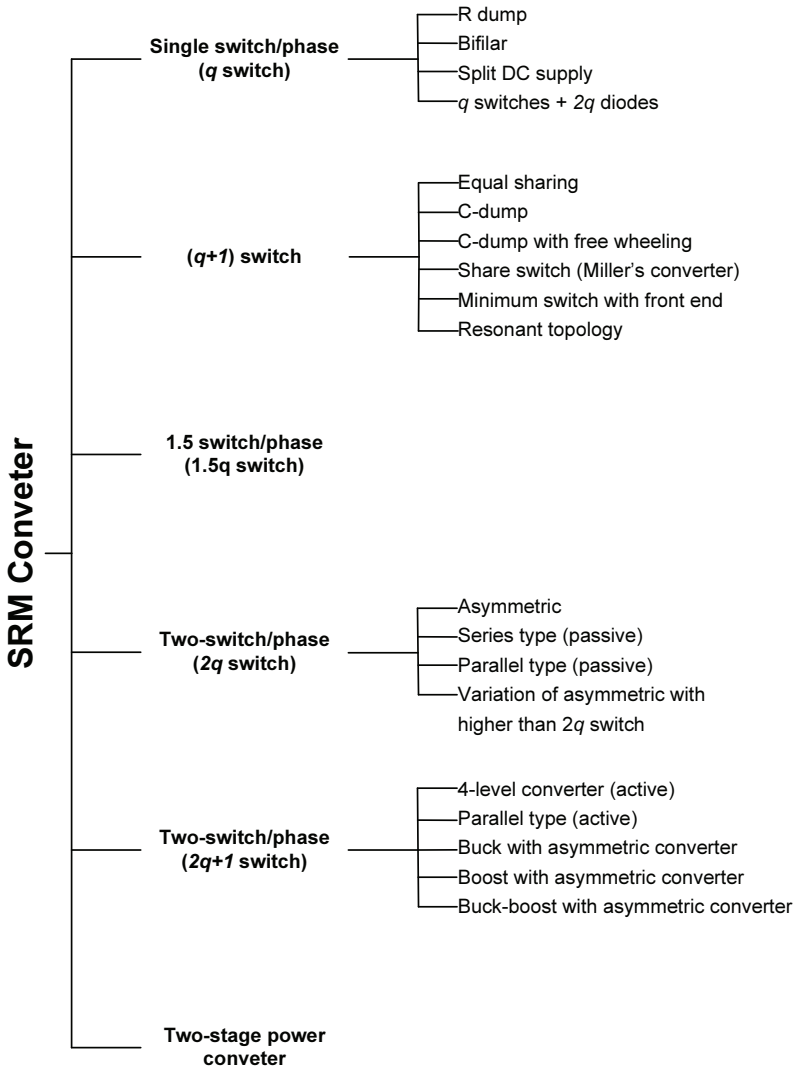

FIGURE 5.1: SRM converter classification by the number of switched per phase [5]

role of snubber circuit. The resonant converter is capable of providing for low voltage for easy boost and the snubber circuit allows an easy control of the dump voltage, but the addition of inductances and power devices increases the size, the cost and the losses of the converter [7].

In the capacitive converters, the magnetic stored energy is fed back directly to the DC-bus capacitor to the so called boost capacitor or to both. If the voltage on the capacitor storing the magnetic energy is controllable then the converter is called active, otherwise passive. Regarding the number of capacitors used, two main categories can be distinguished, also being an indicator of the topology's complexity: single- and multi-capacitor. No extra components are present in the power circuit and, therefore there are neither extra losses nor increased cost.

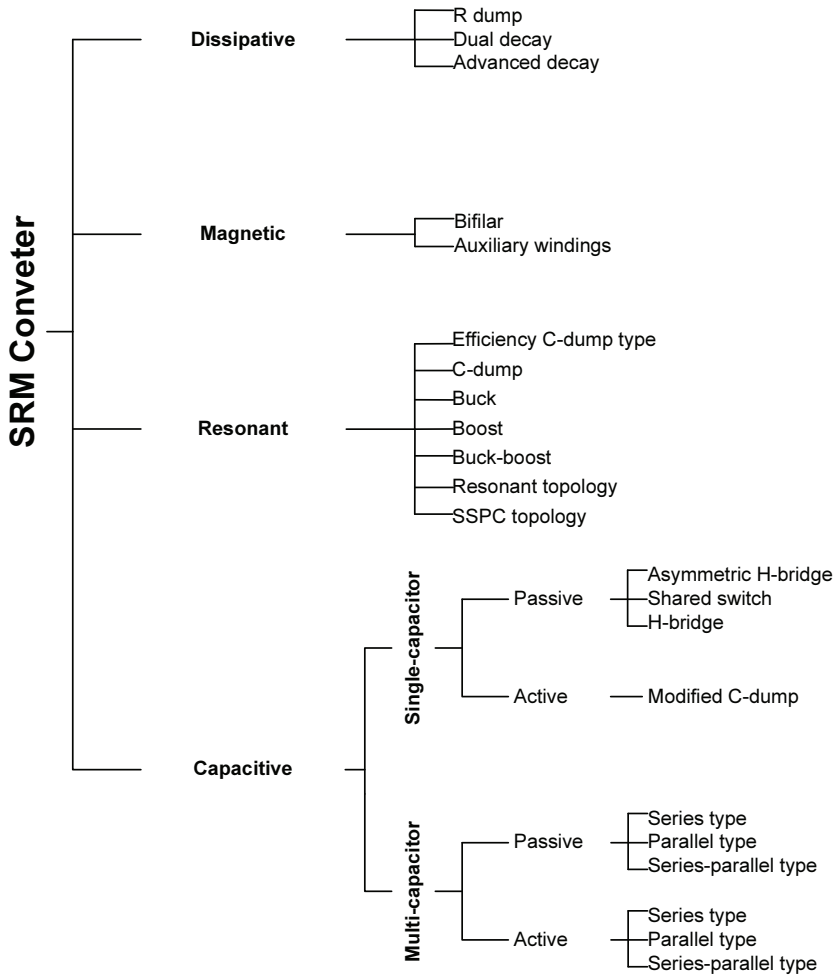

FIGURE 5.2: SRM converter classification by commutation type [6]

5.1 Requirements and Topology Selection

The used 8/6 SRM has a rated power of 15kW and delivers a rated torque of 90Nm at a base speed of 1500rpm. Over a short period of time the machine is able to produce double the rated torque and a peak-power of 30kW. The DC-bus voltage delivered by the battery-pack is nominally 307V and the maximum current supported by the machine is 200A. The maximum speed of the machine is 10000rpm.

Taking into account the operational characteristics of an SRM for vehicle traction, the basic requirements for the converter can be enumerated as follows:

1. It has to control each phase independently and to confer the possibility of overlapping;

2. It needs to be able to magnetize rapidly after the turn-on angle and to demagnetize the phase in a very short time interval after the turn-off angle, to avoid negative torque production while motoring;

3. It needs to have high efficiency, which implies the possibility of recovering the demagnetization energy;

4. It needs to be able to control the current while generating to avoid torque ripple or a too high voltage leading to damage of its components;

5. It needs to have high reliability, robustness and fault tolerance.

The chosen converter topology for the SRD used in vehicle propulsion is the asymmetric H-bridge, due to its capability of meeting all the aforementioned requirements. The asymmetric H-bridge Fig. 5.3 uses two power switches and two diodes per phase. There are no additional components increasing the losses. The asymmetric half-bridge has three modes of operation (see Section4.2). When both switches are closed, the whole DC voltage is applied to the phase minus the voltage drop on the switches, the phase current increases rapidly, energy being supplied from the source to the phase. When one switch is opened, a zero-loop voltage is formed and the current flows in the winding through the closed switch and the corresponding diode. In fact the voltage is not zero, but equal to the voltage drop on the semiconductor components. No energy is transferred from or to the supply. When both switches are opened, negative voltage, equal in amplitude to DC-bus voltage minus the voltage drop on the diodes, is applied to the phase and energy is transferred from the winding to the supply through the free-wheeling diodes.

One disadvantage of this topology would be the high number of power switches per phase compared to other topologies. Compared to AC machines, the same number of power switches per phase is employed, two. Having always two semiconductor components in series with the winding increases the conduction loses. This topology allows the isolation of a phase fault and the drive is capable in running under faulty conditions. This increases the reliability and the robustness of the drive.

The topology of the asymmetric H-bridge permits both soft and hard-chopping, each of them preferred by certain control technique, but this will be further on detailed.

Regarding the functioning of the SRM and the performances demanded from the converter in an SRD, the only suitable power switches are the MOSFETs (Metal oxide semiconductor field effect transistors), the IGBTs (insulated gate bipolar transistors) and MCTs (MOS controlled transistors). The MOSFETs have a large forward voltage drop and consequently high conduction losses. The MCTs have the lowest forward voltage drop and the low power dissipation would make them a good choice for power applications. Having performances comparable to the ones of the MCTs at a much lower price, together with their proven robustness, reliability and their availability make the IGBTs to be the choice for the converter of an SRD [103, 104, 105].

As mentioned before, the input of the converter has to be a DC voltage. In an electric vehicle the DC voltage is provided by a battery pack. On the test bench the AC voltage is rectified with a diode bridge rectifier and filtered by a large capacitor, due to lower cost and simplicity. There is no time lost charging the batteries, thus the bench becomes usable 24/7. The diode bridge rectifier can be 1-phase or 3-phase depending on the rated power of the converter. Taking into account the peak power of the machine, which is 30kW, a 3-phase rectifier was preferred. The large voltage ripple on the rectifier output demands a large capacitor on the DC side working

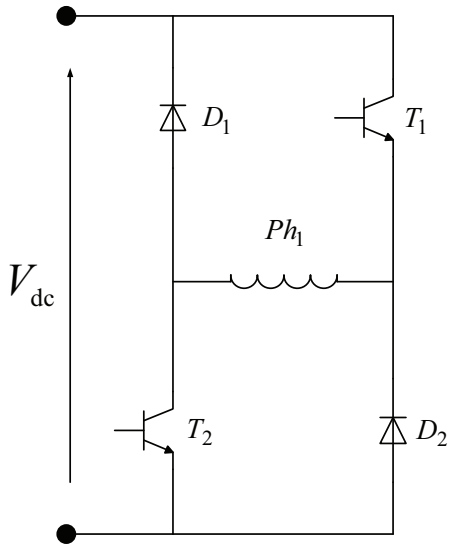

FIGURE 5.3: The asymmetric H bridge

as a filter. During heavy load conditions, a voltage ripple having six times the line frequency can be observed.

The ratings of the rectifier and the DC-link capacitor are calculated on the basis of the machine's peak-power P_{pk} [99]. The rectifier peak current $I_{\mathrm{rec,pk}}$ is :

$$I_{\mathrm{rec,pk}} = 2I_{\mathrm{dc}} = 2\frac{P_{\mathrm{pk}}}{V_{\mathrm{dc}}}, \tag{5.1}$$

where V_{dc} is the DC-bus voltage and I_{dc} the DC-bus current. The RMS value of the DC-bus capacitor current I_{C} is:

$$I_{\mathrm{C}} = \sqrt{I_{\mathrm{L}}^2 + N_{\mathrm{ph}} I_{\mathrm{ph}}^2 - 2I_{\mathrm{dc}}^2}, \tag{5.2}$$

with I_{L} the RMS value of the current through the equivalent DC-bus inductance, I_{ph} the RMS value of the phase current and N_{ph} the number of phases. The minimum value of the capacitor C_{min} is:

$$C_{\mathrm{min}} = \frac{W_{\mathrm{r}}}{DV \cdot I_{\mathrm{dc}}^2}, \tag{5.3}$$

where W_{r} is the average energy returned to the inverter during each stroke and DV the relative increase of the capacitor voltage.

5.2 Device Ratings

Taking into account the functioning of the asymmetric H-bridge, the voltage and current ratings will be equal for both transistors and diodes.

The minimum voltage rating $V_{\mathrm{d,min}}$ of the power electronic devices has to be equal to the DC-bus voltage V_{dc}, in this case considered constant and equal to 307V:

$$V_{\mathrm{d,min}} = V_{\mathrm{dc}} \tag{5.4}$$

In a power converter the voltage increases during generator operation until the DC-bus voltage controller is able to react or voltage spikes can occur due to stray inductances. Therefore, a safety margin Δ_{safe} has to be added to the minimum value of the voltage rating to obtain the voltage rating V_{d} of the devices.

$$V_{\mathrm{d}} = V_{\mathrm{d,min}} + \Delta_{\mathrm{safe}} \tag{5.5}$$

Taking into account the functioning of the SRM, a safety margin of around 600V was considered and a voltage rating of 900V was obtained.

For the choice of the devices, both the peak value I_{pk} and the rms value I_{ph} of the current have to be taken into account. Considering a hysteresis band of Δi, the peak value of the current can be found by adding $\Delta i/2$ to the maximum value of the phase current $i_{\mathrm{ph,max}}$:

$$I_{\mathrm{pk}} = i_{\mathrm{ph,max}} + \frac{\Delta i}{2} \tag{5.6}$$

Having a maximum phase current of 200A and a hysteresis band Δi of 10A the resulting peak value of the current is 205A. Considering a sufficiently large safety margin, the peak current rating for the devices, $I_{\mathrm{d,pk}}$, is obtained:

$$I_{\mathrm{d,pk}} = (1.5 \div 2) I_{\mathrm{pk}} \tag{5.7}$$

The considered peak current rating for the devices is 400A.

The rms value of the current [5] depends on the instantaneous phase current i_{ph}, the dwell angle θ_{dwell}, the rotor pole pitch angle θ_{rp} and the angle needed for the current to rise from zero to its reference value θ_{r}:

$$I_{\mathrm{ph}} = i_{\mathrm{ph}} \sqrt{\frac{\theta_{\mathrm{dwell}}}{\theta_{\mathrm{rp}}} - \frac{2}{3}\frac{\theta_{\mathrm{r}}}{\theta_{\mathrm{rp}}}} \tag{5.8}$$

The angle needed for the current to rise from zero to its reference value θ_{r} depends on the phase current i_{ph}, the speed of the machine N, the value of the inductance in the unaligned position L_{u}, and the DC-bus voltage V_{dc}:

$$\theta_{\mathrm{r}} = \frac{L_{\mathrm{u}} i_{\mathrm{ph}} N}{V_{\mathrm{dc}}} \tag{5.9}$$

The variation of θ_{r} with the phase current and speed can be observed in Fig. 5.4.

The rotor pole pitch θ_{rp} is 360° divided by the number of rotor poles N_{r}:

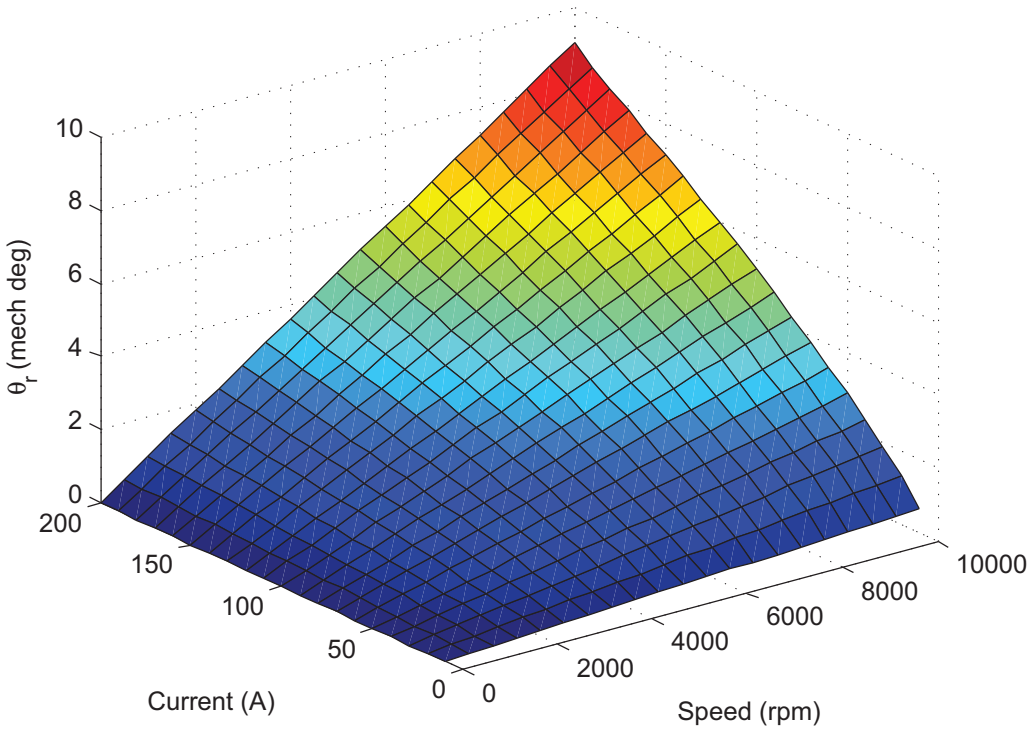

FIGURE 5.4: θ_r vs. speed and phase current

$$\theta_{rp} = \frac{360^\circ}{N_r} \tag{5.10}$$

The dwell angle θ_{dwell} is the difference between the turn-off angle θ_{off} and the turn-on angle θ_{on}:

$$\theta_{dwell} = \theta_{off} - \theta_{on} \tag{5.11}$$

The mean value of the current can be calculated as:

$$I_{mean} = i_{ph} \frac{\theta_{dwell}}{\theta_{rp}} \tag{5.12}$$

5.3 Frequency Stress Calculation

The maximum switching frequency of an IGBT is limited by the amount of heat dissipated before the junction temperature reaches the rated temperature under specific thermal conditions.

The voltage equation of one phase of an SRM can be written:

$$V_{dc} = R_{ph} i_{ph} + L_{ph} \frac{\mathrm{d}i_{ph}}{\mathrm{d}t} + e, \tag{5.13}$$

where V_{dc} is the DC-bus voltage, i_{ph} is the phase current, R_{ph} is the phase resistance, L_{ph} is the phase inductance and e is the back-emf.

Considering the voltage drop on the phase resistance negligible, (5.13) becomes:

$$V_{dc} = L_{ph}\frac{di_{ph}}{dt} + e \tag{5.14}$$

At speeds from 0 to 500rpm, the low-frequency torque ripple generates oscillations that may excite resonant frequencies of the drive train, making the vehicle undrivable. To eliminate the torque ripple, instantaneous torque control techniques are employed, usually using hybrid or hard chopping techniques. Thus, the current is decreasing within the hysteresis band under the influence of the negative DC-bus voltage:

$$-V_{dc} = L_{ph}\frac{di_{ph}}{dt} + e \tag{5.15}$$

At speeds over 500rpm, average torque control techniques employing soft switching are used to control the SRM. Thus, the current decreases within the hysteresis band under the influence of the back-emf:

$$0 = L_{ph}\frac{di_{ph}}{dt} + e \tag{5.16}$$

The rising time of the current, t_r, from the minimum to the maximum limit of the hysteresis band is obtained from (5.14):

$$t_r = \frac{L_{ph}\Delta i}{V_{dc} - e} \tag{5.17}$$

When the upper value of the hysteresis band is reached, the current has to be decreased. The time for the current to decrease, t_f, depends on the switching technique employed. For hard chopping the falling time, t_{fh}, is:

$$t_{fh} = \frac{L_{ph}\Delta i}{V_{dc} + e} \tag{5.18}$$

For soft chopping the falling time t_{fs}, is:

$$t_{fs} = \frac{L_{ph}\Delta i}{e} \tag{5.19}$$

Having the rising and the falling time of the current, the switching frequency, f_{sw}, is obtained:

$$f_{sw} = \frac{1}{t_r + t_f} = \frac{e(V_{dc} - e)}{L_{ph}\Delta i V_{dc}} \tag{5.20}$$

The back-emf can be written as [106]:

$$e = V_{\mathrm{dc}} \frac{N}{N_0} \tag{5.21}$$

where N is the instantaneous speed of the machine and N_0 is the base speed. Thus, the switching frequency can be further written as follows:

$$f_{\mathrm{sw}} = \frac{V_{\mathrm{dc}}}{L_{\mathrm{ph}} \Delta i} \frac{N}{N_0} \left(1 - \frac{N}{N_0}\right) \tag{5.22}$$

The voltage of each phase has to be controlled only between the turn-on angle, θ_{on}, and the turn-off angle, θ_{off}. Thus each phase is chopped during a fraction of an electric cycle, α, which is calculated as the ratio between the dwell angle, θ_{dwell}, and the rotor pole pitch [5]:

$$\alpha = \frac{\theta_{\mathrm{dwell}}}{\frac{360^\circ}{N_{\mathrm{r}}}} = \frac{N_{\mathrm{r}}(\theta_{\mathrm{off}} - \theta_{\mathrm{on}})}{360^\circ} \tag{5.23}$$

where N_{r} is the number of rotor poles.

The rise of the temperature in the switches can be put on the account of the average chopping frequency, $f_{\mathrm{sw,avg}}$:

$$f_{\mathrm{sw,avg}} = \frac{\alpha V_{\mathrm{dc}}}{L_{\mathrm{ph}} \Delta i} \frac{N}{N_0} (1 - \frac{N}{N_0}) \tag{5.24}$$

At very high speeds, due to the increased emf, the current does not have the necessary time to reach the reference and the SRM will operate in single pulse mode. So, the average frequency will be equal to the phase frequency:

$$f_{\mathrm{ph}} = \frac{N}{60} N_0 \tag{5.25}$$

Fig. 5.5 illustrates the variation of speed with rotor position for both hard and soft chopping when a hysteresis band of 10A is considered. In the case of hard chopping the frequencies are clearly higher. Above the speed where the current is not able to reach the imposed value, the frequency is equal to the frequency of the phase.

5.4 Power Losses in the Converter

The power losses in the electronic converter occur during conduction period due to the voltage drop on the internal resistance and due to switching transients of the semiconductor devices and are called conduction losses and switching losses, respectively.

The conduction losses can be calculated as the product of the voltage drop across the device and the current passing through it [107]:

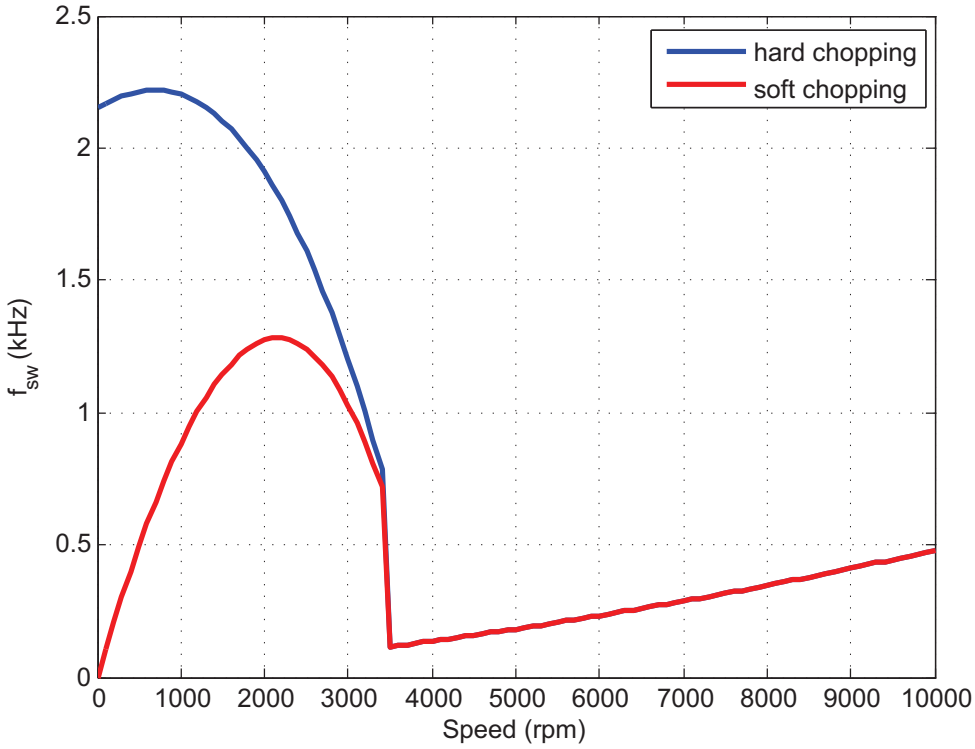

FIGURE 5.5: Switching frequency vs. speed

$$P_{\mathrm{con,T}} = \frac{1}{T}\int_0^T v_{\mathrm{ce}} i_{\mathrm{c}} \mathrm{d}t = \frac{1}{T}\int_0^T (V_{\mathrm{CE0}} + r_{\mathrm{CE}} i_{\mathrm{c}}) i_{\mathrm{c}} \mathrm{d}t = \frac{V_{\mathrm{CE0}}}{T}\int_0^T i_{\mathrm{c}} \mathrm{d}t + \frac{r_{\mathrm{CE}}}{T}\int_0^T i_{\mathrm{c}}^2 \mathrm{d}t = V_{\mathrm{CE0}} I_{\mathrm{mean}} + r_{\mathrm{CE}} I_{\mathrm{rms}}^2 \tag{5.26}$$

where T is the conduction period, v_{ce} and i_{c} the instantaneous values of the current and voltage, respectively, passing through the device, I_{mean} and I_{rms} the mean and the rms values of the current, respectively, V_{CE0} the DC portion of the saturated voltage and r_{CE} the equivalent resistance of the saturated device.

The switching losses is the sum of the turn-on and turn-off losses:

$$P_{\mathrm{sw,T}} = f_{\mathrm{sw}} E_{\mathrm{on}} + f_{\mathrm{sw}} E_{\mathrm{on}} = f_{\mathrm{sw}} (E_{\mathrm{on}} + E_{\mathrm{off}}) \tag{5.27}$$

with f_{sw} the switching frequency.

The total power losses of the IGBT is the sum of its conduction and switching losses:

$$P_{\mathrm{T}} = P_{\mathrm{sw,T}} + P_{\mathrm{con,T}} \tag{5.28}$$

In the modern fast recovery diodes used with IGBTs, the turn-on losses are negligible compared to the turn-off losses, representing less than 1% of the turn-off losses [107]. The turn-off losses, P_{rr}, are caused by the reverse recovery of the diode and are obtained as:

$$P_{\mathrm{rr}} = f_{\mathrm{sw}} E_{\mathrm{rr}} \tag{5.29}$$

with f_{sw} the switching frequency.

The conduction losses are calculated as for the IGBTs, but replacing V_{CE0} and r_{CE} with V_{F0} and r_{F}:

$$P_{\mathrm{con,D}} = V_{\mathrm{F0}} I_{\mathrm{mean}} + r_{\mathrm{F}} I_{\mathrm{rms}}^2 \tag{5.30}$$

The total losses in the diode are:

$$P_{\mathrm{D}} = P_{\mathrm{con,D}} + P_{\mathrm{rr}} \tag{5.31}$$

5.5 Thermal Model of the Converter

The trend in the domain of power electronics towards greater packing density, higher switching frequency and higher power dissipation leads to increased operating temperatures and decreased reliability. Thus the thermal analysis of the converter plays an important role in the design.

To predict the thermal behaviour of the converter the thermal models of its components have to be firstly considered. The model used in the prediction of thermal performances of the devices is the π-model shown in Fig. 5.6. Each semiconductor component is represented by an RC network. The transient thermal impedance can expressed as:

$$Z_{\mathrm{thj-c}} = \sum_{i=1}^{n} R_{\mathrm{th}i} \left(1 - e^{\frac{-t}{\tau_i}}\right) \tag{5.32}$$

where $Z_{\mathrm{thj-c}}$ is the thermal transient impedance from junction to case, R_{thi} is the thermal resistance of the i-th component and τ_{i} is the thermal time constant of the same i-th pair calculated obtained as:

$$\tau_{\mathrm{i}} = R_{\mathrm{i}} C_{\mathrm{i}} \tag{5.33}$$

The previously calculated total losses of each semiconductor device represent the source of the equivalent circuit. Having all the parameters given in the datasheet of the devices and total losses, the variation of the temperature can be calculated. Fig. 5.7 illustrates the variation of the junction-case temperature when considering the maximum current passing through the phase winding and the maximum switching frequency. This means that both conduction and switching losses are at their maximum value. It can be seen that the junction-case temperature of the IGBT increases with 18.97K and of the diode with 23.96K.

To keep the functioning temperature in a safe area, the semiconductor components are mounted on a heatsink. The global thermal behaviour of the converter, besides the thermal impedance

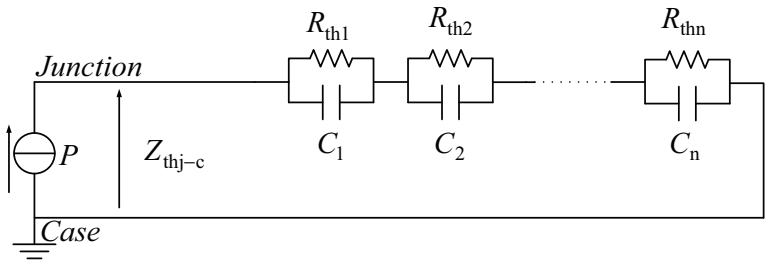

FIGURE 5.6: Thermal RC network for semiconductor devices from junction to case

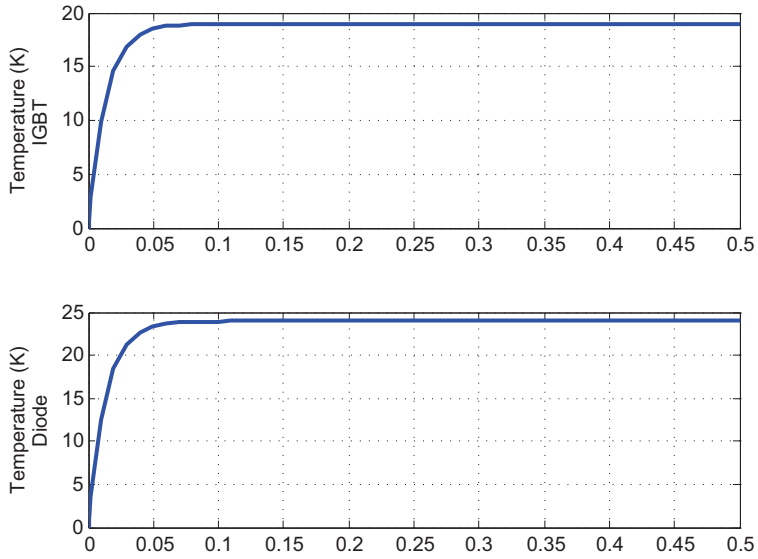

FIGURE 5.7: Junction case temperature rise of the IGBT and diode in the worst case scenario

of the semiconductor components, is also influenced by the heatsink's thermal behaviour and the thermal impedance of the interface between the case and the heatsink represented by the thermal grease.

The complete transient thermal model of the converter is illustrated in Fig. 5.8. Four identical modules are mounted on the same heatsink. The ambient temperature is represented by T_a, while P_T and P_D are power losses on the IGBTs and diodes, respectively.

The thermal resistance of the heatsink is the parameter which defines its efficiency. The cooling method of the heatsink (natural air, forced air or water) influences the value of its thermal resistance. The heatsink has to be chosen as to keep the junction-case temperature of the semiconductor components under its maximum allowable value of 150°C. Also a safety margin of 20°C is considered, thus the maximum junction temperature should be 130°C. To be able to keep the junction temperature under its maximum value a heatsink with a thermal resistance under 0.075K/W should be considered.

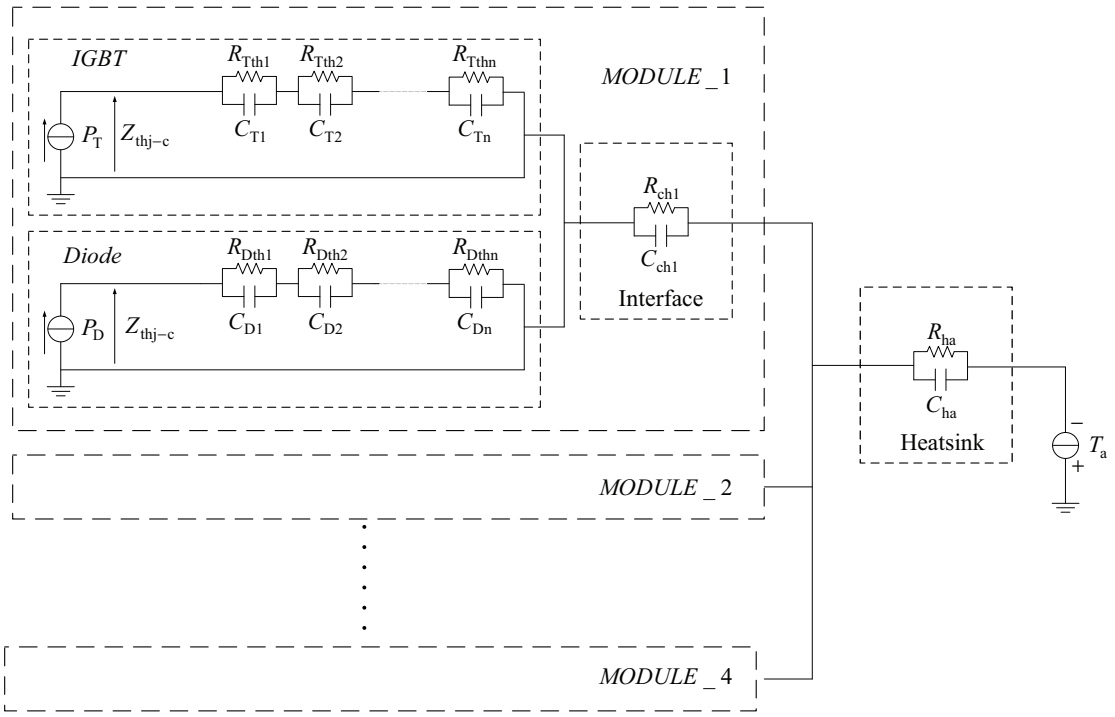

FIGURE 5.8: Equivalent thermal network of the converter

5.6 Construction of the Converter

The previously described converter has been built in so as to allow an easy implementation of different control methods of the SRM. The power circuit of the converter is illustrated in Fig. 5.9 and the components are further described.

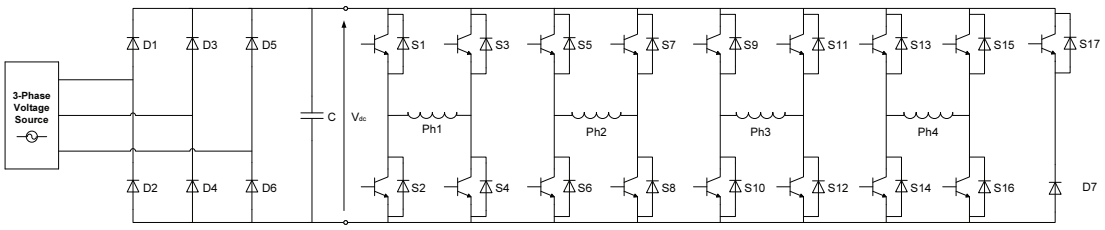

FIGURE 5.9: The power circuit of the converter

Taking into account the above mentioned requirements but also the price and the availability of the semiconductor components, the SKM400GB12V module from Semikron (Fig. 5.10) was selected to build the converter. The module is composed of two IGBTs equipped with diodes connected in anti-parallel, but only one transistor and the diode from the other are going to be

used to form the asymmetric H-bridge. The module has a V_{CE} of 1200V and a I_{Cnom} of 400A. For the chopper is chosen an SKM400GAL125V module with 1200V V_{CE} and 400A I_{Cnom}.

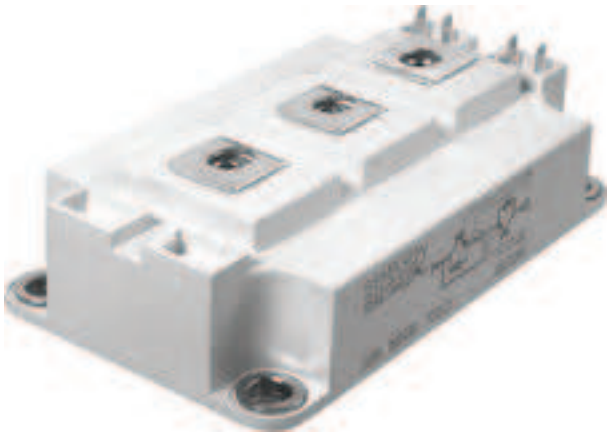

FIGURE 5.10: SKM400GB12V IGBT module

The function of the IGBT drivers is to convert the signals coming from the controller into signal with sufficient power to ensure a safe switching of the transistor. Also the driver has to offer electrical insulation between the controller and the power switches through opto-couplers or transformers, it has to detect and to protect against short-circuits and over-voltages. This means that besides the gate-drive function the driver has to guarantee a protection function.

The drivers used are SKHI23/12R (Fig. 5.11) for SKM400GB12V and SKHI10/12R (Fig. 5.12) for SKM400GAL125V from the same manufacturer. The drivers are capable of providing the necessary energy to properly switch the power switches and besides the previously mentioned requirements they also provide a fault memory and a fault feed-back to the controller and high electromagnetic immunity. They are also equipped with an under-voltage protection of the supply. The SKHI23/12R disposes of an interlocking circuit which prevents the IGBT turn-on before the gate of the other IGBT is completely discharged, avoiding shoot-through situations.

FIGURE 5.11: SKHI23/12R IGBT driver

FIGURE 5.12: SKHI10/12R IGBT driver

The DC input of the converter is provided by two diode bridge rectifiers connected in parallel equipped with a battery of capacitors on the output to smooth the voltage. The diode bridge rectifiers used are 160MT120KPBF (Fig. 5.13) from Vishay; they have a peak forward current of 200A at a maximum reverse repetitive voltage of 1600V. For the voltage smoothing three aluminium electrolytic capacitors B43580A5228M (Fig. 5.14) from EPCOS connected in series

are used. Each capacitor has a capacity of 2200μF, a voltage of 450V and a rated ripple current of 8.4A.

FIGURE 5.13: 160MT120KPBF diode bridge rectifier

FIGURE 5.14: B43580A5228M electrolytic capacitor

To avoid the over-voltages and other parasitic effects which occur during switching due to stray inductances and capacitance, capacitive snubber circuits are used. A metallized polypropylene film capacitor MKPB32656S (Fig. 5.15) from EPCOS is connected in parallel with each power module. In this manner a higher protection is ensured for the power switches in front of transient over-voltages and at the same time the immunity to EMI is increased.

FIGURE 5.15: MKP B32656S snubber capacitor

As a controller for the system a dSPACE 1103 prototyping tool was used (Fig. 5.16). The processor around which the system is built is a PPC 750GX with a CPU clock at 1 GHz. It provides a large selection of interfaces, including 50 bit-I/O channels, 36 A/D channels, and 8 D/A channels. For additional I/O tasks, a DSP controller unit built around Texas Instruments TM320F240 DSP is used as a subsystem [108].

The real-time workshop from MATLAB Simulink allows the user to use the graphical programming and generates the C-code for the processor automatically. In this manner the researcher is able to focus on the development of the control rather than on writing software. Thus, the models created for simulation can be straightforwardly implemented on the test bench after a short interfacing.

The interface between the user and the controller is realized by the ControlDesk software. Different interfaces for each control strategy have been developed and are presented in Appendix C.

The switching signals provided by the prototyping tool have a voltage level of 0-5V, but for the drivers a voltage level of 0-15V is required. An interface board was built to convert the voltage from 0-5V to 0-15V (Fig. 5.17). The electronic circuit of each signal is presented in Fig. 5.18.

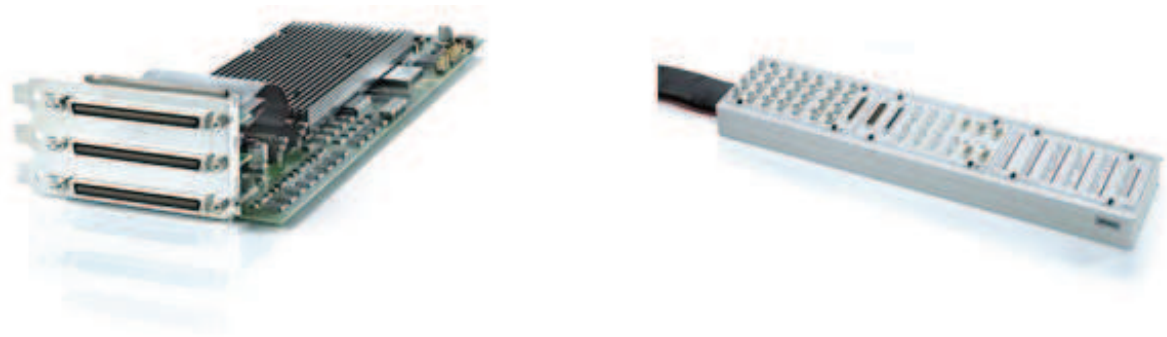

FIGURE 5.16: dSPACE 1103 controller board and connector panel

The galvanic insulation between the dSPACE board and the IGBT drivers is ensured by a single-channel optocoupler 6N137. The IGBT drivers are using positive logic while dSPACE prototyping tool is working on inverse logic. The adaptation of the logic is made using a NPN transistor having the collector connected via a current limiting resistance to the positive connector of the source and the emitter to the ground. When the transistor Q1 is closed, on its collector, which is the output of the interface circuit, it can be found 0V and when the transistor is opened on the collector it can be found 15V. The error detection signal of the drive has 0-15V and has to be converted to 0-5V to be processed by the controller.

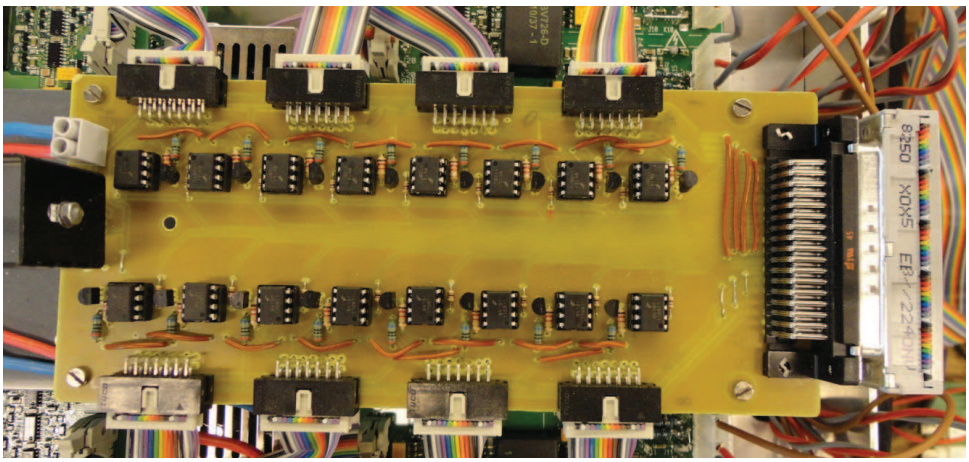

FIGURE 5.17: Signal conversion interface

For the measurement of the phase currents, LA205-S hall effect sensors from LEM are used, capable of measuring a maximum current of 300A (Fig. 5.19). The output of the sensors is 100mA corresponding to a primary nominal current of 200A. To read the value of the current with the dSPACE system, the current signal is transformed to a voltage signal by means of a resistance. For the measurement of the DC-bus voltage a CV3-1200 sensor from LEM is used, capable or measuring voltages from 0 to 1200V (Fig. 5.20). The output signal of the sensor is a voltage signal, so no interfacing is needed for the connection to dSPACE.

Two views of the final converter are presented in Fig. 5.21 and Fig. 5.22. The power components of the converters have been shielded to avoid EMI.

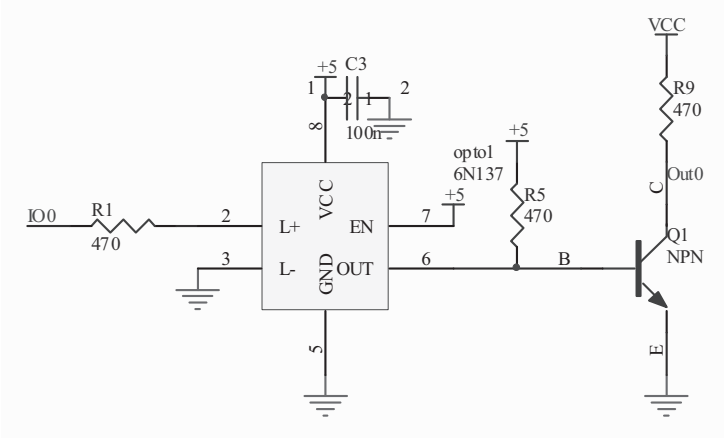

FIGURE 5.18: Electronic scheme of one channel of the signal conversion interface

FIGURE 5.19: LEM LA205-S current transducer

FIGURE 5.20: LEM CV3-1200 voltage transducer

5.7 Test Bench Description

The test bench (Fig. 5.23) is built around the 30kW peak-power switched reluctance machine which is mechanically connected to a DC machine. The SRM is controlled by the dSPACE 1103 system via the built power converter. A 100kVA transformer represents the power source of the system and the initial charge of the DC-bus is done with the aid of auxiliary resistors, which are short-circuited when the voltage reaches the steady-state. Due to the high current density in the windings, a water cooling circuit is needed composed from a car radiator and a car water pump. It was preferred to use a circuit similar to the one from a common road vehicle to avoid unnecessary and expensive modifications when the SRM is mounted on the vehicle's chassis.

The DC machine is controlled with the same dSPACE system. The power converter for DC machine's armature is a SKiiP 132GD120-3DU converter from Semikron. The DC-link voltage for the SKiiP module is provided through a diode bridge rectifier with three capacitors connected in series between them and in parallel with the output of the rectifier. For the field winding, the same system composed from a diode bridge rectifier and capacitors is used. The levels of both DC voltages are controlled with two autotransformers. The DC machine is air-cooled with a fan driven by a three-phase asynchronous machine.

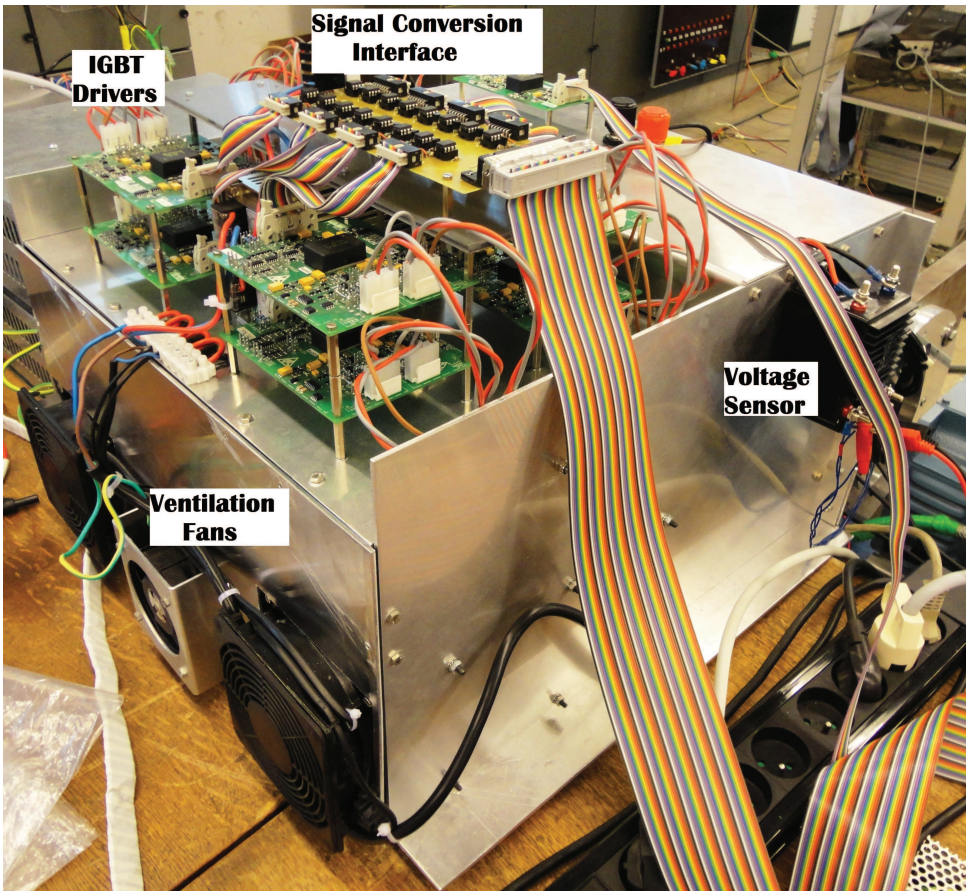

FIGURE 5.21: Final converter - front view

For the position detection of the SRM two different sensors are used. A 1024-pulse incremental encoder (Fig. 5.24) is mounted on the free end-shaft of the DC machine. The incremental encoder is not capable to memorize the position when the system is reset or shut down, thus, an alignment procedure has to be carried out every time the system is turned-on. To eliminate the problems caused by the sensibility of encoders with respect to vibrations an elastic coupling connects the shaft of the device to the shaft of the machine.

The second position sensor is a variable reluctance resolver (Fig. 5.25)integrated in the SRM. Variable reluctance resolvers are highly reliable brushless resolvers without rotary transformers. Unlike conventional resolvers, they have both primary and secondary windings on the stator and no windings on the rotor. This offers significant advantages in price, weight and envelope dimensions. Variable reluctance resolvers are capable to provide accurate absolute positioning or velocity feedback. The lack of brushes and windings on the rotor makes them extremely reliable and compact, suited for vehicle applications.

The sine and cosine signals coming from the resolver are usually noisy and a filtering has to be done. But the filters introduce delays making the analogue signal treatment only suited for a limited speed range. Thus an electronic board (Fig. 5.26) converting the analogue signals into digital ones has been built. The board is constructed around a AD2S1205 chip from Analog Devices. The output signal feeding the primary of the resolver is a 12kHz sine wave which is amplified using two operational amplifiers and an H-bridge to provide enough power. The input waveforms, the sine and cosine coming from the resolver, are internally treated and the position signal is transmitted on 12 bits to the dSPACE. A basic C procedure was developed

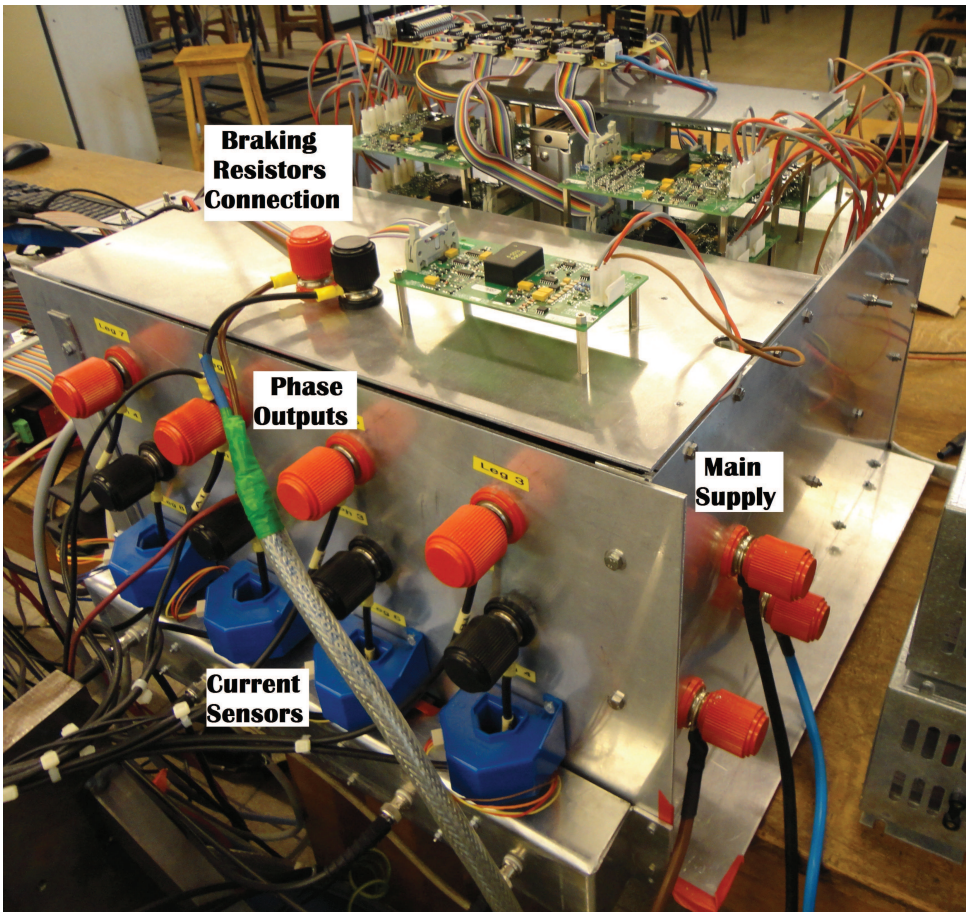

FIGURE 5.22: Final converter - back view

to translate the 12 bits into a position and a speed signal which can be read at each sampling time. Four DAC connectors are used to provide the chip with !RESET, !RD, !SAMPLE and !RDVEL signals.

5.8 Switching Strategies in Switched Reluctance Drives

The control of the SRM is a difficult task demanding highly trained specialists. Each phase is controlled independently using hysteresis or PWM control. Most applications are employing an asymmetric H-bridge to control the current within a hysteresis band. The asymmetric H-bridge allows three voltage states, $+V_{\mathrm{dc}}$, 0 and $-V_{\mathrm{dc}}$, thus, depending on the control method, only two or all three states are employed.

When a simple hysteresis control or an average torque control is performed, a certain value of the current is imposed between turn-on and turn-off angles. The current has to be controlled between the limits of the hysteresis band and for that both hard and soft chopping can be employed. If hard chopping is used, the value of current increases when both transistors are turned on and a positive voltage equal to the DC-bus voltage is applied to the phase. When the upper limit of the hysteresis band is reached and the current needs to decrease, both transistors are turned off, the current flows through the diodes and a negative voltage is applied to the phase. Thus the phase voltage step on the phase has a value twice as big as the DC-bus voltage,

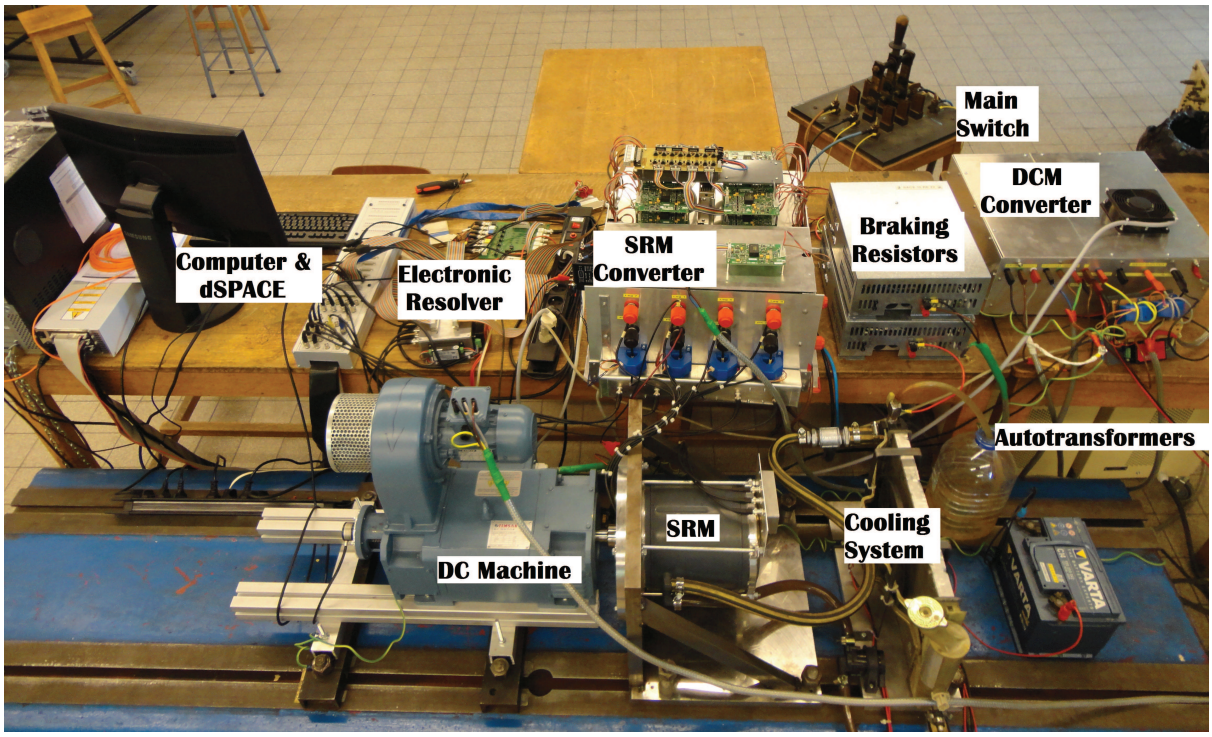

FIGURE 5.23: The experimental set-up

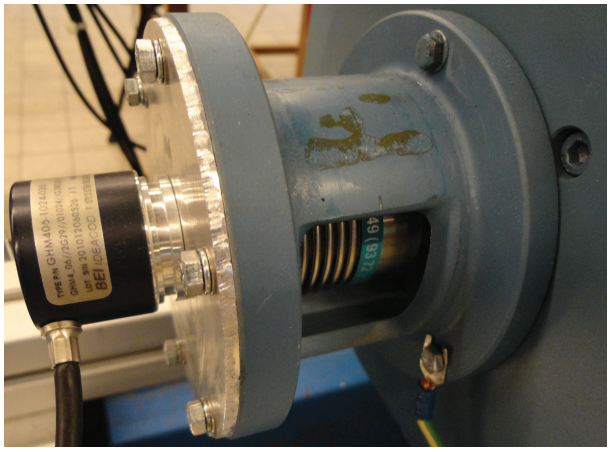

FIGURE 5.24: Incremental encoder mounted on DC machine

leading to a rapid deterioration of the winding insulation. Also, the life of the DC-bus capacitor is diminished due to accentuated voltage ripple. The switching frequency of the method is high, resulting in great switching losses on semiconductor components.

While employing soft chopping, the current rises under the influence of a voltage equal to the DC-bus voltage and when the upper value of the hysteresis band is reached only one transistor is turned off and a zero voltage loop occurs and the current decreases much slower compared to the hard chopping case. The switching frequency being reduced, the switching losses are reduced. The life of the DC-bus capacitor and the insulation of the winding is increased. At turn-off angle both transistors are opened and a negative voltage is applied to the phase, the current rapidly cancels and the production of negative torque is avoided.

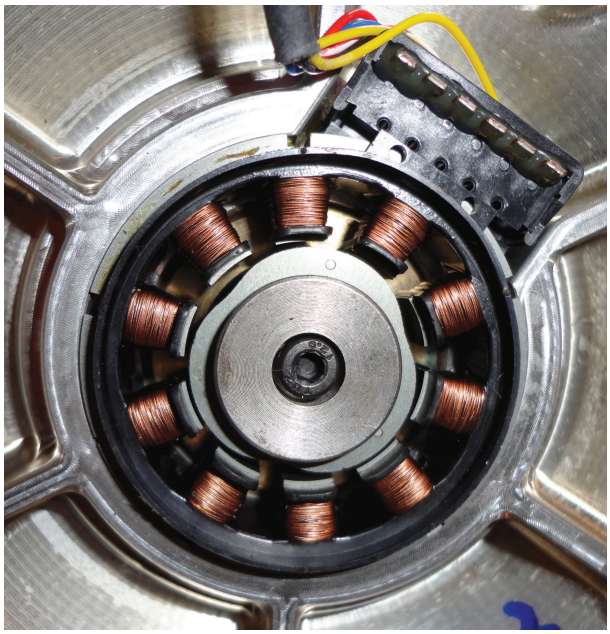

FIGURE 5.25: Variable reluctance resolver mounted on SRM

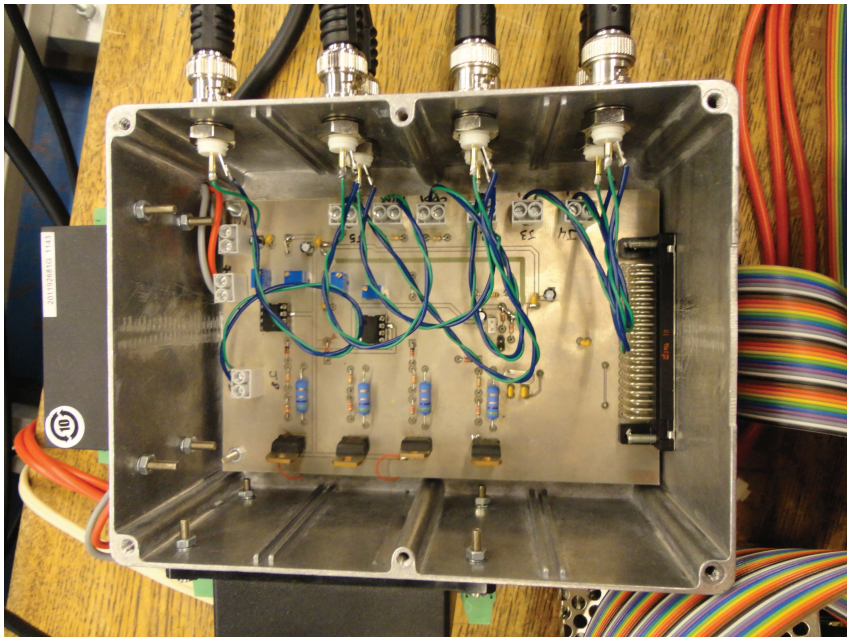

FIGURE 5.26: Electronic board used for resolver signal treatment

The instantaneous torque control techniques DITC and DTC are using all three states of the phase voltage. The current profiling techniques cannot benefit from the advantages offered by the soft switching. If a negative slope of the current is imposed as reference, applying zero voltage to the phase is not always enough for the phase current to follow. This forces the usage of hard chopping.

Also a hybrid controller can be used which makes use of all three voltage states allowed by the asymmetric bridge. Besides the hysteresis band, another threshold value higher than the upper value of the hysteresis band is defined. When the current reaches the upper limit of the band,

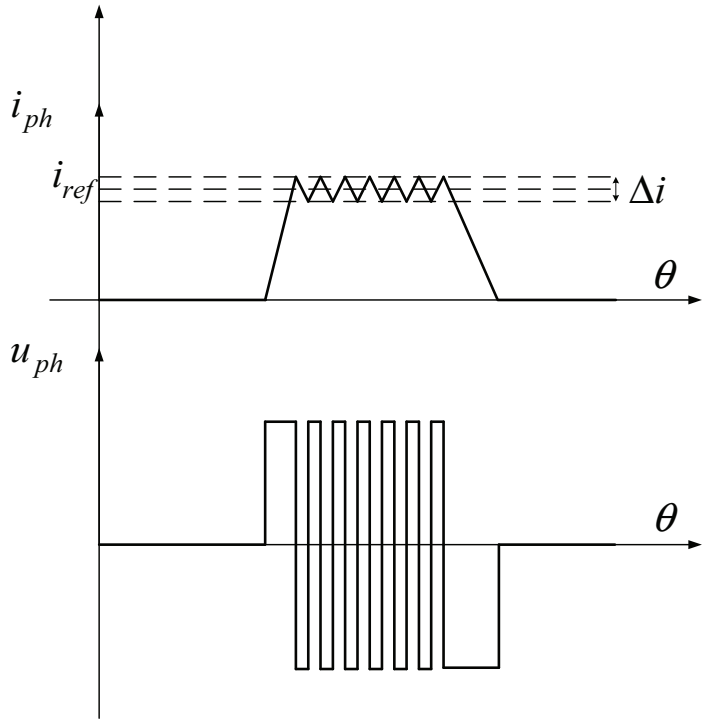

FIGURE 5.27: Hysteresis current control using hard switching

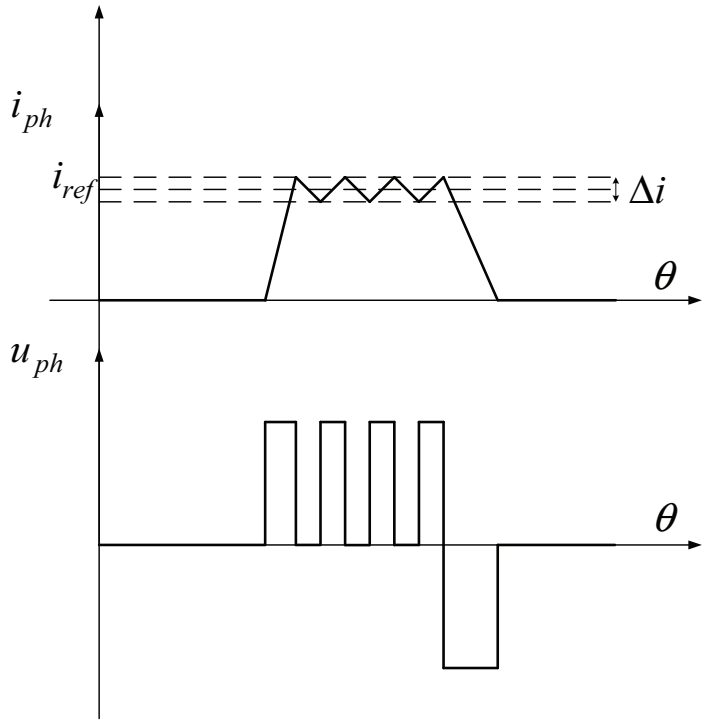

FIGURE 5.28: Hysteresis current control using soft switching

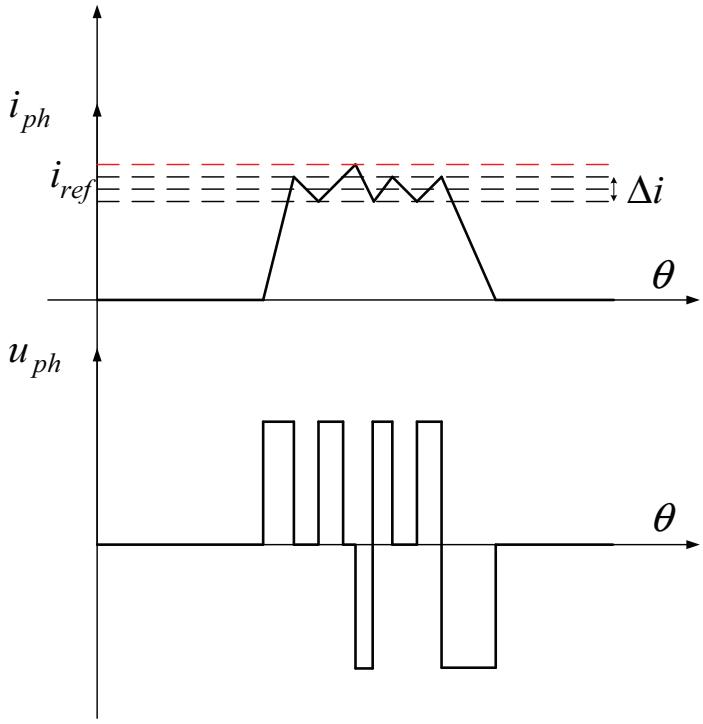

FIGURE 5.29: Hysteresis current control using hybrid switching

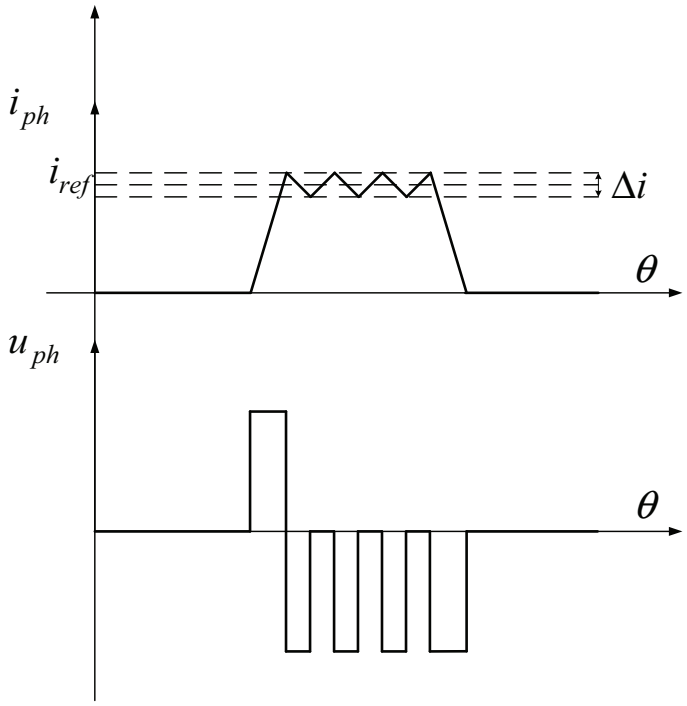

FIGURE 5.30: Switching strategy in generator mode

one transistor is turned-off and zero voltage is applied to the phase. If the current continues to increase the second transistor is closed and $-V_{\mathrm{dc}}$ is applied to the phase. This strategy reduces significantly the switching frequency and the associated losses.

In generator mode, due to high back emf, negative voltage is required to decrease the current and hard chopping is usually used. Due to the negative slope of the inductance, the current increases under the influence of the back-emf even if the phase is not energized with positive voltage. Thus, the current can be controlled by applying zero voltage to the phase when the current has to increase and negative voltage when the current has to decrease. Positive voltage will be applied to the phase only at the beginning of the conduction period until the current reaches the imposed value. This reduces the switching frequency and the associated losses and reduces the degradation of the windings and DC-bus capacitor.

5.9 Conclusions

The fifth chapter entitled has been focused on the design and the construction of a converter for controlling the SRMs on a wide speed range. The chapter starts by classifying the converters by the number of switches per phase and by their commutation type. The classic asymmetric H-bridge topology has been chosen for supplying each phase due to the flexibility granted for the control. After choosing the semiconductor devices, the frequency stress and the losses on each device have been calculated. The losses have been introduced in the thermal model of the converter to find the thermal resistance of the heatsink.

The converter has been built, together with a whole test bench for testing SRMs also described in the chapter. As a load a DC machine has been preferred as a load because it could be used also as a torque meter. The brain of the system has been represented by a dSPACE 1103 commercially available prototyping tool and it has chosen due to its interfacing with MATLAB. By doing so, the researcher can focus on the development of the control rather than on writing software.

The chapter ends with a discussion on the switching strategies employed in SRDs.

Chapter 6

Noise in SRDs

Together with the torque ripple inconvenience, the acoustic noise emission remains the most problematic issue in SRMs, which is far from being solved. After the sources of noise in the SRM were identified, [109, 110]. different approaches for the study of the noise problem were developed. In [111, 112, 113], rapid analytical methods to estimate the natural frequencies of the stator structure were proposed. Taking into consideration the complex geometry of the SRM, 2D [111] or 3D [114] FEM analysis was conducted for the determination of the frequencies. A better a determination of the eigen frequencies and the analysis of the aerodynamic noise is possible through means of measurements [115, 116, 117].

6.1 Noise Sources in SRMs

The noise in electric machines have different causes which can be split up into four main groups [118]: magnetic, mechanical, aerodynamic and electronic. Fig. 6.1 illustrates a classification of the noise sources.

6.1.1 Magnetic Sources

The magnetic origin of the noise in SRMs is related to the radial and tangential forces occurring at the crossing of the airgap by the magnetic flux. This is considered to be the main cause of the acoustic noise in the SRMs.

The radial forces are acting as attraction forces between rotor and stator pole causing deformation of the stator. The displacement of the outer stator surface is leading to acoustic noise. When the frequency of the radial force coincides with one of the natural frequencies of the stator, the acoustic noise is increased due to the occurring resonance. The magnetic force is dependent on the physical construction and the material properties of the motor's magnetic and electric circuit and on the control strategy.

The radial force component in SRMs can be reduced by enlarging the airgap. But then, the ratio between the aligned and the unaligned inductances is reduced, leading to a reduced power density and greater volume. Skewing can be used in small machines to reduce radial forces, but in large machine it produces torsional forces increasing noise [3]. Skewing, also, removes the manufacturing simplicity advantage from the SRM.

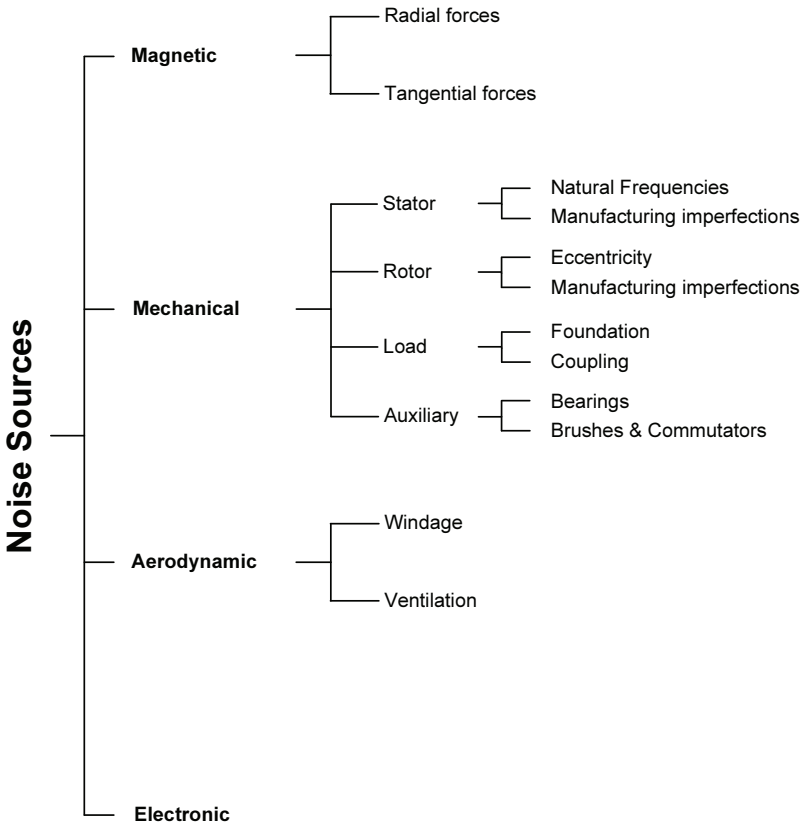

FIGURE 6.1: Noise sources in electric machines [5]

The tangential forces and their commutation due to phase commutation lead to vibrations of the stator poles. The pole vibrations can be attenuated by employing current profiling techniques.

The electromagnetic forces in electric machines, with both their radial and tangential components, can be calculated using analytical approaches or FEM-based softwares.

6.1.2 Mechanical Sources

The stator structure represents itself a source of noise in the machine through its natural or eigen frequencies. When stator natural frequency coincides with the frequencies of the exciting forces, resonance occurs the acoustic noise its increased. In SRMs, resonance occurs when the fundamental frequency, also known as phase frequency, or one of its odd harmonics, coincide with one of the stator eigen frequencies. The machine has to be designed in such a manner to

have the natural frequency as high as possible and, during operation, it is preferred to mismatch the frequencies. In a wide speed range drive, most likely, the two frequencies will not be always mismatched and resonance is possible to occur.

Non-uniform radial forces can be excited due to a non-uniform airgap. The non-uniformity of the airgap is caused by manufacturing imperfections leading to elliptical stator bore or rotor surface. The non-uniformities of the material properties, also, lead to uneven distribution of forces. The non-uniform force distribution and the created unbalance produce rotor vibrations.

Likewise, the eccentricity of the rotor leads to non-uniform magnetic or mechanical force distribution. The eccentricity appears if the mass centre of the rotor does not correspond to its geometrical centre or if the rotor is not mounted in the centre of the stator.

An improper stacking of the laminations can lead to vibrations both on the stator and rotor under the influence of magnetostrictive forces. An improper manufacturing or mounting of the phase windings can allow the individual turns or the whole winding to move, producing additional noise. The latter two effects can be also considered to have both mechanical and magnetic origin, taking into account that the vibration appear only under the influence of the magnetic field.

The foundation on which the machine is mounted and the coupling with the load have a strong influence on the vibrations and noise production. A proper foundation and a proper alignment of the machine with the load may reduce noise. The machine can be connected with the load by a coupling having a certain degree of elasticity.

The quality of the used bearings influences the noise in the machine. A good alignment of the machine with the load and the mismatch of the natural frequency of the bearing with the natural frequency of the machine can ameliorate the noise produced by the bearings. The brushes and the collector can create important noise in a machine, but they are not present in the classical SRM.

6.1.3 Aerodynamic Sources

The SRM is a doubly salient machine and when the machine is turning the rotor poles behave like blades and the so called windage effect appears. The windage effect be attenuated by shaping the edges of the rotor poles. The windage can also be avoided by filling the rotor slots with non magnetic material [117]. This increases the manufacturing cost and complexity. A mechanic stability has to be assured at high speed, taking into consideration the centrifugal forces. The heat transfer coefficients in the machine are changed and higher operating temperatures can be reached. To prevent the stalling of the airflow each time a rotor pole passes a stator pole, spacers between the stator poles can be employed [117]. The spacers also improve of the stator structure's stiffness.

The cooling systems employing a fans produce noise, but is not the case of the studied machine.

6.1.4 Electronic Sources

The electronic sources of noise are the harmonics of phase current and phase voltage. The switching frequency of the semiconductor components also participates at noise production.

6.2 Calculation of Structural Eigen Frequencies

The radial forces tend to ovalize the stator yoke in different eigen modes. Each eigen mode has its characteristic mode shape and mode frequency, also named natural or eigen frequency. The most predominant mode is the second order mode, also called fundamental mode [112]. The fourth order mode tends to cause a double ovalization the stator. The zero order mode, also known as pulsating mode or breathing mode, has a uniform radial action on all the circumference of the stator. Due to the symmetry of the excitation, only the even order modes will participate at noise production, the odd order modes not being developed in a eight pole stator.

The eigen frequency can be determined analytically for simple structures, by finite element analysis, or experimentally by shaker test and hammer impact test for complex structures [113].

To calculate analytically the natural frequencies, the stator lamination stack is approximated by a cylinder. The cylinder has the radius equal to the mean radius of the stator yoke R_{m}, the thickness equal to the back iron thickness h_{sy} and length equal to the stack length L_{stk}.

6.2.1 Roark and Young Method

In [111] the natural frequency is calculated by taking into account the energy conservation principle, on the basis of the theory developed by Roark and Young [119], further referred to as R&Y method.

To calculate the potential energy, the deflection D_{v} of the ring's diameter under the action of a vertical load W is considered:

$$D_{\mathrm{v}} = \frac{R_{\mathrm{m}}^3 W}{EI}\left(\frac{\pi}{4} - \frac{2}{\pi}\right) \tag{6.1}$$

where R_{m} is the radius of the ring, E the modulus of elasticity and I the polar moment of inertia. For a rectangular section having the length l and thickness h_{sy}, the product $E \cdot I$ is:

$$EI = \frac{E h_{\mathrm{sy}}^3 L_{\mathrm{stk}}}{12(1-\nu^2)} \tag{6.2}$$

Considering the Poisson ratio ν equal to 0.3 and introducing (6.2) in (6.1), the vertical deflection of the diameter becomes:

$$D_{\mathrm{v}} = 1.625 \frac{W}{L_{\mathrm{stk}}} \frac{R_{\mathrm{m}}^3}{h_{\mathrm{sy}}^3} \frac{1}{E} \tag{6.3}$$

The spring constant per unit length K is defined as:

$$K = \frac{W}{D_{\mathrm{v}} L_{\mathrm{stk}}} = 1.625 \frac{R_{\mathrm{m}}^3}{h_{\mathrm{sy}}^3} \frac{1}{E} \tag{6.4}$$

Considering the radial deflection Δ as being half of the vertical defection of the ring's diameter, the potential energy per unit length E_{p} is:

$$E_{\mathrm{p}} = 2K\Delta = \frac{2}{1.625}\frac{h_{\mathrm{sy}}^3}{R_{\mathrm{m}}^3}E\Delta^2 \tag{6.5}$$

To find the kinetic energy the assumption that the ring is deformed as an ellipse is made. The radius of the ellipse $R_{\mathrm{m}}(\theta)$ can be written as:

$$R_{\mathrm{m}}(\theta) = R_{\mathrm{m}} + \delta(t)\cos(2\theta) \tag{6.6}$$

with the time variation of the radius:

$$\delta(t) = \delta\sin(\omega t) \tag{6.7}$$

The local velocity of any point on the ring can be calculated as:

$$v = \frac{\mathrm{d}R_{\mathrm{m}}}{\mathrm{d}t} = \omega\delta\cos(\omega t)\cos(2\theta) \tag{6.8}$$

Considering the mass density of the lamination material ρ, the kinetic energy of the whole ring can be written as:

$$E_{\mathrm{k}} = \int_0^{2\pi}(vR_{\mathrm{m}}h_{\mathrm{sy}}L_{\mathrm{stk}}\rho)\mathrm{d}\theta \tag{6.9}$$

Introducing 6.8 and solving the integral, 6.9 becomes:

$$E_{\mathrm{k}} = \pi v R_{\mathrm{m}}h_{\mathrm{sy}}L_{\mathrm{stk}}\rho\omega^2 \tag{6.10}$$

The ratio between the vertical and the horizontal deflection is 1.089 [3]. Considering δ to be the average radial deflection

$$\delta = \frac{\Delta}{1.0445}, \tag{6.11}$$

and equalizing the potential and kinetic energy, the natural frequency can be calculated as:

$$\omega^2 = \frac{2\cdot 1.0445^2}{1.625\pi}\frac{E}{\rho}\frac{h_{\mathrm{sy}}^4}{R_{\mathrm{m}}^4} \tag{6.12}$$

The zero mode natural frequency f_0 is obtained as being equal to ω and for the studied machine to 8072Hz. The fact that this method provides only the natural frequency of the zero order mode and none of the other superior mode frequencies represent the main drawback of R&Y method.

6.2.2 Jordan, Frohne and Uner Method

In [112, 120] the natural frequency of mode zero is calculated with the formula developed by Jordan, Frone and Uner, taking into consideration the effects of shear, rotary inertia, teeth and windings:

$$f_0 = \frac{1}{2\pi R_\mathrm{m}} \sqrt{\frac{E}{\rho k}} \tag{6.13}$$

This method will be further referred to as JFU method. The natural frequencies for modes greater than 2 are:

$$f_\mathrm{m} = \frac{f_0 i m(m-1)}{\sqrt{(m^2+1)+i^2(m^2-1)(4m^2+m^2 k_\mathrm{m}/k+3)}} \tag{6.14}$$

where

$$i = \frac{1}{2\sqrt{3}} \frac{h_\mathrm{sy}}{R_\mathrm{m}}$$

$$k = 1 + \frac{W_\mathrm{t}}{W_\mathrm{y}}$$

$$W_\mathrm{t} = W_\mathrm{p} + W_\mathrm{w} + W_\mathrm{i}$$

$$k_\mathrm{m} = 1 + \frac{1.91 N_\mathrm{s} A_\mathrm{sp} h_\mathrm{s}^3 W_\mathrm{t}}{R_\mathrm{m} L_\mathrm{stk} h_\mathrm{sy}^3 W_\mathrm{p}} \left(\frac{1}{3} + \frac{h_\mathrm{sy}}{2h_\mathrm{s}} + \left(\frac{h_\mathrm{sy}}{2h_\mathrm{s}} \right)^2 \right)$$

with

m, m_m - the circumferential mode and mode frequency,

k, k_m - the mass addition factors of displacement and rotation,

W_y, W_y - the total mass of the poles and yoke,

W_w, W_i - the total mass of the windings and insulation,

N_p, h_s - the stator pole number and stator pole height,

A_sp - the cross-section area of the stator pole.

Evaluating the equations, the frequencies of 7256Hz, 1076Hz, 2538Hz and 4057Hz are found to be the natural frequencies of the zero order mode, second order mode, third order mode and fourth order mode, respectively.

6.2.3 Rayleigh Method

In [113] Fiedler is using the same method used by Rasmussen [121, 122] and developed by Rayleigh [123] to calculate the natural frequencies:

$$f_{\mathrm{m}} = \frac{1}{2\pi} \underbrace{\sqrt{\frac{E}{\rho(1-\nu^2)}}}_{\text{material}} \underbrace{\frac{h_{\mathrm{sy}}}{\sqrt{12}R_{\mathrm{m}}^2}}_{\text{geometry}} \underbrace{\frac{m(m^2-1)}{\sqrt{m^2+1}}}_{\text{mode}} \tag{6.15}$$

The three factors of the equation show the dependency of the eigen frequencies on geometry, material properties and the order of the mode. The natural frequencies for the second, third and fourth mode are 1596Hz, 4513Hz and 8653Hz, respectively. The Rayleigh method does not supply a value for the zero order mode natural frequency.

6.3 FEA Frequency Determination

The resonance and a high acoustic noise appear in the SRM when a harmonic of the radial force excites a natural frequency of the stator. Increasing the value of the natural frequencies by changing the geometrical dimensions of the stator yoke can have a positive influence on the noise reduction. Modifying the stator yoke width by changing its inner or outer diameter has the highest influence on the noise production, while the influence is insignificant when changing the stack length [124]. Increasing the stator yoke width is not always beneficial considering the increase of the price, volume and weight. Due to the small influence of the stack length and taking into consideration the lower computational cost, a 2D analysis is preferred for finding the eigen frequencies.

Starting from the electromagnetic analysis model, where the nodal forces on the stator poles were calculated, Fig. 6.2, and keeping the same mesh, the resonant frequencies of the stator's structure are calculated. The radial component of the force on the stator pole is dependent on the phase current and rotor position, as illustrated in Fig. 6.3.

The mode shapes for the zero order, second order, third order and fourth order modes are illustrated in Fig. 6.4, Fig. 6.5, Fig. 6.6 and Fig. 6.7, respectively. The red contour represents the initial shape of the stator and with blue is represented the mode shape. The amplitudes of the shapes are greatly exaggerated. The four presented modes correspond to the frequencies of 7853Hz, 1401Hz, 4428Hz and 7482Hz, respectively. The other vibration modes of the stator structure up to 20kHz can be seen in Appendix D

6.4 Measurements on the Test Bench

Taking into account the functioning of the SRM, the switching of the phases leads to a radial force spectrum formed by the fundamental frequency of the machine and its harmonics. The fundamental frequency of the machine is found by multiplying the number of rotor poles N_{r} by the speed N of the machine in Hz:

$$f = N_{\mathrm{r}} N \tag{6.16}$$

Thus, the harmonics of the fundamental frequency become harmonics of a N_{r} times greater order of speed. In the given situation the number of rotor poles being equal to six, the first, second, third and so on order harmonics of the fundamental frequency can be regarded as the

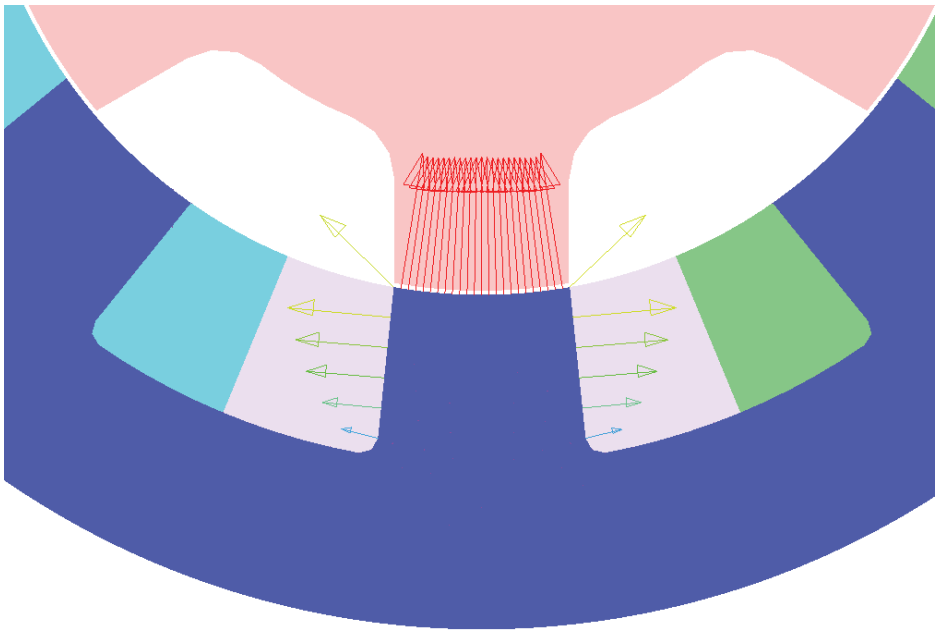

FIGURE 6.2: Nodal magnetic force on a stator pole

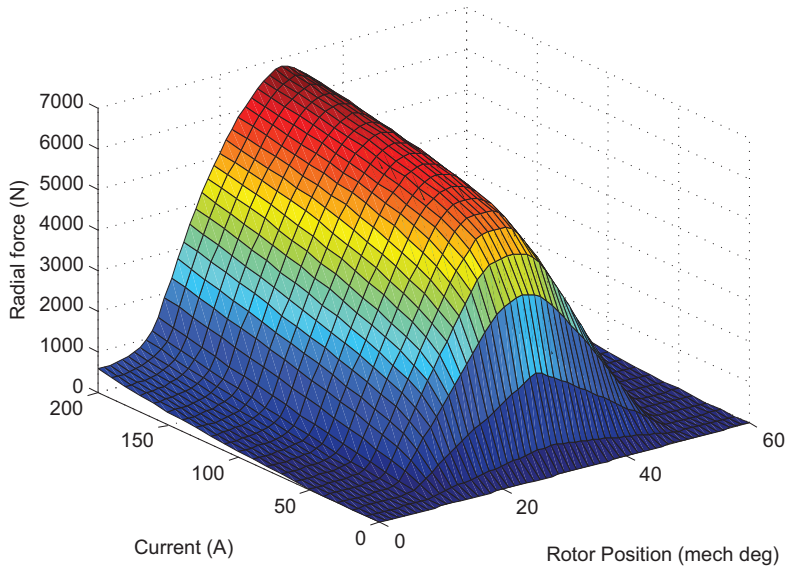

FIGURE 6.3: Radial force on a stator vs. current and rotor position

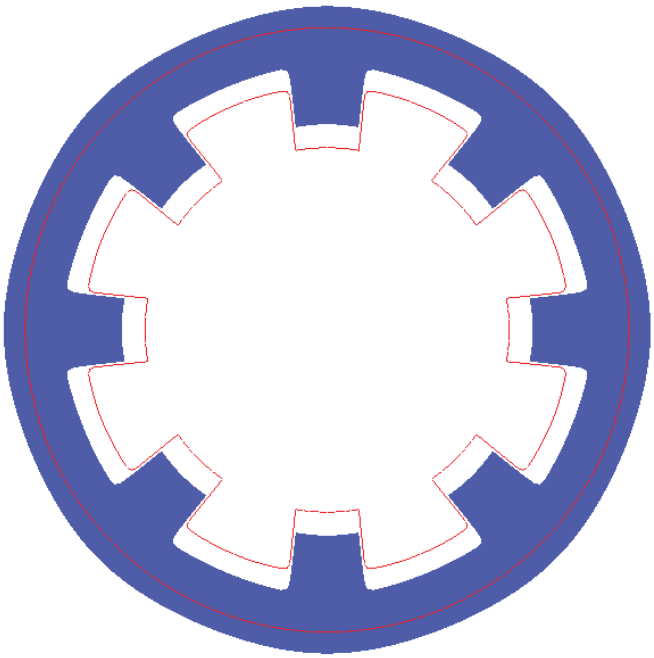

FIGURE 6.4: Vibration mode 0 of the 8/6 SRM

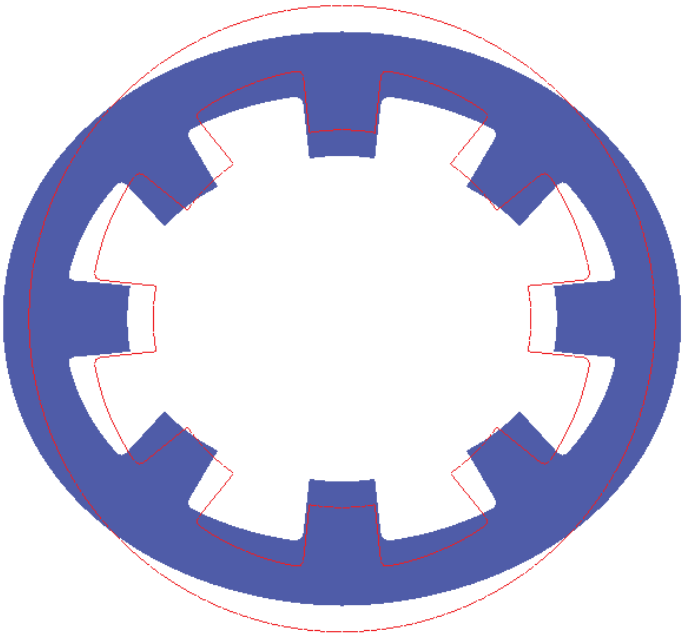

FIGURE 6.5: Vibration mode 2 of the 8/6 SRM

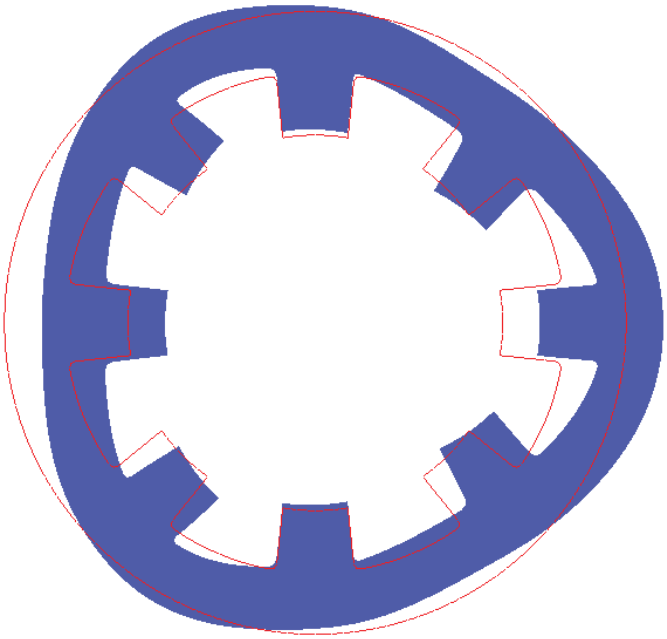

FIGURE 6.6: Vibration mode 3 of the 8/6 SRM

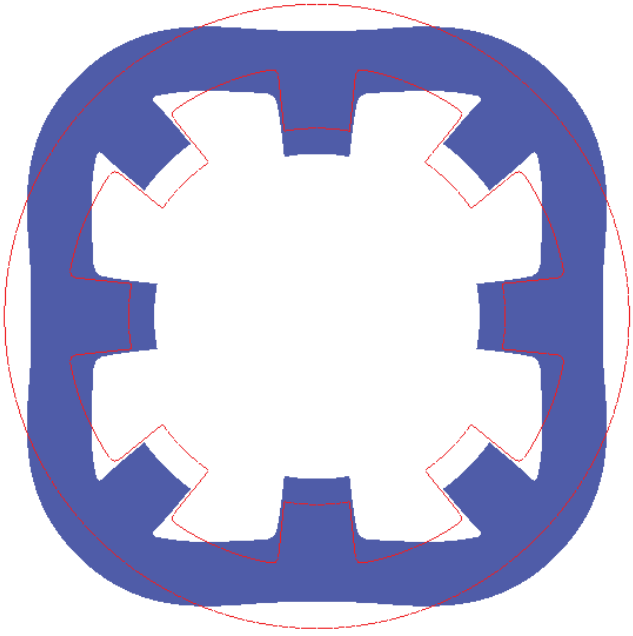

FIGURE 6.7: Vibration mode 4 of the 8/6 SRM

sixth, twelfth, eighteenth and so on order harmonics of the speed, respectively. Fig. 6.8 and Fig. 6.9 illustrate the spectrum of frequencies, with and without marking them, for a run-up test from 0 to 1000rpm.

It can be clearly observed that the even order harmonics of the fundamental frequency have a less important contribution to noise generation than the odd order harmonics. According to registered data, the first eigen frequency is situated around 1434Hz.

A switched reluctance machine is emitting more noise when a eigen frequency is hit by one of the relevant harmonics of the fundamental frequency. The speeds where the coincidence of the frequencies occurs are often called in the literature noisy speeds and the others are called quiet speeds.

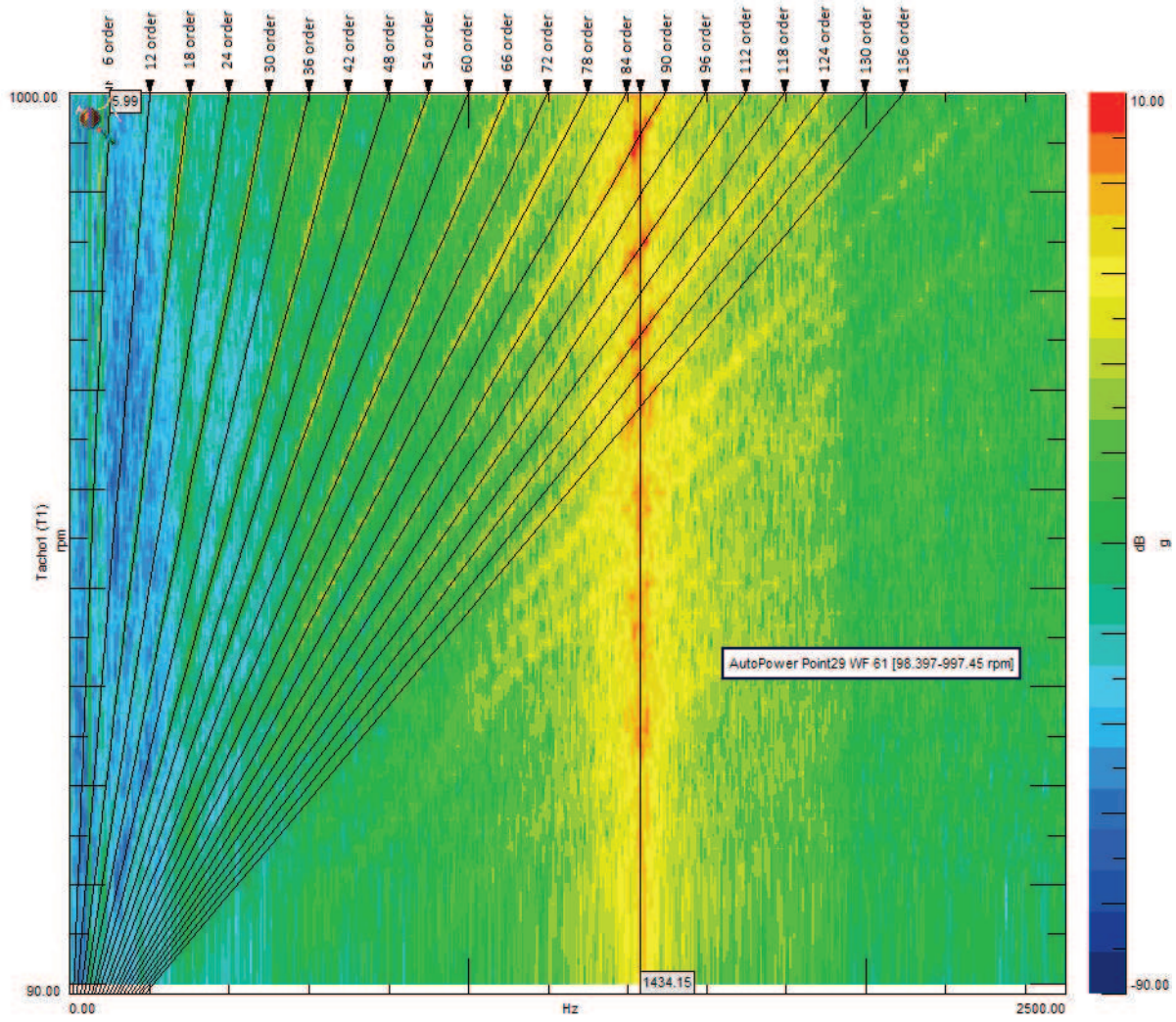

FIGURE 6.8: Spectrogram of surface acceleration during run-up test from 0 to 1000rpm

6.5 Comparison of Frequency Determination Methods

The values of the eigen frequencies previously determined are gathered in Table 6.1. Regarding zero mode frequency, the values calculated with R&Y and by FEM analysis are close, but

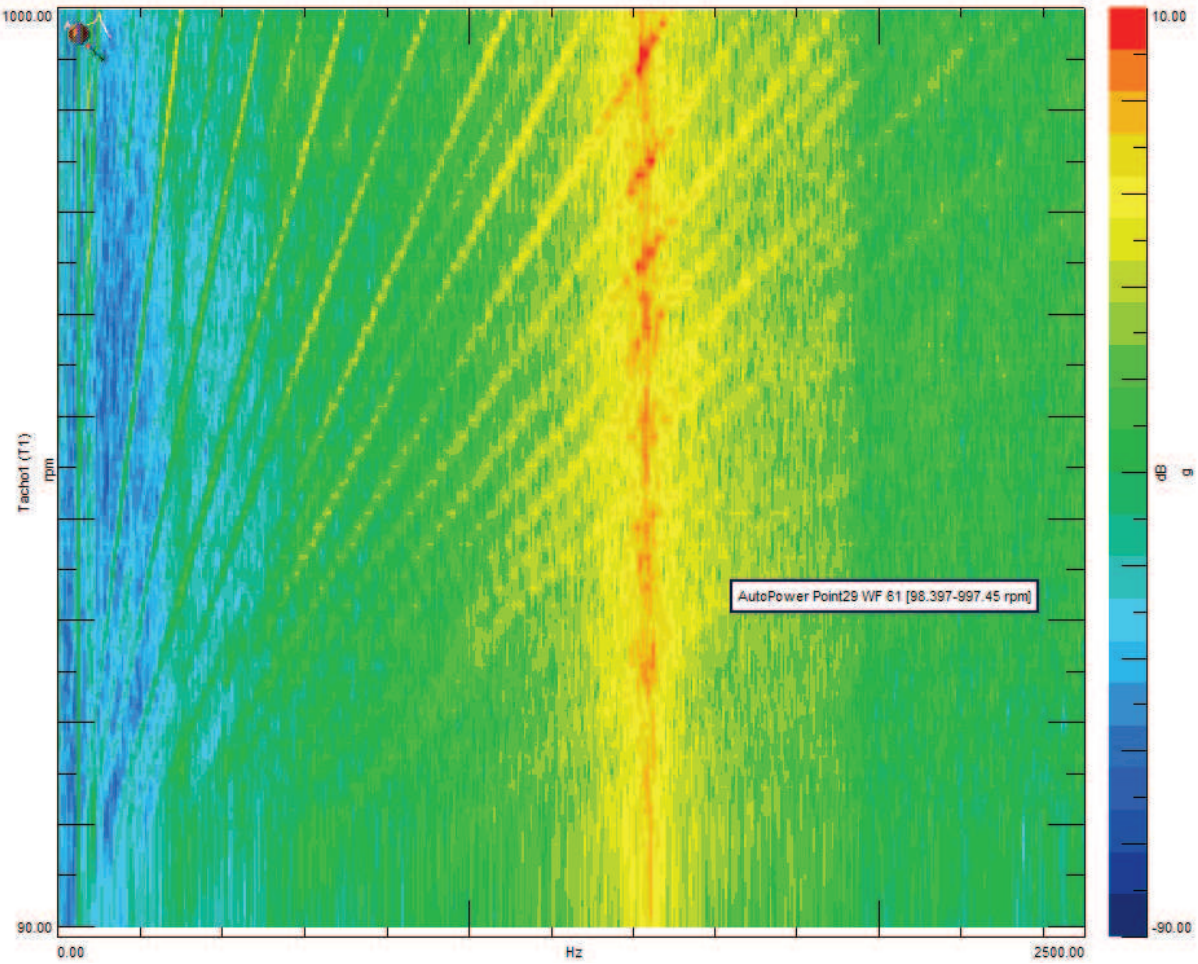

FIGURE 6.9: Spectrogram of surface acceleration during run-up test from 0 to 1000rpm

also JFU method gives a result close to the others. Regarding second, third and fourth mode frequencies, Rayleigh method and FEM offer close solutions and in the case of the second order mode frequency the measured value corresponds to the estimated ones. The JFU method is offering solutions with over 30%, 45% and 55% lower than the other methods for the second third and fourth mode, respectively.

The analytical methods could be used in a pre-design procedure where a rapid approximation of the vibration modes is sufficient. Considering the results, the Rayleigh method would be the most suited for eigen frequencies estimation. The results are close to results obtained by FEM simulations and measured on the test bench. If the breathing mode frequency is required, the R&Y method is recommended, giving the closest result to the one obtained by FEM analysis.

6.6 Conclusions

The sixth chapter entitled has been focused on the calculation of the eigen frequencies of the stator of SRMs.

The chapter has identified the noise sources in SRDs. After acknowledging the deformation of the stator under the influence of the radial forces as to be the most important source of

Table 6.1: Eigen frequencies of the 8/6 SRM in Hz

Mode	R&Y	JFU	Rayleigh	FEM	Measurement
0	8072	7256	-	7853	-
2	-	1076	1596	1401	1434
3	-	2538	4513	4428	-
4	-	4057	8653	7482	-

noise in SRDs, it has been proceeded to the identification of the eigen frequencies of the stator structure. The frequencies have been analytically identified using three different approaches: Roark & Young method, Jordan, Fronhe & Uner method and Rayleigh method. Also, the frequencies have been calculated using FEM based softwares. The results of the three analytical methods and obtained by FEM have been compared to results obtained by measurements on the test bench.

The data measured on the test bench shows the greater influence of the even harmonics compared to the odd harmonics of the fundamental frequency of the phase on the noise generation and the second order eigen frequency of the stator has been identified.

The values of the zero mode frequency calculated with R&Y and by FEM analysis are close, but JFU method gives a result close to the others. Regarding second, third and fourth mode frequencies, Rayleigh method and FEM offer close solutions and in the case of the second order mode frequency the measurements are confirming the result. The JFU method is offering results with over 30%, 45% and 55% lower than the other methods for the second third and fourth mode, respectively.

For a fast presizing procedure, the Rayleigh method would be the most appropriate.

Chapter 7

Conclusions

World and European associations are implementing policies to reduce emissions from transportation. Personal and freight transportation is one of the key contributors in GHG emissions, being the second biggest GHG emitter after energy sector in the EU. The policies to reduce emissions from transportation are focusing on the optimization of the efficiency of the existing vehicles, the development of new sustainable fuels and propulsion systems and the electrification of the vehicles

New vehicle technologies like more electric vehicle, hybrid electric vehicle, plugged-in hybrid electric vehicle and electric vehicle have emerged in the goal of reaching zero emissions transportation.

The continuously increasing price of the permanent magnets and the shortage of rare earths demand the finding of alternatives for the permanent magnet synchronous machines which is currently the leading technology in several domains as hybrid and full electric propulsion and wind turbines due to their best overall performances.

The good efficiency and the large constant power-speed ratio in addition to low the cost, high reliability and fault-tolerance make the switched reluctance machine a candidate with real chances on the market of vehicle propulsion. The main drawbacks of the SRM related to the torque ripple, noise and vibration make the research object in R&Ds all over the world.

The main goal of the thesis has been to developed an efficient and robust SRD that can be integrated in a hybrid dive train or can be solely used for electric vehicle traction. To achieve this goal, different instantaneous and average torque control techniques have been implemented and compared. A converter has been designed, built and integrated on a test bench that allowed the testing of the control methods. The keen acoustic noise related issue of the SRDs was also studied.

The main contributions of the thesis and some recommendations for the future work are presented in the following sections.

7.1 Contributions

The second chapter has been focused on the electromagnetic characterization of SRMS by investigating the flux/current/rotor position characteristics. An accurate torque model of the

machine capable of eliminating the unwanted approximations and capable of providing a close to reality behaviour of the machine has been built based on the magnetization curves.

Firstly, a standard approach using 2D FEM has been used to determine the family of curves. Then, several experimental methods for finding the magnetization curves have been described, together with their advantages and shortcomings: AC method, flux linkage method and torque measurement method. The available measurement devices, incapable of measuring the true RMS values, are not taking into account the saturation of the magnetic circuit and thus, the AC method has not been performed. The flux linkage method measuring the falling current was preferred over the method measuring the rising current due to the inaccuracies introduced in the measurement by the voltage oscillations. A rotor blocking system for maintaining fixed the rotor position during measurements has been built.

The third chapter has been dealing with the control of the average torque of SRMs taking into consideration both motor and generator operation. The control parameters of the average torque controller (reference current, turn-on angle, turn-off angle) have been calculated using an optimization procedure for two different scenarios. This helps to eliminate the inaccuracies introduced by the analytical formulas describing the dependency of the control parameters on speed and torque. Through means of simulation and experimental results, the shortcomings of the open-loop average torque controller, mainly regarding the offset between the reference and the measured torque, have been shown.

To overcome these shortcomings, a closed loop control technique called direct average torque control has been implemented. For the implementation of the closed-loop average torque controller an on-line estimation of the average torque has been made on the basis of the coenergy per phase energy cycle. From simulation, good results have been shown in steady state, but slow torque response. The response can be increased 4 times by using the terminal quantities of all phases for the estimation. The observed torque ripple and the slow torque response make this method to be suited only for high speed where torque pulsations in SRMs are inevitable.

The generator operation of the SRM has been studied and the control parameters have been calculated using the same procedure as for motoring. The soft switching is not usable in generator operation and hard switching has been replaced with a hybrid technique reducing the switching frequency and thus the associated losses.

A speed controller has been implemented based on a proportional integral regulator to satisfy the road vehicle demand of cruise control option.

The fourth chapter has been presented the implementation of two closed-loop control techniques, namely direct instantaneous torque control and direct torque control, whose results are compared to the results obtained by using current profiling technique employing three different torque sharing functions.

DITC is developed on the basis of the paper of de Doncker. The issue of on-line estimation of the instantaneous torque is first addressed in the chapter, by describing three different estimation methods. The first uses the rotor position and the phase currents to estimate the torque. The second uses flux calculated on the basis of the terminal quantities and the rotor position to estimates torque. In the third, the need of knowing of rotor position is eliminated from the estimation by using the characteristics of torque as a function of phase current and flux linkage. In a similar way, by using the table of rotor position as a function of phase current and flux, a sensorless operation can be achieved on a limited range. A method to estimate the phase voltage using the switching signals and an inexpensive voltage sensor is also presented.

DITC is using the phase torque sharing principle without using precalculated torque sharing functions. The switching of the phase voltages is based on the hysteresis control of the total torque of the machine and the commutation of phases does not necessitate a precise knowledge of rotor position.

DTC makes an analogy between the AC rotating field machines and SRMs. Voltage vectors are defined for all phases and are further used for the definition of the switching vectors. An interesting discussion on how to choose the switching vector for all SRMs, regardless of the number of phases, is made.

The chapter ends with a comparison regarding torque ripple and copper losses between DTC and DITC on one hand and current profiling using three different torque sharing functions on the other hand. In terms of torque ripple both DTC and DITC have shown good results and both methods have been capable of eliminating the offset between the reference and the measured value of torque. In terms of copper losses DITC has shown slightly better results than profiling techniques, but the lack of a travelling field in the machine has led to higher losses when DTC was employed. The easy and rapid implementation on any type of SRM, without complex and time-consuming precalculations confers a substantial advantage of DITC and DTC over profiling techniques.

The fifth chapter entitled has been focused on the design and the construction of a converter for controlling the SRMs on a wide speed range. The chapter starts by classifying the converters by the number of switches per phase and by their commutation type. The classic asymmetric H-bridge topology has been chosen for supplying each phase due to the flexibility granted for the control. After choosing the semiconductor devices, the frequency stress and the losses on each device have been calculated. The losses have been introduced in the thermal model of the converter to find the thermal resistance of the heatsink.

The converter has been built, together with a whole test bench for testing SRMs also described in the chapter. As a load a DC machine has been preferred as a load because it could be used also as a torque meter. The brain of the system has been represented by a dSPACE 1103 commercially available prototyping tool and it has chosen due to its interfacing with MATLAB. By doing so, the researcher can focus on the development of the control rather than on writing software. The chapter ends with a discussion on the switching strategies employed in SRDs.

The sixth chapter entitled has been focused on the calculation of the eigen frequencies of the stator of SRMs. After the noise sources in SRDs have been identified and after acknowledging the deformation of the stator under the influence of the radial forces as to be the most important source of noise in SRDs, it has been proceeded to the identification of the eigen frequencies of the stator structure. The frequencies have been analytically identified using three different approaches: Roark & Young method, Jordan, Fronhe & Uner method and Rayleigh method. Also, the frequencies have been calculated using FEM based softwares. The results of the three analytical methods and obtained by FEM have been compared to results obtained by measurements on the test bench.

The data measured on the test bench shows the greater influence of the even harmonics compared to the odd harmonics of the fundamental frequency of the phase on the noise generation and the second order eigen frequency of the stator has been identified.

The values of the zero mode frequency calculated with R&Y and by FEM analysis are close, but JFU method gives a result close to the others. Regarding second, third and fourth mode frequencies, Rayleigh method and FEM offer close solutions and in the case of the second order

mode frequency the measurements are confirming the result. The JFU method is offering results with over 30%, 45% and 55% lower than the other methods for the second third and fourth mode, respectively. For a fast presizing procedure, the Rayleigh method would be the most appropriate.

7.2 Future Work

The SRDs proved to be a promising technology for electric propulsion power trains. As a continuation of the present work, some recommendation can be made for the future research.

Improvements of the efficiency of the whole drive should be made by means of multi-physics optimization.

Predictive torque control at constant switching frequency may be attempted for DITC to solve the problem of variable switching frequency of the hysteresis torque control which implies higher noise and higher commutation losses.

Solutions to one of the most stringent problems in SRDs, namely noise, can be brought by means of control. Thus, the influence of various control strategies on noise generation should be studied.

Regarding the test bench, te existing load should be replaced with anther capable of reaching greater torque and speed. The current prototyping tool should be replaced with an FPGA which allows higher sampling frequencies.

A stability study of the controller should be conducted in order to test its reliability.

Appendix A

Average Torque Control Drive Parameters

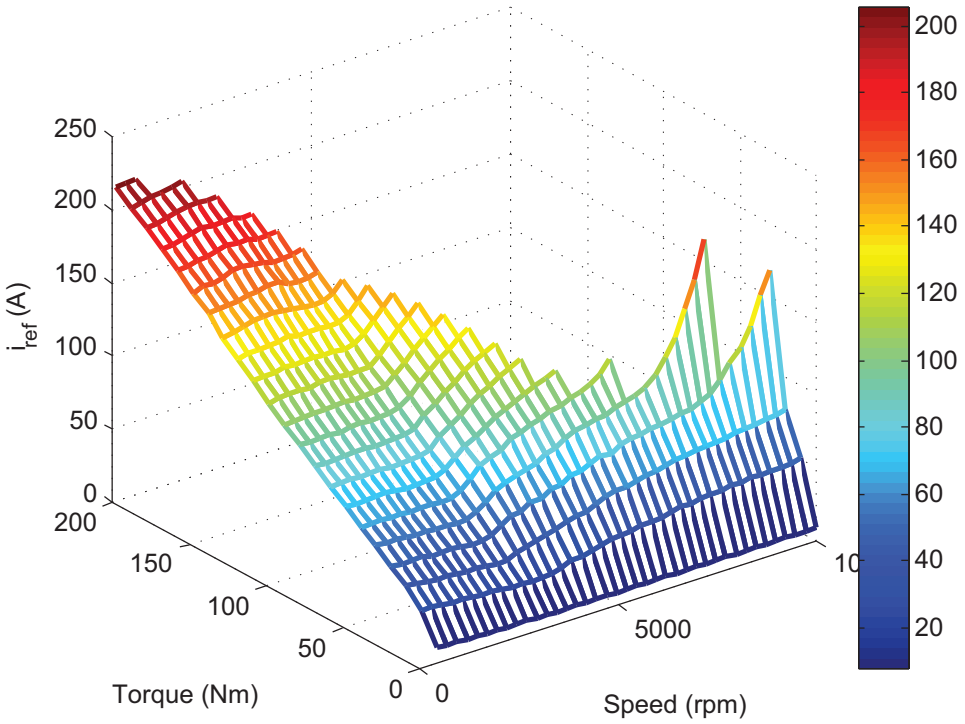

FIGURE A.1: Reference current versus torque and speed (scenario 1)

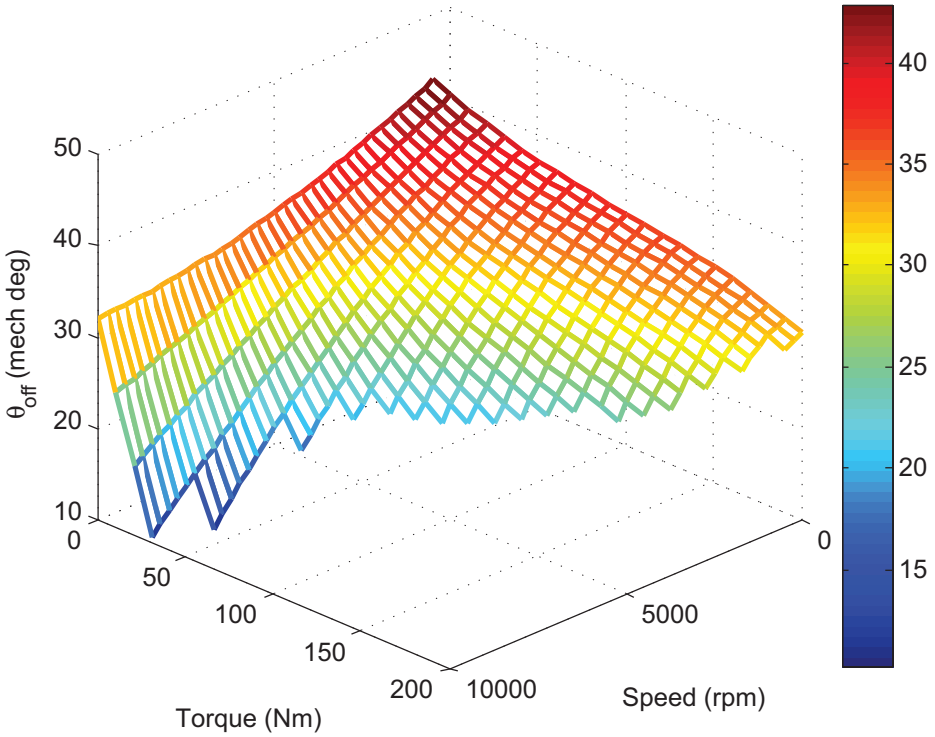

FIGURE A.2: Turn-on angle versus torque and speed (scenario 1)

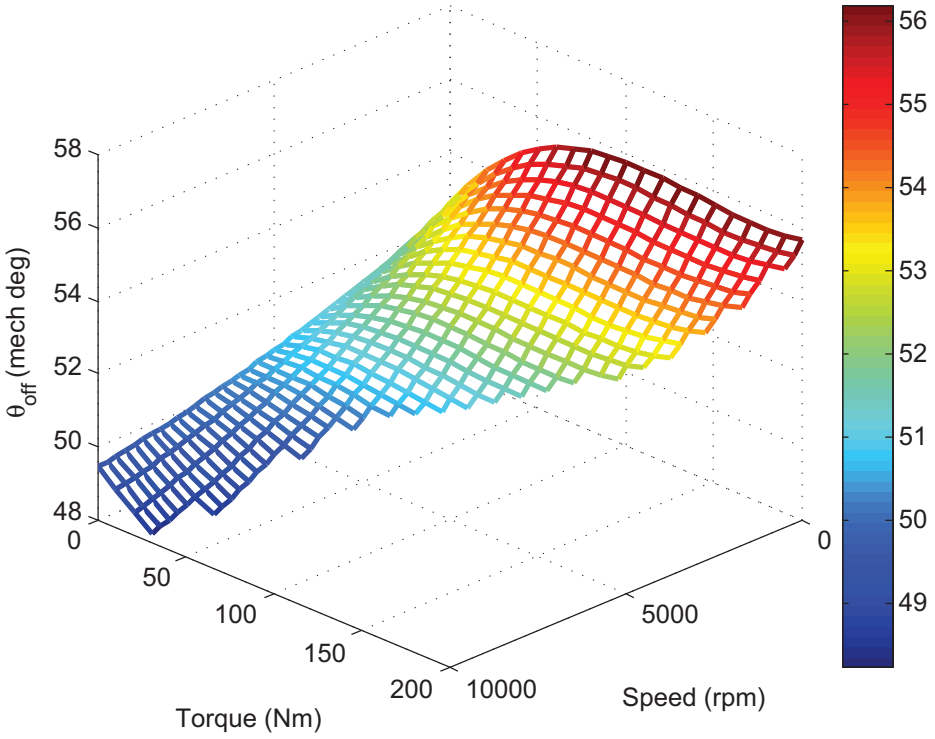

FIGURE A.3: Turn-off angle versus torque and speed (scenario 1)

Appendix B

Converter Types for SRMs

B.1 Dissipative Converters

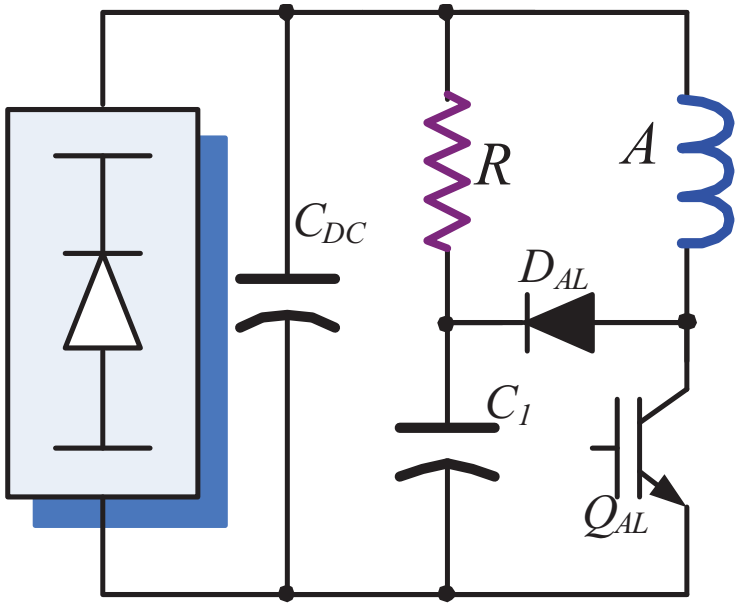

FIGURE B.1: Dissipative converter: R-dump [7]

B.2 Magnetic Converters

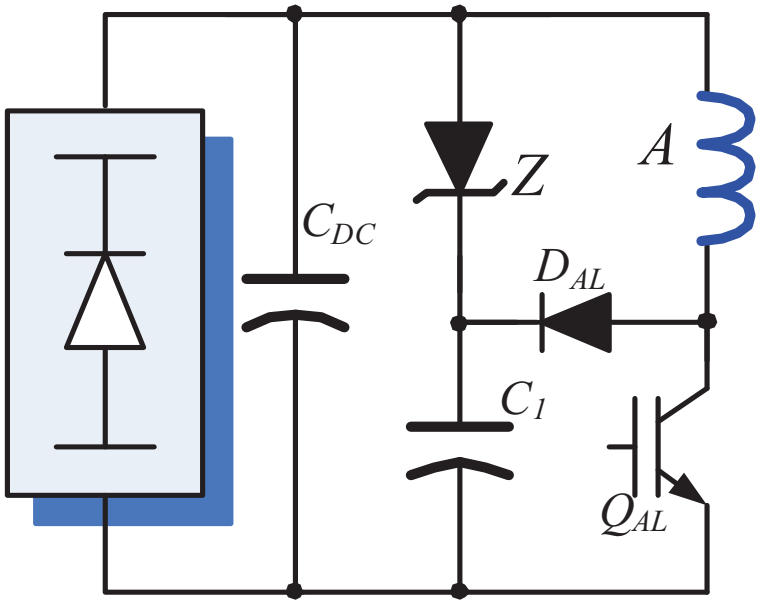

FIGURE B.2: Magnetic converter: single controllable switch [7]

B.3 Resonant Converters

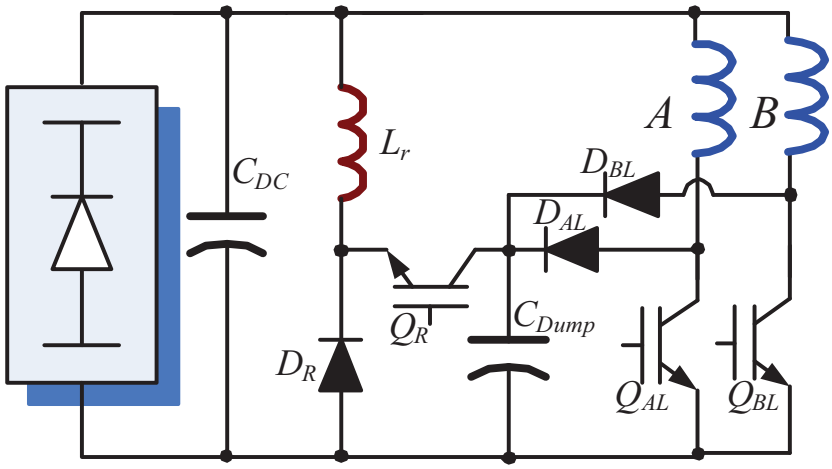

FIGURE B.3: Resonant converter: C-dump [7]

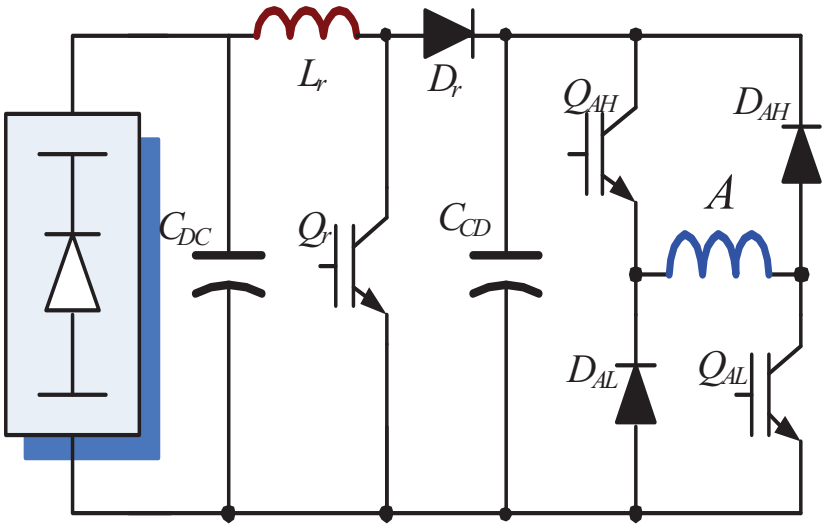

FIGURE B.4: Resonant converter: Boost [7]

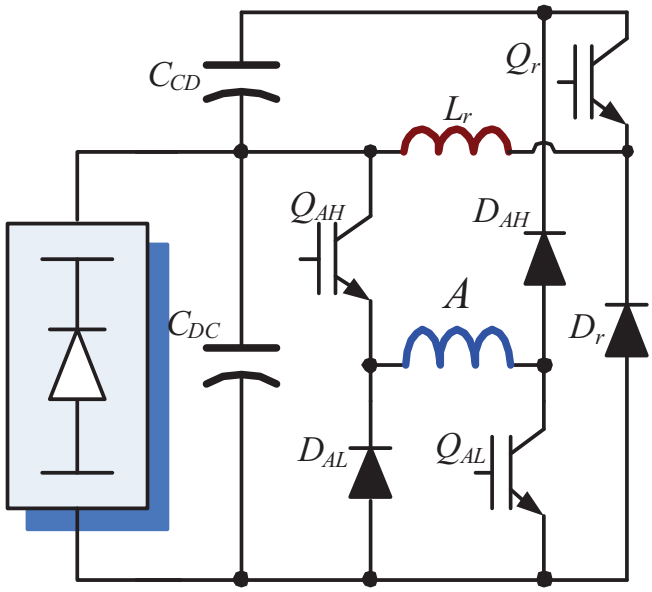

FIGURE B.5: Resonant converter: High demagnetization [7]

B.4 Capacitive Converters

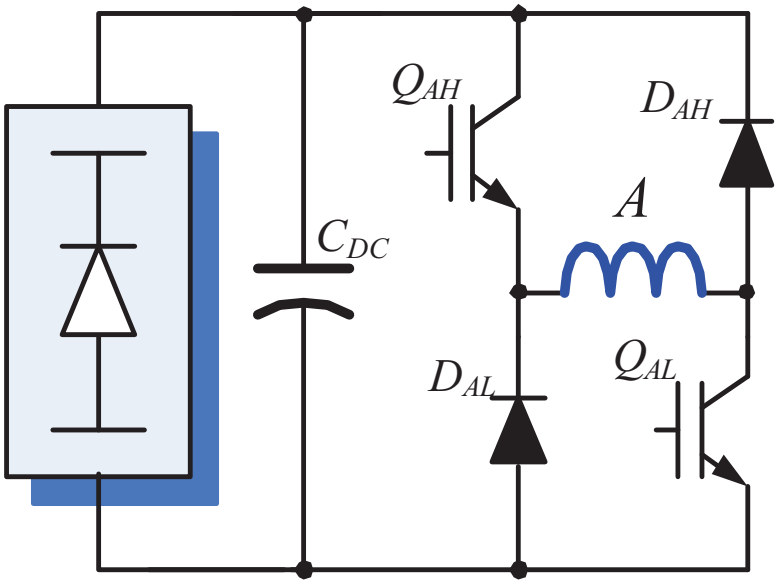

FIGURE B.6: Single-capacitor converter: Asymmetric H-bridge [7]

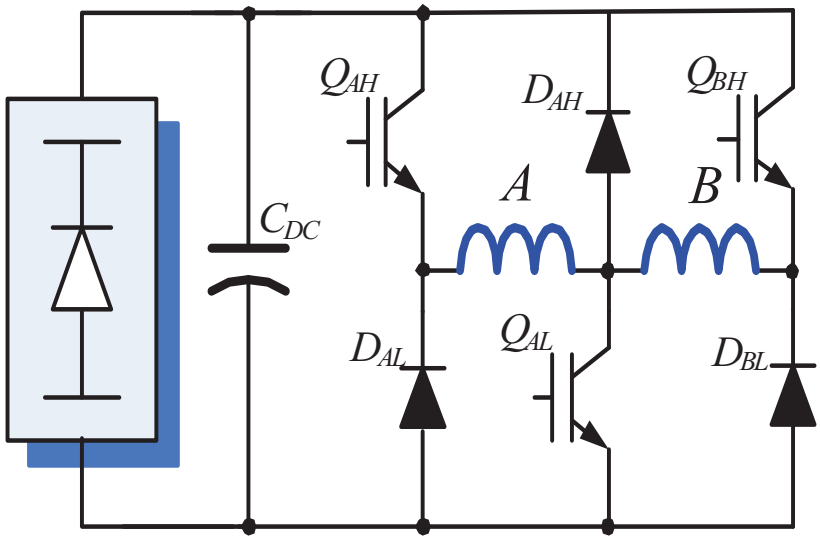

FIGURE B.7: Single-capacitor converter: Shared switch [7]

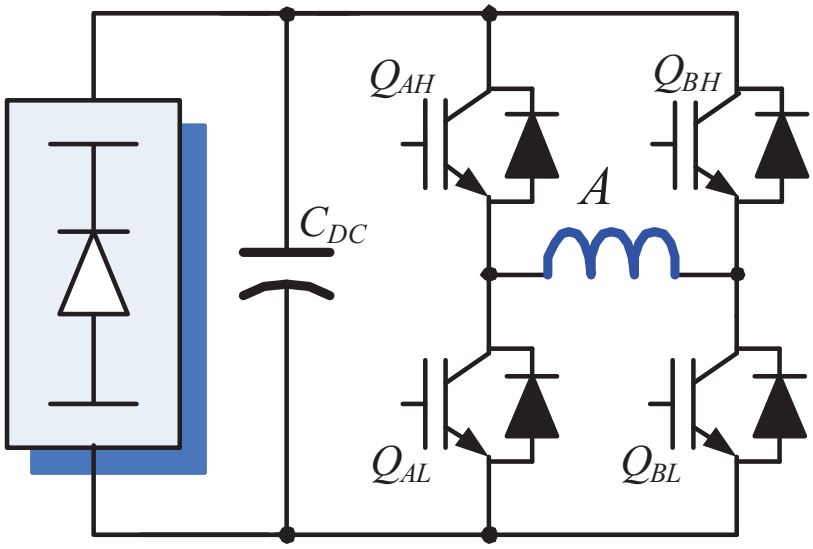

FIGURE B.8: Single-capacitor converter: H-bridge [7]

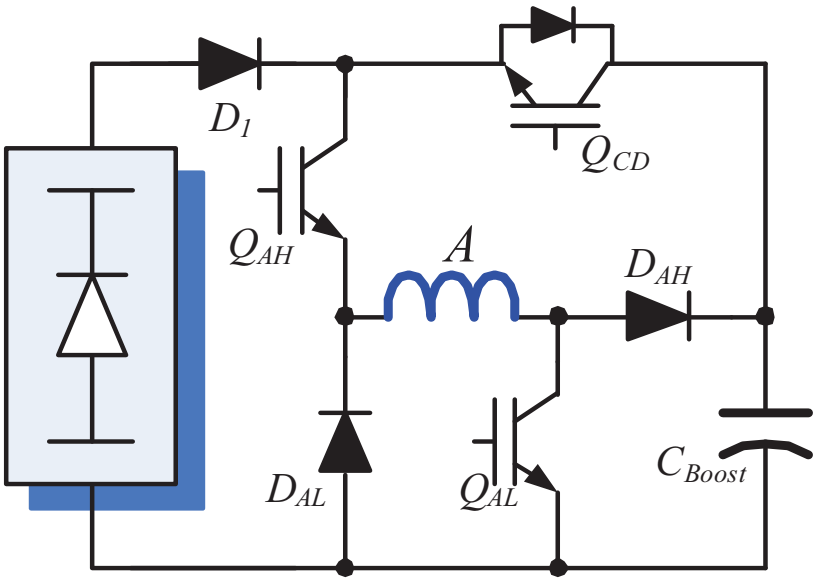

FIGURE B.9: Single-capacitor converter: Modified C-dump [7]

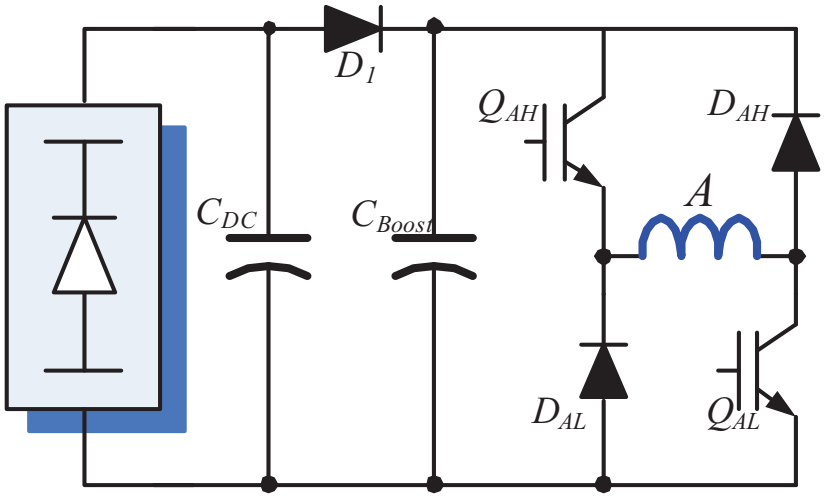

FIGURE B.10: Passive boost with two capacitors: Parallel type [7]

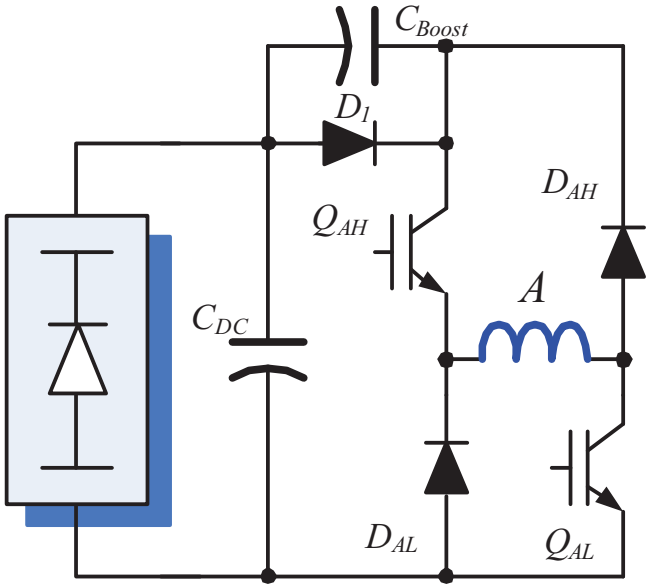

FIGURE B.11: Passive boost with two capacitors: Series type [7]

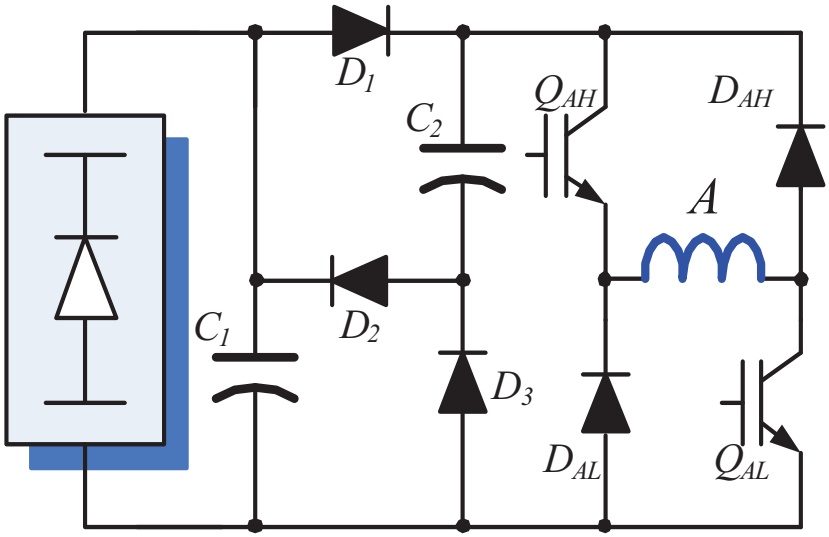

FIGURE B.12: Passive boost with two capacitors: Series-parallel type [7]

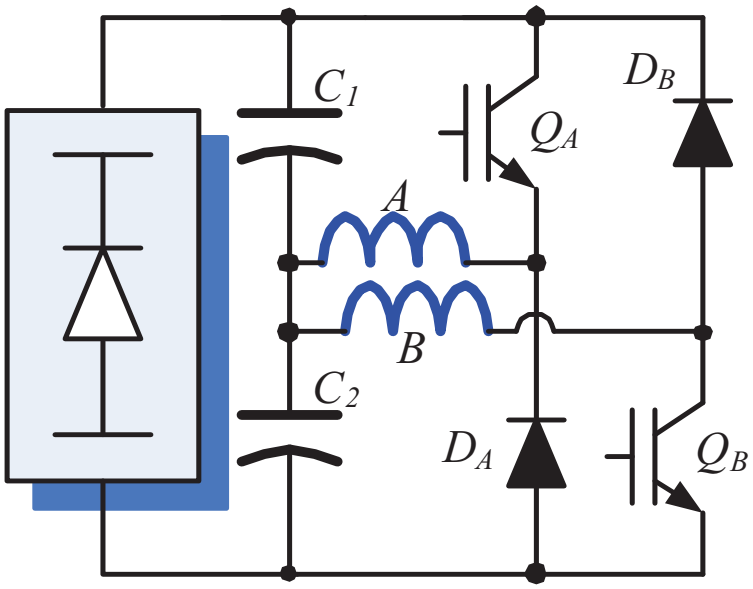

FIGURE B.13: Series type passive converter: Split DC-link [7]

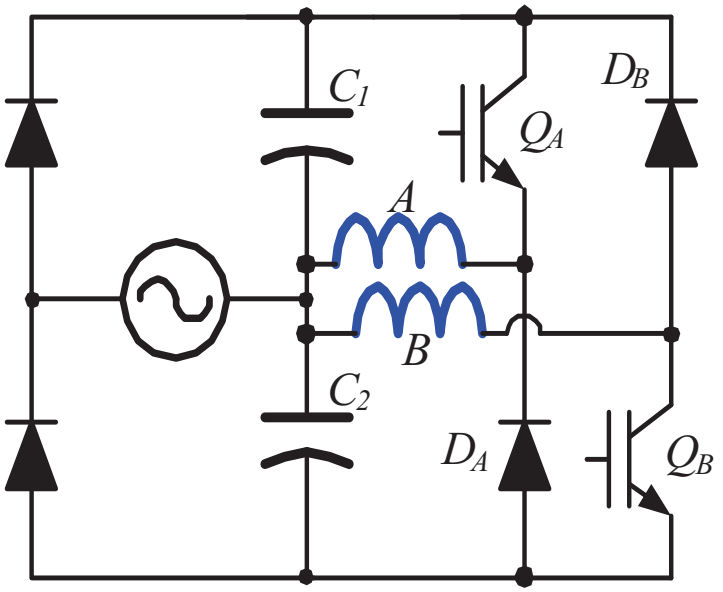

FIGURE B.14: Series type passive converter: Doubler DC-link [7]

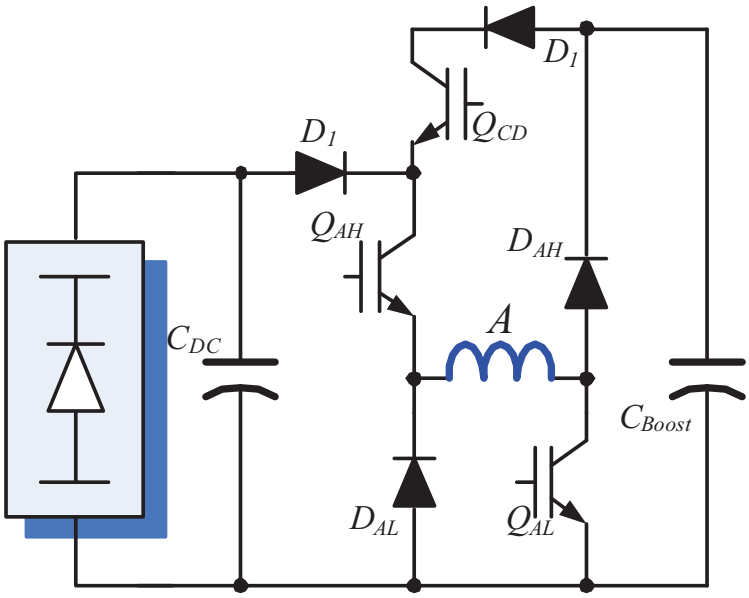

FIGURE B.15: Active boost converter: Parallel type 1 [7]

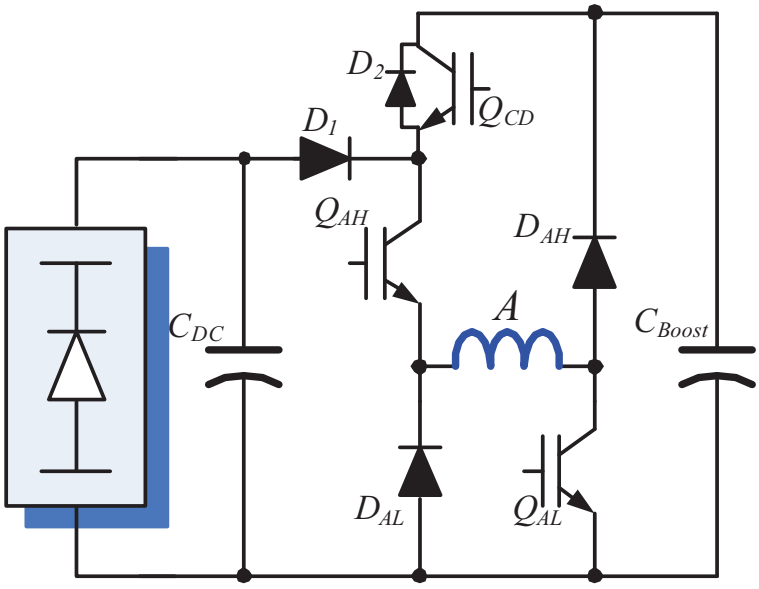

FIGURE B.16: Active boost converter: Parallel type 2 [7]

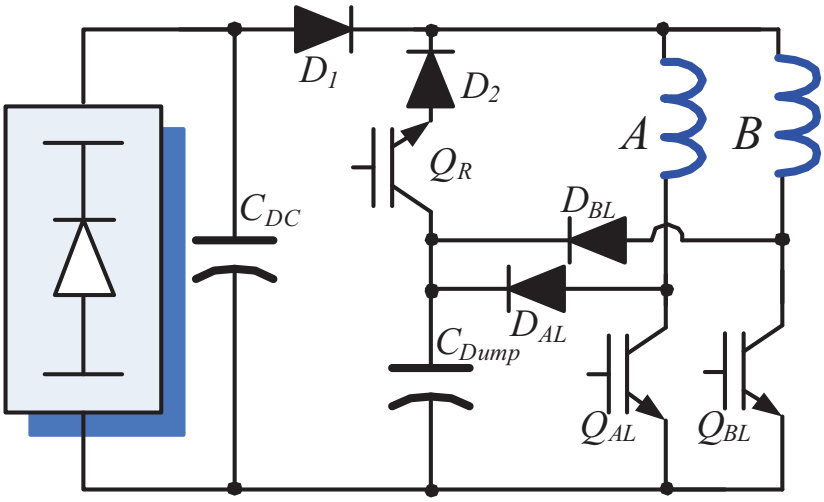

FIGURE B.17: Active boost converter: Parallel type 3 [7]

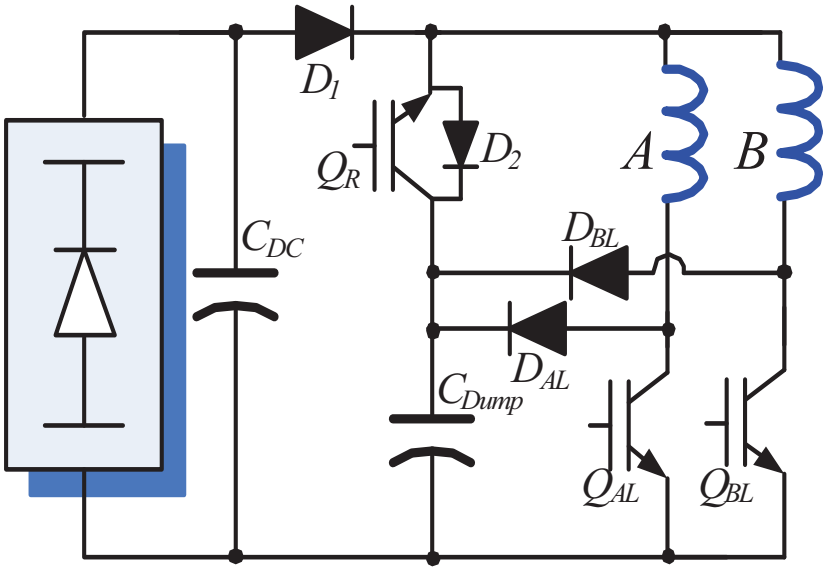

FIGURE B.18: Active boost converter: Parallel type 4 [7]

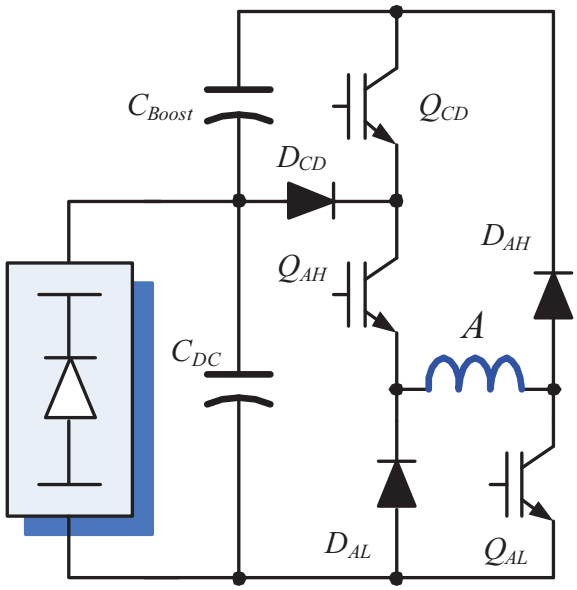

FIGURE B.19: Active boost converter: Series type [7]

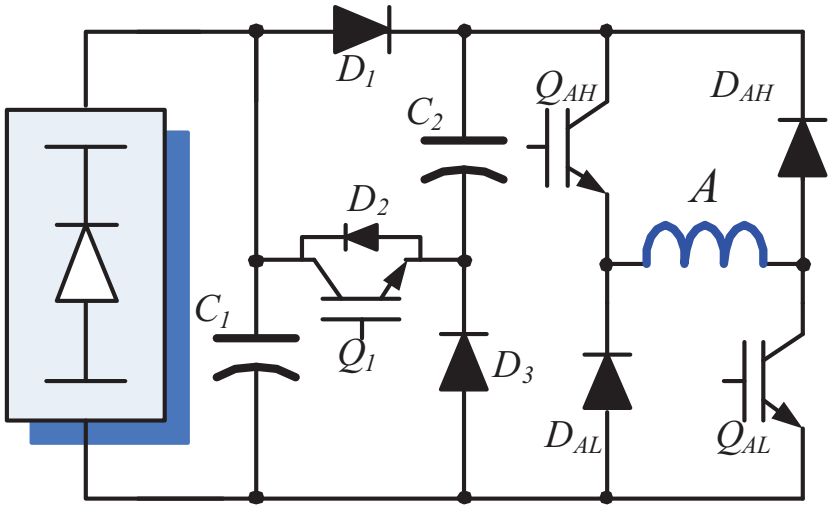

FIGURE B.20: Active boost converter: Series-parallel type [7]

Appendix C

Control Desk Interfaces

Appendix C presents the interfaces built in ControlDesk for all control strategies implemented, namely hysteresis control in Fig. C.1, DATC in Fig. C.2, DITC in Fig. C.3, DTC in Fig. C.4 and current profiling in Fig. C.5, respectively.

In all five figures it can be seen that both the SRM and the DC machine used as load can be torque or speed controlled. The choice for the control type is made manually. A virtual LED is used for both machine to indicate the time when the machines are on (green) or off (red). For the DC machine quantities like excitation current, armature current and armature DC-bus voltage are permanently supervised. The resistive torque is calculated as the sum of the friction torque of the system and the electromagnetic torque of the DC machine. For the control of the SRM, the quantities that have to be supervised are the DC-bus voltage, the rotor position. The phase currents and the instantaneous torque are visualized in real time in the upper-left corner. A manual procedure for the alignment of the rotor has been implemented

The hysteresis control in Fig. C.1 was used to study the influence of the reference torque and firing angles on the torque production. These quantities can be modified on-line. In the lower-right corner the current on one phase and the torque produced by that phase are to be observed.

In the lower-right corner from the DATC in Fig. C.2 one phase voltage and the corresponding phase current are measured. From these quantities, the electrical energy and the average torque are further estimated.

In the lower-right corner from the DITC in Fig. C.3, one phase current and the corresponding phase torque can be observed.

The DTC in Fig. C.4 besides the phase currents and instantaneous torque allows the visualisation in real time of the flux vector amplitude and the flux vector trajectory.

For the current profiling in Fig. C.5 the reference current can be seen and compared to the real shape of the phase current.

The ControlDesk software permits the visualisation and the real-time control of all parameters and quantities.

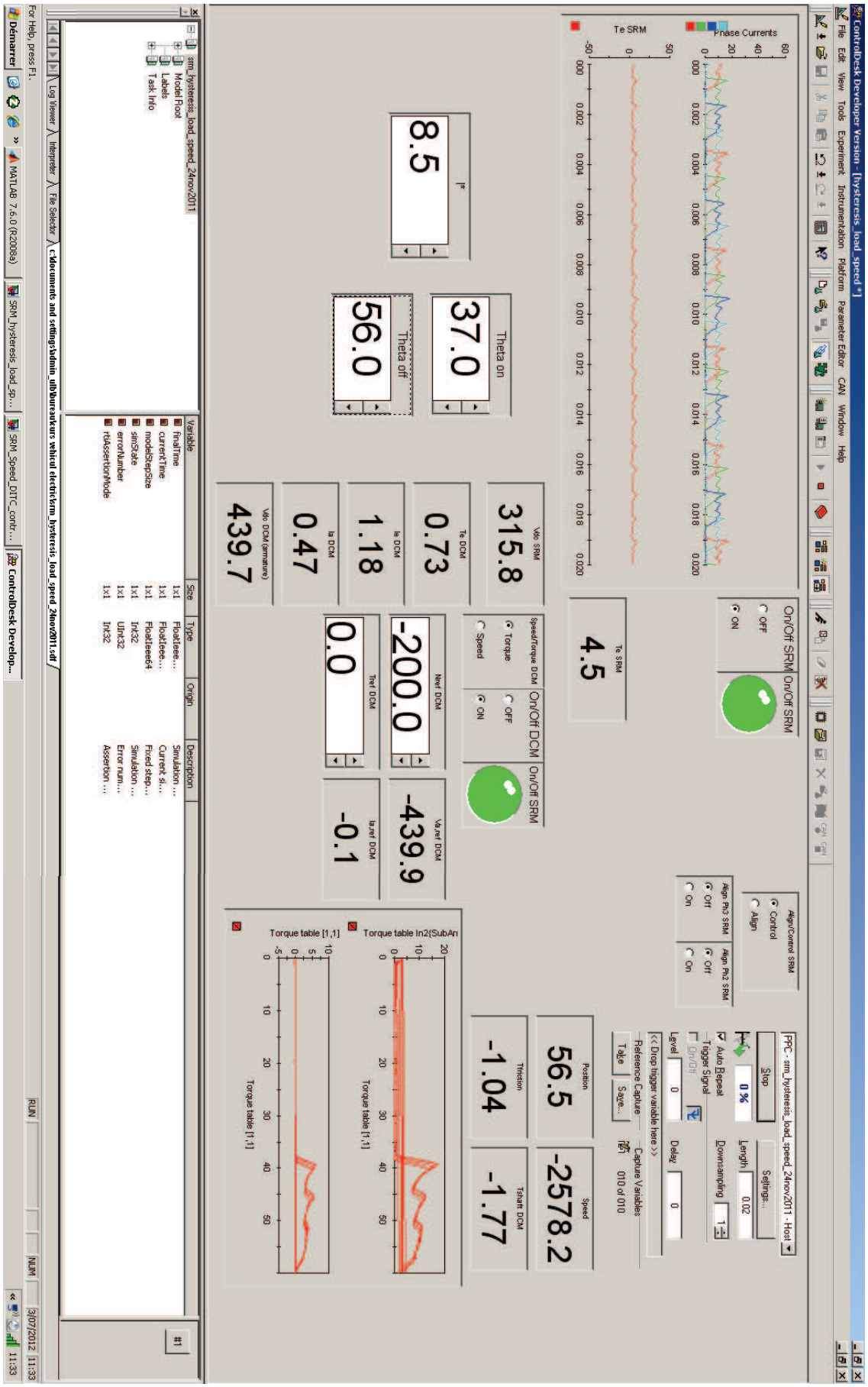

FIGURE C.1: Control Desk Interface: Hysteresis control

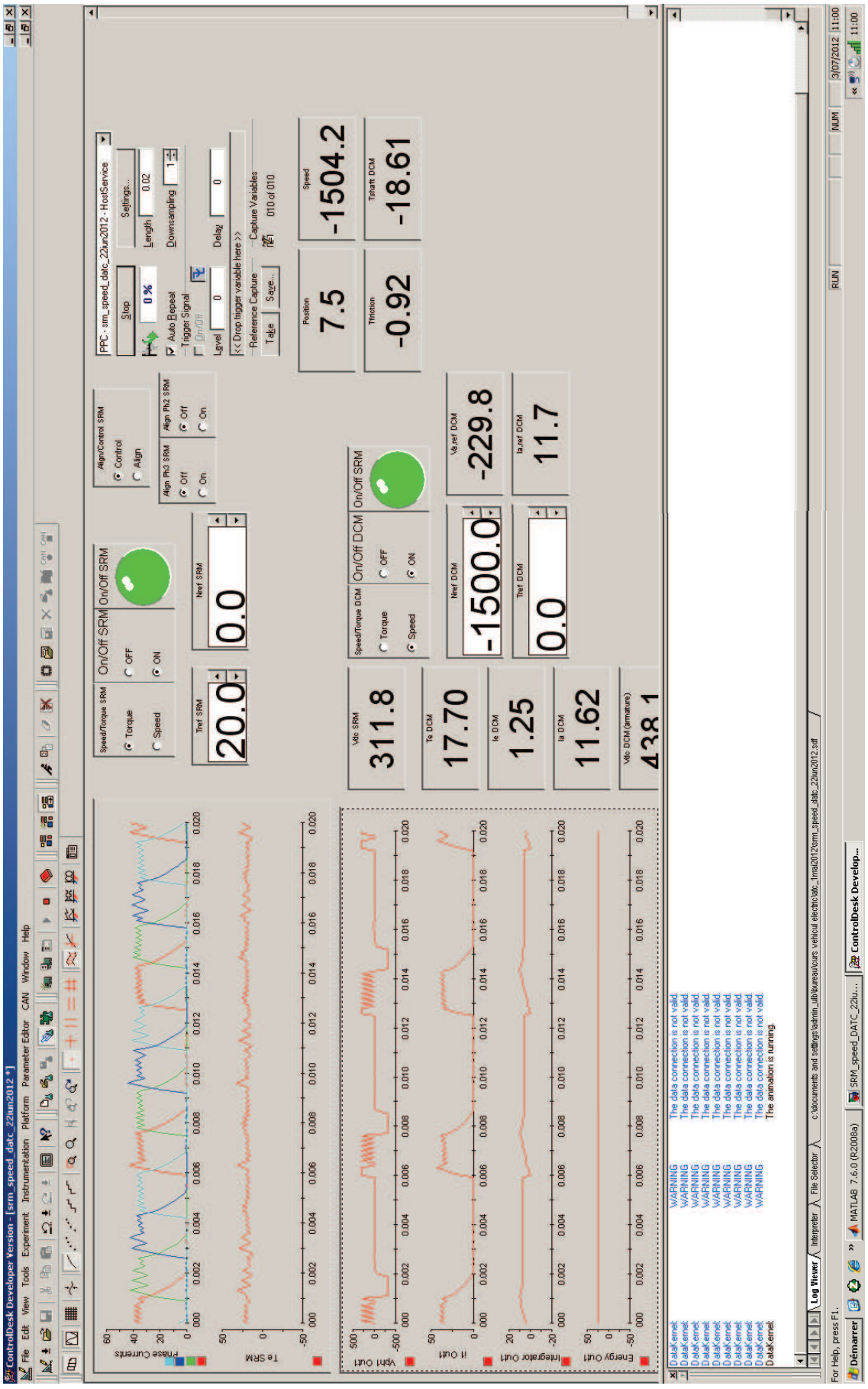

FIGURE C.2: Control Desk Interface: DATC

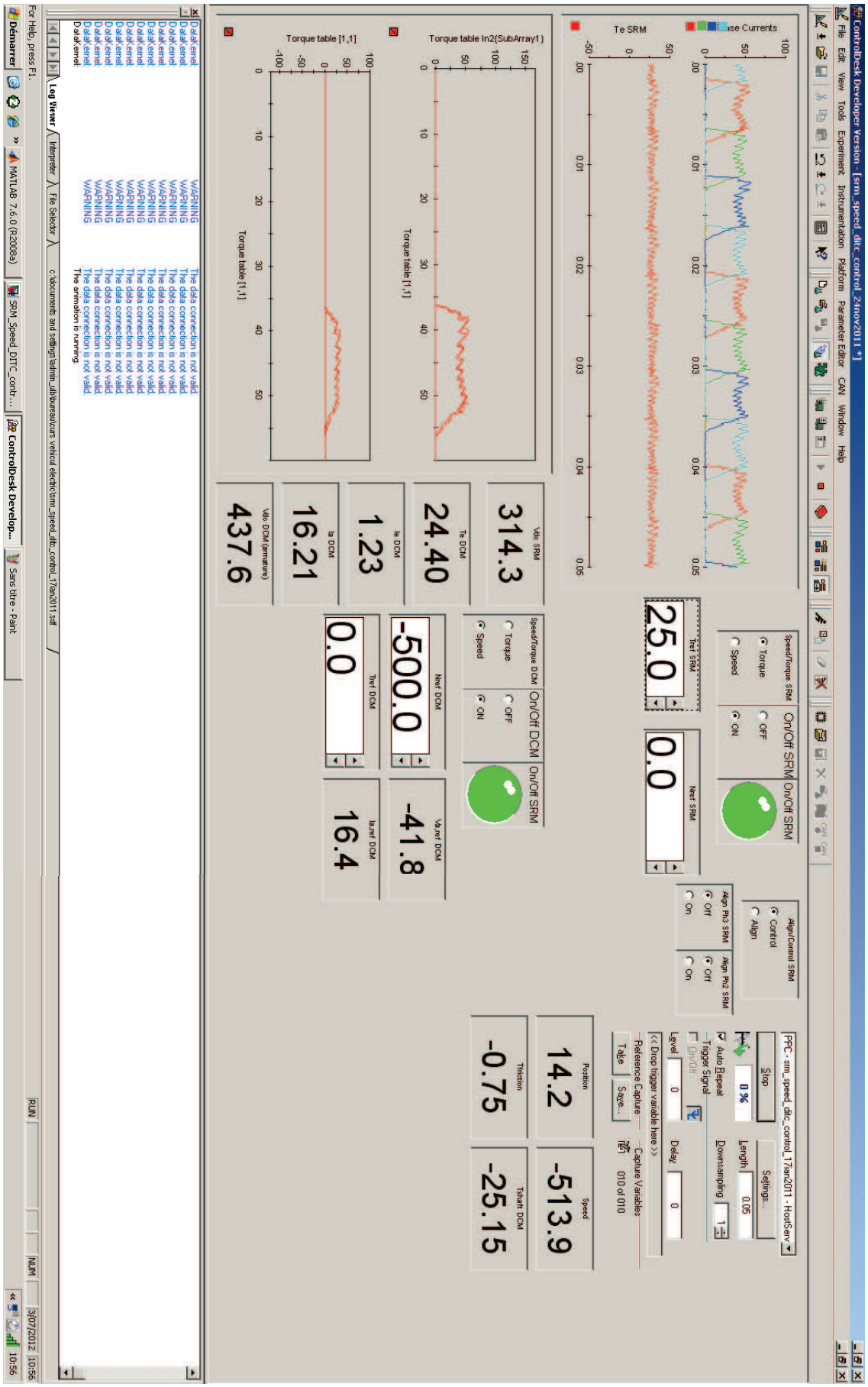

FIGURE C.3: Control Desk Interface: DITC

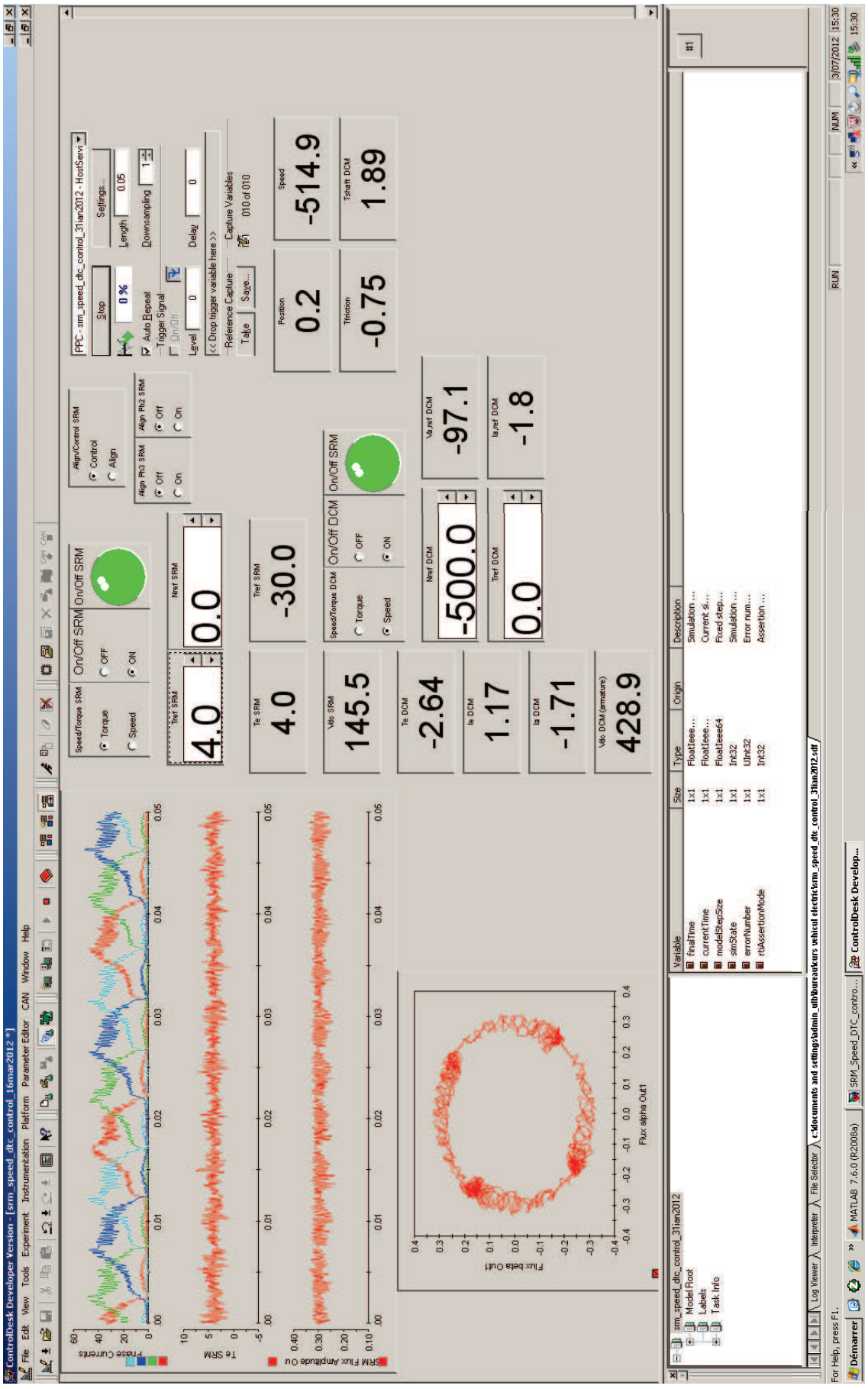

FIGURE C.4: Control Desk Interface: DTC

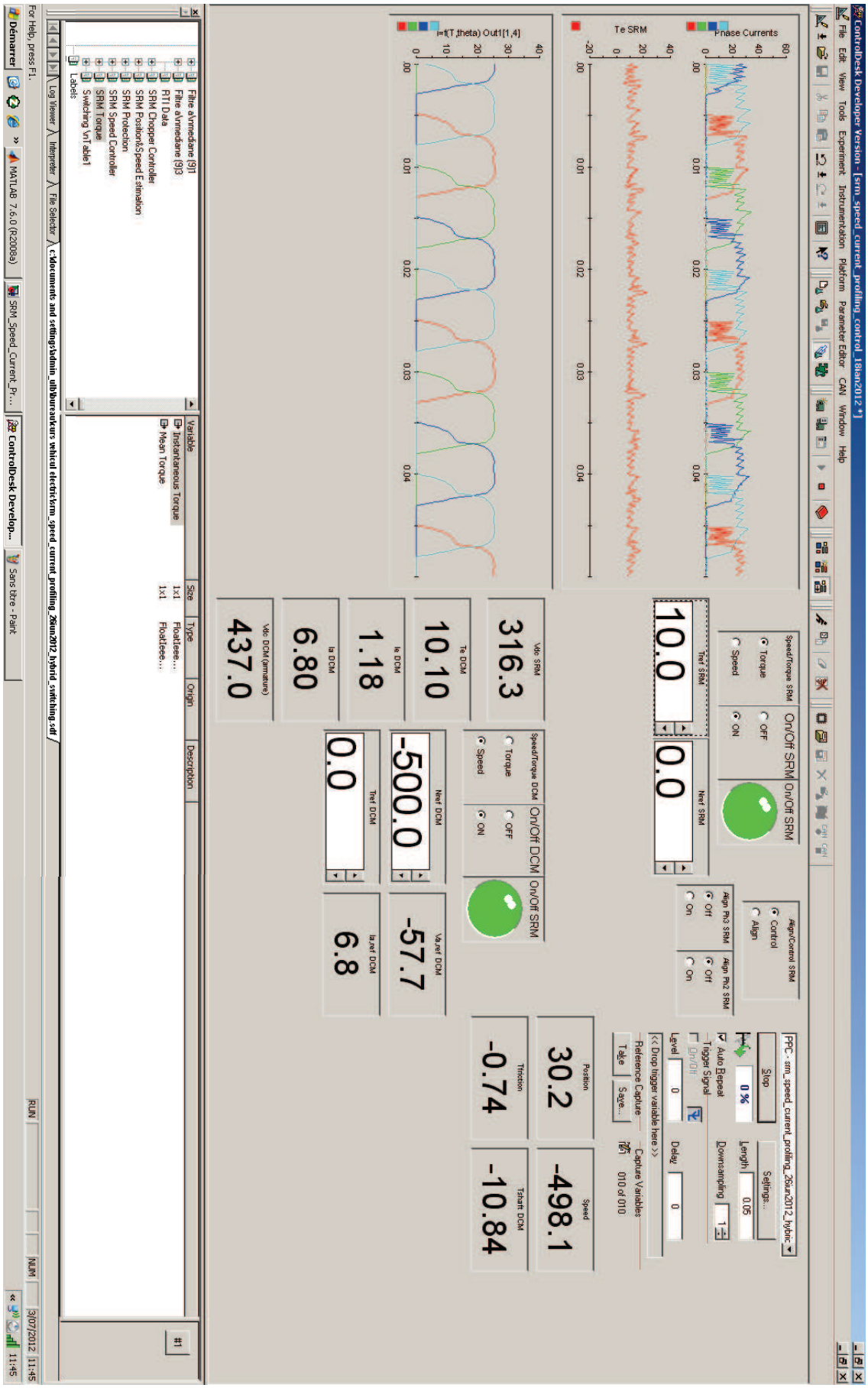

FIGURE C.5: Control Desk Interface: Current profiling

Appendix D

Superior Vibration Modes of the Stator Structure

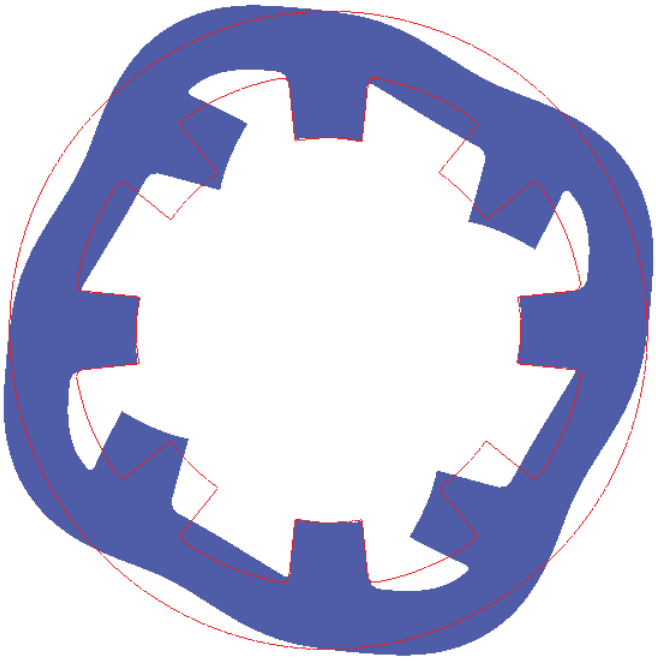

FIGURE D.1: Vibration mode corresponding to 9053Hz

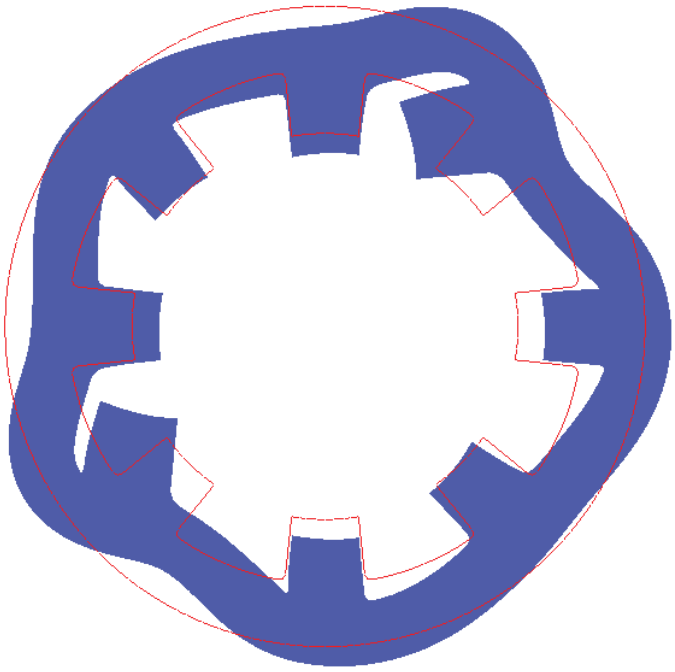

FIGURE D.2: Vibration mode corresponding to 11527Hz

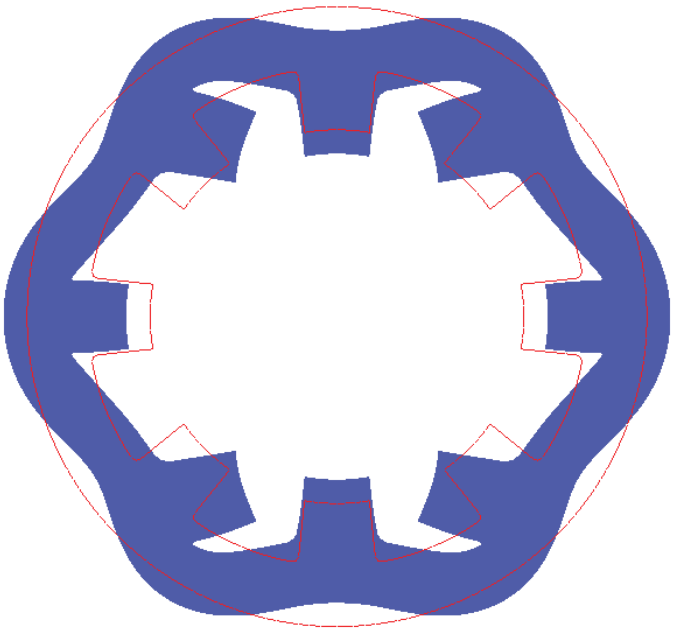

FIGURE D.3: Vibration mode corresponding to 12778Hz

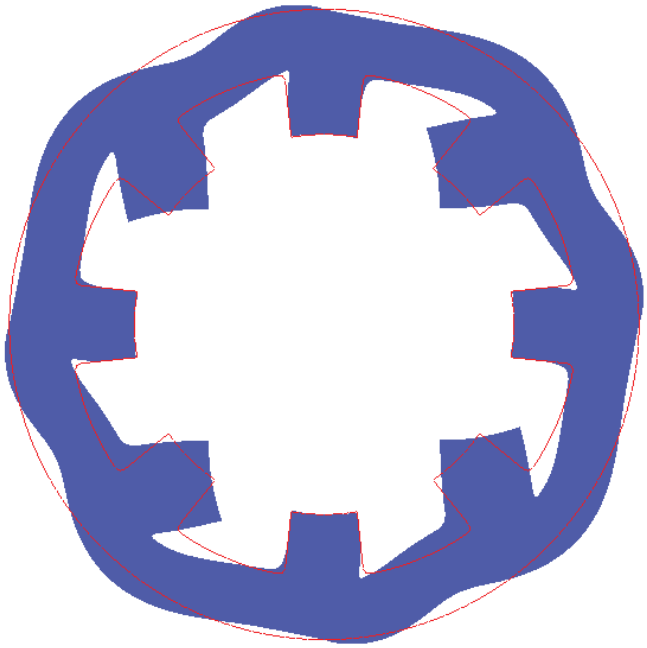

FIGURE D.4: Vibration mode corresponding to 19388Hz

Bibliography

[1] (2012) Ec dg climate action. [Online]. Available: http://ec.europa.eu/clima/policies/transport/index_en.htm

[2] A. Emadi, "Transportation 2.0," *IEEE Power and Energy Magazine*, vol. 9, pp. 18–29, 2011.

[3] T. J. E. Miller, *Electronic Control of Switched Reluctance Machines*. Newnes, 2001.

[4] R. B. Inderka and R. W. D. Doncker, "High dynamic direct average torque control for swiched reluctance drives," *Thirty-Sixth IAS Annual Meeting*, vol. 3, pp. 2111 – 2115, 2001.

[5] R. Krishnan, *Switched Reluctance Motor Drives Modelling, Simulation, Analysis, Design and Applications*. CRC Press, 2001.

[6] M. Barnes and C. Pollock, "Power electronic converters for switched reluctance drives," *IEEE Transactions on Power Electronics*, vol. 13, pp. 1100 – 1111, 1998.

[7] J. W. Ahn, J. Liang, and D. H. Lee, "Classification and analysis of switched reluctance converters," *Journal of Electrical Engineering and Technology*, vol. 5, pp. 571 –579, 2010.

[8] "Annual european union greenhouse gas inven-tory 19902010 and inventory report 2012," European Environment Agency, Tech. Rep. 3/2012, May 2012.

[9] J. Fuglstvedt, T. Berntsen, G. Myhre, K. Rypdal, and R. B. Skeie, "Climate forcing from the transport sector," *Proceedings of the National Acacdemy of Sciences of the United States of America, PNAS*, vol. 105, pp. 454 – 458, 2008.

[10] M. Ehsani, Y. Gao, and A. Emandi, *Modern Electric, Hybrid Electric, and Fuell Cell Vehicles: Fundamentals, Theory, and Design*, 2nd ed. CRC Press, 2010.

[11] I. Husain, *Electric and Hybrid Vehicles: Design Fundamentals*. CRC Press, 2003.

[12] M. Zeraoulia, M. E. H. Benbouzid, and D. Diallo, "Electric motor drive selection issues for hev propulsion systems: A comparative study," *IEEE Transactions on Vehicular Technology.*, vol. 55, pp. 1756 – 1764, 2006.

[13] A. Radun, "Analytical calculation of the switched reluctance motor's unaligned inductance," *IEEE Transactions on Magnetics*, vol. 35, pp. 4473 – 4481, 1999.

[14] ——, "Analytically computing the flux linked by a switched reluctance motor phase when the stator and rotor poles overlap," *IEEE Transactions on Magnetics*, vol. 36, pp. 1996 – 2003, 2000.

[15] S. A. Hossain and I. Husain, "A geometry based simplified analytical model of switched reluctance machines for real-time controller implementation," *IEEE Transactions on Power Electronics*, vol. 18, pp. 1384 – 1389, 2003.

[16] I. A. Viorel, L. Strete, and I. F. Soran, "Analytical flux linkage model of switched reluctance motor," *Revue Roum. de Science et Technique, Electrotechnique et Energetique*, vol. 54, pp. 139–146, 2009.

[17] L. Strete, I. Husain, O. Cornea, and I. A. Viorel, "Direct and inverse analytical models of a switched reluctance motor," *CEFC 2010*, 2010.

[18] C. L. Xia, M. Xue, and T. N. Shi, "A new rapid nonlinear simulation method for switched reluctance motors," *IEEE Transactions on Energy Conversion*, vol. 24, pp. 578–586, 2009.

[19] B. Parreira, S. Rafael, A. J. Pires, and P. J. C. Branco, "Obtaining the magnetic characteristics of an 8/6 swiched reluctance machine: from fem analysis to the experimental results," *IEEE Transactions on Industrial Electronics*, vol. 52, pp. 1635 – 1643, 2005.

[20] C. Roux and M. M. Morcos, "A simple model for switched reluctance motors," *IEEE Transactions on Energy Conversion*, vol. 136, pp. 400 – 405, 2005.

[21] T. J. E. Miller, *Switched Reluctance Motors and Their Control*, M. P. Publishing, Ed., 1993.

[22] R. Krishnan and P. Materu, "Measurement and instrumentation of a switched reluctance motor," *Conference Record of the 1989 IEEE Industry Applications Society Annual Meeting*, vol. 1, pp. 116 – 121, 1989.

[23] C. S. Dragu and R. Belmans, "Measurement of magnetic characteristics of switched reluctance motor," *10th European Conference on Power Electronics and Applications (EPE 2003)*, 2003.

[24] A.-C. Pop, V. Petrus, J. Gyselinck, and C. S. Martis, "Parameter identification and 2d fe modeling of existing switched reluctance motors," *Sixth international conference and exihibtion on ecological vehicles and renewable energies EVER2011*, 2011.

[25] A. Ferrero, A. Raciti, and C. Urzi, "An indirect test method for the caracterization of variable reluctance motors," *IEEE Transactions on Instrumentation and Measurement*, vol. 42, pp. 1020 – 1025, 1993.

[26] P. Chancharoensook and M. F. Rahman, "Determination of magnetisation and static torque characteristics of a four-phase swiched reluctance motor: experimental investigations," *Fourth IEEE Conference on power electronics and drive systems*, 2001.

[27] V. Ramanarayanan, I. Venkatesha, and D. Panda, "Flux-linkeage characteristics of swiched reluctance motor," *Proc. Int. Conf. Power Electron., Drives Energy Syst. Ind. Growth*, 1996.

[28] V. K. Sharma, S. S. Murthy, and B. Singh, "An improved method for the determination of saturation characteristics of switched reluctance motors," *IEEE Transactions on Instrumentation and Measurement*, vol. 48, pp. 995 – 1000, 1999.

[29] G. Henneberger and I. A. Viorel, *Variable Reluctance Electrical Machines*, S. Verlag, Ed. Aachen, 2001.

[30] I. Boldea, *Variable Speed Generators*. CRC Press, 2005.

[31] R. B. Inderka, M. Menne, and R. W. D. Doncker, "Control of swiched reluctance drives for electric vehicle applications," *IEEE Transactions on Industrial Electronics*, vol. 49, pp. 48 – 53, 2002.

[32] C. Mademlis and I. Kioskeridis, "Performance optimization in switched reluctance motor drives with online commutation angle control," *IEEE Transactions on Energy Conversion*, vol. 3, pp. 448–457, 2003.

[33] I. Kioskeridis and C. Mademlis, "Maximum efficiency in single-pulse controlled switched reluctance motor drives," *IEEE Transactions on Energy Conversion*, vol. 20, pp. 809 – 817, 2005.

[34] C. S. Dragu and R. Belmans, "Optimal firing angles control for four-quadrant operation of an 8/6 srm," *10th European Conference on Power Electronics and Applications*, 2003.

[35] ——, "Four-quadrant control of an 8/6 switched reluctance motor," *4th International symposium on advanced electromechanical motion systems-ELECTROMOTION*, vol. 2, pp. 455–460, 2001.

[36] A.-C. Pop, V. Petrus, J. Gyselinck, C. S. Martis, and V. Iancu, "On the firing angles control of a 8/6 switched reluctance machine," *Journal of Electrical and Electronics Engineering*, vol. 4, pp. 189–194, 2011.

[37] B. K. Bose, T. J. E. Miller, P. M. Szczesny, and W. H. Bicknell, "Microcomputer control of switched reluctance motor," *IEEE Transactions on Industrial Applications*, vol. IA-22, pp. 708 – 715, 1985.

[38] J. J. Gribble, P. C. Kjaer, and T. J. E. Miller, "Optimal commutation in average torque control of switched reluctance motors," *IEE Proceedings - Electric Power Applications*, vol. 146, pp. 2–10, 1999.

[39] B. Blanque, J. I. Perat, P. Andrada, and M. Torrent, "Improving efficiency in switched reluctance motor drives with online control of turn-on and turn-off angles," *European Conference on Power Electronics and Applications*, 2005.

[40] P. Andrada, B. Blanque, J. I. Perat, M. Torrent, E. Martinez, and J. A. Snchez, "Conmparative efficiency of switched reluctance and induction motor drives for slowly varying loads," *ICREPQ06*, 2006.

[41] C. Mademlis and I. Kioskeridis, "Smooth transition between optimal control modes in switched reluctance motoring and generating operation," *International Conference on Power Systems Transients, IPST07*, 2007.

[42] ——, "Four-quadrant smooth torque controlled switched reluctance machine drives," *IEEE Power Electronics Specialists Conference, PESC 2008.*, pp. 1216 – 1222, 2008.

[43] R. Orthmann and H. P. Schoner, "Turn-off angle control of switched reluctance motors for optimum torque output," *Fifth European Conference on Power Electronics and Applications*, vol. 6, pp. 20 – 25, 1993.

[44] P. C. Kjaer, P. Nielsen, L. Andersen, and F. Blaabjerg, "A new energy optimizing control strategy for switched reluctance motors," *IEEE Transactions on Industry Applications*, vol. 31, pp. 1088 – 1095, 1995.

[45] A. M. Omekanda, "A new technique for multidimensional performance optimization of switched reluctance motors for vehicle propulsion," *IEEE Transactions on Industry Applications*, vol. 39, pp. 672 – 676, 2003.

[46] J. H. Fisch, Y. Li, P. C. Kjaer, J. J. Gribble, and T. J. E. Miller, "Pareto-optimal firing angles for switched reluctance motor control," *Second International Conference On Genetic Algorithms in Engineering Systems: Innovations and Applications, GALESIA 97*, pp. 90 – 96, 1997.

[47] A.-C. Pop, V. Petrus, J. Gyselinck, C. S. Martis, and V. Iancu, "Wide-speed range control strategy for a 8/6 switched reluctance machine," *ACEMP & Electromotion Joint Conference*, 2011.

[48] R. B. Inderka and R. W. D. Doncker, "High dynamic direct average torque control for swiched reluctance drives," *IEEE Transactions on Industry Applications*, vol. 39, pp. 1040 – 1045, 2003.

[49] D. A. Torrey, "Variable-reluctance generators in wind-energy systems," *24th Annual IEEE Power Electronics Specialists Conference, PESC '93*, pp. 561 – 567, 1993.

[50] ——, "Switched reluctance generators and their control," *IEEE Transactions on Industrial Electronics*, vol. 49, pp. 3 – 14, 2002.

[51] R. Cardenas, W. F. Ray, G. M. Asher, and P. Wheeler, "Switched reluctance generators for wind energy applications," *26th Annual IEEE Power Electronics Specialists Conference, PESC '95*, vol. 1, pp. 559 – 564, 1995.

[52] R. Cardenas, R. Pena, M. Perez, J. Clare, G. Asher, and P. Wheeler, "Control of a switched reluctance generator for variable-speed wind energy applications," *IEEE Transactions on Energy Conversion*, vol. 20, pp. 781 – 791, 2005.

[53] S. R. McMinn and W. D. Jones, "Control of a switched-reluctance aircraft engine starter-generator over a very wide speed range," *Proceedings of the 24th Intersociety Energy Conversion Engineering Conference, IECEC-89*, vol. 1, pp. 631 – 638, 1989.

[54] D. E. Cameron and J. H. Lang, "The control of high-speed variable-reluctance generators in electric power systems," *IEEE Transactions on Industry Applications*, vol. 29, pp. 1106 – 1109, 1993.

[55] A. Radun, "Generating with the switched reluctance motor," *Ninth Annual Applied Power Electronics Conference and Exposition, APEC '94*, vol. 1, pp. 41 – 47, 1994.

[56] J. M. Kokernak and D. A. Torrey, "A switched reluctance starter/ alternator for hybrid electric vehicles," *PCIM'99*, pp. 74 – 80, 1999.

[57] P. Zhang and S. S. Williamson, "Recent status and future prospects of integrated starter-generator based hybrid electric vehicles," *IEEE Vehicle Power and Propulsion Conference, VPPC '08.*, vol. 58, pp. 1 – 8, 2008.

[58] N. Schofield and W. D. Jones, "Generator operation of a switched reluctance starter/generator at extended speeds," *IEEE Transactions on Vehicular Technology*, vol. 58, pp. 48 – 56, 2009.

[59] M. Menne, R. B. Inderka, and R. W. D. Doncker, "Critical states in generating mode of switched reluctance machines," *IEEE 31st Annual Power Electronics Specialists Conference, PESC 00.*, vol. 3, pp. 1544 – 1550, 2000.

[60] R. B. Inderka, M. Menne, and R. W. D. Doncker, "Generator operation of switched reluctance machine drives for electric vehicles," *EPE Journal*, vol. 11, pp. 35 – 40, 2001.

[61] M. Moallem, C.-M. Ong, and L. E. Unnewehr, "Effect of rotor profiles on the torque of a swiched reluctance motor," *IEEE Transactions on Industry Aplication*, vol. 28, 1992.

[62] M. I. Spong, T. J. E. Miller, S. R. McMinn, and J. S. Thorp, "Instantaneous torque control of electric motor drives," *IEEE-PESC Conference Record*, 1985.

[63] I. Husain and M. Ehsani, "Torque ripple minimization in switched reluctance motor drives by pwm current control," *IEEE Transactions on Power Electronics*, vol. 11, 1996.

[64] R. B. Inderka, R. B. Krehenbrink, and R. W. D. Doncker, "On-line estimation of instantaneous torque of switched reluctance machines," *International Symposium on Industrial Electronics IEEE-ISIE*, pp. 385–389, 2000.

[65] N. H. Fuengwarodsakul, S. Bauer, C. Dick, and R. W. D. Doncker, "Sensorless direct instantaneous torque control for switched reluctance machines," *11th European Conference on Power Electronics and Application, EPE05*, 2005.

[66] R. B. Inderka and R. W. D. Doncker, "Ditc direct instantaneous torque control of switched reluctance drives," *IEEE Industrial Application Society 37th Annual Meeting*, 2002.

[67] ——, "Ditc-direct instantaneous torque control of switched reluctance drives," *IEEE Transactions on Industry Applications*, vol. 39, pp. 1046–1051, 2003.

[68] N. H. Fuengwarodsakul, R. B. Inderka, and R. W. D. Doncker, "Instantaneous torque controller for switched reluctance vehicle propulsion drives," *20th Electric Vehicle Symposium (EVS-20)*, 2003.

[69] N. H. Fuengwarodsakul, M. Menne, R. B. Inderka, and R. W. D. Doncker, "High performance four-quadrant switched reluctance traction drive based on ditc," *IEEE 39th IAS Annual Meeting Conference Record*, vol. 3, pp. 1602–1609, 2004.

[70] ——, "High dynamic four-quadrant switched reluctance traction drive based on ditc," *IEEE Transactions on Industry Applications*, vol. 41, pp. 1232–1242, 2005.

[71] H. J. Brauer, M. D. Hennen, and R. W. D. Doncker, "Control for polyphase switched reluctance machines to minimize torque ripple and decrease ohmic machine losses," *IEEE Transactions on Power Electronics*, vol. 27, pp. 370–378, 2012.

[72] J. Kang and S. Sul, "New direct torque control of induction motor for minimum torque ripple and constant switching frequency," *IEEE Transactions on Industrial Applications*, vol. 35, p. 10761082, 1999.

[73] I. Boldea, C. I. Pitic, C. Lascu, G. Adreescu, L. Tutelea, and F. Blaajberg, "Dtfc-svm motion-sensorless control of a pm-assisted reluctance synchronous machine as starter-alternator for hybrid electric vehicles," *IEEE Transactions on Power Electronics*, vol. 21, 2006.

[74] I. Boldea and S. A. Nassar, "Torque vector control (tvc)a class of fast and robust torque speed and position digital controller for electric drives," *Proceedings EMPS*, vol. 15, p. 135148, 1998.

[75] C. Lascu, I. Boldea, and F. Blaajberg, "A modified direct torque control for induction motor sensorless drive," *IEEE Transactions on Industrial Applications*, vol. 36, p. 122130, 2000.

[76] ——, "Variable-structure direct torque controla class of fast and robust controllers for induction machine drives," *IEEE Transactions on Industrial Electronics*, vol. 51, 2004.

[77] G. Buja, D. Casadei, and G. Serra, "Direct torque control of induction motor drives," *Proceedings of ISIE97*, vol. 1, pp. TU2–TU8, 1997.

[78] D. Casadei, G. Serra, A. Tany, and L. Zarri, "Theoretical and experimental analysis of an induction motor drive based on stator flux vector control," *Electromotion Journal*, vol. 6, pp. 43–48, 1999.

[79] D. Casadei, G. Serra, and A. Tany, "Implementation of a direct control algorithm for induction motors based on discrete space vector modulation," *IEEE Transactions on Power Electronics*, vol. 15, pp. 769–777, 2000.

[80] D. Casadei, F. Porfumo, G. Serra, and A. Tany, "Foc and dtc: Two viable schemes for induction motors torque control," *IEEE Transactions on Power Electronics*, vol. 17, p. 779787, 2002.

[81] D. Casadei, F. Porfumo, G. Serra, A. Tany, and L. Zarri, "Performance analysis of a speed-sensorless induction motor drive based on a constant-switching-frequency dtc scheme," *IEEE Transactions on Industry Applications*, vol. 39, p. 476484, 2003.

[82] A. D. Cheok and P. H. Hoon, "A new torque control method for switched reluctance motor drives," *IEEE IECON Proceedings*, vol. 1, p. 387392, 2000.

[83] P. Jinpun and C.-K. Luk, "Direct torque control for sensorless switched reluctance motor drives," *Proc. 7th Int. Conf. Power Electron. Variable*, pp. 329–334, 1998.

[84] P. Veena, R. Jeryabharath, and M. Rajaram, "A new scheme of torque and flux control for switched reluctance machine," *Proceedings of Indian International Conference on Power Electronics*, 2006.

[85] G. Song, Z. Li, Z. Zhao, and X. Wang, "Direct torque control of switched reluctance motors."

[86] M. R. Feyzi and Y. Ebrahimi, "Direct torque control of 5-phse 10/8 switched reluctance motors," *Iranian Journal of Electrical and Electronic Engineering*, vol. 5, 2009.

[87] Y. Min, J. Shengjie, and Y. Xiaoganag, "Direct torque control for four phase switched reluctance motor," *International Conference on Computer, Mechatronics, Control and Electronic Engineering*, 2010.

[88] W. Mianhua, "Four phase switched reluctance motor direct torque control," *Third International Conference on Measuring Technology and Mechatronics Automation*, 2011.

[89] V. Petrus, A.-C. Pop, C. S. Martis, V. Iancu, and J. Gyselinck, "Direct torque control of a 4-phase switched reluctance machine," *ACEMP & Electromotion Joint Conference*, 2011.

[90] A.-C. Pop, V. Petrus, J. Gyselinck, C. S. Martis, and V. Iancu, "Comparative study of different torque sharing functions for losses minimization in switched reluctance motors," *13th International Conference on Optimization of Electrical and Electronic Equipment, OPTIM 2012*, 2012.

[91] R. Krishnan and P. Materu, "Analysis and design of a low cost converter for switched reluctance motor drives," *Conference Record of the 1989 IEEE Industry Applications Society Annual Meeting*, vol. 1, pp. 561– 567, 1989.

[92] ——, "Design of a single-switch-per-phase converter for switched reluctance motor drives," *IEEE Transactions on Industrial Electronics*, vol. 6, pp. 469 – 476, 1990.

[93] C. Pollock and B. W. Williams, "A unipolar converter for a switched reluctance motor," *Conference Record of the 1988 IEEE Industry Applications Society Annual Meeting*, vol. 1, pp. 44 – 49, 1988.

[94] W. Thong and C. Pollock, "Two phase switched reluctance drive with voltage doubler and low dc link capacitance," *Conference Record of the Fourtieth IAS Annual Meeting*, vol. 3, pp. 2155 – 2159, 2005.

[95] J. Liang, S. H. Seok, D. H. Lee, and J. W. Ahn, "Novel active boost power converter for sr drive," *International Conference on Electrical Machines and Systems, ICEMS 2008*, pp. 3353 – 3357, 2008.

[96] A. M. Hava, V. Blasko, and T. A. Lipo, "A modified c-dump converter for variable-reluctance machines," *IEEE Transactions on Industry Applications*, vol. 28, pp. 1017 – 1022, 1992.

[97] J. Liang, D. H. Lee, J. W. Ahn, and Y. J. An, "A novel 4-level converter for high speed sr drives," *37th IEEE Power Electronics Specialists Conference, 2006. PESC '06*, pp. 1 – 6, 2006.

[98] D. H. Lee, J. Liang, T. H. Kim, and J. W. Ahn, "Novel passive boost power converter for sr drive with high demagnetization voltage," *International Conference on Electrical Machines and Systems, ICEMS 2008*, pp. 3353 – 3357, 2008.

[99] S. Vukosavi and R. V. Stefanovic, "Srm inverter topologies: A comparative evaluation," *Conference Record of the 1990 IEEE Industry Applications Society Annual Meeting*, vol. 2, pp. 946 – 958, 1990.

[100] S. Mir, I. Husain, and M. E. Elbuluk, "Energy-efficient c-dump converters for switched reluctance motors," *IEEE Transactions on Power Electronics*, vol. 12, pp. 912 – 921, 1997.

[101] X. D. Xue, K. W. E. Cheng, and S. L. Ho, "Correlation of modeling techniques and power factor for switched-reluctance machines drives," *Journal of Electric Power Components and Systems*, vol. 32, pp. 1207–1223, 2004.

[102] ——, "Correlation of modeling techniques and power factor for switched-reluctance machines drives," *IEE Proceedings - Electric Power Applications*, vol. 152, pp. 710 – 722, 2005.

[103] N. Mohan, T. M. Undeland, and W. P. Robbins, *Power electronics: converters, applications and design*, 2nd ed., J. Wiley and S. Inc, Eds., 2003.

[104] B. Bose, *Power electronics and motor drives: advances and trends*, E. Inc, Ed., 2006.

[105] R. W. Erickson and D. Maksimovic, *Fundamentals of power electronics*, 2nd ed., S. science+buisness media Inc, Ed., 2001.

[106] A. Radun and E. Richter, "A detailed power inverter design for a 250kw switched reluctance aircraft engine starter/generator," *SAE Aerospace Atlantic Conference & Exposition*, 1993.

[107] S. Shoujun, L. Weiguo, and U. Schaefer, "Thermal analysis of a 30kw switched reluctance starter/generator system used in aircraft," *International Conference on Power Engineering, Energy and Electrical Drives, POWERENG '09*, pp. 331 – 336, 2009.

[108] (2012) Ds1103 ppc controller board. [Online]. Available: http://www.dspace.de/shared/data/pdf/flyer2008/dspace_2008_ds1103_en_pi777.pdf

[109] D. E. Cameron, J. H. Lang, and S. D. Umans, "The origin of acoustic noise in variable-reluctance motors," *Conference Record of the 1989 IEEE Industry Applications Society Annual Meeting*, 1989.

[110] ——, "The origin and reduction of acoustic noise in doubly salient variable-reluctance motors," *IEEE Transactions on Industry Applications*, vol. 28, pp. 1250 – 1255, 1992.

[111] R. S. Colby, F. M. Mottier, and T. J. E. Miller, "Vibration modes and acoustic noise in a four-phase switched reluctance motor," *IEEE Transactions on Industrial Applications*, vol. 32, pp. 1357 – 1364, 1996.

[112] M. N. Anwar and I. Husain, "Radial force calculation and acoustic noise prediction i switched reluctance machines," *IEEE Transactions on Industry Aplications*, vol. 36, pp. 1589 – 1597, 2000.

[113] J. O. Fiedler, K. A. Kasper, and R. W. D. Doncker, "Calculation of the acoustic noise spectrum of srm using modal superposition," *IEEE Transactions on Industrial Electronics*, vol. 57, pp. 2939 – 2945, 2010.

[114] M. Boesing and R. W. D. Doncker, "Exploring a vibration synthesis process for the acoustic characterization of electric drives," *IEEE Transactions on Industry Aplications*, vol. 48, pp. 70 – 78, 2012.

[115] J. O. Fiedler and R. W. D. Doncker, "Extended analytic aproach to acoustic noise in switched reluctance drives," *IEEE 33rd Annual Power Electronics Specialists Conference*, vol. 4, pp. 1960 – 1964, 2002.

[116] O. Ilsen, N. Vaninbroukx, B. van Umans, S. Faid, J. Anthonis, and P. Aarnouste, "Analysis of radiated noise in electric vehicles with a switched reluctance motor eindhoven." *Conference Record of the 1989 IEEE Industry Applications Society Annual Meeting*, vol. 8th International Automotive Congress, 2011.

[117] J. O. Fiedler, K. A. Kasper, and R. W. D. Doncker, "Acoustic noise in switched reluctance drives: an aerodynamic problem?" *IEEE International Conference on Electric Machines and Drives*, 2005.

[118] P. Vijayraghavan and R. Krishnan, "Noise in electric machines: A review," *IEEE Transactions on Industry Applications*, vol. 35, pp. 1007 – 1013, 1999.

[119] Roark and Young, *Formulas for stress and strain*, 5th ed. McGraw-Hill, 1982.

[120] A. Matveev, "Development of methods, algorithms and software for optimal design of switched reluctance drives," Ph.D. dissertation, Technical University Eindhoven, 2006.

[121] P. O. Rasmussen, F. Blaabjerg, J. K. Pedersen, and P. C. and T. J. E. Miller, "Acoustic noise simulation for switched reluctance motors with audible output," *European Conference on Power Electronics and Applications, EPE'99*, 1999.

[122] P. O. Rasmussen, "Design and advanced control of switched reluctance motors," Ph.D. dissertation, Aalborg University, 2002.

[123] L. Rayleigh, *Theory of sound*, 2nd ed. Macmillan, 1849.

[124] D. E. Cameron, "Origin and reduction of acouystic noise in variable-reluctance motors," Master's thesis, Massachusetts Institute of Technology, 1990.

List of Publications

[1] **V. Petrus**, A.-C Pop, J. Gyselinck, C. S. Martis, Vasile Iancu „*Average torque control of an 8/6 switched Reluctance Machine for Electric Vehicle Traction*", accepted to be published in the Journal of Computer Science and Control Systems (JCSCS) Vol. 5, No 1, May 2012

[2] A.-C Pop, **V. Petrus**, J. Gyselinck, C. S. Martis, Vasile Iancu „*Finite Element Based Multiphysics Optimal Design of Switched Reluctance Motors Used in Electric Vehicles Propulsion*", accepted to be published in the Journal of Computer Science and Control Systems (JCSCS) Vol. 5, No 1, May 2012

[3] **V. Petrus**, A.-C. Pop, C. S. Martis, V. Iancu, and J. Gyselinck, "*Direct instantaneous torque control of SRMs versus current profiling comparison regarding torque ripple and copper losses*," 13th International Conference on Optimization of Electrical and Electronic Equipment, May, Brasov, Romania, 2012.

[4] A.-C. Pop, **V. Petrus**, J. Gyselinck, C. Martis, and V. Iancu, "*Comparative study of different torque sharing functions for losses minimization in switched reluctance motors used in electric vehicles propulsion*," 13th International Conference on Optimization of Electrical and Electronic Equipment, May, Brasov, Romania, 2012.

[5] **V. Petrus**, A.-C. Pop, C. S. Martis, V. Iancu, and J. Gyselinck, "*Direct torque control of a 4-phase switched reluctance machine*," in ACEMP & Electromotion Joint Conference, Istanbul, Turkey, September 2011

[6] A.-C. Pop, **V. Petrus**, C. S. Martis, V. Iancu, and J. Gyselinck, "*Wide-speed range control strategy for a 8/6 switched reluctance machine*," in ACEMP & Electromotion, Joint Conference, Istanbul, Turkey, September 2011.

[7] A.-C. Pop, **V. Petrus**, C.S. Martis, J. Gyselinck, "*Parameter Identification and 2D FE Modeling of Existing Switched Reluctance Motors*" Sixth International Conference and Exhibition on Ecological Vehicles and Renewable Energies EVER2011", March 31 – April 3, 2011, Monte-Carlo, Monaco.

[8] **V. Petrus**, A.-C. Pop, C.S. Martis, V. Iancu, J. Gyselinck, "*Comparative Study on Different Current Control Techniques for a 4-phase 8/6 Switched Reluctance Machine* " Journal of Electrical and Electronics Engineering, Vol. 4, No. 1, 2011

[9] A.-C. Pop, **V. Petrus**, C.S. Martis, V. Iancu, J. Gyselinck, "*On the Firing Angles Control of a 8/6 Switched Reluctance Machine*" Journal of Electrical and Electronics Engineering, Vol. 4, No. 1, 2011

[10] **V. Petrus**, A.-C. Pop, C. Martis, J. Gyselinck, and V. Iancu, "*Design and comparison of different switched reluctance machine topologies for electric vehicle propulsion*," in XIX International Conference on Electrical Machines (ICEM), 2010.

[11] C. S. Martis, **V. Petrus**, A.-C. Pop, J. Gyselinck, "*Design and Comparison of Different Switched Reluctance Machines Topologies for Automotive Applications*" 9th International Conference on Development And Application Systems, 27-29 May 2010, Suceava, Romania.

[12] **V. Petrus**, A.-C. POP, C. S. Martis, V. Iancu, "*A 5-phase SRM for Electric Vehicle Propulsion*", Journal of Computer Science and Control Systems, vol. 3, nr. 1, pp. 159-162, May 27-28, 2010, Oradea, Romania, ISSN 1844-6043.

[13] A.- C. Pop, **V. Petrus**, C. S. Martis, V. Iancu,"*Electrical Machines For Hybrid/Electrial Vehicle - State Of The Art*", Proceedings of the International Scientific Conference MicroCAD '2010, Section K (Electrotehnics and Electronics), pp. 77-82, March 18-20, 2010, Miskolc, Hungary, ISBN 978-963-661-915-2.

PROGRAMME

INTERNATIONAL AEGEAN CONFERENCE on ELECTRICAL MACHINES and POWER ELECTRONICS & ELECTROMOTION Joint Conference

ISTANBUL TURKEY
8-10 September 2011

Organizers:

Middle East Technical University

Bahçeşehir University

Technically SponsoredBy:

IEEE

PELS

PES Motor Sub-committee

Direct Torque Control of a 4-Phase Switched Reluctance Machine

V. Petruş[1,2], A.-C. Pop[1,2], C. S. Marţiş[1], V. Iancu[1]

[1]Department of Electrical Machines,
Marketing and Management,
Technical University of Cluj-Napoca,
15, Daicoviciu, RO-400020 Cluj-Napoca, Romania
e-mail: vlad.petrus@mae.utcluj.ro

J. Gyselinck[2]

[2]Department of Bio-, Electro- and
Mechanical Systems,
Université Libre de Bruxelles ,
Av. Franklin Roosevelt, 50, B-1050, Brussels, Belgium
e-mail: johan.gyselinck@ulc.ac.be

Abstract **-- Due to its doubly salient structure and highly nonlinear behavior, the Switched Reluctance Machine (SRM) operates with very high torque ripple. To overcome these inconveniences different average and instantaneous torque control techniques were developed. This paper presents an instantaneous torque control technique named Direct Torque Control (DTC) implemented on a 4-phase, 8/6, 0.75kW SRM. Simulations results with modified flux observer and with fast torque response are presented and discussed, along with experimental results. A discussion on choosing the switching vectors for machines with both odd and even phase number is made.**

Keywords **-- Switched reluctance motor, torque ripple minimisation, direct torque control, instantaneous torque control**

I. INTRODUCTION

The SRMs have undeniable advantages in terms of simplicity, robustness, price, low maintenance and proven fault tolerance. The drawbacks of this machine are related to its salient structure and its highly nonlinear behavior which leads to important torque ripple. The torque ripple creates noise and vibrations harmful, not only to the machine, but to the entire drive system.

In automotive industry, the SRM used for traction at low speeds produces low frequency ripple causing vibrations in the whole drive train, making the vehicle undriveable. Increasing the speed, the frequency of the torque ripple rises producing a lot of noise, also undesirable in a vehicle.

Different methods of average and instantaneous torque control were developed to overcome the inconveniences created by the torque ripple. The instantaneous torque control techniques can be split up into two main categories: current profiling [1-3] and direct torque control [4-10].

DTC for ac drive was developed in the early ‘80s and it was quickly accepted by the industry, industrial drives with DTC being available on the today’s market [11]. DTC abandons the current control and controls the torque by directly modifying the stator vector voltage in accordance with the errors of flux and torque. DTC is characterized by fast dynamics, simplicity, and robustness [11-20].

The first papers on DTC for SRMs appeared in the late ‘90s and in the early 2000s, being focused on the 3-phase machines [4-7]. The 5-phase DTC for SRMs is explained in [8], where the phase transposition phenomenon is clarified.

Due to the problems regarding the even number of phases, only very few papers on DTC for 4-phase SRMs are found in the literature. In [9] a machine with shortened flux paths is presented and the consideration that the electrical angle and the mechanical angle between the phases are both equal to 45° is made. The consideration that the electrical angle between the phases is 90° is made in [10], but only few simulation results are presented at fixed values of speed, flux and torque.

This paper presents the DTC technique implemented on a 4-phase, 8/6, 0.75kW SRM.

Section II presents the principle of the 4-phase DTC for SRMs. A discussion on choosing the switching vectors for machines with both odd and even phase number is made at the end of the section. Results of the simulations with modified flux observer and with fast torque response of the implemented control are shown and discussed in Section III. The test bench and the experimental results are presented in the fourth section being followed by some conclusions and future work.

Due to the high currents and the high switching frequency needed, the DTC technique is suitable for starting the machine and for low speed operation where a smooth operating torque is imperative. For high speeds the inertia interferes and smoothens the torque, so such an accurate torque control is not needed anymore, a simple hysteresis with well calculated firing angles being sufficient.

II. DIRECT TORQUE CONTROL FOR SRMS

In order to be able to apply the principles of DTC on a SRM, the functioning equations have to be studied. The stator flux vector ($\vec{\lambda}_s$) is equal to the time integral of the stator voltage vector ($\vec{v}_s$) minus the voltage drop on the stator resistance (R_s):

$$\vec{\lambda}_s = \int_0^t (\vec{v}_s - R_s \vec{i}_s) + \vec{\lambda}_0 \qquad (1)$$

where $\vec{i}_s$ is the stator current vector and $\vec{\lambda}_0$ is the initial flux vector. The resistance being usually small, the resistive

voltage drop can be neglected at high voltage.

$$\vec{v}_s = \frac{d\vec{\lambda}_s}{dt} \quad (2)$$

Considering a sufficiently small time interval, (2) becomes:

$$\Delta\vec{\lambda}_s = \vec{v}_s \Delta t \ , \quad (3)$$

which shows that the space voltage vector applied to one phase produces a variation of the stator flux vector in the same direction as the voltage vector and a variation in magnitude proportional with the vector's magnitude and the time interval during which it is applied. The magnitude of the phase flux is time dependent, but its direction remains along the pole axis. The stator flux vector can be calculated by the transformation of the phase flux vectors onto a stationary orthogonal frame as in Fig.1.

$$\lambda_\alpha = \lambda_1 \cos 45^o - \lambda_2 \cos 45^o - \lambda_3 \cos 45^o + \lambda_4 \cos 45^o \quad (4)$$

$$\lambda_\beta = \lambda_1 \sin 45^o + \lambda_2 \sin 45^o - \lambda_3 \sin 45^o - \lambda_4 \sin 45^o \quad (5)$$

$$\lambda_s = \sqrt{\lambda_\alpha + \lambda_\beta} \ , \ \delta = \arctan\left(\frac{\lambda_\alpha}{\lambda_\beta}\right) \quad (6)$$

According to [3] and [4] the torque can be approximated by:

$$T \approx i \frac{d\lambda_s(\theta, i)}{d\theta} \quad (7)$$

Further it can be written:

$$T \approx \frac{\lambda_s(\theta, i)}{L(\theta)} \cdot \frac{d\lambda_s(\theta, i)}{d\theta} , \quad (8)$$

where $L(\theta)$ is the inductance as a function of rotor position.

Maintaining the magnitude of flux within a hysteresis band, the sign of the produced torque is the same as the sign of the stator flux variation in respect with rotor position. To produce a positive variation of torque, the flux vector has to be ahead of the rotor in the direction of the movement. While the flux vector is behind the rotor in the direction of movement, it produces a negative variation of the torque. These positive and negative variations of flux in respect with the rotor position are called in the literature flux acceleration and respectively flux deceleration.

After this discussion, the two principles of the DTC technique can be expressed [4],[8]:

a) The magnitude of the stator flux vector is kept constant (within a hysteresis band);

b) The torque is controlled by accelerating or decelerating the stator flux vector.

Similar to AC drives, equivalent voltage space vectors can be defined for every phase, the electrical angle between them being equal to $2\pi/m$ rad, where m is the number of phases. For a SRM with each phase fed by an asymmetric H-bridge, for a unidirectional current, three possible voltage states Sj are defined as (Fig.2):

a) Sj=1, both switches are on and positive voltage is applied to the phase;

b) Sj=0, one switch is on and the other is off and a zero voltage loop occurs;

c) Sj=-1, both switches are off, the voltage on the phase is negative and the freewheeling current flows through the diodes.

When the positive voltage is applied to the phase the voltage space vector can be defined, the same vector being defined but in the reverse direction when freewheeling occurs. In Fig.3, the voltage space vectors for the DTC are defined, each of them lying in the center of a sector with $2\pi/8$ radians. Analyzing the vectors and taking into account the two principles of the DTC, the so called switching table can be built (TABLE 1).

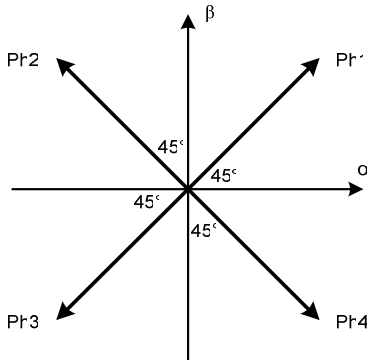

Fig. 1. Definition of two frame reference axis for phase fluxes

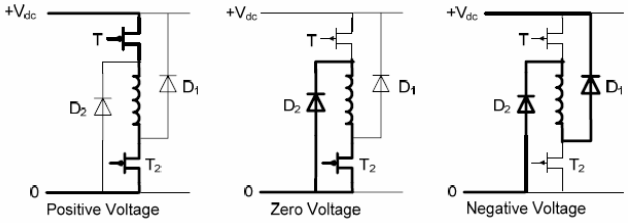

Fig. 2. The three possible voltage states in a phase of a SRM fed with asymmetric H-bridge

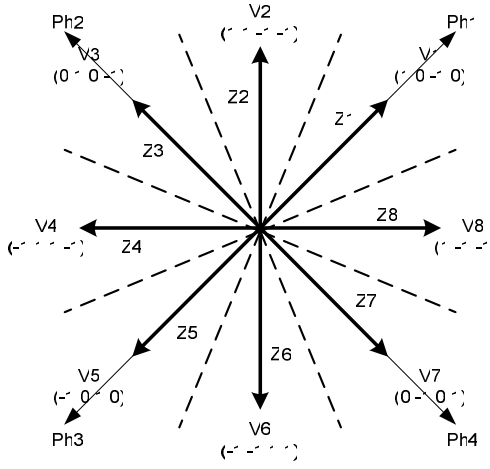

Fig. 3. Space vectors for a 4-phase of a SRM

TABLE I: SWITCHING TABLE

λ	↑	↑	↓	↓
T	↑	↓	↑	↓
V	V_{k+1}	V_{k-1}	V_{k+3}	V_{k-3}

Considering the flux vector laying in an arbitrary k-th zone, the vectors V_{k+1}, V_{k-1} are used to increase the flux, while the vectors V_{k+3}, V_{k-3} to decrease the flux. The torque is increased using vectors V_{k+1}, V_{k+3} and decreased using vectors V_{k+1}, V_{k-3}.

In order to define the switching vectors, both for odd or even phase number the phase voltage vectors need to be drawn with the origin in the same point and an angle between them of $2\pi/m$ rad. Usually the first phase is located on the x-axis of a Cartesian plane, but this is not imperative.

For the odd phase number machine the vectors can be prolonged in the negative side in order to form $2m$ zones of equal angles (π/m rad). In the center of each zone will lay a switching vector which will be obtained by energizing the phase which delimits the zone with its positive direction and freewheeling the current from the phase which delimits the zone with its negative direction. The rest of the phases are controlled in such a manner that the zero loop occurs.

For the machine with even phase number, after drawing the phase voltage vectors, m circle sectors are formed. In the middle of each sector another vector will be drawn. These $2m$ directions will be the directions of the switching vectors. So as to define the vectors a Cartesian coordinate system is considered with its y-axis in the same direction as the vector. The phases that have a positive component on the y-axis are energized and the ones that have a negative component are let to freewheel. If there are phases that have components only on the x-axis they are controlled in such a manner that the zero loops occurs. The $2m$ zones of equal angles (π/m rad) are to be considered with the centers on the above defined vectors.

This theory for defining the voltage vectors can be used for any SRM with odd or even phase number greater than 2.

III. Simulation Results

Based on the above mentioned principles a MATLAB/Simulink model of the drive was developed as shown in Fig.4.

In order to maintain the flux and torque error within the hysteresis bands two hysteresis comparators where used. The selection of the switching vectors is made by the signals from the comparators together with zone determined by the position sensor. The hysteresis bands for both the torque and flux were set at 5% of their value, meaning ± 0.1Nm and ± 0.01Wb, respectively, and they were kept at these values throughout all simulations.

Simulations were conducted at a constant speed of 300rpm. The reference torque was imposed at 4Nm and the flux at 0.4Wb.

It can be seen in Fig.5 that the amplitudes of torque and flux are very well controlled within the hysteresis bands, while Fig.6 shows the flux vector trajectory. The exceeding of torque and flux hysteresis bands with less than ± 0.01Nm and 0.001Wb is attributed to the step size of the simulation.

The waveforms of the phase currents are shown in Fig 7. Due to steady state operation, the phase currents, as well as the phase fluxes, become regularly spaced and periodic even though they are not directly controlled.

The studied machine develops the nominal torque of 4Nm at a nominal current of 4.5A. It can be seen that in order to diminish the torque ripple and to maintain the nominal torque, the instantaneous current reaches values of 6.5A, which represents 145% of the nominal current. This high current leads to high copper losses, thus to heating, making the DTC suitable for starters and for low speeds operation up to a certain speed where the inertia smoothens the torque and another method of average torque control can be used. Also it can be seen that the overlapping of the phases is accentuated and the currents never reach 0 value which leads to a low torque/ampere ratio.

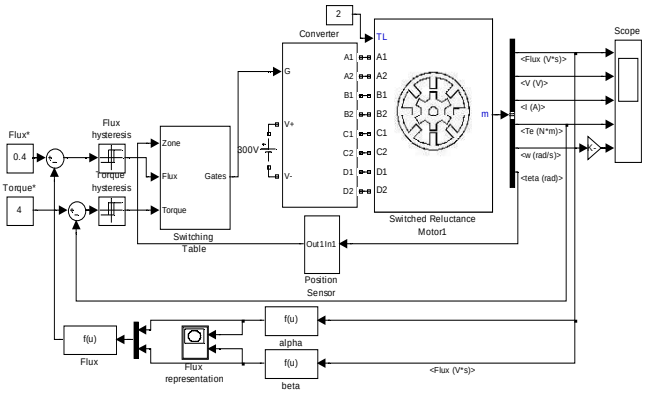

Fig. 4. The diagram of the simulation of the DTC for SRM

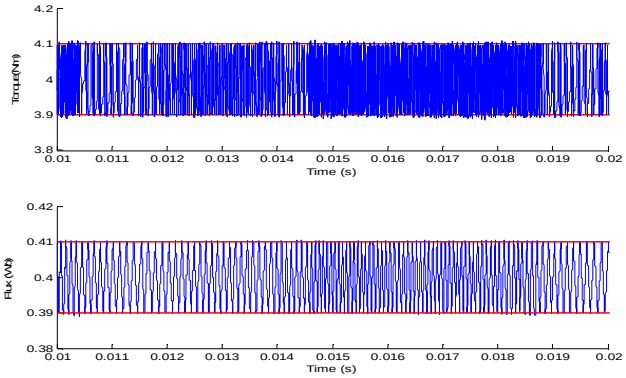

Fig. 5. Torque and total flux amplitude obtained by simulation

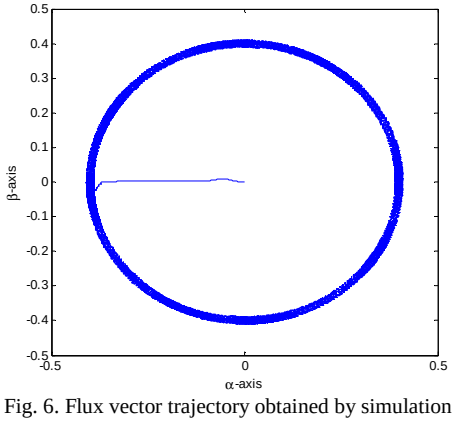

Fig. 6. Flux vector trajectory obtained by simulation

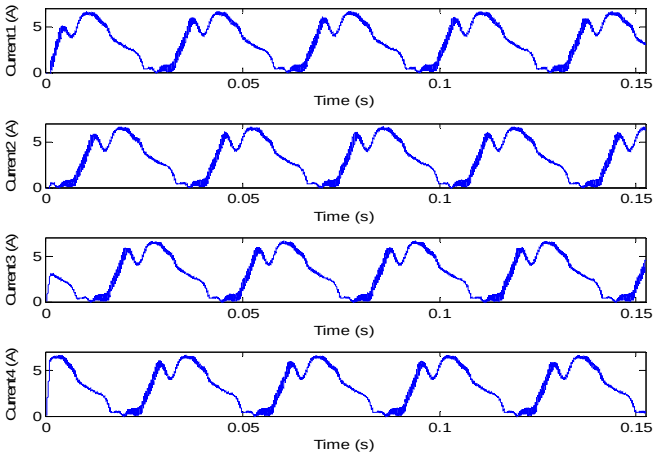

Fig. 7. Phase currents obtained by simulation

More simulations were conducted in order to test the capabilities of the control method. A speed of 200rpm is imposed and will remain constant throughout the simulation process, unless otherwise mentioned. The torque reference is step changed from a steady state value of 4Nm to a value of 2Nm. The flux is maintained constant at 0.4Wb. The torque response is very fast, reaching the given value in less than 0.2ms. The maximum value of the current decreases from 6.4A to 5.3A, as can be seen in Fig.8.

Afterwards the torque reference is linearly changed, from a steady state of 2Nm to 4Nm in a time interval of 0.05s and then decreased in the same time interval at 2Nm. The torque response and the current waveforms are presented in Fig.9. The maximum value of current is increasing from 5.3A to 6.4A and then decreasing again to 5.3A in order to maintain the torque value within the hysteresis bands.

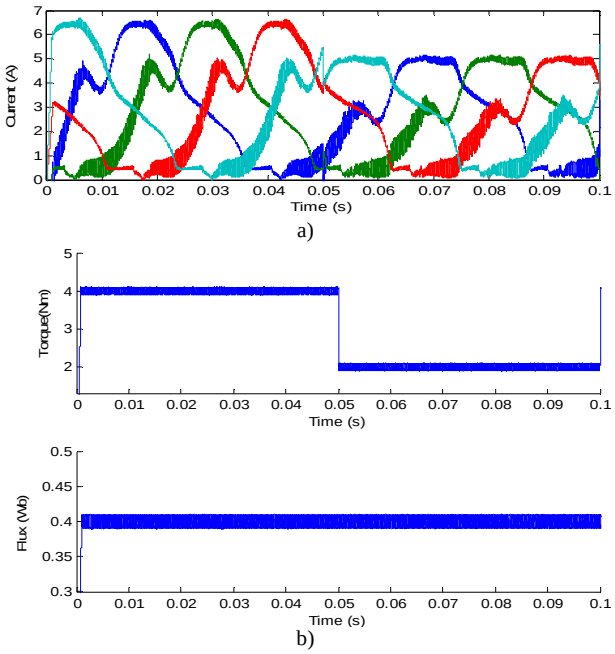

Fig. 8. Simulation results for a step change of torque reference: a) phase currents, b) torque and flux amplitude

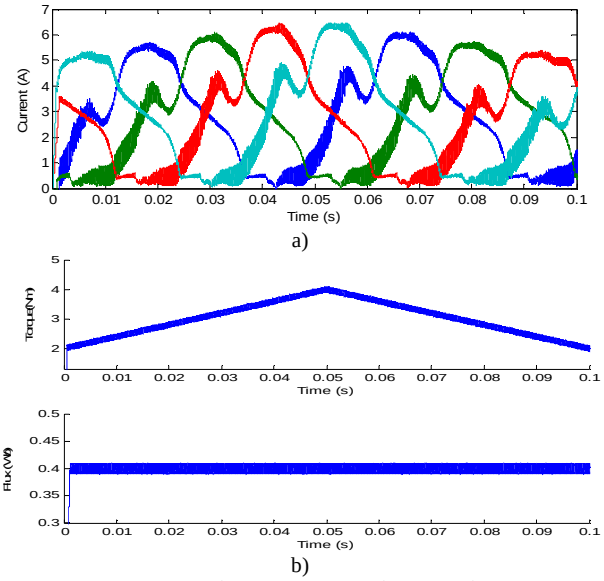

Fig. 9. Simulation results for a step change of torque reference: a) phase currents, b) torque and flux amplitude

For both situations the torque ripple is minimized but the maximum value of the current still remains higher than the rated value and the overlapping of the phases is pronounced.

After the reliability of DTC in steady state and transient torque control was tested, simulations for a transient flux reference are conducted.

Fig.10. presents the response of the system for a step change in the reference of flux from a steady state value of 0.4Wb to a value of 0.2Wb. The imposed value of the torque is constant at 4Nm. The flux response corresponds to time interval of less than 3ms.

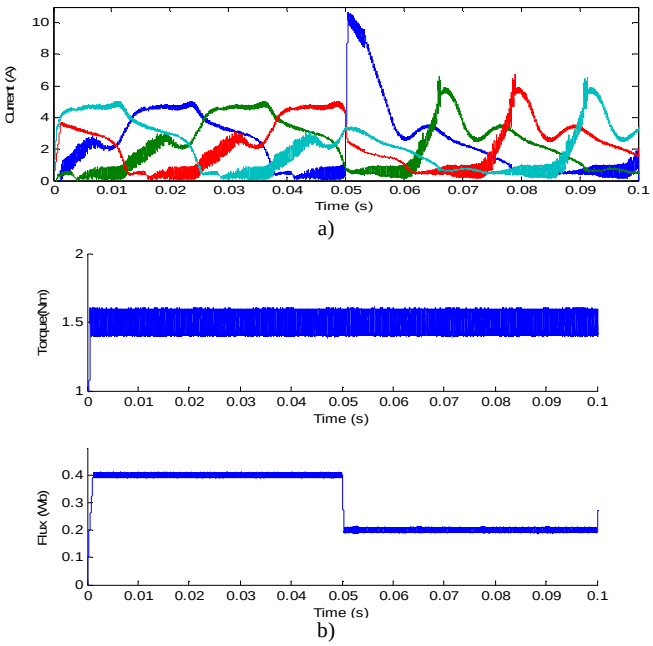

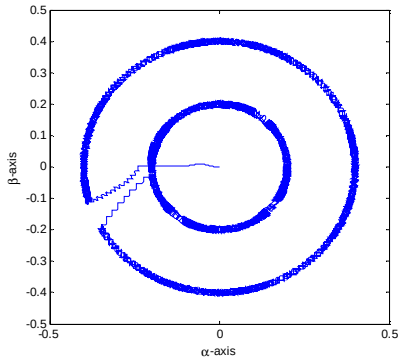

c)

Fig. 10. Simulation results for a step change of flux reference: a) phase currents, b) torque and flux amplitude, c) flux vector trajectory

Latter a linear change of the reference flux was imposed. During a 0.05s time range, the flux was increased from 0.2Wb to 0.4Wb and then again decreased to 0.2Wb keeping the same time range. The response of the system can be seen in Fig.11.

In Fig.10.a it can be seen that during the transitory regime at a high step change in flux reference, the currents can reach values three times bigger than the nominal current. It also can be seen in both Fig.10.a and Fig.11.a that for values of flux far from the nominal flux the current increases, but in such a manner that it decreases the flux vector amplitude. This leads to high copper losses and low torque/ampere ratio.

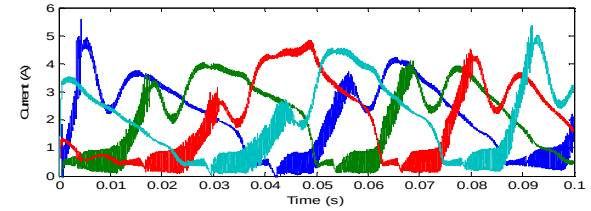

a)

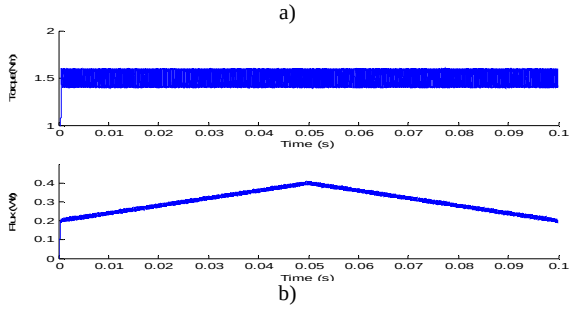

b)

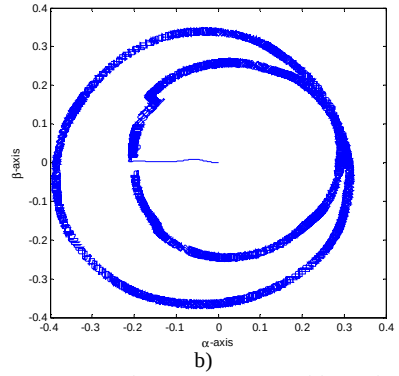

b)

Fig. 11. Simulation results for a linear change of flux reference: a) phase currents, b) torque and flux amplitude, c) flux vector trajectory

Further simulations were conducted at standstill and at extremely low speeds. The results for a step change in torque and flux reference are presented in Fig.12 and Fig.13, respectively, at a speed of 2rpm.

The DTC technique has proven its reliability and performance for steady state and transient control of both torque and flux. The torque and the flux are well control within the hysteresis bands, the torque ripple being reduced to the given value.

IV. Experimental Results

An experimental set-up, was developed in order to validate the theoretical approach. The SRM is feed via an asymmetric H-bridge based converter, with a DC machine serves as a load. Due to its compatibility with MATLAB/Simulink, a dSPACE system is used to implement the control logic.

The actual experimental set-up and the tests carried on are a first step in building a test bench for SRM used in vehicle traction.

The tests were conducted imposing the maximum switching frequency at 20kHz. Also, it needs to be mentioned that during the process the speed is not controlled. The imposed values of the torque and flux are 0.4Wb and 4Nm, respectively, and they are controlled in the same hysteresis bands as in simulations.

The differences between the simulated and the experimental results are given by the effect of the mutual inductances, non-ideal devices, noise, delays, measurement error, etc.

Fig.14 shows the measured phase currents. The torque and flux amplitude and the flux vector trajectory can be seen in fig.15 and fig.16, respectively.

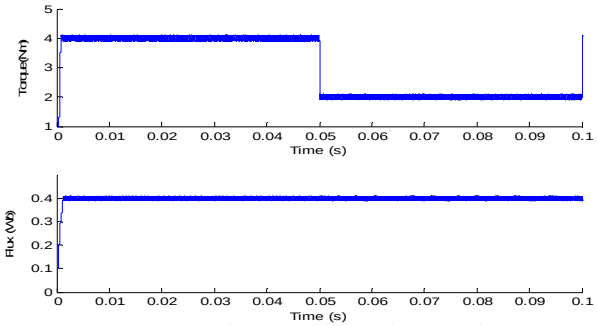

Fig. 12. Simulation results for a step change of torque reference at 2rpm

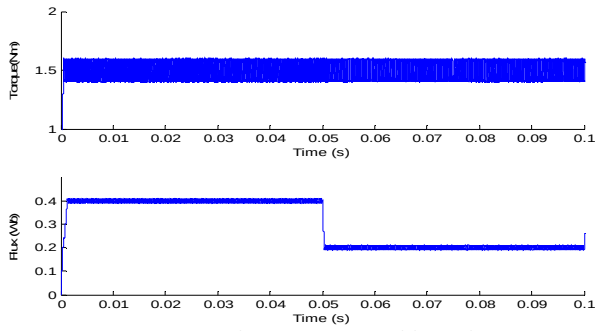

Fig. 13. Simulation results for a step change of flux reference at 2rpm

V. Conclusions and Future Work

The reliability of the DTC for 4-phase SRMs was proven by simulation and experimental results.

The influence of linear and step changes of both flux and torque references on the currents waveforms and on the performance of the control scheme was studied and discussed. The DTC method managed to maintain the torque within the hysteresis bands. The flux needs to be kept close to the rated value, else unnecessarily current increase is detected.

A discussion on choosing the switching vectors for machines with both odd and even phase number was made.

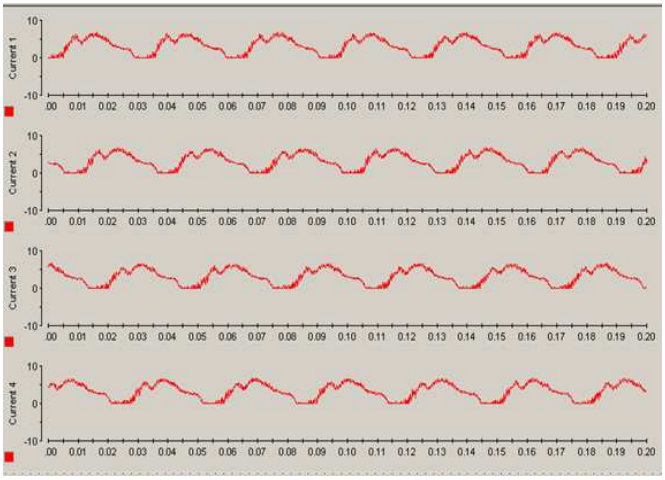

Fig. 14. Measured phase currents

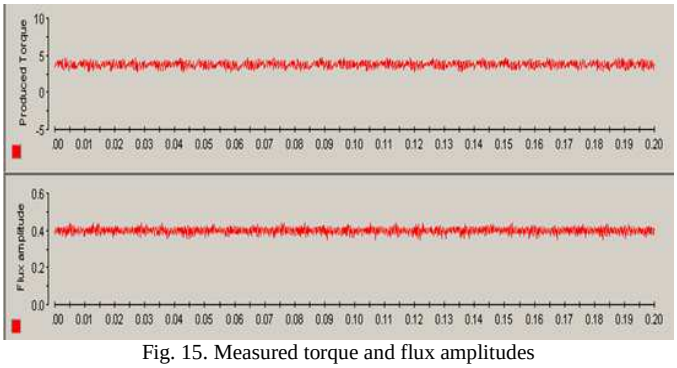

Fig. 15. Measured torque and flux amplitudes

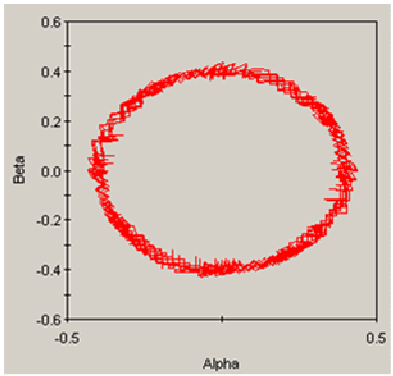

Fig. 16. Measured flux vector trajectory

Acknowledgment

This research was financially supported in the frame of the project "Doctoral studies in engineering sciences with purpose to develop knowledge-based society – SIDOC (abbreviation from Romanian)", Contract POSDRU/88/1.5/S/60078.

References

[1] I. Hussain, M. Ehsani, “Torque Ripple Minimization in Switched Reluctance Motor Drives by PWM Current Control”, IEEE Transactions on Power Electronics, Vol. 11, No. 1, January 1996

[2] R. Krishnam, “Switched Reluctance Motor Drives – Modelling, Simulation, Analysis, Design and Applications”, CRC Press, 2001

[3] M. I. Spong, T. J. E. Miller, S. R. McMinn, J. S. Thorp, “Instantaneous torque control of electric motor drives”, IEEE-PESC Conf. Rec. ’85

[4] A. D. Cheok, P. H. Hoon, “A new torque control method for switched reluctance motor drives,” Proc. IEEE IECON, vol. 1, Nagoya, Japan, 2000, pp. 387–392;

[5] P. Jinupun, P. C.-K. Luk, “Direct torque control for sensorless switched reluctance motor drives”, Proc. 7th Int. Conf. Power Electron. Variable Speed Drives, 1998, pp. 329–334;

[6] P. Veena, R. Jeryabharath, M. Rajaram, “A new scheme of torque and flux control for switched reluctance machine”, Proceedings of Indian International Conference on Power Electronics, 2006;

[7] G. Song, Z. Li, Z. Zhao, X.Wang, “Direct torque control of switched reluctance motors”, Tianjin, China

[8] M. R. Feyzi, Y. Ebrahimi, ”Direct torque control of 5-phse 10/8 switched reluctance motors”, Iranian Journal of Electrical and Electronic Engineering, Vol. 5, No.3, Sep. 2009;

[9] Y. Min, J. Shengjie, Y. Xiaogang, “Direct Torque Control for Four Phase Switched Reluctance Motor”, International Conference on Computer, Mechatronics, Control and Electronic Engineering, 2010

[10] W. Mianhua, “Four Phase Switched Reluctance Motor Direct Torque Control”, Third International Conference on Measuring Technology and Mechatronics Automation, 2011

[11] J.-K. Kang, S.-K. Sul, “New direct torque control of induction motor for minimum torque ripple and constant switching frequency,” IEEE Trans. Ind. Applicat., vol. 35, pp. 1076–1082, Sept./Oct. 1999.

[12] G. Buja, D. Casadei, G. Serra, “Direct torque control of induction motor drives”, Proc. of ISIE’97, Guimaraes (Portugal), Vol. 1, pp. TU2-TU8.

[13] D. Casadei, G. Serra, A. Tani, L. Zarri, “Theoretical and experimental analysis of an induction motor drive based on stator flux vector control”, Electromotion Journal, Vol. 6, No. 1-2, 1999, pp. 43-48.

[14] D. Casadei, G. Serra, A. Tani, “Implementation of a direct control algorithm for induction motors based on discrete space vector modulation”, IEEE Trans. on Power Electronics, Vol. 15 No. 4, July 2000, pp. 769 -777.

[15] D. Casadei, F. Profumo, G. Serra, A. Tani, “FOC and DTC: Two Viable Schemes for Induction Motors Torque Control”, IEEE Transactions on Power Electronics, Vol. 17, NO. 5, September 2002, pp. 779-787.

[16] D. Casadei, F. Profumo, G. Serra, A. Tani, L. Zarri, “Performance Analysis of a Speed-Sensorless Induction Motor Drive Based on a Constant-Switching-Frequency DTC Scheme”, IEEE Trans. on Industry Applications, Vol. 39, NO. 2, March/April 2003, pp. 476-484.

[17] I. Boldea and S. A. Nasar, “Torque vector control (TVC)—A class of fast and robust torque speed and position digital controller for electric drives”, in Proc. EMPS, vol. 15, 1988, pp. 135–148.

[18] C. Lascu, I. Boldea, and F. Blaabjerg, “A modified direct torque control for induction motor sensorless drive”, IEEE Trans. Ind. Applicat., vol. 36, pp. 122–130, Jan./Feb. 2000.

[19] C. Lascu, I. Boldea, F. Blaabjerg, “Variable-Structure Direct Torque Control—A Class of Fast and Robust Controllers for Induction Machine Drives”, IEEE Trans. on Industrial Electronics, vol. 51, no. 4, August 2004.

[20] I. Boldea, C.I. Pitic, C. Lascu, G.-D. Andreescu, L. Tutelea, F. Blaabjerg, P. Sandholdt, “DTFC-SVM Motion-Sensorless Control of a PM-Assisted Reluctance Synchronous Machine as Starter-Alternator for Hybrid Electric Vehicles”, IEEE Trans. on Power Electronics, vol. 21, no. 3, May 2006

OPTIM 2012

13th International Conference on

OPTIMIZATION OF ELECTRICAL AND ELECTRONIC EQUIPMENT

May 24-26, 2012, Brasov, Moieciu "Cheile Gradistei"

http://www.info-optim.ro

Power Systems and Electromagnetics

Electrical Machines, Industrial Drives and Control

Power Electronics and Power Conversion

Renewable Electric Energy Conversion, Processing and Storage

Mechatronics, Industrial Automation and Control

Applied Electronics and System Integration

Electrical Engineering Education and

Emerging Technologies

Industry news

Student forum

Special session proposals: January 10, 2012
Contributed full papers: January 15, 2012
Notification of acceptance: March 15, 2012
Final submissions due: April 5, 2012
Early registration closes: April 17, 2012

Direct Instantaneous Torque Control of SRMs versus Current Profiling – Comparison Regarding Torque Ripple and Copper Losses

V. Petrus[1,2], A.-C. Pop[1,2],C. S. Martis[1], V. Iancu[1]

J. Gyselinck[2]

[1]Technical University of Cluj-Napoca
Dpt. of Electrical Machines and Drives
28, Memorandumului st., 400114 Cluj-Napoca, Romania
Email: vlad.petrus@mae.utcluj.ro

[2]Université Libre de Bruxelles
BEAMS Dpt., Energy Group
50, F. Roosevelt Av., B-1050 Brussels, Belgium
Email: johan.gyselick@ulb.ac.be

***Abstract*—This paper presents the implementation of an instantaneous torque control technique named Direct Instantaneous Torque Control (DITC) on a 4-phase, 8/6, 30kW peak-power Switched Reluctance Machine (SRM) used for electric vehicle traction. On-line instantaneous torque estimation methods and the principles of the DITC are discussed. Simulation and experimental results are presented in the paper and a comparative study with current profiling techniques using three different torque-sharing functions is made.**

I. Introduction

The undeniable advantages of the SRM, in terms of simplicity, robustness, fault tolerance, low maintenance and price, make it a candidate with real chances on the market of electric traction. The salient structure of the machine and its highly non-linear behaviour lead to important torque ripple, representing the main drawback of the machine.

At low speeds, the low-frequency torque ripple generates oscillations that may excite resonant frequencies of the drive train, making the vehicle undrivable. At higher speeds the frequency of the ripple increases, causing high-frequency acoustic noise, disturbing for the human ear.

To overcome these drawbacks, different torque-ripple minimization techniques were proposed in the literature regarding the design and the control of SRMs.

Rotor skewing and pole shaping are the main mechanical design features used to minimize the ripple. These methods are effective only on a limited operating range and also the maximum torque is decreased due to the enlarged air-gap [1]. This can be translated into lower torque density which is not an option for the vehicle traction applications confronting the limited space in a vehicle.

To overcome the inconveniences represented by the salient structure and the highly non-linear behaviour of the SRM, different torque control techniques (instantaneous & average) were developed.

A wider operating range, but still limited, can be achieved by profiling the waveforms of the current or flux, off-line or on-line [2]-[4]. The cumbersome and time-consuming pre-calculations needed in order to find the optimal profile of the phase current or flux together with the demand for a precise position measurement and the lack of highly trained specialists in the field may cause a delay in the spread of SR drives on the market.

The well-known Direct Torque Control (DTC) technique for rotating-field AC machines can be transposed to SRMs [5], [6]. This method can be used over a wide operating range, but it requires an additional flux estimator and controller. Moreover the currents in the phases are never shut down, thus the machine works with high copper losses.

The Direct Instantaneous Torque Control technique was proposed by Inderka and De Doncker from RTW Aachen in the early 2000s [7]. The proposed closed-loop architecture (Fig. 1) uses a simple hysteresis controller to compare the instantaneous value of torque with its reference in order to generate the switching signals for the electronic converter [7]-[10]. DITC does not use flux or current profiling techniques and it does not require a very precise position measurement.

This paper presents the implementation of the DITC technique on a 4-phase, 8/6, 30kW peak-power SRM. Section II presents the existing instantaneous-torque estimation techniques, while section III discusses the principle of the DITC and its advantages. Results of the simulations with fast torque response of the implemented control are shown and analysed in Section IV. The test bench and the experimental results are presented in the fifth section together with a comparative study with the current profiling technique using three different torque-sharing functions. The paper ends with conclusions and future work.

II. On-line instantaneous torque estimation techniques

DITC is a closed-loop instantaneous-torque control technique, thus, an instantaneous-torque feedback is imperative. In the absence of an efficient torque meter the instantaneous torque has to be precisely estimated. In the automotive industry, due to aspects regarding space and price, the estimation

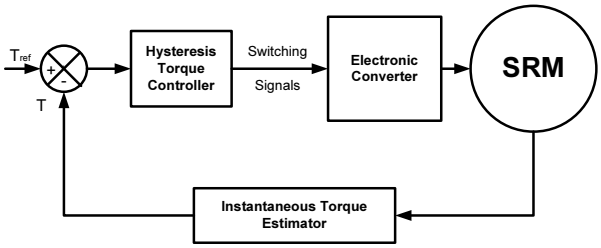

Fig. 1. The architecture of the closed-loop instantaneous torque control

is also preferred over the measurement.

The instantaneous-torque estimation in a SRM is not a trivial task. Thus, several estimation techniques were developed over time [12]. The first developed analytical methods are not taking into consideration the non-linearities of the model of the SRM. To compensate the non-linearities, tables for correction were added to the linear models. The accuracy of the estimation did not reach acceptable error tolerances.

Nowadays, the models of the machines are created using experimental measurements and/or finite element analysis. So obtained data can be further used for an accurate estimation of the machine's performances.

The estimation of instantaneous torque can be done using different characteristics of the machine stored in look-up tables: $T(i,\theta)$, $T(\lambda,\theta)$, $T(i,\lambda)$, where T is the electromagnetic torque, θ is the rotor position, i is the phase current and λ is the flux linkage.

The first table, torque versus phase current and rotor position (Fig. 2), and likely the most used one, employs the phase currents and the rotor position for the estimation of the torque. The need of a continuous and accurate rotor position measurement represent a drawback of this method.

The second table, torque as a function of flux linkage and rotor position, does not use the phase current but the phase flux for the torque estimation.

To calculate the flux linkage, the phase voltage equation of an SRM has to be considered:

$$u = Ri + \frac{\mathrm{d}\lambda}{\mathrm{d}t}, \tag{1}$$

with R the phase resistance, from which the flux linkage can be obtained by integration:

$$\lambda = \int (u - Ri)\mathrm{d}t. \tag{2}$$

To estimate the flux linkage, both the phase voltages and currents have to be used. So, besides the already existing current sensors, at least one voltage sensor has to be installed on one phase. The existence of only one voltage sensor forces the controller to consider a constant torque over four strokes, situation unacceptable for an instantaneous control technique. Thus the existence of a voltage sensor on each phase is required. This increases the overall price of the drive, also

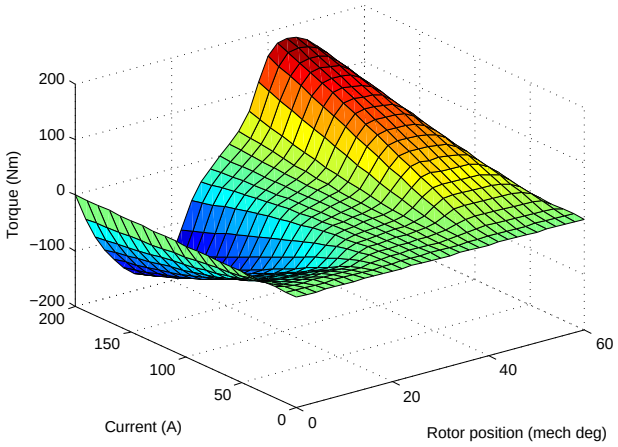

Fig. 2. The electromagnetic torque dependence on phase current and rotor angular position

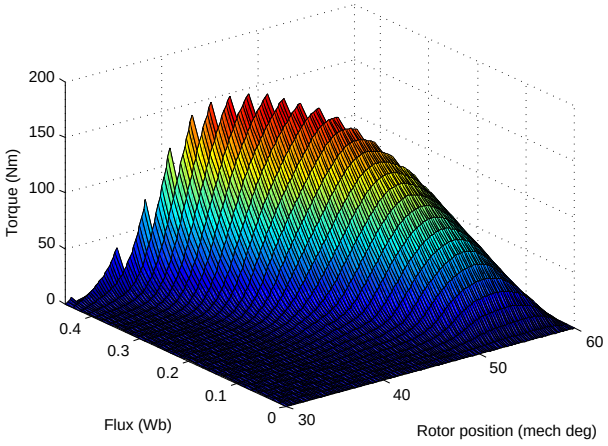

Fig. 3. The electromagnetic torque dependence on flux linkage and rotor angular position

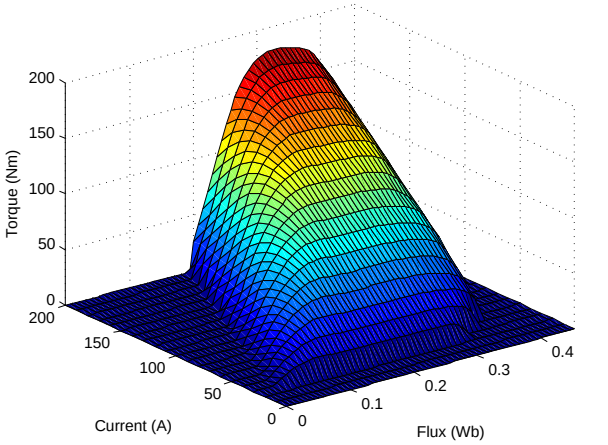

Fig. 4. The electromagnetic torque dependence on phase current and flux linkage

a sensitive problem in the automotive industry. Moreover, the implementation of (2) in the controller will introduce delays All these, make the second table (Fig. 3) not to be implemented in real life applications.

To avoid the mounting of voltage sensors on each phase, an estimation of the phase voltages can be done from the switching signals and using only one inexpensive voltage sensor for the measurement of the DC-bus voltage.

Another instantaneous torque estimation technique uses the $T(i,\theta)$ and $\lambda(i,\theta)$ tables in order to avoid the need of a precise position measurement. Combining the static torque characteristics with the flux linkage characteristics and eliminating the rotor position, the characteristics of torque as a function of phase current and flux linkage, $T(i,\lambda)$, can be obtained (Fig. 4). The table has to be mirrored versus current-flux plane for negative values of the torque. Using the data in this table the torque can be estimated independently of the rotor position, only by measuring the phase currents and voltages. To be able to estimate the torque from the phase voltages and currents, (2) has to be implemented in the controller.

By combining the $T(i,\theta)$ and $\lambda(i,\theta)$ tables and eliminating the torque, a table for the position as a function of phase current and linkage flux can be obtained. Thus, a sensorless control can be achieved [9].

Taking into account the price of high resolution voltage sensors and the frequency limitations imposed by the prototyping tool the authors decided to estimate the instantaneous torque from the table, $T(i,\theta)$.

III. Operating principles of DITC

The DITC is a closed loop instantaneous torque control technique employing a simple hysteresis controller equipped with two hysteresis bands (an interior band and an exterior band) in order to maintain the torque at its reference value, within the imposed tolerances. The method uses the concept of phase torque sharing without using pre-calculated torque-sharing functions.

During single-phase conduction interval of phase N, between the turn-off angle of the phase $N-1$ and the turn-on angle of the phase $N+1$, the controller changes only the state of the energized phase N in order to regulate the torque. At phase commutation, between the turn-on angle of the incoming phase , $N+1$, and the turn-off angle of the outgoing phase, N, the states of the two phases are being modified and their individual torque is controlled by controlling the total torque. The commutation strategy further implemented in the controller is presented in Table I. The small "x" means the phase is not taken into account for torque production, while the states of one torque productive phase are explained in Fig. 5.

For an SRM with each phase fed by an asymmetric H-bridge, for a unidirectional current, three possible voltage states S are defined as (Fig. 5):

a) $S = 1$, both switches are closed and positive voltage is applied to the phase;

b) $S = 0$, one switch is closed, the other is opened and a zero voltage loop occurs;

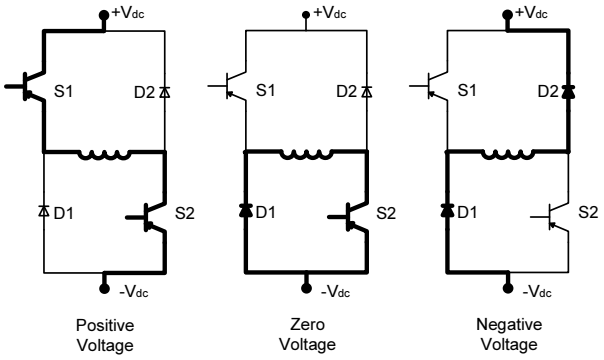

Fig. 5. The three possible voltage states of a phase of an SRM fed by asymmetric H-bridge

TABLE I
MOTORING COMMUTATION STRATEGY TABLE OF THREE ADJACENT PHASES FOR DITC

Ph N-1 Enable	Ph N Enable	Ph N+1 Enable	Ph N-1 State	Ph N State	Ph N+1 State
0	0	0	x	x	x
1	0	0	1/0	x	x
1	1	0	1/0/-1	1/0	x
0	1	0	-1/x	1/0	x
0	1	1	x	1/0/-1	1/0
0	0	1	x	-1/x	1/0

c) $S = -1$, both switches are opened, the voltage on the phase is negative and the current is free wheeling through the diodes.

Each phase is enabled between its turn-on and turn-off angles. Soft chopping is employed by the converter in single-phase conduction: either the positive DC-link voltage is applied to the phase ($S = 1$), either a zero-voltage loop is created ($S = 0$). The states of two phases are being switched at phase commutation. While the incoming phase is not capable of producing the required torque, the outgoing phase, previously switched to zero-voltage state, contributes to the torque production by changing the state to $S = 1$. After it reaches its turn-off angle, the outgoing phase is being demagnetized, $S = -1$. Also, the outgoing phase can be demagnetized during phase commutation, if the incoming phase is capable of producing the reference torque by itself.

As can be seen in Fig. 6, at the beginning of the conduction period the incoming phase is energized and the outgoing phase is switched into zero-voltage state. When the total torque reaches a value lower than the one permitted by the exterior hysteresis band, the outgoing phase will be excited again with positive voltage, $S = 1$. After a certain point, the incoming phase is able to control the torque by itself, so the outgoing phase will be switched into the zero-voltage loop. If the highest value of torque is reached, the outgoing phase is demagnetized, $S = -1$, in order not to demagnetize the incoming phase. For preventing negative torque production, at the end of the

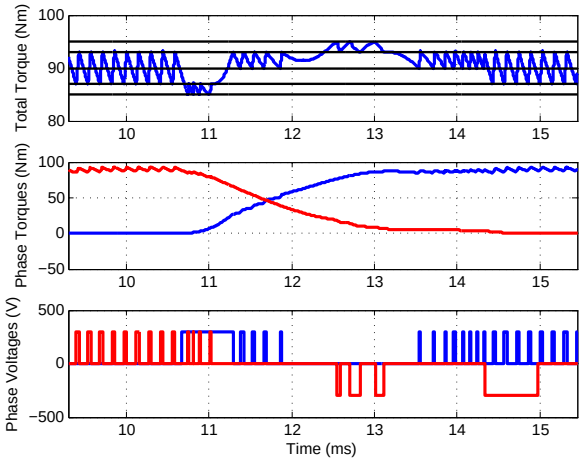

Fig. 6. Principle exemplification of DITC switching strategy

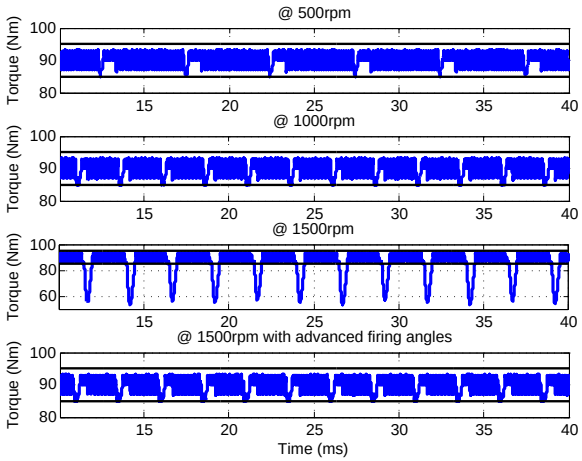

Fig. 7. Simulated torque waveforms at different speed values obtained by using DITC

conduction period, negative voltage is applied to the phase and the current is rapidly shut down.

The strategy used by the DITC automatically commutates the phases and regulates their torque independently of a precise knowledge of rotor position or switching angles.

Due to the usage of the zero-voltage state, the switching frequencies of DITC are considerably reduced compared to the switching frequencies of current profiling techniques employing hard chopping. DITC can be used over a wide operating range with good ripple reduction performances.

DITC does not necessitate cumbersome and time-consuming pre-calculations and it can straightforwardly be applied to any of the SRMs, regardless of the number of phases, rotor and stator poles, while the profiling has to be done independently for every machine.

The algorithm of DITC can be extended to a multiphase torque-sharing theory for SRMs with the number of phases higher than four [10].

IV. Simulation Results

The MATLAB/Simulink model of DITC, developed in order to test the reliability of the above discussed principles, is based on a 4-phase, 8/6, 30kW peak-power SRM with a rated power of 15kW at a base speed of 1500rpm and a rated torque of 90Nm. The hysteresis controller used to generate the switching signals has the inner band set at $\pm$3Nm and the outer band at $\pm$5Nm.

The extensive simulations carried out prove the attainability of a smooth rated torque up to the base speed, by advancement of the switching angles in accordance with the operation point. Fig. 7 shows the performance of the controller in maintaining the rated torque at different speed up to 1500rpm. A smooth waveform of torque is reached at the base speed after the necessary correction of the angles was made.

The reaction of the controller at changes in the reference is tested and the results are presented in Fig. 8. Throughout all simulations the speed is maintained constant at 1000rpm.

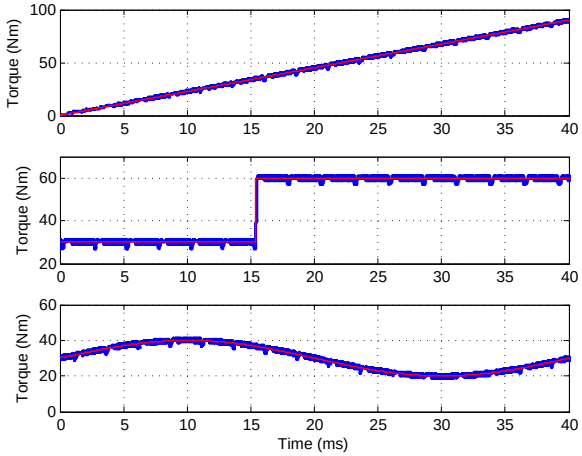

Fig. 8. The simulated reaction of DITC controller at changes in the reference torque at 1000rpm

Firstly, the reference torque is linearly increased from 0Nm up to the rated torque. The controller proves its capability in maintaining the instantaneous torque value within the hysteresis bands.

Secondly the reference is step varied from 30Nm to 60Nm. The time for the controller to reach the new value is less than 0.2ms and no overshoots are spotted.

Thirdly, the reference of the torque is sinusoidally varying with an amplitude of 10Nm and a continuous component of 30Nm. The controller reacts with the same performances and robustness as in the precedent cases and the instantaneous torque remains within the imposed tolerances.

After proving its capability in maintaining a smooth torque against highly varying reference, the performance of the DITC is further tested regarding its efficiency. The DITC technique is recommended for operation points below the base speed,

where the copper losses play the most important role in the equation of the overall efficiency. The copper losses are calculated with:

$$P_{\mathrm{Cu}} = \sum_{k=1}^{m} I_k^2 R \tag{3}$$

where P_{Cu} are the copper losses, I_k is the RMS value of the k-th phase current, R is the phase resistance and m is the number of phases.

The increase of the copper losses with the torque at constant speed can be observed in Fig. 9. While operating in the constant torque region of the speed-torque characteristic, below the base speed, every value of torque up to the rated value can be attained. For a constant torque reference, the copper losses will decrease with speed, Fig. 10, due to the changes in the ascending and descending slopes of the phase current.

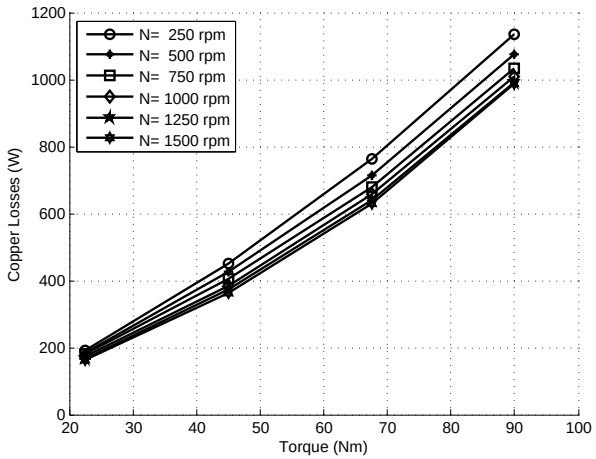

Fig. 9. The variation of copper losses with the electromagnetic torque at constant speed

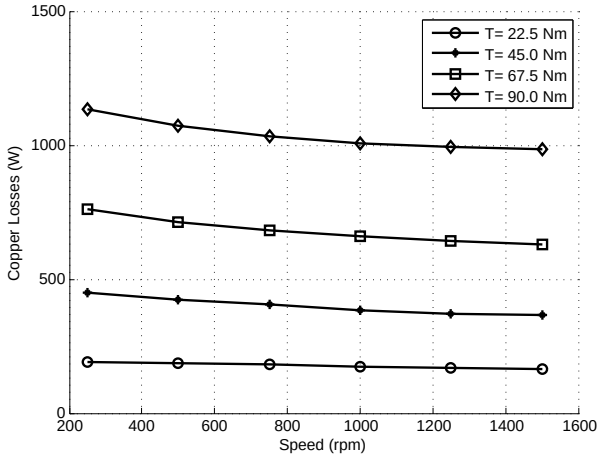

Fig. 10. The variation of copper losses with the speed at constant electromagnetic torque

V. Experimental results

The experimental set-up developed for the validation of the theoretical approach is presented in Fig. 11. The SRM loaded with a DC machine is fed via an asymmetric H-bridge based converter.

A dSPACE 1103 prototyping platform is used to implement the control logic. A 1024-pulse incremental encoder was employed for rotor position measurement. The tests are conducted imposing the maximum switching frequency at 10kHz.

A. Experimental results of DITC

The estimated total torque together with the phase currents for two sets of different firing angles can be observed in Fig. 12 and Fig. 13. The operating point of the machine in both cases is 500rpm and 15Nm. In the first case the turn-on angle is 37° and the turn-off angle is 58°, while in the second case the angles are 33° and respectively 54°. The values of the hysteresis bands are set and preserved during all performed experiments at ±1Nm and respectively ±2Nm.

The total instantaneous torque is successfully maintained within the hysteresis bands at the expense of increased copper losses in the case of improperly set switching angles. Crossings of the exterior band can be observed due to the limited switching frequency admitted by the prototyping tool. The DITC controller is not affected by inaccurate rotor position detection or by inaccurate switching instances. Still, the accuracy of rotor position detection is of an extreme importance for the instantaneous torque estimation in the actual case.

The capability of the controller in following rapid variation of the references, while an external speed loop maintains constant the speed of the drive at 500rpm, is demonstrated in Fig. 14. In the first case a ramp reference increasing and decreasing linearly from 10Nm to 20Nm and back to 10Nm in 0.7 seconds is imposed. The controller is able to maintain, with a small deviation, the instantaneous value of the torque within the hysteresis band.

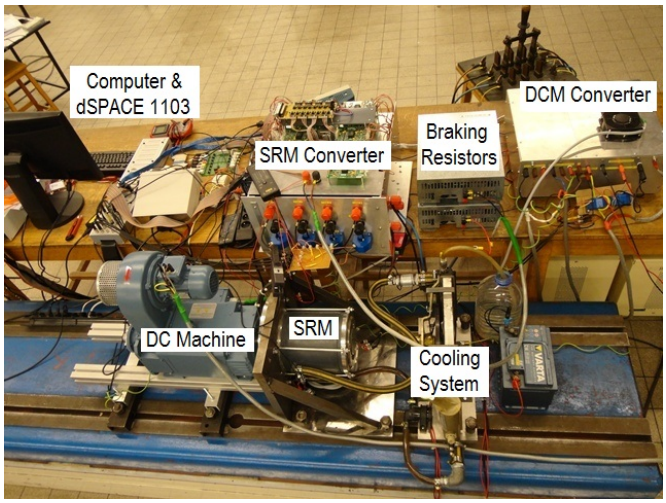

Fig. 11. Experimental set-up

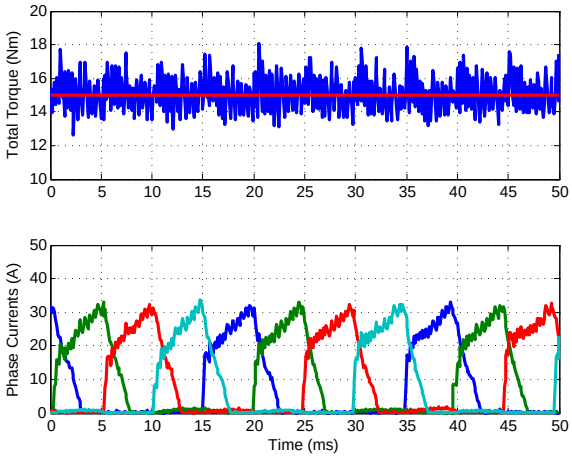

Fig. 12. Measured torque and phase currents at 500rpm, 15Nm, turn-on angle 37° and turn-off angle 58°

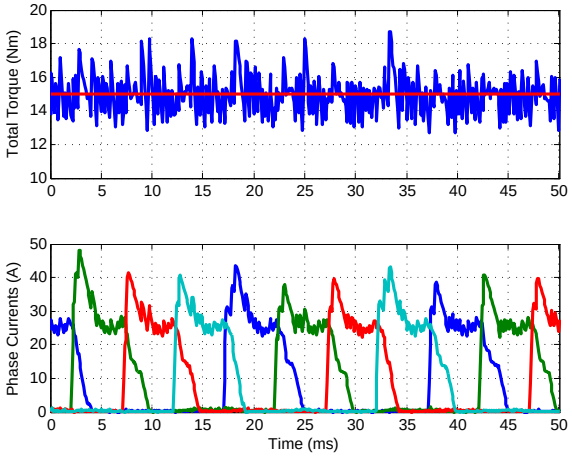

Fig. 13. Measured torque and phase currents at 500rpm, 15Nm, turn-on angle 33° and turn-off angle 54°

In the second case the reference is step changed from 5Nm to 15Nm and back. The produced torque is able to reach the new value in 2ms and without unnecessary and unwanted overshoots.

In the third case a sinusoidal reference with an amplitude of 5Nm, a continuous component of 15Nm and a frequency of 1.5Hz is followed with the same stringency.

B. Coparison with current-profiling technique

In [11] three torque-sharing functions for current-profiling, optimised for low losses while operating in smooth torque conditions, are discussed and implemented on the same SRM. Starting from the basic rectangular variation, the ascending and the descending flanks of the function are modelled using a cosine, exponential and a generalisation of the cubic variation (further referred to as piecewise cubic torque-sharing function).

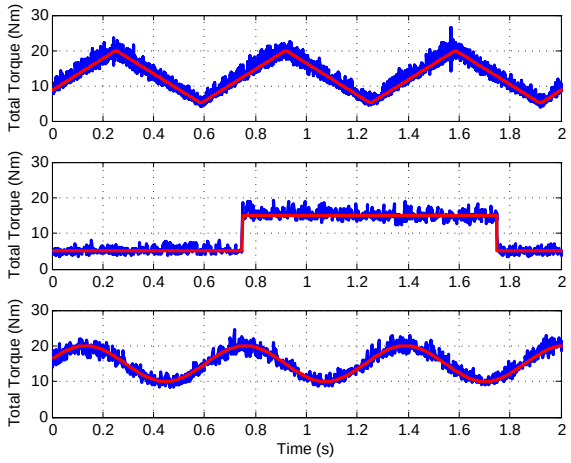

Fig. 14. The measured reaction of DITC controller at changes in the reference torque at 500rpm

Fig. 15 shows the instantaneous torque and the mean value of torque for the three torque-sharing functions and for DITC at 650rpm and a reference torque of 30Nm. For the open-loop current-profiling control, offsets between the reference and the mean value of the torque are noticed: 1.64Nm for the cosine function, 2.37Nm for the exponential function and 2.22Nm for the piecewise cubic function. The offsets appear due to DC-bus voltage variation, the phase resistance dependency on the temperature, manufacturing imperfections or other environmental influences.

Being a closed-loop instantaneous-torque control technique, DITC does not allow any offset between the reference and the output value of torque like the open-loop torque-control techniques do. DITC is capable to compensate the less torque produced by the last pahse in SRMs with long flux-paths. If the torque is measured with a torque meter directly on the shaft, the method is able to damp oscillations or ripples of the torque caused by mechanical reasons.

The currents measured on the phases of the machine in all four cases at 650rpm and 30Nm are presented in Fig. 16. The cosine and exponential functions need considerably more peak current to produce the same torque as the piecewise cubic function and DITC. The copper loses at 250rpm and 650rpm and a reference torque of 30Nm are calculated on the basis of the measured currents and presented in Table II. At very low speed (250rpm) the variation of the efficiency of the mentioned methods regarding the copper losses is less than 5%. Increasing the speed higher variations of the efficiency can be noticed. At 650rpm the copper losses of piecewise cubic function are 200W, with 15% less than the exponential function and 50% less than cosine function. The DITC technique has 7.5% less copper losses than the piecewise cubic function. The losses of DITC can be further improved by calculating optimised switching angles.

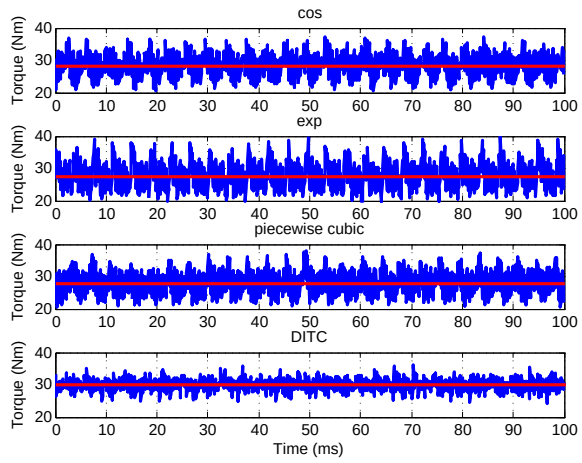

Fig. 15. The measured instantaneous and average torque of current profiling techniques vs. DITC at 650rpm and 30Nm

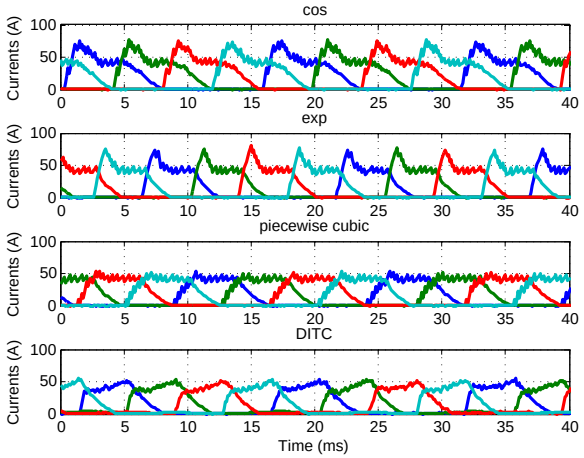

Fig. 16. The measured phase currents of current profiling techniques vs. DITC at 650rpm and 30Nm

TABLE II
COMPARISON OF COPPER LOSSES COMPUTED BASED ON MEASURED CURRENTS OF DIFFERENT INSTANTANEOUS TORQUE CONTROL TECHNIQUES AT 30Nm

Method	Copper losses (W)	
	@250rpm	@650rpm
cos	180.9	299.3
exp	187.7	228.4
piecewise cubic	183.8	200.4
DITC	190.4	185.4

VI. CONCLUSIONS

In this paper the Direct Instantaneous Torque Control technique was implemented on a 4-phase Switched Reluctance Machine used for electric vehicle propulsion.

The reliability of the method was tested through means of simulation and experimental measurements on the test bench. The DITC proved its performances regarding torque ripple minimization and wide operation range, being able to maintain a smooth rated torque at the base speed.

The switching losses were reduced and the audible noise diminished by the lower employed switching frequency of DITC compared to the profiling techniques using hard-chopping.

The immunity against inaccurate rotor position detection and against inaccurate switching instances confers an increased robustness to this technique.

The controller was capable of fast reaction to large and rapid changes in the reference and it is able to reduce the torque anomalies inflicted by non-electrical considerations.

The easy and rapid implementation on any type of SRM, without complex and time-consuming pre-calculations provides a substantial advantage of DITC over profiling techniques.

The copper losses of DITC can be further improved by calculating low losses optimised switching angles.

ACKNOWLEDGEMENT

This research was financially supported in the frame of the project ”Doctoral studies in engineering sciences with purpose to develop knowledge-based society SIDOC (abbreviation from Romanian)”, Contract POSDRU/88/1.5/S/60078.

REFERENCES

[1] M. Moallem, C.-M. Ong, L. E. Unnewehr, “Effect of Rotor Profiles on the Torque of a Swiched reluctance Motor,” *IEEE Trans. on Industry Aplication*, vol. 28, no. 2, March/April 1992.

[2] I. Hussain, M. Ehsani, “Torque Ripple Minimization in Switched Reluctance Motor Drives by PWM Current Control,” *IEEE Trans. on Power Electronics*, vol. 11, no. 1, January 1996.

[3] R. Krishnan, “Switched Reluctance Motor Drives Modelling, Simulation, Analysis, Design and Applications,” CRC Press, 2001.

[4] M. I. Spong, T. J. E. Miller, S. R. McMinn, J. S. Thorp, “Instantaneous torque control of electric motor drives,” *IEEE-PESC Conf. Rec.*, 1985.

[5] A. D. Cheok, P. H. Hoon, “A new torque control method for switched reluctance motor drives,” *IEEE IECON. Proc.*, vol. 1, pp. 387-392, Nagoya, Japan, 2000.

[6] V. Petrus, A.-C. Pop, C. S. Martis, V. Iancu, J. Gyselinck, “Direct Torque Control of a 4-Phase Switched Reluctance Machine,” *ACEMP & Electromotion Joint Conference*, Istanbul, Turkey, 08-10 September 2011.

[7] R. B. Inderka, R. W. De Doncker, “DITC Direct Instantaneous Torque Control of Switched Reluctance Drives,” *IEEE Industrial Application Society 37th Annual Meeting*, Pittsburgh, USA, 2002.

[8] R. B. Inderka, R. W. De Doncker, “DITC-Direct Instantaneous Torque Control of Switched Reluctance Drives,” *IEEE Trans. on Industry Applications*, vol. 39, no. 4, pp. 1046-1051, July/August 2003.

[9] N. H. Fuengwarodsakul, S. Bauer, C. Dick, R. W. De Doncker, “Sensorless Direct Instantaneous Torque Control for Switched Reluctance Machines,” *11th European Conference on Power Electronics and Application EPE05*, Dresden, Germany, September 2005.

[10] H. J. Brauer, M. D. Hennen, R. W. De Doncker, “Control for Polyphase Switched Reluctance Machines to Minimize Torque Ripple and Decrease Ohmic Machine Losses,” *IEEE Trans. on Power Electronics*, vol. 27, no. 1, pp. 370–378, 2012

[11] A.-C. Pop, V. Petrus, J. Gyselinck, C. S. Martis, V. Iancu, “Comparative Study of Different Torque Sharing Functions for Losses Minimization in Switched Reluctance Motors,” *submitted for acceptance at 13th International Conference on Optimization of Electrical and Electronic Equipment, OPTIM 2012*, 24-26 May, Brasov, Romania.

[12] R. B. Inderka, R. B. Krehenbrink, R. W. De Doncker, “On-line estimation of instantaneous torque of switched reluctance machines,” *International Symposium on Industrial Electronics IEEE-ISIE*, pp. 385–389, 2000